MID-AMERICA
TRANSPORTATION CENTER

Report # MATC-KU: 146

Final Report
WBS: 25-1121-0003-146

Geosynthetic Reinforcement to Protect Underground Pipes against Damage from Construction and Traffic

Jie Han, Ph.D., PE
Professor
Department of Civil, Environmental, and Architectural Engineering
University of Kansas

Ryan Corey
Graduate Research Assistant

Deep K. Khatri
Graduate Research Assistant

Robert L. Parsons, Ph.D., PE
Professor

2016

A Cooperative Research Project sponsored by
U.S. Department of Transportation-Research
and Innovative Technology Administration

The contents of this report reflect the views of the authors, who are responsible for the facts and the accuracy of the information presented herein. This document is disseminated under the sponsorship of the Department of Transportation University Transportation Centers Program, in the interest of information exchange. The U.S. Government assumes no liability for the contents or use thereof.

Geosynthetic Reinforcement to Protect Underground Pipes against Damage from Construction and Traffic

Jie Han, Ph.D., PE
Professor
Department of Civil, Environmental, and Architectural Engineering
University of Kansas

Ryan Corey
Graduate Research Assistant
Department of Civil, Environmental, and Architectural Engineering
University of Kansas

Deep K. Khatri
Graduate Research Assistant
Department of Civil, Environmental, and Architectural Engineering
University of Kansas

Robert L. Parsons, Ph.D., PE
Professor
Department of Civil, Environmental, and Architectural Engineering
University of Kansas

A Report on Research Sponsored by

Mid-America Transportation Center

University of Nebraska-Lincoln

February 2016

Technical Report Documentation Page

1. Report No. WBS # 25-1121-0003-146	2. Government Accession No.	3. Recipient's Catalog No.	
4. Title and Subtitle Geosynthetic Reinforcement to Protect Underground Pipes against Damage from Construction and Traffic		5. Report Date February 2016 6. Performing Organization Code	
7. Author(s) Jie Han, Ryan Corey, Deep K. Khatri, and Robert L. Parsons		8. Performing Organization Report No. 25-1121-0003-146	
9. Performing Organization Name and Address University of Kansas, Lawrence Transportation Research Institute 2117 Learned Hall 1530 W 15th Street Lawrence, KS 66045		10. Work Unit No. (TRAIS) 11. Contract or Grant No.	
12. Sponsoring Organization Name and Address U.S. DOT Office of the Assistant Secretary for Research and Technology 1200 New Jersey Avenue, SE Washington, DC 20590		13. Type of Report and Period Covered Final Report 14. Sponsoring Agency Code MATC TRB RiP No. 33526	
15. Supplementary Notes			

16. Abstract

Shallowly buried pipes are subjected to surface loading, such as construction and traffic loading, and they may be damaged due to excessive loading and penetration by excavation equipment. A number of pipe incidents happened in the United States and around the world that resulted in fatalities, injuries, and significant property damage and loss. Therefore, protection of underground pipes against damage from construction and traffic are important and necessary. Unfortunately, no effective method is available so far. This proposed research was to develop a technology using geosynthetic reinforcement to protect underground pipes (either existing or new pipes) against damage from construction or traffic. The geosynthetic reinforcement is laid across the trench between the surface and the top of the pipe. The objective of this proposed research was to evaluate the level of protection provided to a steel-reinforced HDPE pipe by geogrid.

Seven static plate load tests, three cyclic plate load tests, and five rod penetration tests were conducted on shallowly-buried steel-reinforced HDPE pipes in the large geotechnical box (3 m x 2 m x 2 m) at the University of Kansas. Of the fifteen tests, five tests were run without geosynthetic as control sections for comparison to the geogrid-reinforced sections. Two backfill materials were used, which included a compacted sand backfill and a poured aggregate backfill. For all tests the in-situ soil was a fat clay. Earth pressure cells, displacement transducers, and strain gauges were installed around or on the pipe and the geosynthetic to investigate the effects of the geogrid and the backfill on the pipe performance and the surface deformation.

The analysis of test results shows that the type of backfill had an important effect on the pipe performance and the surface deformation and the benefits of geogrid reinforcement. Under static and cyclic plate loading tests, the geogrid placed underneath the base course was more effective in reducing the settlement of the plate, the vertical and horizontal deflections of the pipe, and the vertical earth pressures at the pipe crown and invert than that placed inside the trench. The inclusion of geogrid improved the distribution of earth pressures around the pipe and resulted in more uniform deformation of the pipe and minimized the bending of steel ribs at the pipe crown. Under static and cyclic plate loading tests and rod penetration tests, the geogrid provided lateral restraint to soil particle movement and reduced the longitudinal strains in the pipe liner. Geogrid reinforcement above the pipe increased the rod penetration resistance at the constant penetration depth or reduced the penetration depth under the same force. The inverted U-shape geogrid and wrapped-around geogrid layouts were more effective than the single and double geogrid layouts.

17. Key Words		18. Distribution Statement No restrictions.	
19. Security Classification (of this report) Unclassified	20. Security Classification (of this page) Unclassified	21. No. of Pages 236	22. Price NA

Abstract

Shallowly buried pipes are subjected to surface loading, such as construction and traffic loading, and they may be damaged due to excessive loading and penetration by excavation equipment. A number of pipe incidents happened in the United States and around the world that resulted in fatalities, injuries, and significant property damage and loss. Therefore, protection of underground pipes against damage from construction and traffic are important and necessary. Unfortunately, no effective method is available so far. This proposed research was to develop a technology using geosynthetic reinforcement to protect underground pipes (either existing or new pipes) against damage from construction or traffic. The geosynthetic reinforcement is laid across the trench between the surface and the top of the pipe. The objective of this proposed research was to evaluate the level of protection provided to a steel-reinforced HDPE pipe by geogrid.

Seven static plate load tests, three cyclic plate load tests, and five rod penetration tests were conducted on shallowly-buried steel-reinforced HDPE pipes in the large geotechnical box (3 m x 2 m x 2 m) at the University of Kansas. Of the fifteen tests, five tests were run without geosynthetic as control sections for comparison to the geogrid-reinforced sections. Two backfill materials were used, which included a compacted sand backfill and a poured aggregate backfill. For all tests the in-situ soil was a fat clay. Earth pressure cells, displacement transducers, and strain gauges were installed around or on the pipe and the geosynthetic to investigate the effects of the geogrid and the backfill on the pipe performance and the surface deformation.

The analysis of test results shows that the type of backfill had an important effect on the pipe performance and the surface deformation and the benefits of geogrid reinforcement. Under static and cyclic plate loading tests, the geogrid placed underneath the base course was more effective in reducing the settlement of the plate, the vertical and horizontal deflections of the pipe,

and the vertical earth pressures at the pipe crown and invert than that placed inside the trench. The inclusion of geogrid improved the distribution of earth pressures around the pipe and resulted in more uniform deformation of the pipe and minimized the bending of steel ribs at the pipe crown. Under static and cyclic plate loading tests and rod penetration tests, the geogrid provided lateral restraint to soil particle movement and reduced the longitudinal strains in the pipe liner. Geogrid reinforcement above the pipe increased the rod penetration resistance at the constant penetration depth or reduced the penetration depth under the same force. The inverted U-shape geogrid and wrapped-around geogrid layouts were more effective than the single and double geogrid layouts.

Table of Contents

List of Figures

List of Tables

Chapter 1 – Introduction

1.1 Background

In pipeline and buried conduits, as with any engineered structural or geotechnical system, it is generally desired to improve efficiency and performance and lower economic impact. Less than optimum conditions may exist for buried pipes, such as low cover or low-quality backfill, or an existing buried conduit may need to be restored or reconditioned. Methods of relieving stress and strain, reducing surface deflection, and reducing deflections in buried pipes and conduits include: induced trenches, relieving slabs, casings, and more recently, geosynthetics. Geosynthetics potentially offer a number of innovative and economical methods to enhance the performance of the pipe-soil system. Geosynthetics, which are factory-manufactured polymer materials in sheets (e.g., geotextiles, geogrids, and geomembranes) or cells (e.g., geocells), can be used as a stand-alone protection, or as a supplement to one of the other methods of protecting pipes and improving their performance. Geosynthetics have been used extensively to reinforce soil in retaining walls, embankments, and pavement applications. There appears to be an opportunity to increase the use of geosynthetics used with pipes, culverts, or underground utility lines to reduce the effect of surface loading (such as footings, highway traffics, and rails) and prevent damage by excavation equipment.

Projections of new buried pipe and conduit projects, replacements, and repairs of existing pipes and conduits indicate that there is a need for improved installation and protection methods. For the fiscal years 2013 to 2016, the state of Kansas alone has an estimated obligation of 9.8 million dollars for culvert replacement and repair (KDOT 2012).

In addition to culverts and drainage type applications there appears to be a need for improved protection of pipelines carrying hazardous materials. In the United States, between 1999

and 2009, there were over 5000 significant pipe incidents that resulted in 364 fatalities, 3406 injuries, and 4.4 billion dollars of property damage. Of those serious incidents, 25 percent were caused by excavation damage (Pipeline and Hazardous Materials Safety Administration [PHMSA], 2011). Currently, there are approximately 2.5 million miles of hazardous liquid and natural gas lines in the Unites States (PHMSA, 2011). Protection of other utilities such as water, effluent, electric lines, and fiber optic cables would be beneficial as well. Although damage of these utilities does not necessarily result in catastrophic events, there is a significant economic impact of damaged utilities.

A simple online search reveals numerous accidents involving natural gas or other hazardous material pipelines. In the summer of 2010, in Nanjing, China, workers dug into a gas pipeline. The resulting blast killed at least 12 people and injured another 300 people (Kuo, 2010). In Johnson County Texas, in June, 2010, workers installing utility poles caused a natural-gas line explosion, killing one and sending more to the hospital (Goldstein, 2010). In 2004, near Kingman, Kansas, 204,000 gallons of anhydrous ammonia was released. Although no one was injured, the total cost of the accident, $680,715, was primarily due to needed environmental remediation (NTSB, 2007).

1.2 Research Objective

The objective of this research is to identify the mechanism of interaction and distribution of forces and strains between geosynthetics and the soil and on pipe structure. It is also a goal to demonstrate an improvement in the performance of pipes and conduits protected by geosyntethics. This report is based on the static and dynamic plate loading tests, and penetration load tests performed in this study.

1.3 Organization of Report

Chapters 1 and 2 of this report cover the introduction and literature review of existing research on geosynthetic and pipes. Chapter 3 includes a description of the test setup, test procedures, and material properties used in the tests. The results of the static plate load tests, cyclic plate load tests, and penetration load tests are covered in Chapters 4, 5, and 6. Chapter 7 presents conclusions and recommendations from this study. Appendices A, B, C, and C provide the test data obtained in this study.

Chapter 2 Literature Review

2.1 Geosynthetics in Pipe Applications

The literature study revealed several methods of applying geosynthetics with pipe systems, which have been previously investigated and used. The pipe protection research can be grouped into the method and function of the reinforcement including: trench reinforcement, reinforcement for static loads, and reinforcement for repeated loads, utility cut repair, and protection from penetrating loads. Most of the previous research was limited to model testing, small scale testing, and numerical modeling. Only a few examples of full scale testing or case studies were available.

2.1.1 Trench Reinforcement

Jeypalan (1983) investigated the use of geofabric layers along a trench wall (Fig. 2.1) to reduce the deflections and bending strains for pipes buried in soft in-situ soil. By increasing the overall stiffness at the spring line, Jeypalan (1983) showed, with numerical analysis, that the pipe performance could be increased to a degree, comparable to improving the quality of the backfill. The improved lateral support for the flexible pipe reduced the pipe deflections and pipe wall moments. The inclusion of geosynthetics did increase the axial force in the pipe wall, which was foreseeable, as the stiffer backfill increased “ring compression”.

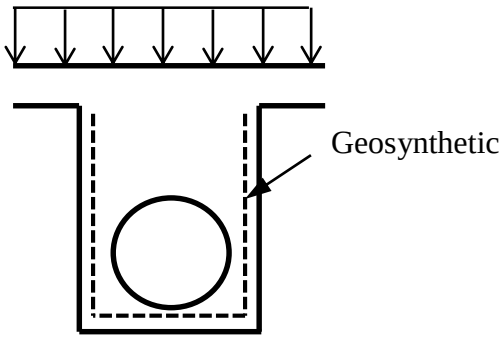

Figure 2.1 Trench Reinforcement (Jeypalan, 1983)

2.1.2 Reinforcement for Static Loads

Kennedy et al. (1988) performed model tests and numerical analysis on reinforced soil-steel bridges, which are a variation of the buried conduit. In soil-steel bridges, the corrugated steel plates that form the span are usually founded on footings and the span to depth of the arch is much greater than a conventional buried pipe. The height of cover is also generally small compared to the span that is wide enough to form a "bridge." In the study, the authors reinforced the layers of the backfill similar to a mechanically stabilized earth retaining wall (Fig 2.2), by attaching steel strip reinforcement to the conduit wall. In addition to an unreinforced soil steel bridge, continuous reinforcing above the crown of the arch was excluded in one case, and included in two other cases of varying cover. The authors showed that reinforcing the backfill increased the shear strength and improved the shear-failure plane in a manner similar to a geosynthetic reinforced retaining wall. The authors also demonstrated that the redundancy of the system was increased, specifically by including the reinforcement above the soil-steel bridge, significantly reducing the chances of a sudden catastrophic failure.

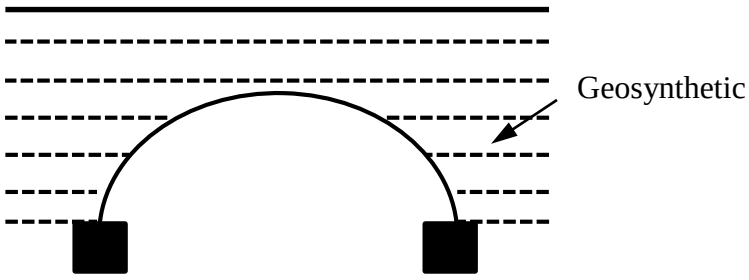

Figure 2.2 Soil-Steel Bridge Reinforced Backfill (Kennedy et al., 1988)

Pearson and Milligan (1991) performed a parametric scale-model study of a single layer of reinforcement, in this case, steel strips over a long-span flexible steel pipe. The long-span pipe is

generally defined as a pipe with a high enough span-to-stiffness ratio that the bending stiffness controls the behavior of the pipe. Although visually the graphic of the model test (Fig. 2.3) appears to represent a conventional buried pipe, the investigation was similar to the research of Kennedy et al. (1988) based on the factors controlling the design of the pipe, bending and deflection at the crown. The height of cover was varied from 1/8 to 1/4 of the span, and the height of the reinforcing layer varied from right on the crown, to the top of the cover. The width of the reinforcement was limited to the span (diameter) of the pipe. The load was applied to a 32 mm wide footing, which was also as long as the pipe, until the pipe soil system failed. It was found that, for a cover of 1/4 the span of the pipe, the optimum location was right at the crown of the pipe and the reinforcing effect diminished with increased height of reinforcement above the crown of the pipe. At the optimal location of the reinforcement, the pipe had an ultimate capacity increase of 25% and a maximum bending strain and deflection reduction of 50%.

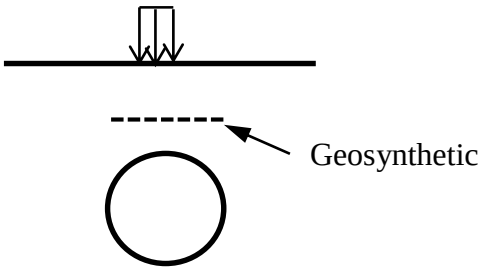

Figure 2.3 Single Reinforcement Layer over Pipe (Pearson and Milligan, 1991)

As part of a study on geogrid reinforcement of unpaved roads, Bauer (1994) conducted full-scale static load tests on an unpaved roadway with a 150 mm diameter steel conduit. The tests were performed in a 1.6 m wide by 2 m long box filled with sand, which included both unreinforced and reinforced conditions. The height of fill over the pipe and the depth of the geogrid reinforcement, which covered the entire box, was also varied. The static load was applied with a

0.15 m square footing concentrically, directly over the pipe and eccentrically at 150 mm off the center line of the pipe. Bauer (1994) demonstrated a reduction in the pipe and surface deflections due to the inclusion of the geogrid.

Kawabata et al. (2003) performed tests in a sand filled test pit of 2 m wide by 1 m long by 1 m deep with a 150 mm diameter aluminum pipe under a 450 mm thick cover. Three layers of geogrid were placed over the pipe and a uniform load was applied over the entire width and length of the test pit, duplicating an overburden load in a deeply buried condition. At 150 mm below the pipe, a movable plate was installed to simulate subsidence below the pipe. After the surface was loaded to 600 kN, the plate below the pipe was lowered 15 mm. The total vertical load on the pipe, as calculated by the prism method, was reduced by 25% by including the geosynthetic layers. Around the pipe, the normal and tangential soil stresses on the pipe were also significantly reduced.

Bueno et al. (2005) investigated combining geosynthetics with the trench condition in an application similar to Marston's early work, in which loose fill or compressible materials were placed directly over the pipe to reduce pressures on the pipe. The authors proposed a construction method, in which the pipe trench was excavated wider above the pipe, and a geosynthetic was placed at the bottom of the over-excavated trench (Fig. 2.4a). Under this condition the geosynthetic had anchorage and supported the load of the soil prism through tensioned membrane action and arching action. The authors suggest a number of backfill conditions can be used including compacted or loose backfill, and purposefully leaving a gap between the geosynthetic and the pipe. The authors also introduce a construction method for embankments where a fabricated channel piece or re-excavation over the pipe acts as the gap for the geosynthetic to bridge (Fig. 2.4b).

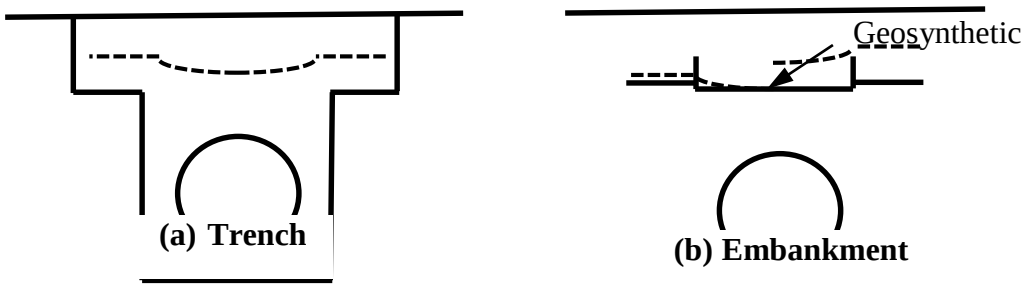

Figure 2.4 Geovala Method (Bueno et al., 2005)

Bueno et al. (2005) provided data on a large scale test they performed for a trench condition constructed with their proposed method. A 400 mm diameter pipe was placed in a narrow trench and the over excavation was widened to 600 mm. Backfill was not placed in the trench. Three different non-woven geotextiles were placed in three separate tests and a fill height of 200 mm was placed above the geosynthetic. A standard trench condition was also monitored. Uniform pressures were applied directly to the surface with an air bladder. An earth pressure cell measured the pressures above the pipe. In all cases with the proposed construction method, the earth pressures above the pipe were approximately half that under the standard trench condition.

Bathurst and Knight (1998) performed a series of numerical analysis of geocell reinforcement over long span pipes. Based on calibrations of full scale and reduced-scale tests, the authors were able to model the 0.2 m thick geocell reinforced soil as a composite material in a two-dimensional plane strain analysis of the pipe and backfill. The 6 meter span pipe with a varying cover thickness was loaded with a 0.2 m wide concentrated load. Analysis of the long span pipe with concentric (loaded at the mid span) and eccentric loading was provided. Failure resulted from the bearing failure of the soil or the axial load in the pipe exceeding the buckling capacity of

the pipe wall. The authors showed a marked increase in the ultimate capacity of the long span pipe with the inclusion of the geocell.

Rajkumar and Ilamparuthi (2008) ran tests with a 200 mm wide continuous loading plate on a 200 mm diameter PVC buried pipe. The tests were conducted at cover thicknesses of 200, 400, and 600 mm. A comparison of the 400 mm cover condition was run with a single layer of geogrid at 200 mm above the crown of the pipe. The reinforced condition had a pipe vertical deflection of 1.6 mm at 150 kPa versus 2.3 mm at 150 kPa for the unreinforced condition. The vertical and horizontal deflections of the pipe for the unreinforced and reinforced conditions were similar until the geogrid engaged; the deflections then linearly diverged and were smaller for the reinforced condition. At the maximum applied load the vertical and horizontal deflections of the pipe decreased approximately 0.3% with respect to the initial pipe diameter.

2.1.3 Reinforcement for Dynamic Loads

Lundvall and Turner (1997) investigated settlement of roadways over culverts and methods of minimizing the settlement. The authors experimentally investigated methods including using geosynthetic reinforced soil for mitigating rutting and settlement over culverts. The tests were run in a 1.4 m by 1.7 m by 1.5 m tall testing box. The authors performed model tests on a 200 mm corrugated metal pipe in a uniform clay backfill with the same clay acting as a 204 mm thick cover. An unreinforced condition and a reinforced condition were run with one layer of geogrid at 102 mm above the pipe. A dynamic load of 16 kN was applied with a 660 mm by 364 mm loading plate at a frequency of 0.204 Hz. The clay was placed in 100 to 120 mm lifts at maximum dry density and optimum moisture content. Results from the cyclic loading tests indicated no appreciable improvement of surface settlement as compared to the unreinforced condition, and for

both cases the surface settlement increased with the number of load cycles, indicating that the system was “unstable” and prone to rutting.

Mogohaddas Tafreshi and Khalaj (2007) performed laboratory tests and analysis on small diameter (110 mm) High Density Polyethylene (HDPE) pipes subjected to repeated loads. The height of fill above the pipe varied from 165 mm to 330 mm, and the fill above the pipe was reinforced with 1 to 5 equally spaced layers of geogrid (Fig. 2.5). The densities of the sand backfill were varied in tests at 42%, 52%, and 72% relative density. The width of the geosynthetic cover was 4.5 times the diameter of the pipe, and for the single layer of geosynthetic the width varied from 1 to 5 times the diameter of the pipe. Control runs without any geogrid reinforcement were also performed. The dynamic load was applied as 540 kPa pressure on a 100 mm plate at a frequency of 0.3 Hz to simulate traffic loads. The surface settlement was monitored with LVDTs and the pipe diameter was monitored with eight displacement transducers at the invert crown, spring line and quarter points between. Overall, a comprehensive array of 86 tests was run. Mogohaddas Tafreshi and Khalaj (2010) expanded on their 2007 research by varying the amplitude of the applied pressure from 550 kPa to 400 kPa and 220 kPa.

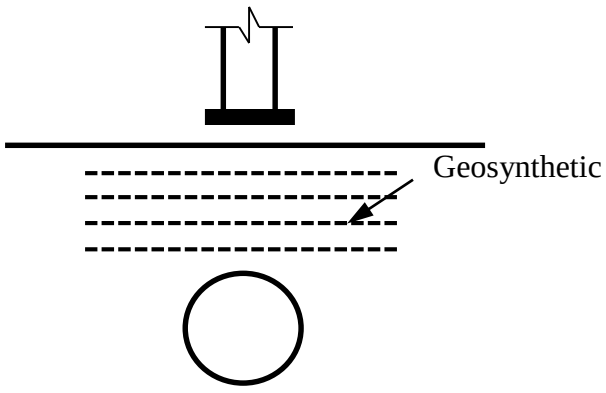

Figure 2.5 Dynamic Load Tests (Mogohaddas Tafreshi and Khalaj, 2010)

Mogohaddas Tafreshi and Khalaj (2010) found that increasing the number of geosynthetic layers, increasing the relative density of the soil, and increasing the depth of cover improved, or decreased, the final surface settlement and the vertical pipe deflection. Maximum deflections were in the vertical axis because of the concentric load and the rate of deformation decreased with the number of cycles. There was a significant reduction of the surface and pipe deflections with the inclusion of geosynthetic, specifically in lower density sands.

2.1.4 Utility Cut Repair

Kazemin et al. (2010) provided a case study of the use of geosynthetics to remediate improperly backfilled trenches that are subjected to traffic loading. The original construction consisted of a 1 m wide and 3 m deep trench constructed below a roadway. Remediation of the roadway with the geogrid was performed only at two man-holes spaced every 100 meters. An unreinforced (control) section was monitored in addition to two locations with two different geogrids. At the locations of the man-holes the trench was 2 meters wide. Sand was placed up to the crown of the pipe (approximately 50 mm), in-situ soil was placed into the trench up to 1.25 m below the surface, and the remainder of the fill was crushed gravel. Finally a 20 mm thick base course of crushed rock and a 50 mm layer of asphalt were used. In the locations where the geogrid layers were used, the 24 m wide geogrid reinforcement was placed directly on the base course centered over the pipe and manhole. The surface settlement was monitored at 3 months, 6 months, and 12 months. After monitoring, the authors stated that there was no visual distress in the reinforced section while there were visible settlements in the unreinforced section. Measured reductions in the displacements of the reinforced sections, at the end of 12 months, as compared to the unreinforced section were in the range of 40 - 50%.

2.1.5 Protection from Penetrating Loads

Palmeira and Andrade (2010) proposed and performed full scale tests of the protection of buried pipes using geosynthetics (Fig. 2.6). In their tests 75 mm diameter pipes were buried with a 150 mm thick cover and geosynethics with varying configurations: single layer, inverted U-shape, and complete envelopment around the pipe. The geosynthetic was placed at 75 mm deep for all reinforcing conditions and additionally in a separate test at 37.5 mm deep. Penetrating loads in the form of a 20 mm thick continuous plate were used to simulate excavation or similar equipment. The inclination and location of the penetrating load was also varied. Plate penetration, earth pressures around the crown invert and the spring line, and pipe strains on the crown invert and the spring line were monitored. In the full scale tests, the pipe strains were reduced, pressures on the pipe were reduced for the envelopment condition, and most significantly, the force required to achieve the same amount of plate penetration as the unreinforced condition was significantly higher.

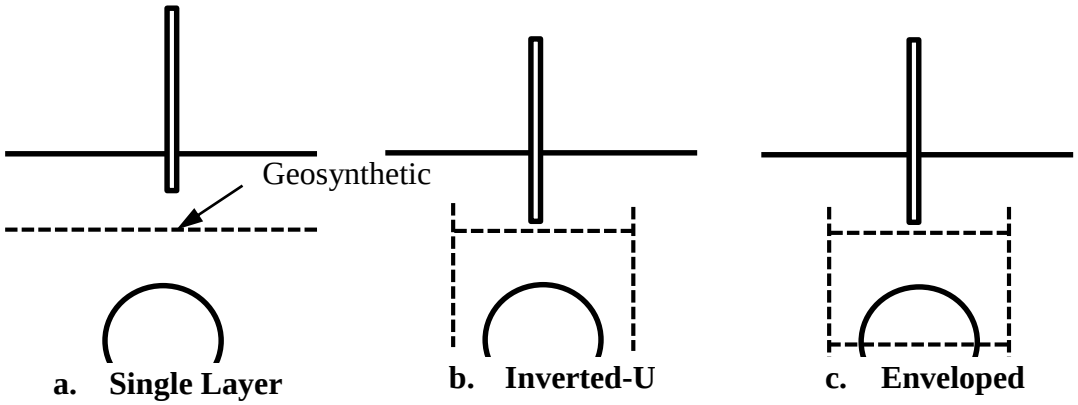

Figure 2.6 Geosynthetic Protection (Palmeria and Andrade, 2010)

Chapter 3 - Materials and Experimental Setup

3.1 Introduction

To complement research on flexible pipes, this study introduced geosynthetic reinforcing to the same sections tested for unreinforced conditions to investigate the interaction between the geosynthetic, the soil, and the pipe. The tests were designed to investigate the pipe, soil, and geosynthetic interaction with static loads, cyclic loads, and protection from penetrating loads. Tests were run in a 3 meter wide by 2 meter long by 2 meter deep box (Fig. 3.1) at the Department of Civil, Environmental, and Architectural Engineering at the University of Kansas. The box was extended to a width of 3 meters specifically for the pipe tests in this study.

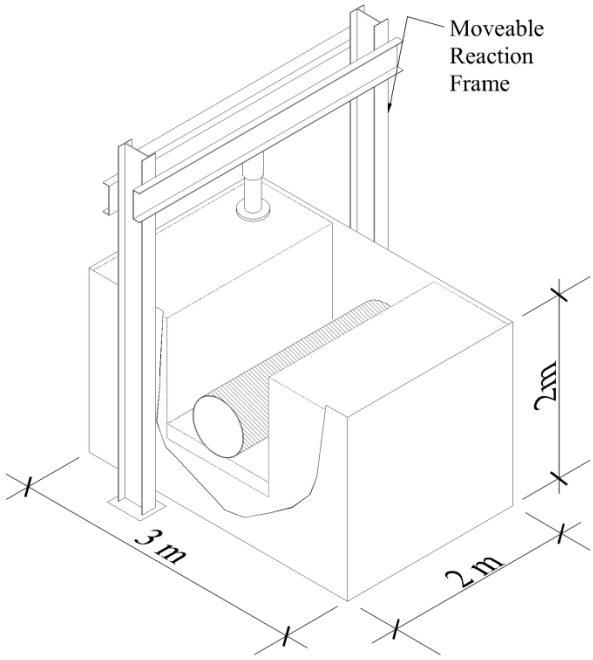

Figure 3.1 Big Box Setup

For the full scale investigations the materials used were chosen based on common practice in the state of Kansas. A 0.61 m diameter 2 m long steel-reinforced HDPE pipe was centered in the 3 meter width of the box. The pipe was placed in a 1.22 m wide by 1.14 m deep trench created in a Fat Clay (CH) in-situ soil. Poorly-graded Kansas River sand and clean aggregate materials were used as backfill inside the trench. A layer of compacted, well graded aggregate (called AB-3) or poorly-graded Kansas River sand was used to create a base course or an unpaved road condition. The specifics of the pipe and soil properties are discussed in the following sections of this chapter.

The tests were completed at three unique times in between which the pipe, backfill, base course and in-situ soil were removed. These three test sets, and the applicable materials, are shown in Tables 3.1, 3.2, and 3.3. Figure 3.2 shows the reinforcement layouts. At the end of each test set, the pipe sample, the geogrid and strain gauges were scrapped. During testing of the three sets, for instance between tests 1-9, only the backfill and the base course were removed to change base course materials or add reinforcing layers. The pipe was not removed, strain gauges were replaced if necessary, and the new materials were placed and compacted to meet the initial conditions.

Table 3.1 Plate Load Tests with Sand Backfill

Test No.	Test Type	Base Course	Reinforcing
1	SPL	AB-3	U.R.
2	SPL	Sand	U.R.
3	SPL	Sand	Single Layer
4	SPL	AB-3	Double Layer

SPL – Static Plate Load, CPL –Cyclic Plate Load Test, U.R. – Unreinforced

Table 3.2 Plate Load Tests with Aggregate Backfill and AB-3 Base Course

Test No.	Test Type	Base Course	Reinforcing
5	SPL	AB-3	U.R.
6	CPL	AB-3	U.R.
7	SPL	AB-3	Single Layer
8	CPL	AB-3	Single Layer
9	SPL	AB-3	Double Layer
10	CPL	AB-3	Double Layer

SPL – Static Plate Load, CPL –Cyclic Plate Load Test, U.R. – Unreinforced

Table 3.3 Penetration Tests with Aggregate Backfill and AB-3 Base Course

Test No.	Reinforcing
11	U.R.
12	1 Layer
13	2 Layers
14	Inverted U-shape
15	Wrapped Around

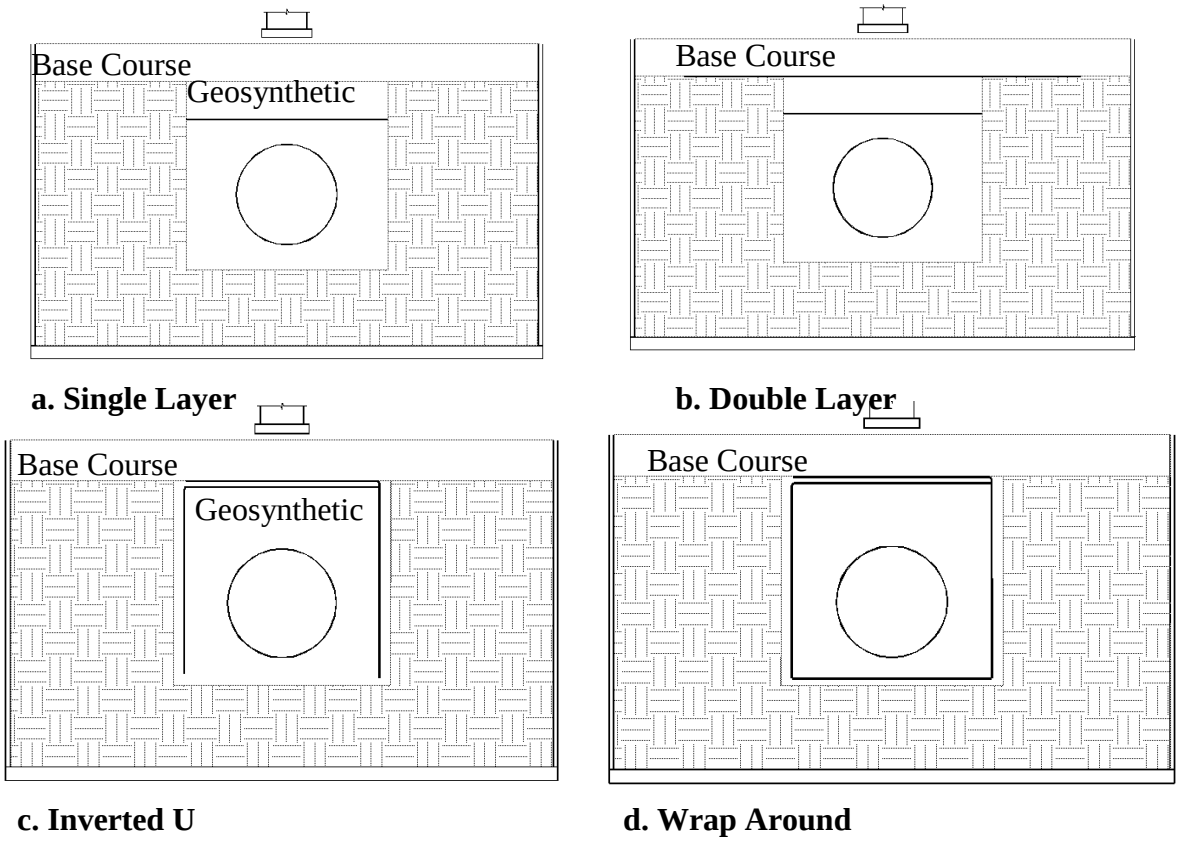

Figure 3.2 Geogrid Reinforcing

The properties of the materials (pipe, insitu soil, base course, and geogrid) and instrumentation used in this study are discussed below.

3.2 Steel-Reinforced HDPE Pipe

3.2.1 Pipe Material

The pipe used for the full-scale tests was a 0.61 m diameter helically-wound steel-reinforced HDPE pipe. The pipe consisted of an HDPE shell with 13 mm by 1.5 mm steel ribs outstanding from the pipe wall. Each outstanding rib was 25.4 mm on center and encapsulated in HDPE which is integral with the pipe wall. The pipe material properties are shown in Table 3.4.

Khatri (2012) completed parallel plate load tests on the steel-reinforced HDPE pipe. The results from a typical test can be seen in Figure 3.3. Calculating the pipe stiffness (PS) from the parallel plate load tests at a 5% vertical deflection (30.5 mm) yields a stiffness of 295 kPa. Currently, this pipe is a fairly new technology, and an important aspect of this report is the performance and behavior of the pipe selected. A comparison of published pipe stiffness values for HDPE, CSP, and RCP to the pipe stiffness for the steel-reinforced HDPE pipe is shown in Figure 3.4.

Table 3.4 Pipe Structural Properties

(Provided by the manufacturer)

Nominal Pipe Diameter (m)	0.61
Moment of Inertia (Steel Only) (mm^4/mm)	10.5
Modulus of Elasticity Steel, E_s (GPa)	200
Steel Yield Strength, F_y (MPa)	522
Pipe Wall Area (Steel Only) (mm^2/mm)	0.752
Modulus of Elasticity HDPE, E_p (MPa)	441

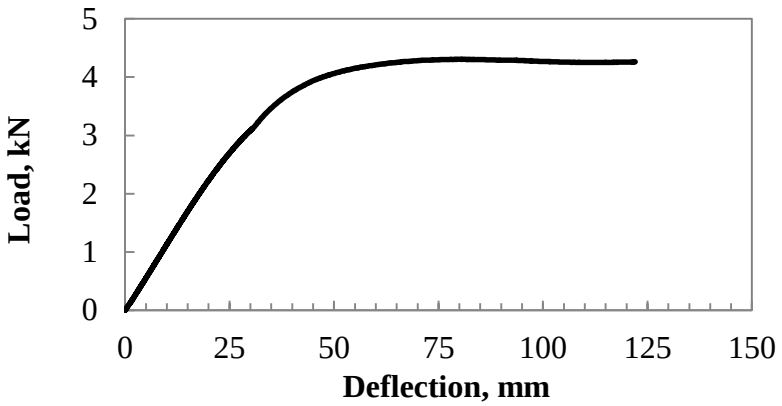

Figure 3.3 Parallel Plate Load Test for 610 mm Diameter Steel Reinforced HDPE Pipe

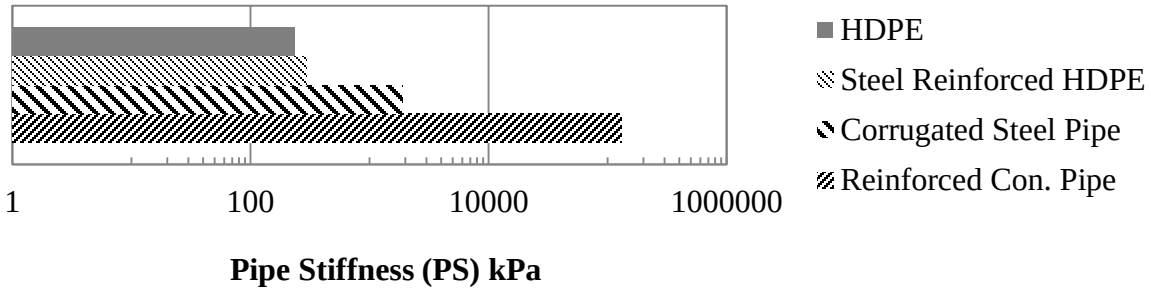

Figure 3.4 Steel Reinforced Pipe Stiffness (PS)

The steel-reinforced HDPE pipe stiffness, as measured by the parallel plate test, is most comparable to the HDPE pipe. It is important to note that the parallel plate loading test is primarily a representation of the bending stiffness of the pipe. The steel reinforcement in the pipe wall is a magnitude of order greater in the axial stiffness than the HDPE. It is expected that with a well compacted backfill, the buried pipe will behave more like a corrugated steel pipe because of the axial stiffness.

3.2.2 Pipe Instrumentation

For each of the following tests, two displacement transducers were placed at the center of the pipe directly under the loading plate to measure the relative vertical displacement of the crown and the invert, and the relative horizontal displacements of the spring line. One transducer was placed vertically to measure the vertical displacements of the pipe, while the second transducer was placed in a horizontal position to measure horizontal displacements of the pipe section. A third displacement transducer was placed vertically at the center line of the pipe and 300 mm longitudinally from the loading plate. The three displacement transducers DT 1, DT 2, and DT 3 can be seen in Figure 3.5.

Two string potentiometers as tell-tales were attached to the crown of the pipe to measure the movement of the crown of the pipe in relation to a stationary datum. One tell-tale was attached to the crown of the pipe directly under the loading plate/rod while the second was placed 300 mm longitudinally similar to the displacement transducer setup.

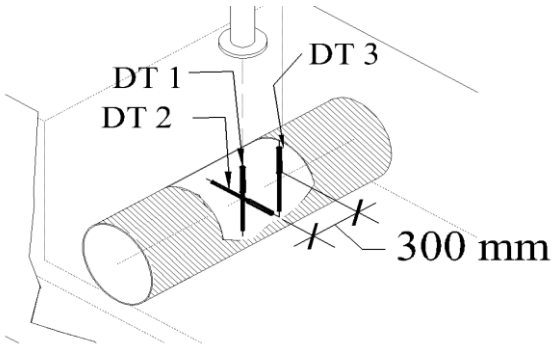

Figure 3.5 Displacement Transducer Setup

Strain gauges were placed around the pipe to monitor the strains in the pipe wall during construction of the experiment and during the experiment itself. The strain gauges were uniaxial foil-type electrical resistance strain gauges (C2A-13-250 LW-120). The manufacturer's specifications show that this type of strain gauge has accuracy of 1μ or 0.0001%. Strain gauges were placed at the invert, the crown, and the spring line of the pipe, directly under the loading plate. The circumferential and radial strain gauges were placed on both sides of the outstanding steel and plastic portions of the ribs, while the longitudinal strain gauges were placed on the inside and outside of the pipe wall. A section of the pipe wall with strain gauges can be seen in Figure 3.6.

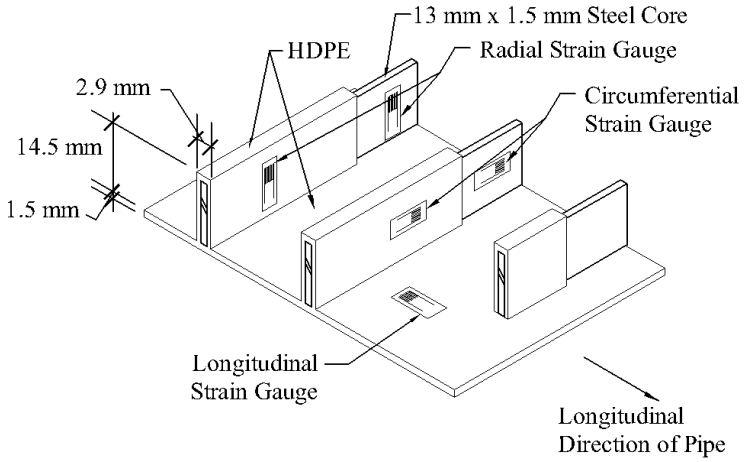

Figure 3.6 Pipe Wall Section and Strain Gauge Orientation

Twenty five strain gauges were placed on the pipe in the radial (R), the circumferential (C), and longitudinal (L) directions. All strain gauges were placed within 25 mm of the longitudinal centerline of the pipe, directly under the loading plate. Since the pipe is a composite material, the strain gauges were placed on the steel (Fig. 3.7a) and the plastic cover (Fig. 3.7 b). In the

longitudinal direction there is no steel and the strain gauges were placed on the plastic only (Fig 3.8).

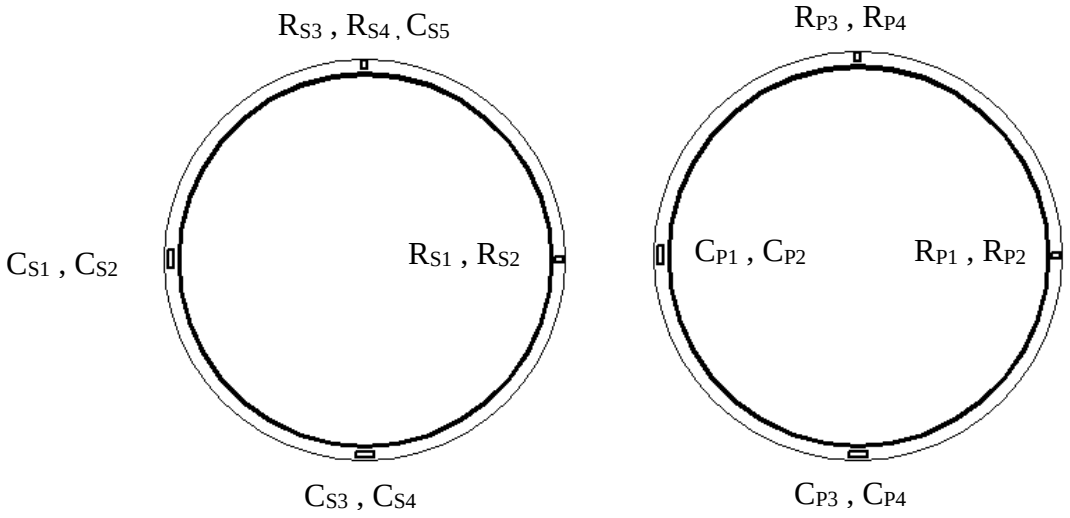

a. Steel **b. Plastic**

Figure 3.7 Circumferential and Radial Strain Gauge Locations

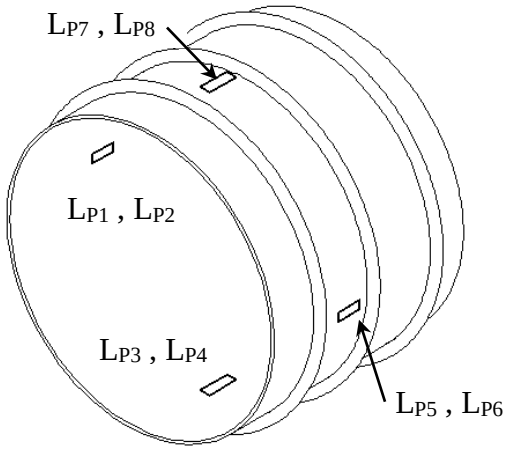

Figure 3.8 Longitudinal Strain Gauge Locations

3.3 Insitu soil

The insitu soil in which the pipe and backfill were placed was a Fat Clay (CH). The Fat Clay is a locally available soil in Kansas and many pipes have been buried in this type of soil. The properties of this soil are provided in Table 3.5. Vane shear and CBR tests were run on standard Proctor test samples to correlate the Fat Clay compaction curve to CBR and undrained shear strengths (Khatri 2013).

To avoid the need for excavation of a trench in the laboratory, the trench was built from the floor of the box up. A 0.46 m thick Fat Clay was laid across the width of the box. Each side of the trench was shored with plywood walls, and the remainder of the Fat Clay was placed behind the shored walls. After the clay was placed and compacted, the shored walls were removed leaving a 1.22 m by 1.14 m trench (Fig 3.9). The lifts were placed at 26% moisture content and compacted to maintain a CBR between 2% and 3%. The CBR values correlated to a placed dry density of 14.4 kN/m^3 and undrained shear strength of 75 kPa. Dynamic cone penetrometer (DCP) and vane shear tests were conducted to maintain the uniformity and strength of the Fat Clay for each lift.

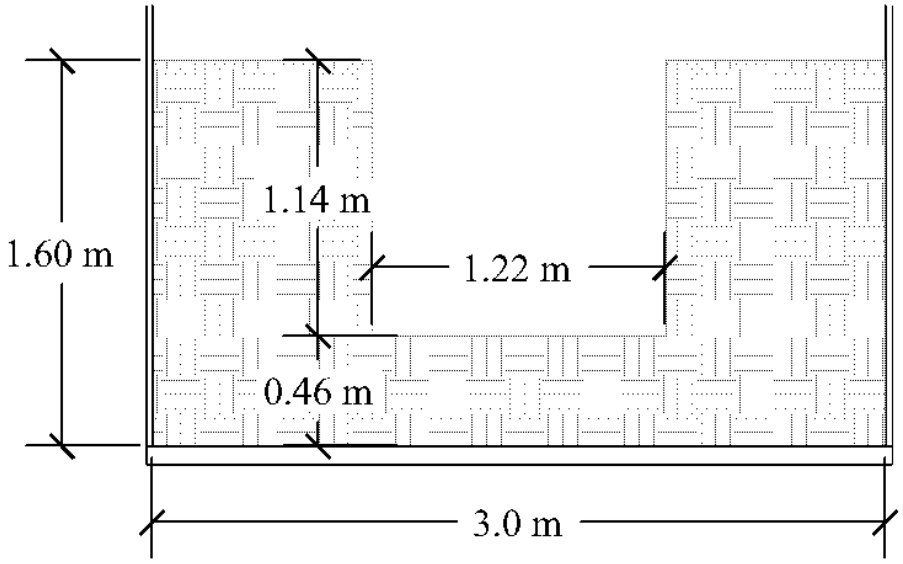

Figure 3.9 Fat Clay Trench

Table 3.5 Fat Clay Properties

Liquid/Plastic Limit, LL/PL	54/26
Specific Gravity, G_s	2.71
Maximum Dry Unit Weight, γ_{dmax} (kN/m^3)	15.4
Optimum Moisture Content, w_{opt} (%)	24
Unconfined Compressive Strength q_u at installed density (kPa)	75

3.4 Backfill

3.4.1 Backfill Material Properties

In the large box tests, two backfills were used in the trench: Kansas River sand and crushed stone aggregate. The sand was chosen as a backfill material for a less than optimal cohesionless backfill condition, while the crushed stone aggregate was selected as an optimal backfill material. This would give a range of backfill conditions that could be used in subsequent research.

Nine triaxial tests were run on the sand backfill materials at varying densities. Tests for a loose condition, a condition of minimal compaction, and a heavily compacted sample, which had relative densities of 25%, 40% and 77% respectively, were completed. For each density, triaxial shear tests were completed at three confining stresses: 103.4, 68.9, and 34.5 kPa. The deviator strain was applied at a constant rate of 0.2% per minute. The results of the triaxial tests can be seen in Figures 3.10 through 3.12.

An isotropic compression test was also run on the loose sand condition to capture the bulk modulus of the sand. At the beginning of this test a uniform pressure outside and an equal pressure inside the sample were applied to saturate the sample. An external confining pressure was then applied in 13.8 kPa steps. The change in volume of the test sample was monitored with the burette.

An attempt was also made to determine the ratio of the plastic volumetric strain to the elastic volumetric strain. At the pressure of 96.5 kPa, the confining pressure was reduced in two 13.8 kPa steps. A positive confining pressure was then applied again in 13.8 kPa steps until a maximum pressure of 151.7 kPa was reached. The results of the isotropic compression test can be seen in Figure 3.13.

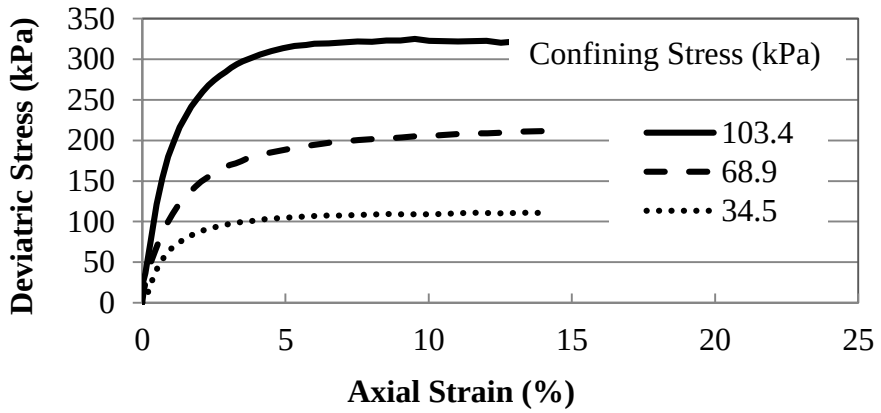

Figure 3.10 Triaxial Compression Test of Loose Sand at 25% Relative Density

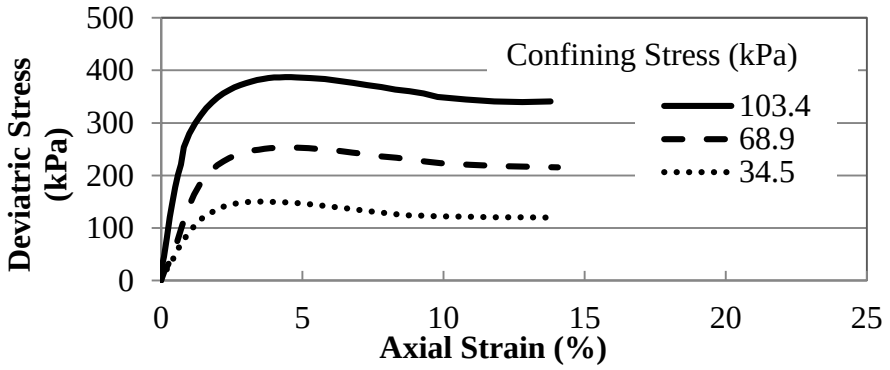

Figure 3.11 Triaxial Compression Test of Medium Dense Sand at 40% Relative Density

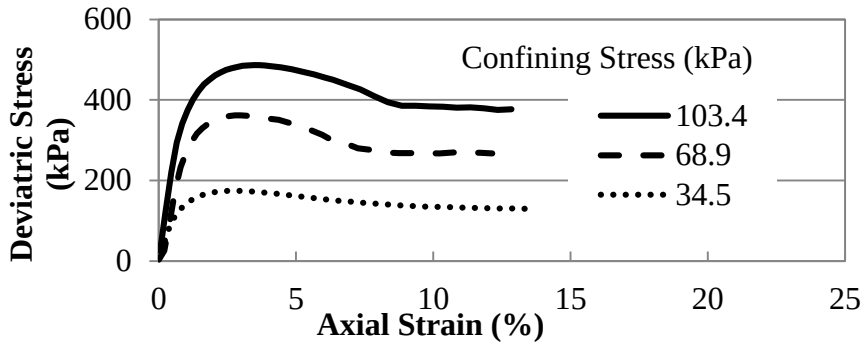

Figure 3.12 Triaxial Compression Test of Dense Sand at 77% Relative Density

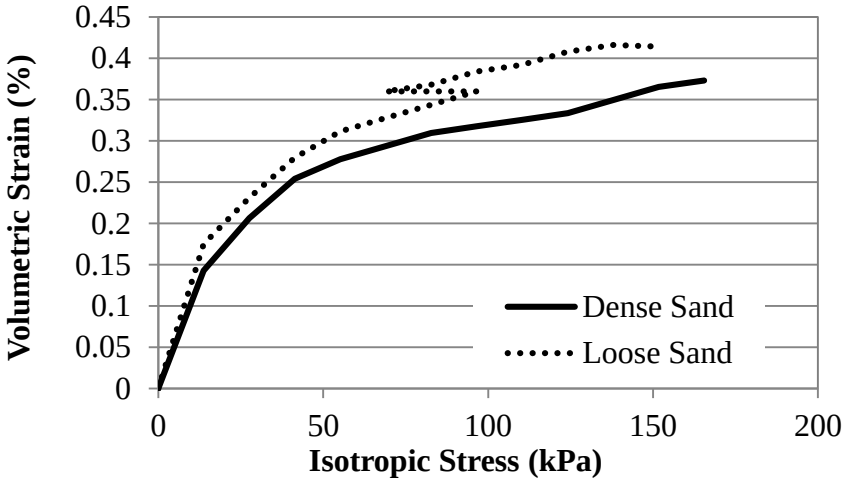

Figure 3.13 Isotropic Compression Test Results of Loose and Dense Sand

Triaxial tests were also run on the crushed stone aggregate backfill material at one density, which corresponds to a dumped condition with no compaction. For the triaxial tests three confining stresses: 68.9, 51.7, and 34.5 kPa were used. The deviator strain was applied at a constant rate of 0.2% per minute. The results of the triaxial tests can be seen in Figures 3.14. The backfill material properties can be seen in Tables 3.6 and 3.7.

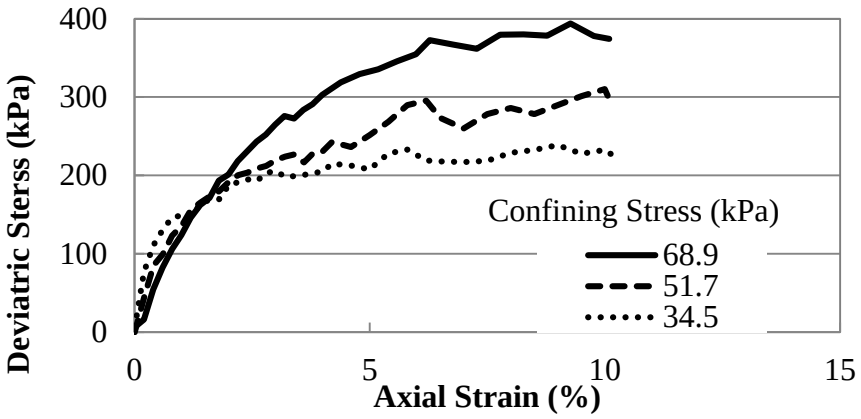

Figure 3.14 Triaxial Compression Test of Aggregate

Table 3.6 Kansas River Sand Material Properties

Maximum Dry Unit Weight, γ_{dmax} (kN/m^3)	19
Minimum Dry Unit Weight, γ_{dmax} (kN/m^3)	16
Coef. of Curvature / Uniformity, Cc/Cu	0.93/3.18
Mean Particle Size (mm)	0.5
Friction Angle ϕ_P/ϕ_R at 25% D_r (Triaxial Test)	38^o/38^o
Friction Angle ϕ_P/ϕ_R at 40% D_r (Triaxial Test)	41.5^o/39^o
Friction Angle ϕ_P/ϕ_R at 77% D_r (Triaxial Test)	45.5^o/41.5^o

Table 3.7 Aggregate Material Properties

Maximum Dry Unit Weight, γ_{dmax} (kN/m^3)	16.2
Minimum Dry Unit Weight, γ_{dmax} (kN/m^3)	13.5
Coef. of Curvature / Uniformity, Cc/Cu	1.01/2.3
Mean Particle Size (mm)	11.2
Max Particle size (mm)	19
Peak Friction Angle ϕ at 45% D_r (Triaxial Test)	49^o

3.4.2 Backfill Installation

The material used for the backfill and the bedding in the first set of tests was Kansas River sand. The bedding for the pipe was placed in a 152 mm lift. The sand was placed in 152 mm lifts in the trench and the last lift at the top of the trench was 76 mm thick. Each lift was compacted to a relative density of 70%, and was controlled by knowing the appropriate volume of sand required for the desired lift thickness and density. The placement of the backfill can be seen in Figure 3.15. The middle third of the bedding was not compacted, consistent with the Kansas Department of Transportation specification (2007), to alleviate a stress concentration at the base of the pipe. Lifts 1 through 4 were placed with an electric jack hammer and a vibratory plate compactor was used for the bedding and the remaining lifts.

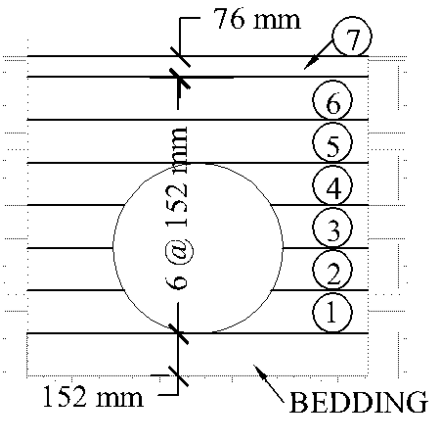

Figure 3.15 Backfill Installation

The second and third set of tests were run with an aggregate bedding and backfill. The aggregate backfill was dumped in 152 mm lifts without compaction at a dry density of 14.6 kN/m^3. The lifts of aggregate were "dumped" into the trench simultaneously on each side of the pipe at the same time to prevent the pipe from distorting laterally. A comparison of the pipe deflections during placement of the different lifts of backfill can be seen in Figures 3.16 and 3.17. Lifts 8 and 9, not shown in Figure 3.15, represent the placement of the base course in two 190 mm lifts.

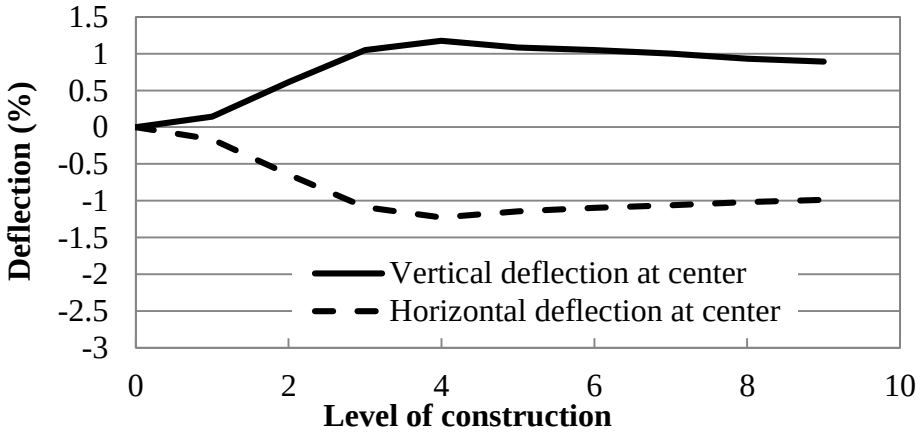

Figure 3.16 Pipe Deflection during Sand Backfill Placement

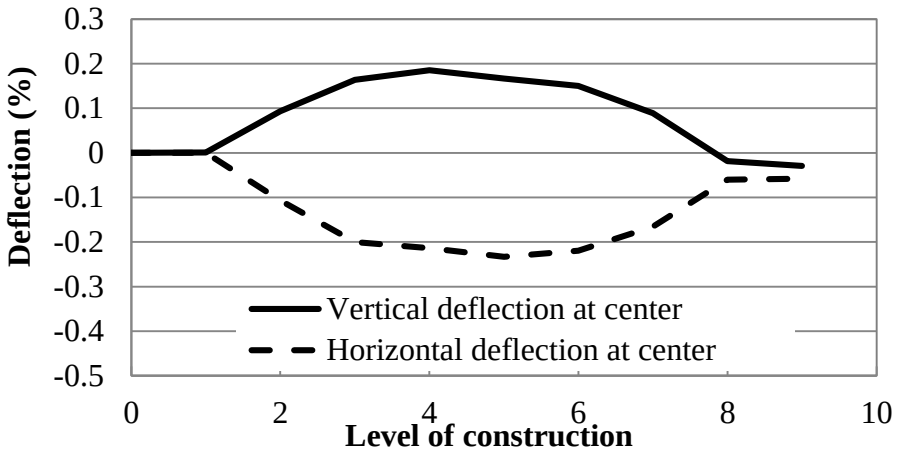

Figure 3.17 Pipe Deflection during Crushed Aggregate Placement

3.4.3 Backfill Instrumentation

During the installation of the backfill, earth pressure cells were placed at the crown, the invert, and the spring line (Fig. 3.18). A total of five earth pressure cells (I_1, S_1, S_2, C_1, and C_2) were placed for the first set of tests (1-4). For the second set of tests (5-10), five additional earth pressure cells were placed for a total of 10 earth pressure cells. In the final penetration tests, pressure cell C_4 was removed. Two models of earth pressure cell were used, one with a 200 kPa (KDE-200) capacity and the second with a 500 kPa (KDE-500) capacity. With the crushed aggregate backfill, the earth pressure cells were protected by sand filled bags.

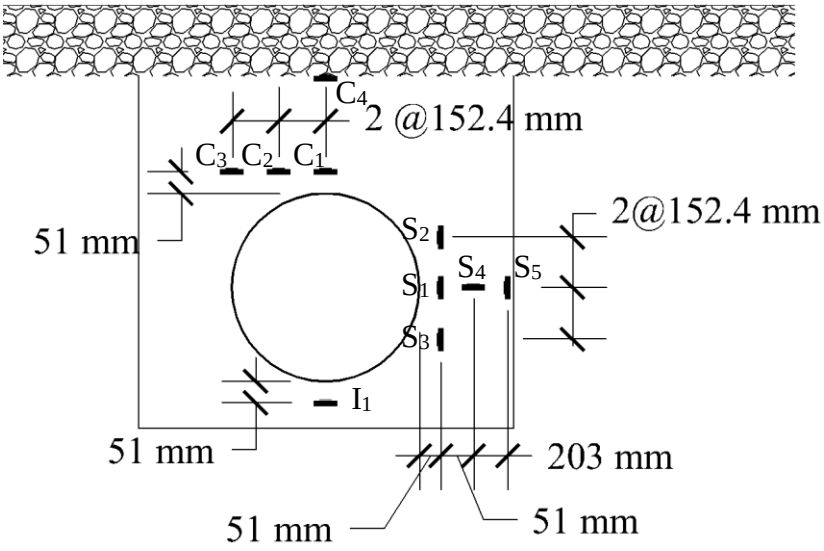

Figure 3.18 Earth Pressure Cell Locations

3.5 Base Course

The first test set used aggregate and sand base courses in separate testing runs while the second and third test sets were run exclusively with a 230 mm thick aggregate base course. The properties of the base course summarized by Yang (2010) are listed in Table 3.8. The base course was installed and compacted to a 95% maximum dry density from the Standard Proctor Test. Dynamic Cone Penetration tests were conducted at four locations to control the stiffness and consistency of the base course throughout the tests.

The same Kansas River sand that was used as backfill material was also used as a 0.23 m thick base course in two of the tests. The sand was placed in two 115 mm lifts. The density was controlled by knowing the volume of sand necessary to fill the lift and be compacted to a relative density of 70%.

Table 3.8 Properties of Aggregate Base Course

Liquid/Plastic Limit, LL/PL	20/13
Specific Gravity, G_s	2.69
Maximum Dry Unit Weight, γ_{dmax} (kN/m^3)	20.6
Optimum Moisture Content, w_{opt} (%)	10
Coef. of Curvature / Uniformity, Cc/Cu	1.55/21
Mean Particle Size (mm)	7.0
Peak Friction Angle, ϕ_P/ϕ_R (Direct Shear)	$52^o/47^o$
Cohesion Peak/Residual (kPa)	7.2/4.7

3.6 Geogrid

3.6.1 Geogrid Material Properties

The geogrid used for the protection of the pipe was a biaxial polypropylene geogrid with a 25 mm by 33 mm aperture size, manufactured by Tensar International. The strengths of the geogrid were published by the manufacturer as follows: (1) strengths in the cross-machine direction were 9 kN/m at 2% strain and 19.6 kN/m at 5% strain, (2) strengths in the machine direction were 6 kN/m at 2% strain and 11.8 kN/m at 5 % strain, and (3) ultimate strengths were 28.8 kN/m in the cross-machine direction and 19.2 kN/m in the machine direction.

Considering how a geosynthetic layer would be applied in a pipeline project, the geogrid was laid with the machine direction parallel to the pipe. Conceivably, this would allow the geogrid to be rolled out along the pipe in an application in the field. When the wrapped-around and inverted U-shape reinforcements were used, it was decided to change the machine direction of the

geogrid to perpendicular to the pipe to ease the placement of the geogrid “around” the pipe and backfill.

3.6.2 Geogrid Instrumentation

In each test that included geogrid reinforcement, uniaxial foil-type electrical resistance strain gages (C2A-13-250 LW-120) were placed on the layers of geogrid in the machine direction and cross-machine direction, parallel to the pipe and perpendicular to the pipe, respectively, as seen in Fig. 3.19. The lower geogrid, when used, was placed at 0.15 m above the pipe crown. The width of the lower geogrid was limited by the trench width for these tests. The upper geogrid was placed at the interface of the base course and the subgrade, allowing the width of coverage to be expanded to 2.4 m. The geogrid covered the length of the pipe and the coverage perpendicular to the pipe length can be seen in Fig. 3.19. Four strain gages were placed in each direction starting directly under the loading plate and incrementally farther away from the center line of the geogrid. On the lower layer of geogrid, the strain gages in the cross-machine direction were placed at 150 mm on center to accommodate four strain gages before reaching the trench wall. All other strain gages were placed at 200 mm on center. For the wrapped-around condition the geogrid was placed between the backfill and the trench wall (Fig. 3.20).

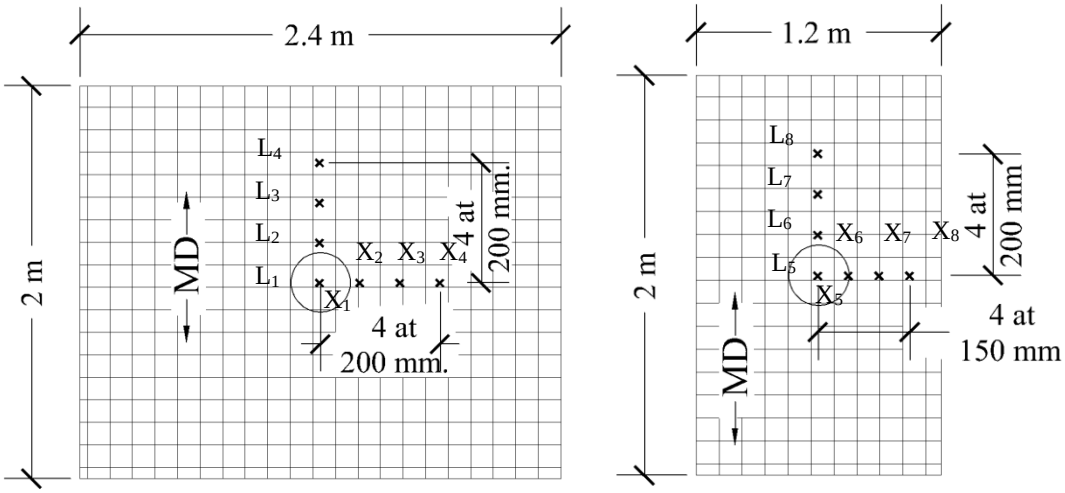

A. Upper Layer **B. Lower Layer**

Figure 3.19 Strain Gauges on Single and Double Geogrid Layers

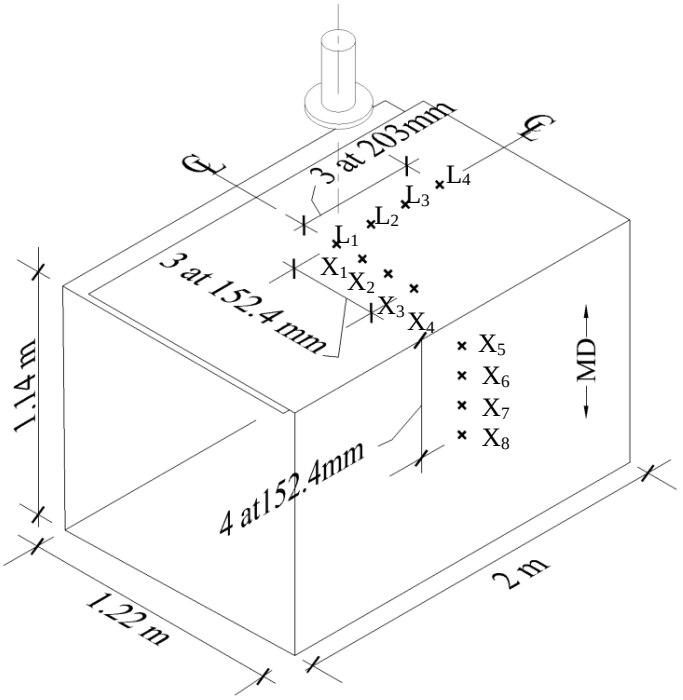

Figure 3.20 Strain Gauges on Inverted U-shape and Wrapped-Around Geogrids

Because the machine direction of the geogrid varied on the penetration tests, the L designation means longitudinal with the pipe and the X designation refers to the cross direction, or perpendicular to the longitudinal axis of the pipe.

3.7 Load Application

The plate and penetrating loads were controlled and monitored by an integrated actuator, hydraulic pump, and software package. The actuator had a maximum 245 kN capacity and was attached to a moveable reaction frame. A displacement transducer inside the actuator was used to monitor the displacement of the plate and the penetrating rod. An MTS actuator was used to apply the load and Multi-Purpose Test Ware software was used to monitor the applied loads and the displacements of the loading plate.

3.7.1 Static Plate Load Tests

A 0.30 m diameter loading plate with a rubber base was used to apply a static load in the load increments as shown in Table 3.9. Additional three tests labeled as Tests 6, 8, and 10 were conducted under cyclic loading and will be presented in next section. The maximum plate pressure of 552 kPa approximates a tire pressure of a wheel in a standard axle of a highway truck. Based on prior experience and observation, however, it was apparent that the sand base course would not be able to support the 552 kPa pressure. Therefore, a reduced load of 345 kPa was chosen. The interval was selected to ensure there were at least eight to ten data points for each pressure-settlement curve. After the maximum pressure was reached, the load was reduced and the data from instrumentation was recorded at three data steps including the removal of all load from the plate.

Table 3.9 Static Load Tests

Test No.	Backfill	Base Course	Geogrid Reinforcement	Pressure Increment (kPa)	Maximum Pressure (kPa)
1	Sand	AB-3	U.R.	68.9	551
2	Sand	Sand	U.R.	34.5	345
3	Sand	Sand	Single Layer	34.5	345
4	Sand	AB-3	Double Layer	68.9	551
5	Agg.	AB-3	U.R.	68.9	689
7	Agg.	AB-3	Single Layer	68.9	689
9	Agg.	AB-3	Double Layer	68.9	689

3.7.2 Cyclic Plate Load Tests

Cyclic loads as shown in Table 3.10 were applied to simulate the traffic loading with the same 0.3 m diameter loading plate as the static loading test. Each cyclic load had a trough value of 7 kPa, which was applied to keep the plate in contact with the surface and to prevent impact loading on the surface. The loading wave frequency was 0.77 Hz. The cyclic wave form is shown in Figure 3.21.

Table 3.10 Cyclic Load Tests

Test No.	Backfill	Base Course	Geogrid Reinforcement	Pressure Increment (kPa)	Maximum Peak Pressure (kPa)
6	Agg.	AB-3	U.R.	137.8	689
8	Agg.	AB-3	Single Layer	137.8	689
10	Agg.	AB-3	Double Layer	137.8	689

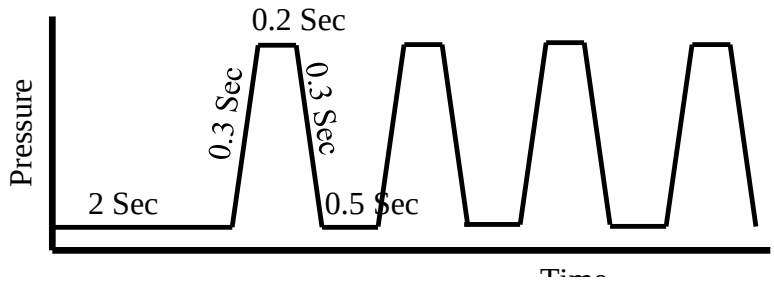

Figure 3.21 Cyclic Wave Form

3.7.3 Penetrating Load Tests

To simulate a construction equipment accident, a 100 mm diameter by 350 mm long steel round bar was connected to the actuator to penetrate the test sections vertically using the hydraulic actuator. The penetration was carried out at intervals of 12.7 mm up to a maximum penetration of 305 mm. The force was monitored during and after the penetration increment. The next penetration step was taken only after the load, the deflection and strains had balanced.

Chapter 4 Static Plate Test Results

4.1 Introduction

A total of seven static load plate tests were run; four with sand backfill and three with crushed stone aggregate backfill (Table 4.1). Tests 6, 8, and 10 were conducted under cyclic loading as shown in Table 3.10 and will be discussed later. The geogrid placement is show in Figure 4.1.

Table 4.1 Static Plate Load Tests

Test No.	Back fill	Base Course	Reinforcement
1	Sand	AB-3	U.R.
2	Sand	Sand	U.R.
3	Sand	Sand	Single Layer
4	Sand	AB-3	Double Layer
5	Agg.	AB-3	U.R.
7	Agg.	AB-3	Single Layer
9	Agg.	AB-3	Double Layer

U.R. – Unreinforced

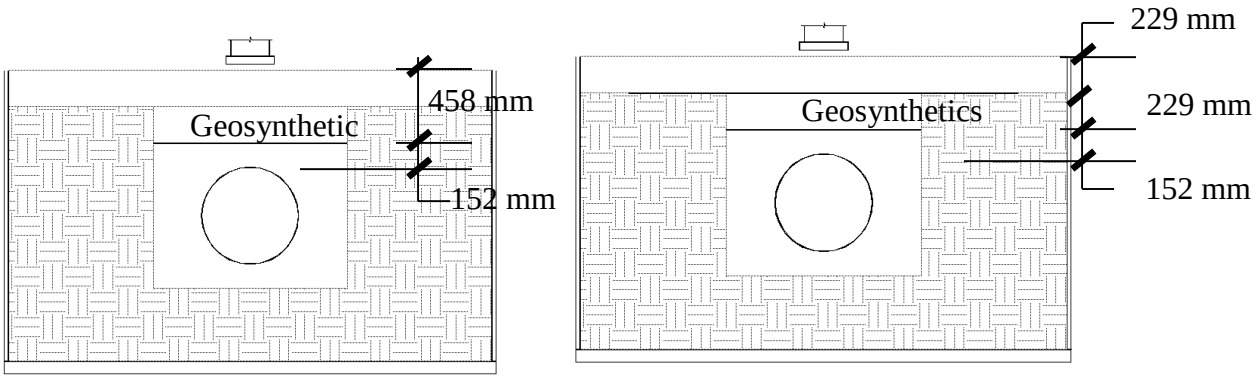

a. Single Layer **b. Double Layer**

Figure 4.1 Geogrid Placement

4.2 Plate Settlement

The settlement of the loading plate at the surface was monitored during loading and unloading of the test section. The test results are shown in Figures 4.2 through 4.4. The effectiveness of the geosynthetic in reducing the plate settlement appears to be most dependent on the relative stiffness of the backfill and the geosynthetic, and the vertical location of the geosynthetic. In the case of the AB-3 base course and sand back fill tests (Tests 1 and 7) there was only a minor reduction (11%) in the settlement of the loading plate between the unreinforced and reinforced conditions. Comparatively, in the case with the sand backfill and the sand base course in Tests 3 and 5, there was a 25% decrease in the settlement between the reinforced and unreinforced conditions at the maximum load. In the case of the dumped aggregate, the double layer of reinforcement decreased the plate settlement by 38% as compared with the unreinforced condition. Conversely, the single layer of reinforcement in the aggregate backfill increased the plate settlement by 26% at the maximum load.

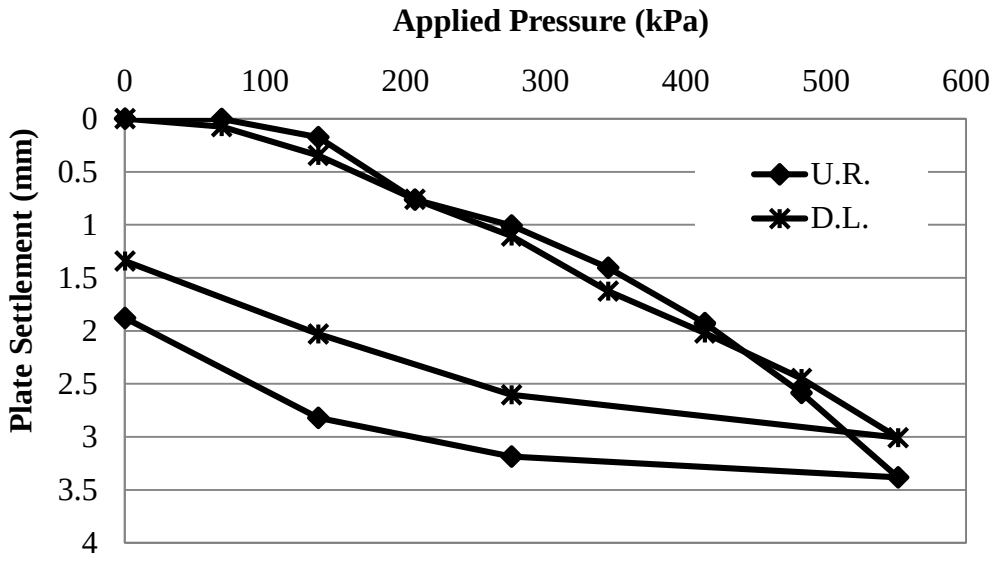

Figure 4.2 Loading Plate Settlement of Sand Backfill and AB-3 Base Course (Tests 1 and 4)

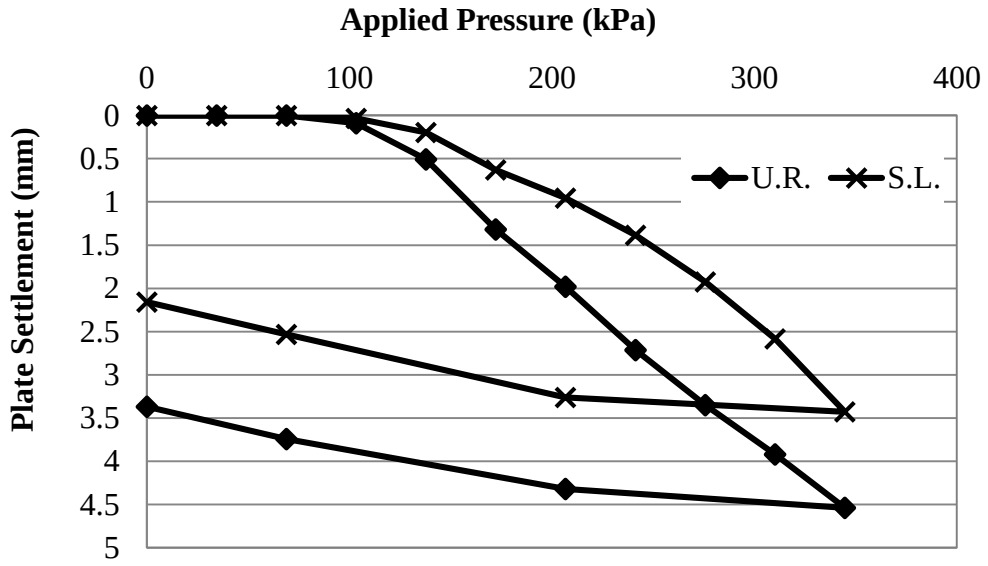

Figure 4.3 Loading Plate Settlement of Sand Backfill and Sand Base Course (Tests 2 and 3)

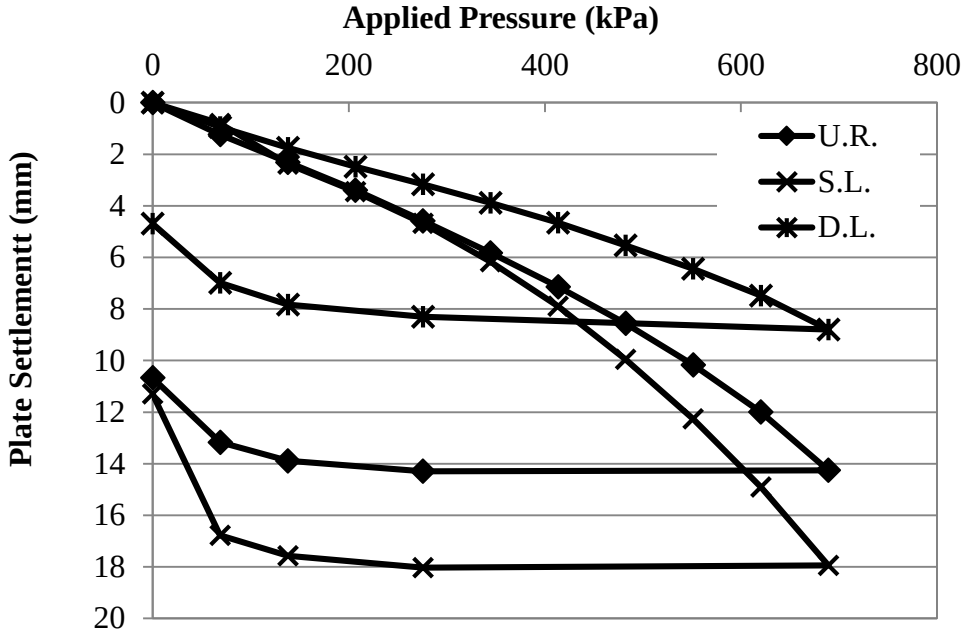

Figure 4.4 Loading Plate Settlement of Aggregate Backfill and AB-3 Base Course (Tests 5, 7, and 9)

4.3 Pipe Deflection

4.3.1 Vertical Pipe Deflection

During the plate loading tests, two displacement transducers continuously recorded the movements of the pipes along the vertical and horizontal principal axes. A third displacement transducer continuously recorded the vertical displacements of the pipe at 305 mm from the center of the loading pipe along the longitudinal axis of the pipe. The displacement at the end of each loading step, after the section appeared to be stable, was plotted against the 69 kPa loading steps (Figures 4.5 through 4.10). With the sand backfill, the double layer of the reinforcement reduced the vertical deflection of the pipe, while the single layer of geogrid reinforcement did not affect

the deflection of the cross section. The same trend was observed with the aggregate backfill (Fig. 4.7).

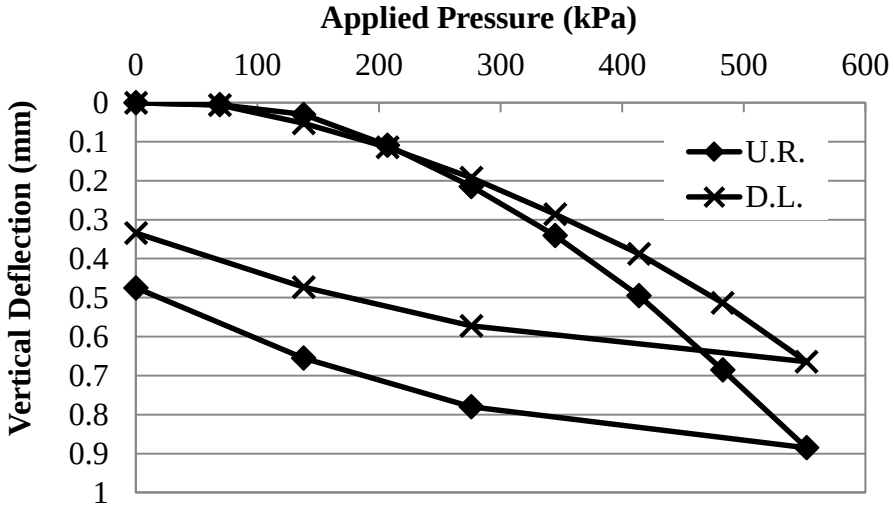

Figure 4.5 Vertical Deflection of the Pipe Cross Section with Sand backfill (Tests 1 and 4)

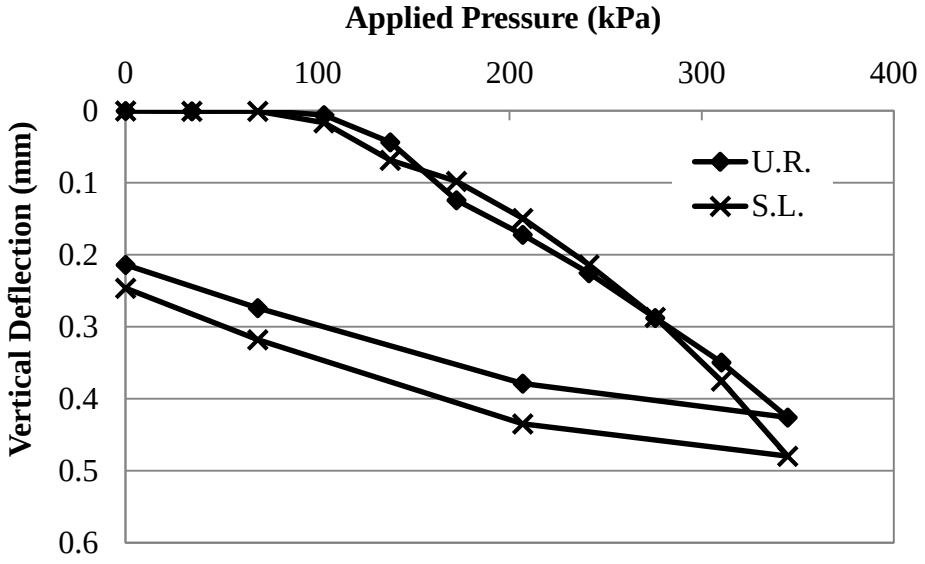

Figure 4.6 Vertical Deflection of the Pipe Cross Section with Sand Backfill (Tests 2 and 3)

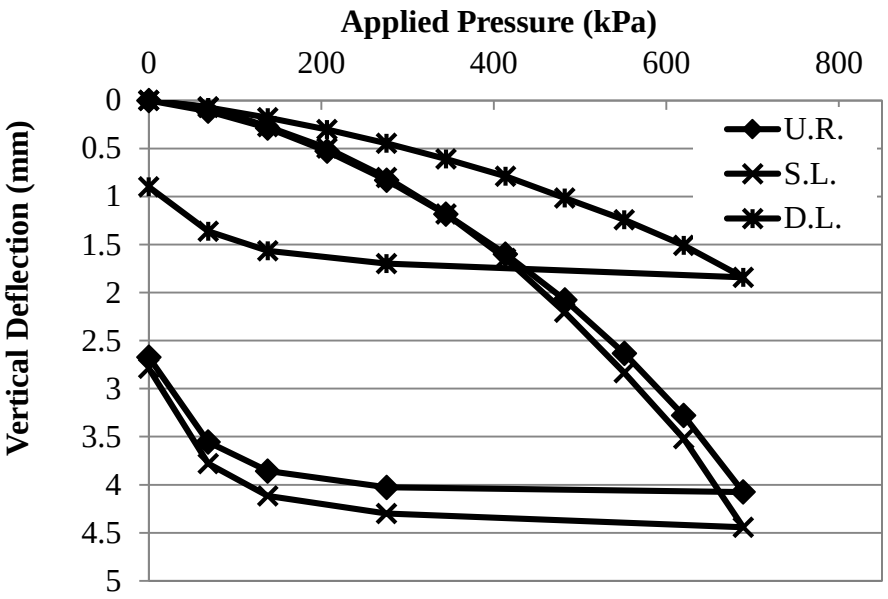

Figure 4.7 Vertical Deflection of the Pipe Cross Section with Aggregate Backfill (Tests 5, 7, and 9)

The deflection of the pipe at 305 mm from the loading plate was less than the deflection directly under the loading plate (Figs. 4.8, 4.9, and 4.10).

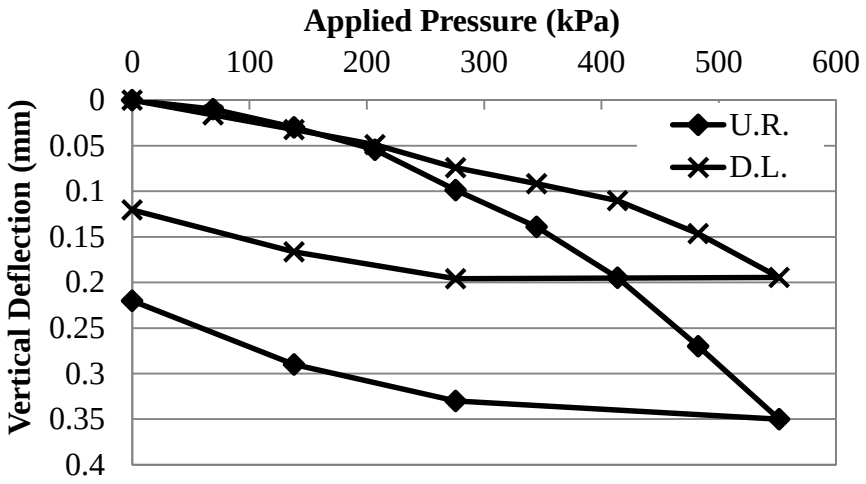

Figure 4.8 Vertical Pipe Deflection at 305 mm from the Plate with Sand Backfill (Tests 1 and 4)

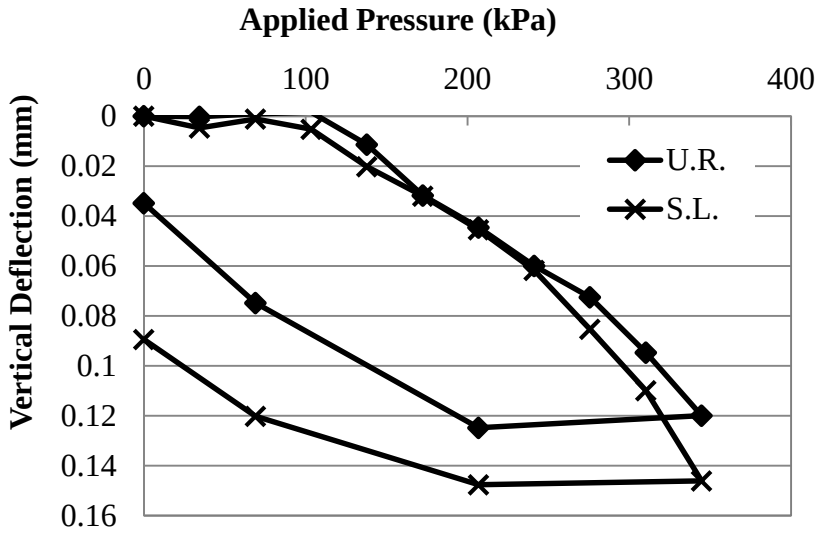

Figure 4.9 Vertical Pipe Deflection at 305 mm from the Plate with Sand Backfill (Tests 2 and 3)

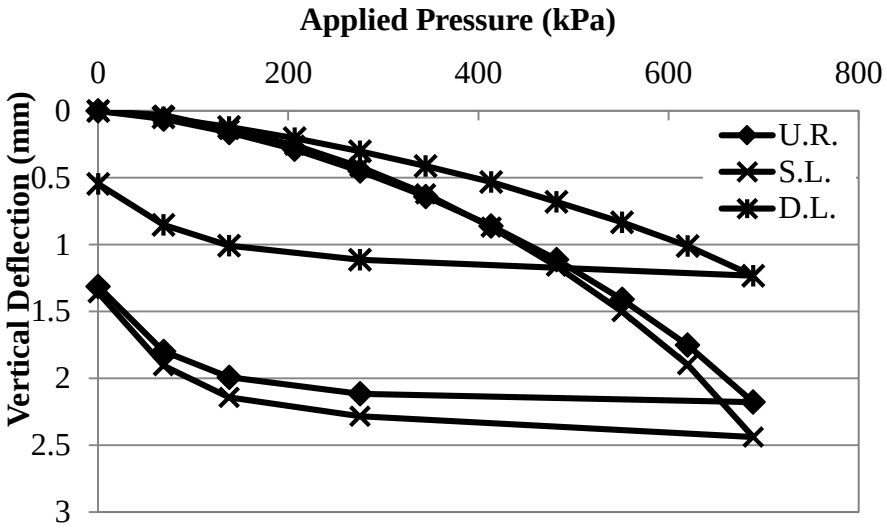

Figure 4.10 Vertical Deflection at 305mm from the Plate with Aggregate Backfill (Tests 5, 7, and 9)

Also during the tests the vertical displacement of the crown of the pipe was measured relative to a static datum. During Tests 1 through 4 the tell-tale became unattached to the crown of the pipe, and the data is not available. The tell-tale remained attached to the pipe during the tests 5, 7, and 9 (Fig. 4.11). There was a significant reduction, nearly 80%, in movement of the crown with the inclusion of the geogrid.

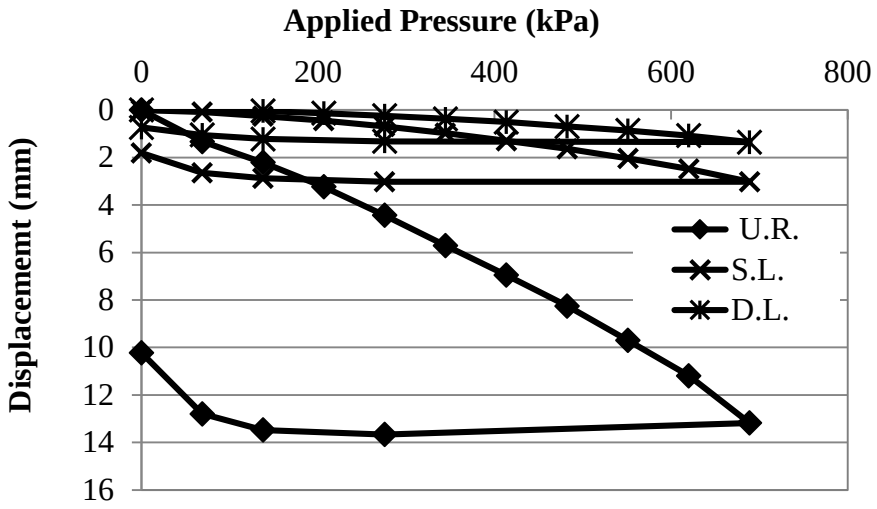

Figure 4.11 Vertical Displacement of the Pipe Crown with Aggregate Backfill (Tests 5, 7, and 9)

4.3.2 Horizontal Pipe Deflection

In addition to the vertical displacement transducers a horizontal transducer continuously recorded the displacement at the horizontal axis of the pipe, in each test (Figures 4.12, 4.13, and 4.14). The inclusion of the geogrid resulted in horizontal deflections of the pipe having similar relationships between the reinforced and unreinforced cross sections with respect to the vertical deflections. The single layer only slightly affected the distortion of the pipe, while the double layer reduced significantly the horizontal deflection.

A plot of the ratio of vertical to horizontal deflection with the applied pressure reveals some information about the general shape of the pipe cross section. Assuming that the pipe was deflected by a uniformly applied pressure in all directions the ratio of vertical to horizontal deflection would be nearly 1. Because of the wheel load, a non-uniform pipe distortion would take place, which is confirmed by the test results in Figs. 4.15 and 4.16. In the test runs with the aggregate backfill,

two layers of geogrid reinforcement improved the distortion of the pipe by improving the ratio from 2 to 1.5.

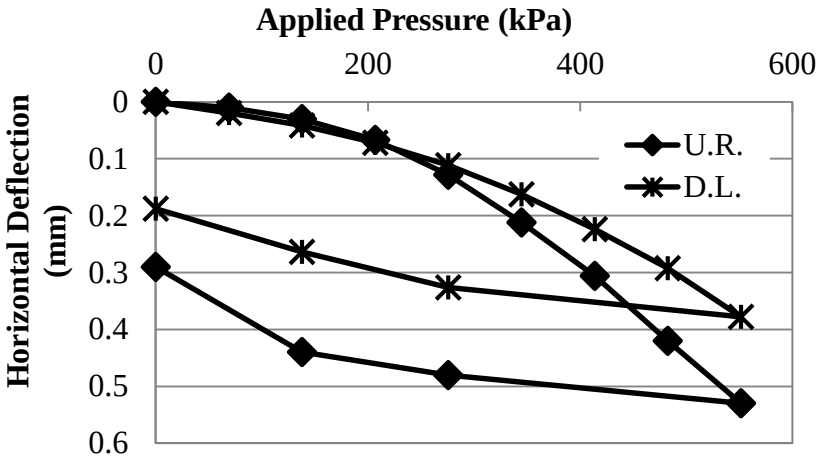

Figure 4.12 Horizontal Deflection of Pipe Cross Section with Sand Backfill (Tests 1 and 4)

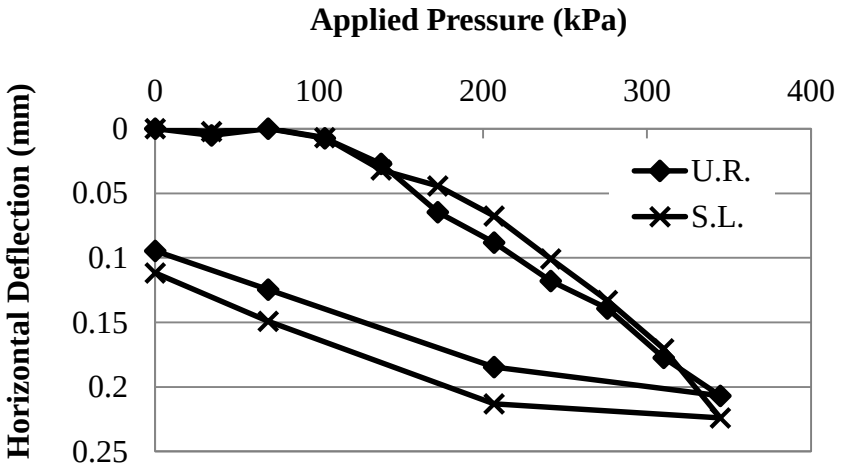

Figure 4.13 Horizontal Deflection of Pipe Cross Section with Sand Backfill (Tests 2 and 3)

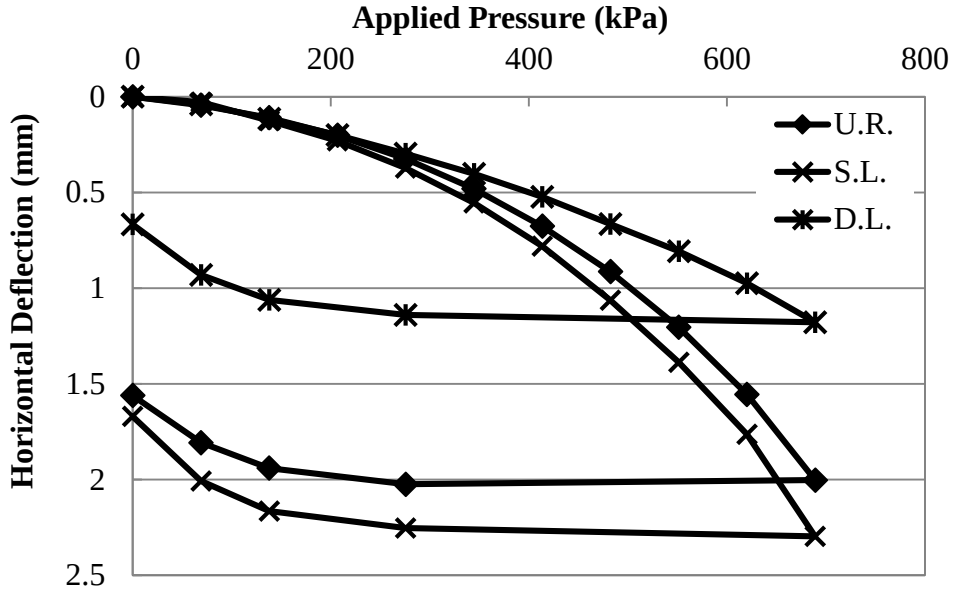

Figure 4.14 Horizontal Pipe Deflection with Aggregate Backfill (Tests 5, 7 and 9)

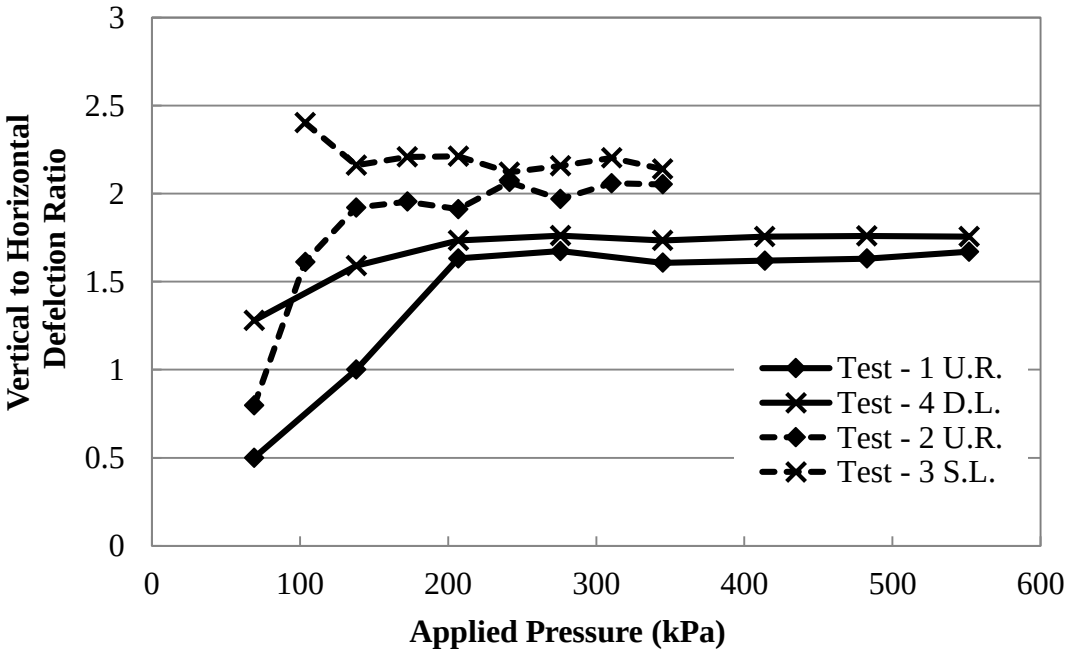

Figure 4.15 Applied Pressure vs. Vertical to Horizontal Deflection Ratio with Sand Backfill

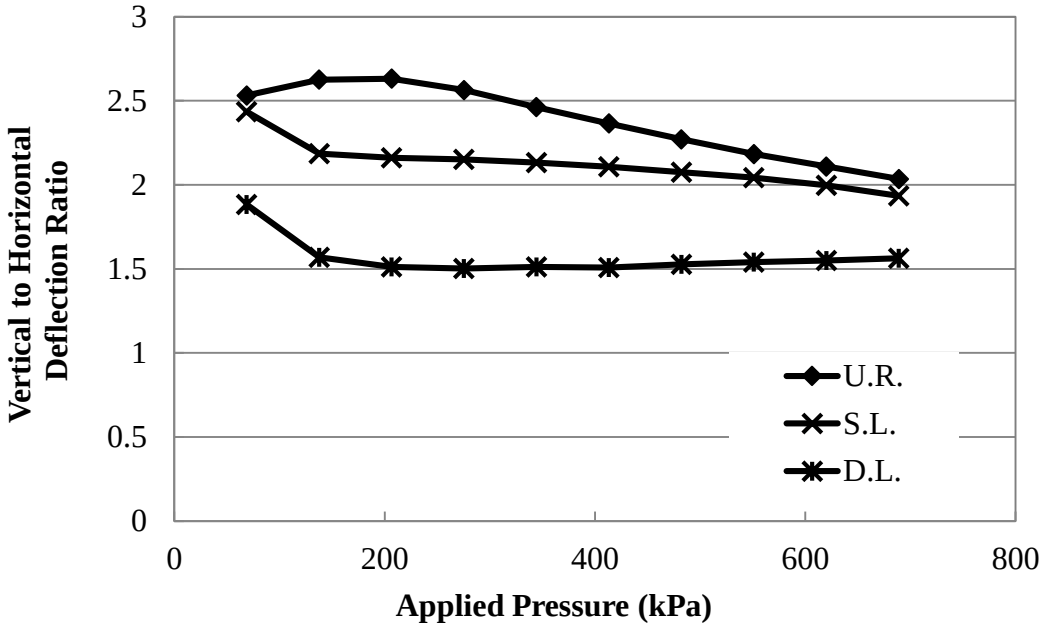

Figure 4.16 Applied Pressure vs. Vertical to Horizontal Deflection Ratio with Aggregate Backfill (Tests 5, 7, and 9)

4.4 Earth Pressure

During the static plate loading tests, earth pressures were monitored and recorded. In the first four tests only pressure cells I_1, S_1, S_2, C_1, and C_2 were included in the backfill. After these tests it was decided to expand the number of pressure cells. The remainder of the pressure cells shown in Fig. 3.18 were included in Tests 5, 7, and 9. The plots of the recorded earth pressures versus the applied plate pressures are organized by region of the pipe: invert, spring line, and crown in the following sections.

4.4.1 Earth Pressure at Pipe Invert

The earth pressure cell readings at the invert of the pipe are shown in Figures 4.17 through 4.19. Observing the earth pressures measured at the invert, the effect of the backfill stiffness can

be seen in the results. Where the earth pressure cells measured moderate pressures when buried in the dumped aggregate, the earth pressure cell measured low earth pressures when buried in the compacted sand backfill. In the unreinforced condition there was a pressure reading of zero until an applied pressure at the surface of 138 kPa. The pressures at the invert of the pipe in the sand backfill did not decrease with the reduction of the plate pressure at the surface. In the test sections with the aggregate backfill, there was a marked reduction of the pressure at the pipe invert when the plate load was reduced. Figure 4.19 shows that the single geogrid-reinforced section had much lower earth pressures than the unreinforced section and the double geogrid-reinforced section. This result implies that the bedding layer in the single geogrid-reinforced section might be looser than those in other two sections. This result may also explain why the single geogrid-reinforced section had larger deformations than the unreinforced section.

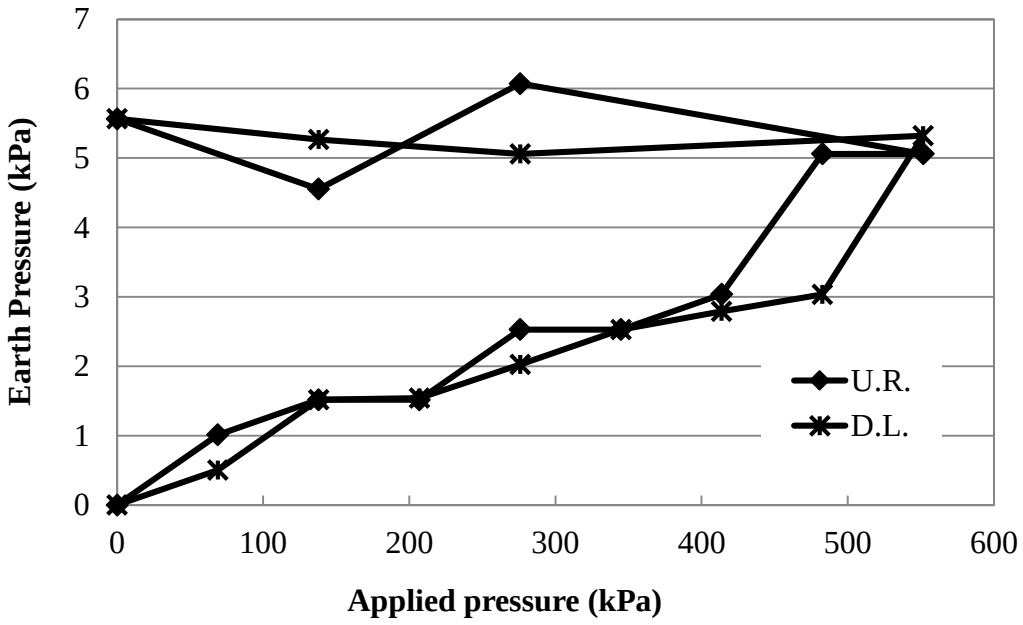

Figure 4.17 Measured Vertical Earth Pressure at Pipe Invert (I_1) with Sand Backfill (Tests 1 and 4)

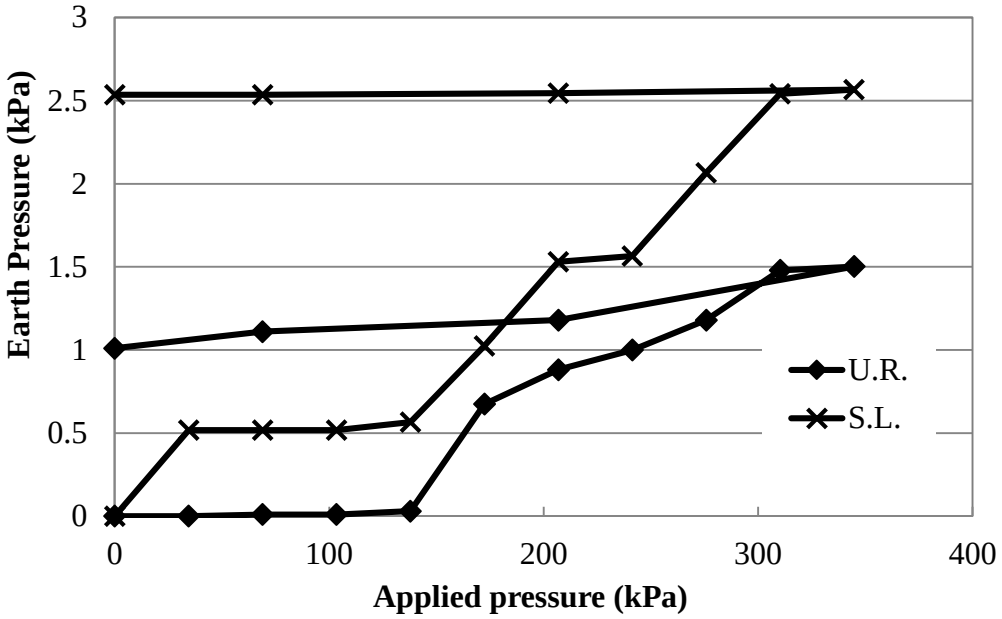

Figure 4.18 Measured Vertical Pressure at Pipe Invert (I_1) with Sand Backfill (Tests 2 and 3)

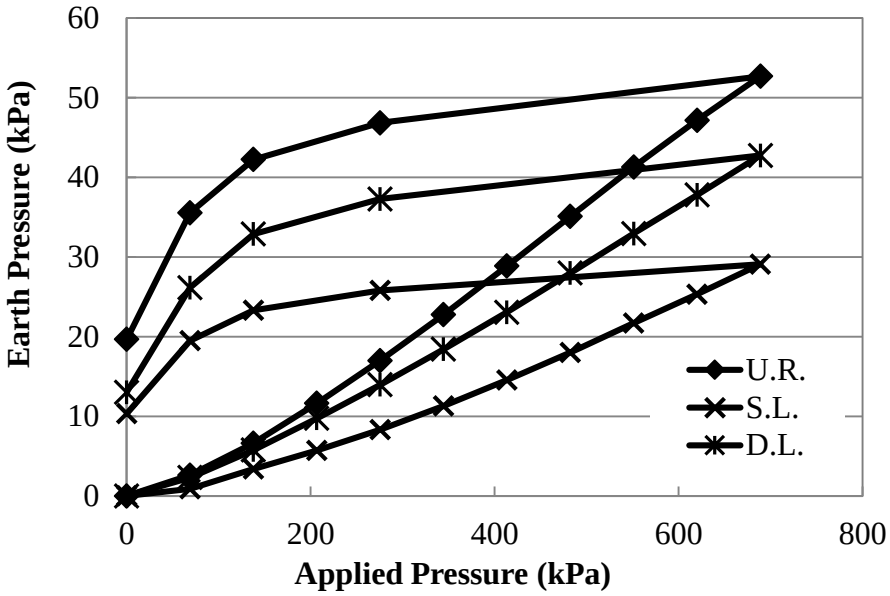

Figure 4.19 Measured Vertical Earth Pressure at Pipe Invert (I_1) with Aggregate Backfill (Tests 5, 7, and 9)

4.4.2 Earth Pressure at Pipe Spring Line

The spring line pressures were monitored and recorded to determine the effect of the geogrid on the intensity and distribution of the horizontal pressures. Figures 4.20 through 4.26 show the recorded horizontal pressure versus the applied plate load test. Similar to the earth pressure cells at the pipe invert, at the beginning of the test there were almost no recorded pressures due to the applied plate loading. Unlike the pressure at the invert, the pressures at the spring line nearly returned to a zero pressure when the plate load was removed.

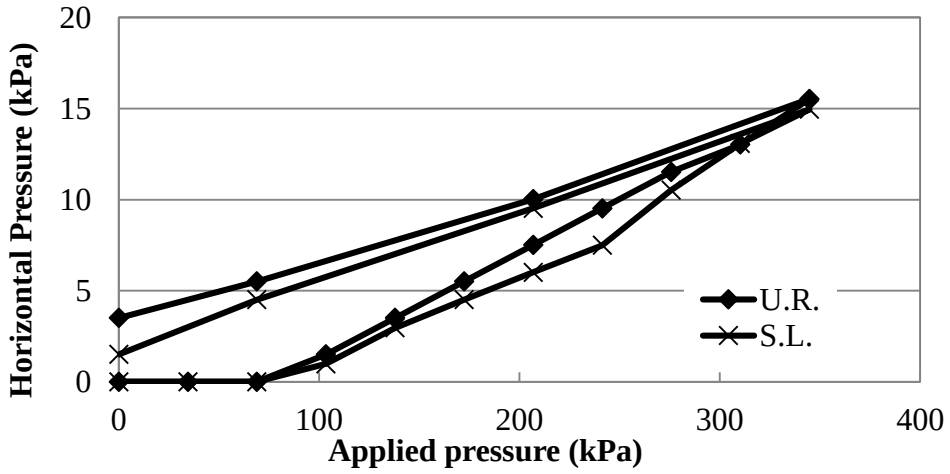

Figure 4.20 Measured Horizontal Earth Pressure at Pipe Spring line (S_1) with Sand Backfill (Tests 2 and 3)

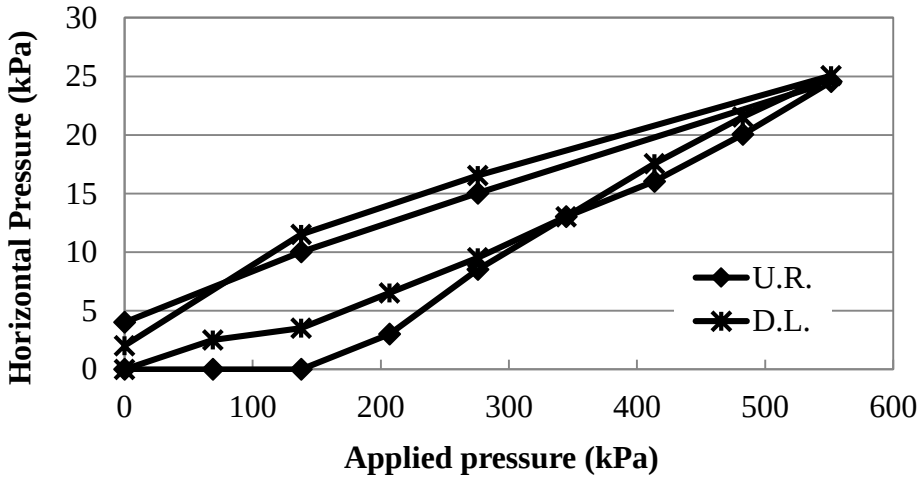

Figure 4.21 Measured Horizontal Pressure at Pipe Spring Line (S_1) with Sand Backfill (Tests 1 and 4)

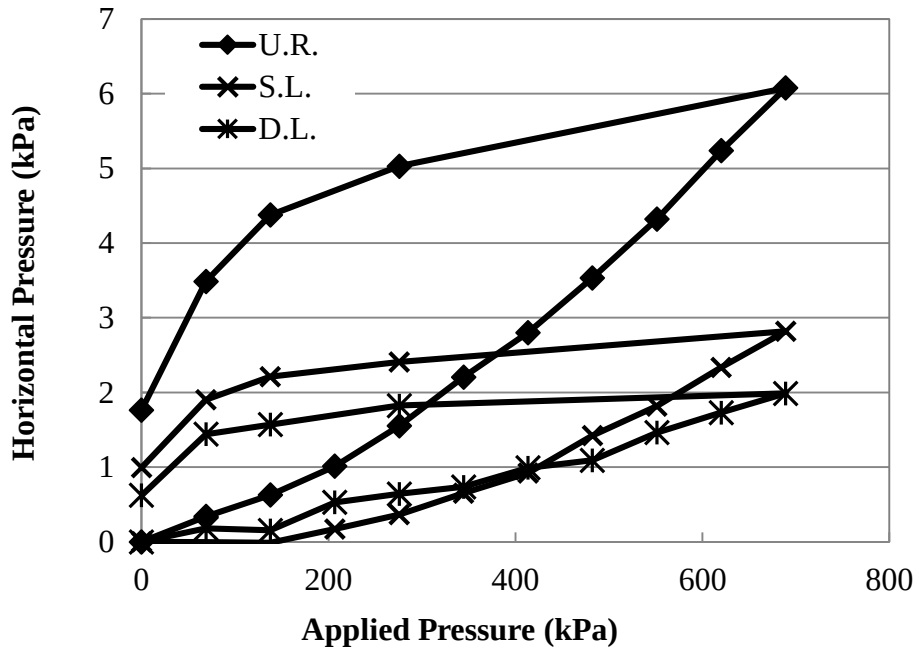

Figure 4.22 Measured Horizontal Earth Pressure at the Pipe Spring line (S_1) with Aggregate Backfill (Tests 5, 7 and 9)

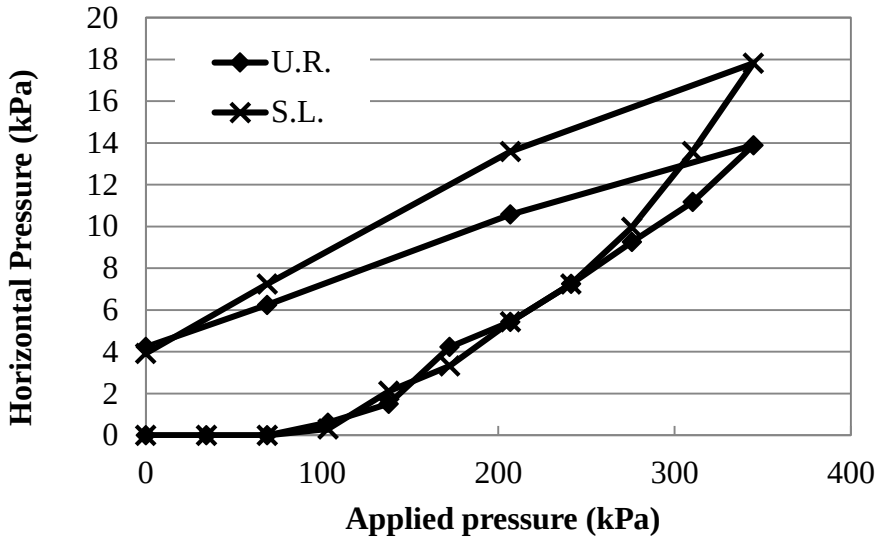

Figure 4.23 Measured Horizontal Earth Pressure at Pipe Shoulder (S_2) with Sand Backfill (Tests 2 and 3)

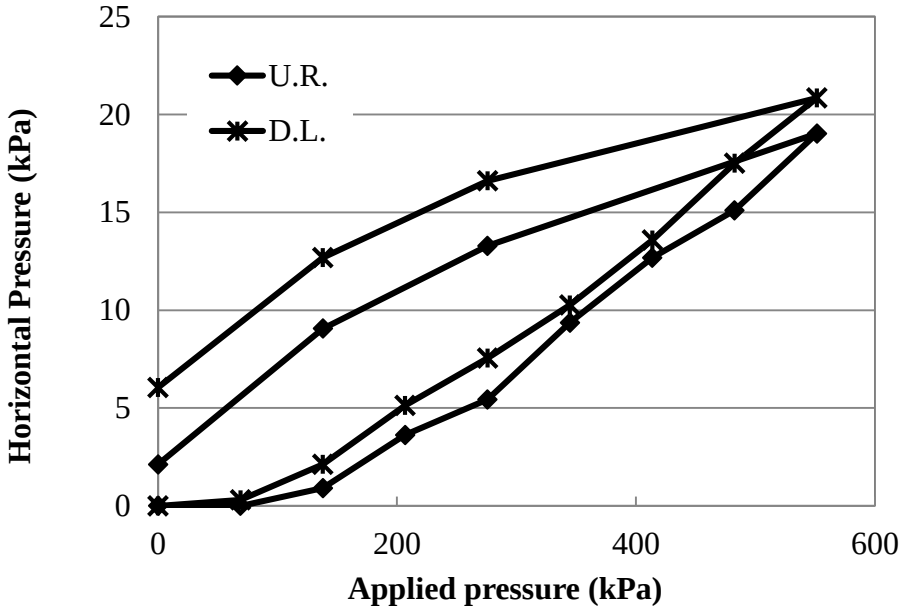

Figure 4.24 Measured Horizontal Pressure at Pipe Shoulder (S_2) with Sand Backfill (Tests 1 and 4)

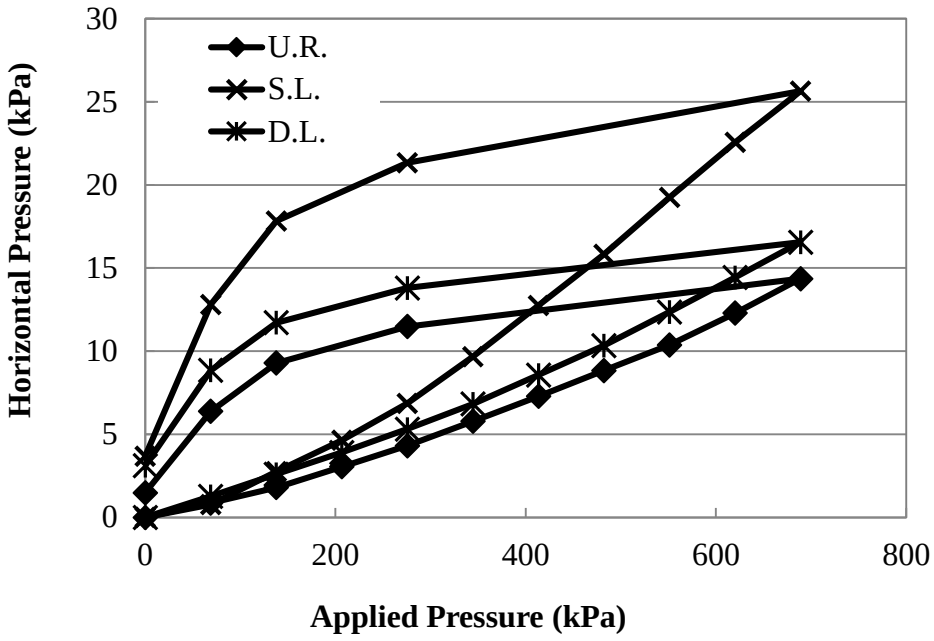

Figure 4.25 Measured Horizontal Earth Pressure at Pipe Shoulder (S_2) with Aggregate Backfill (Tests 5, 7, and 9)

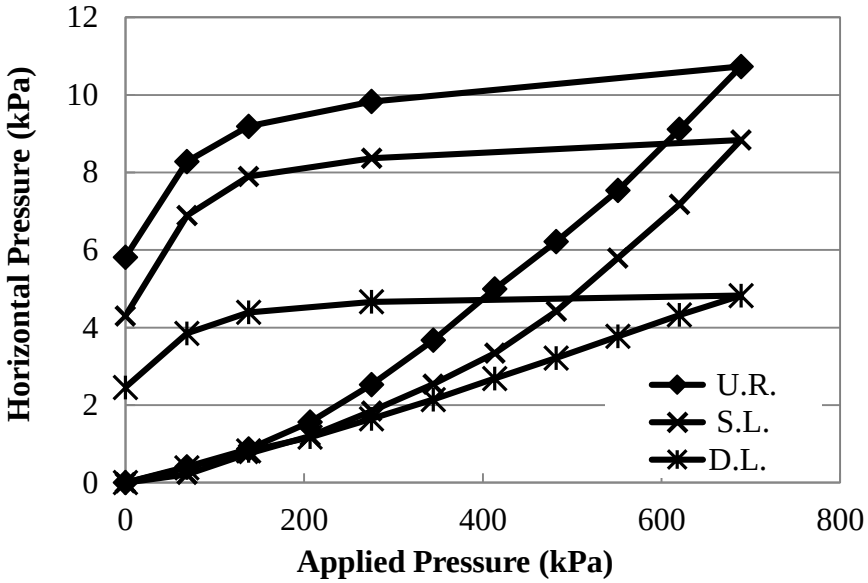

Figure 4.26 Measured Horizontal Earth Pressure at Pipe Haunch (S_3) with Aggregate Backfill (Tests 5, 7, and 9)

The distribution of earth pressures around the spring line can be seen in Figures 4.27 and 4.28. The earth pressure distribution in the sand backfill is incomplete without the pressure at the haunch area of the pipe, but is included for comparison. Figure 4.28 shows that the single geogrid-reinforced section had the highest horizontal earth pressure at the pipe shoulder, followed by the double geogrid-reinforced section and then the unreinforced section. The reason is that the pipe invert in the single geogrid-reinforced section carried the least load, followed by the double geogrid-reinforced section and then the unreinforced section. If the pipe invert carried less load, more load was transferred to the backfill in the trench.

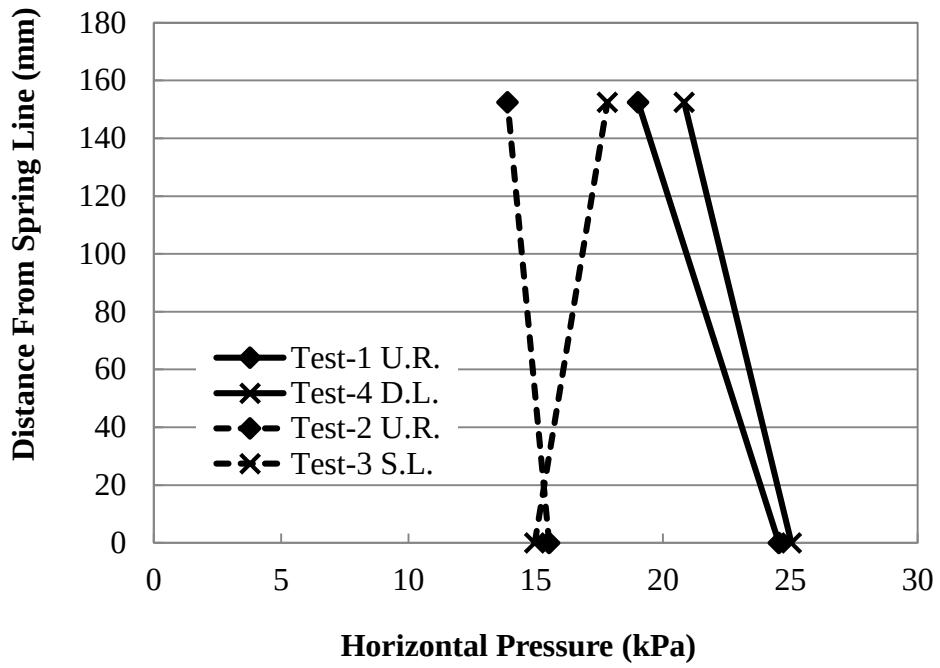

Figure 4.27 Horizontal Pressure Distribution at the Pipe Spring line with Sand backfill at Applied Pressure of 552 kPa (Tests 1 and 4) or 345 kPa (Tests 2 and 3)

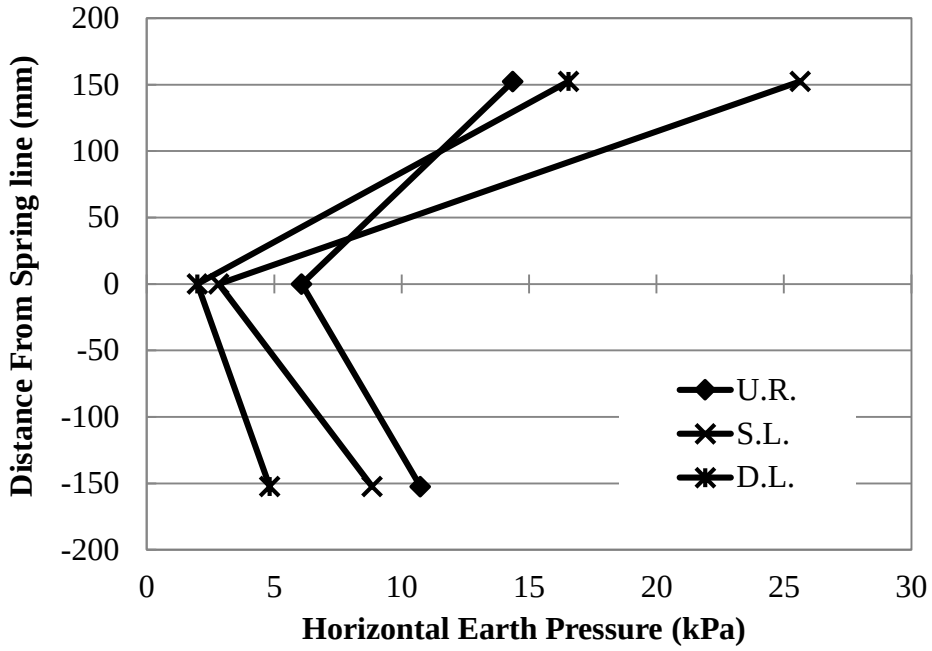

Figure 4.28 Horizontal Pressure Distribution around the Pipe Spring line with Aggregate Backfill at Applied Pressure of 689 kPa (Tests 5, 7, and 9)

In Tests 5, 7, and 9, additional earth pressure cells measured the vertical pressures at the spring line of the pipe. The horizontal earth pressures at the trench wall were also measured. The vertical pressures at the spring line are shown in Figure 4.29. Figure 4.30 shows the ratios of horizontal pressure at the spring line (S_1) to the vertical pressure (S_4). It is shown that the double geogrid-reinforced section had the lowest ratio of the horizontal to vertical pressure. This result is consistent with the ratio of the vertical to horizontal deflection of the pipe discussed earlier. In other words, there was less distortion of the pipe with the double layer of reinforcement, and more distortion with the single layer of reinforcement. The measured pressures at the trench wall increased significantly with the inclusion of the single layer of geogrid (Figure 4.31).

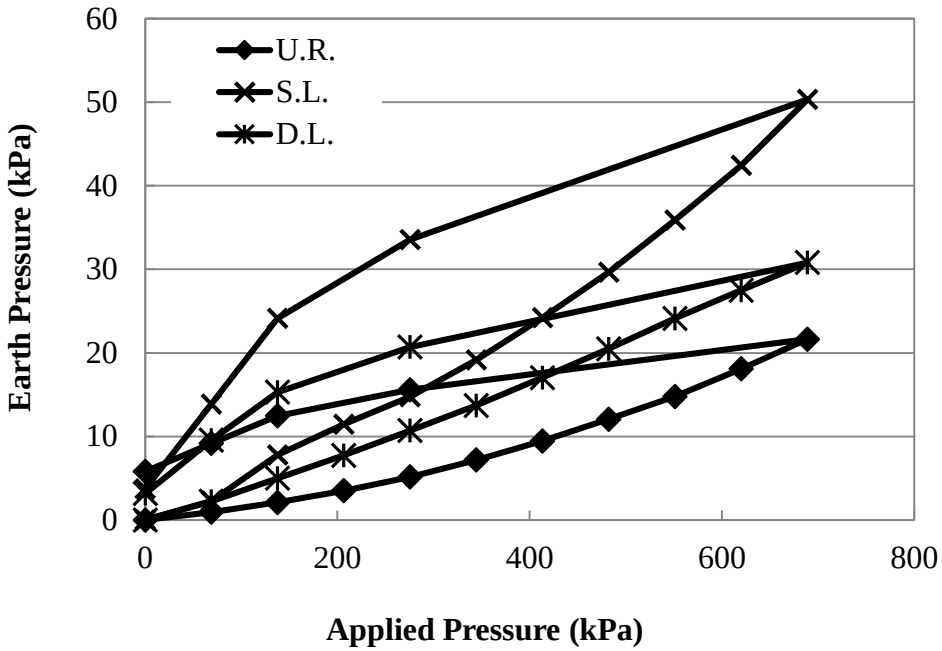

Figure 4.29 Measured Vertical Earth Pressure at Spring line (S_4) (Tests 5,7, and 9)

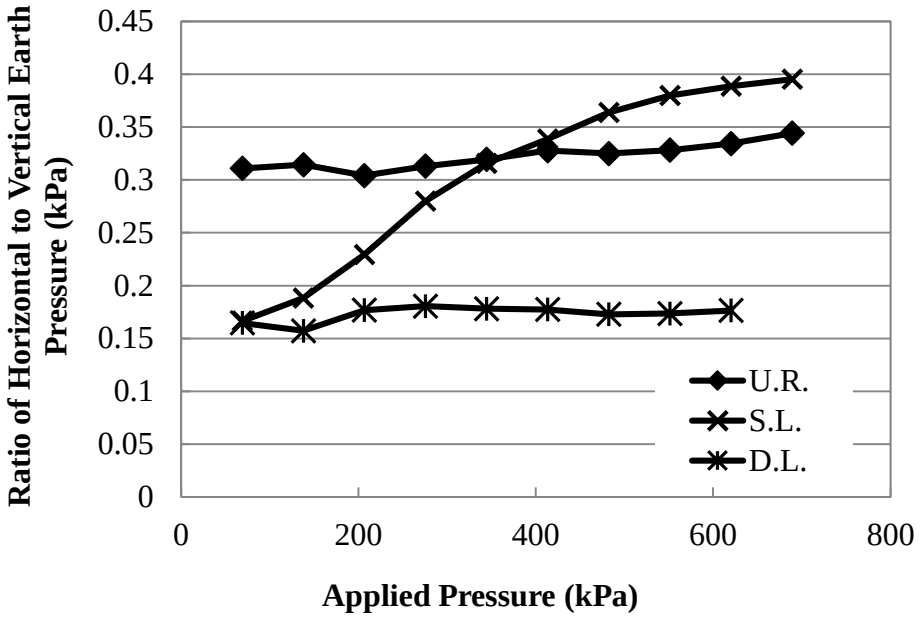

Figure 4.30 Measured Ratio of Horizontal to Vertical Pressure at Pipe Spring Line (S_1/ S_4) (Tests 5, 7, and 9)

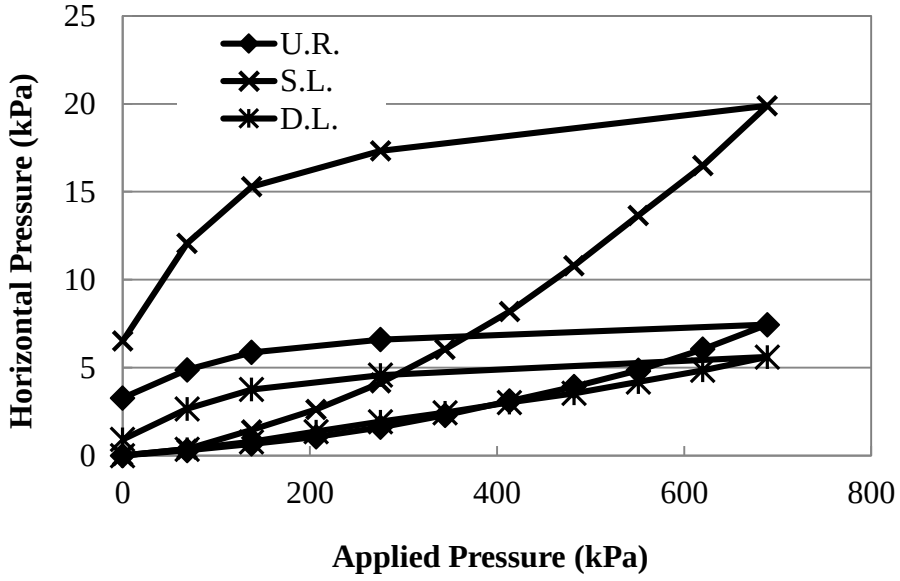

Figure 4.31 Measured Horizontal Earth Pressure at the Trench Wall (S_5) (Tests 5, 7, and 9)

4.4.3 Earth Pressure at Pipe Crown

The earth pressures at the crown were measured and are plotted versus the applied plate pressure in Figures 4.32 through 4.38. There was almost no reduction in earth pressures directly over the crown with the sand backfill and a slight reduction with the aggregate backfill. However, moving away from the crown, the earth pressure increased with the inclusion of the geogrid. With the sand backfill, this trend continued for the earth pressure cells at the horizontal distances of 152 mm and 304 mm from the crown. The pressure distribution at top of the pipe crown in the aggregate backfill can be seen in Figure 4.39. The addition of the geogrid reinforcement in the aggregate backfill distributed the earth pressures away from the crown and towards the shoulders of the pipe. The earth pressures directly under the base course were significantly affected by the geogrid, i.e., reduction of the earth pressure by 26% for the single layer and by 43% for the double layer. Figure 4.40 shows the earth pressures directly under the base course.

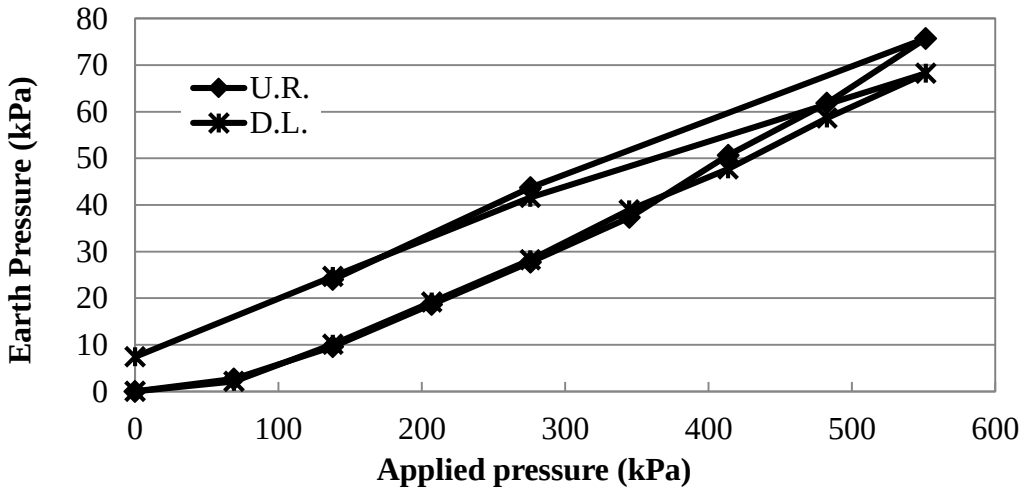

Figure 4.32 Measured Vertical Earth Pressure at Pipe Crown (C_1) with Sand Backfill (Tests 1 and 4)

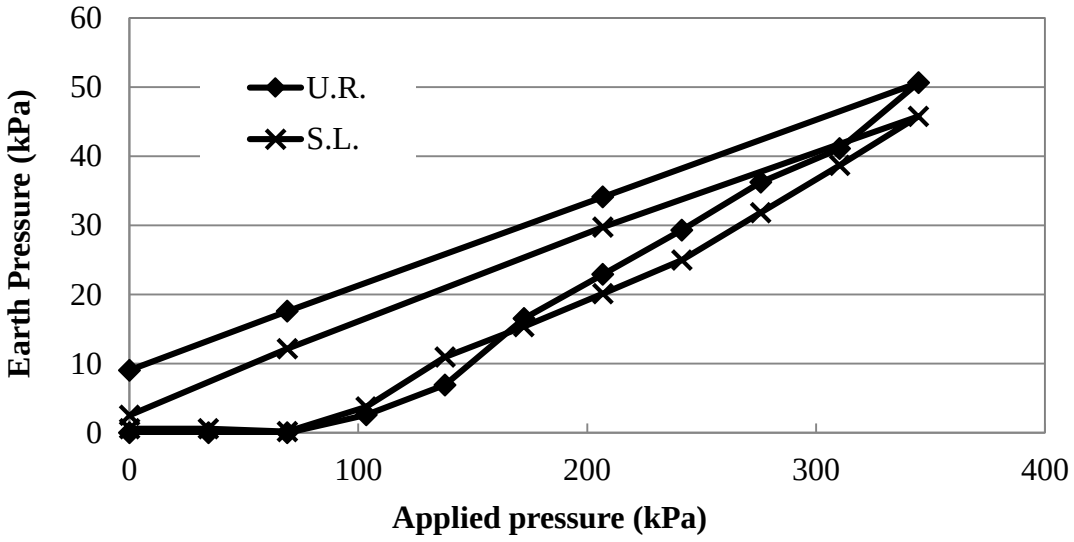

Figure 4.33 Measured Vertical Earth Pressure at Pipe Crown (C_1) with Sand Backfill (Tests 2 and 3)

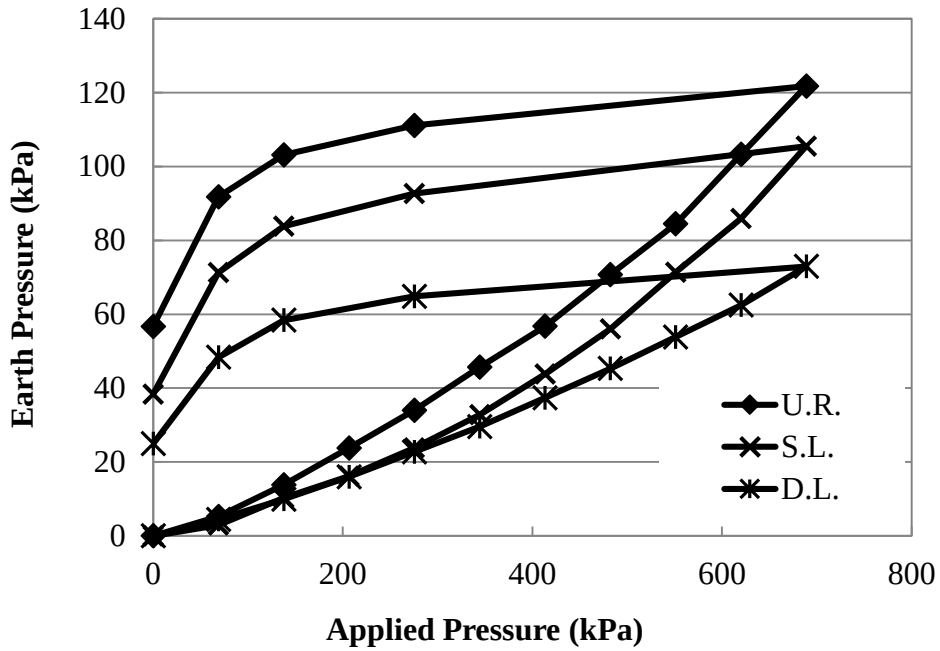

Figure 4.34 Measured Vertical Earth Pressure at Pipe Crown (C_1) with Aggregate Backfill (Tests 5, 7, and 9)

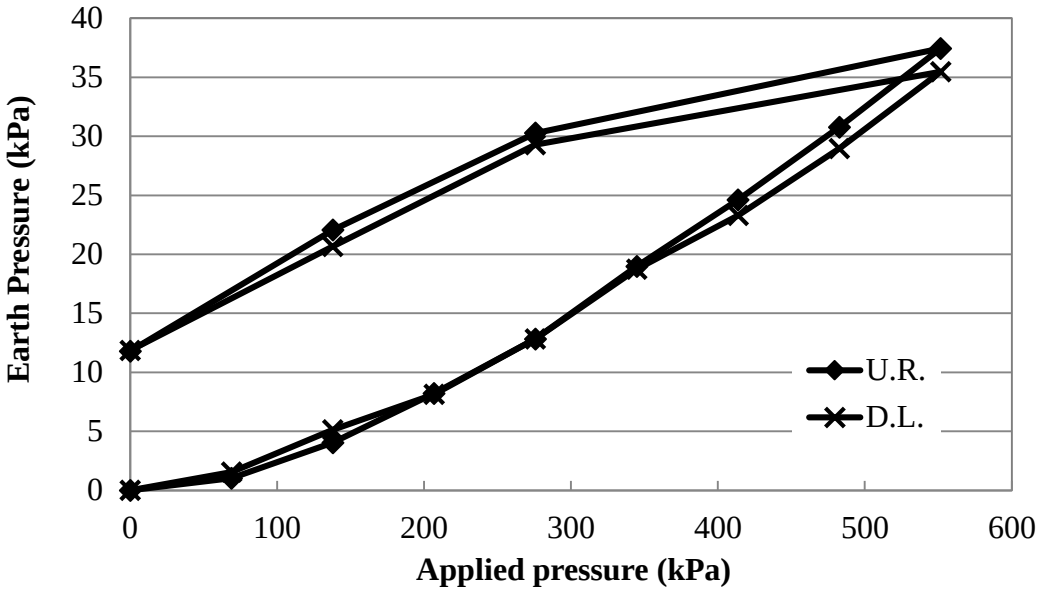

Figure 4.35 Measured Vertical Earth Pressures at Pipe Crown (C_2) with Sand Backfill (Tests 1 and 4)

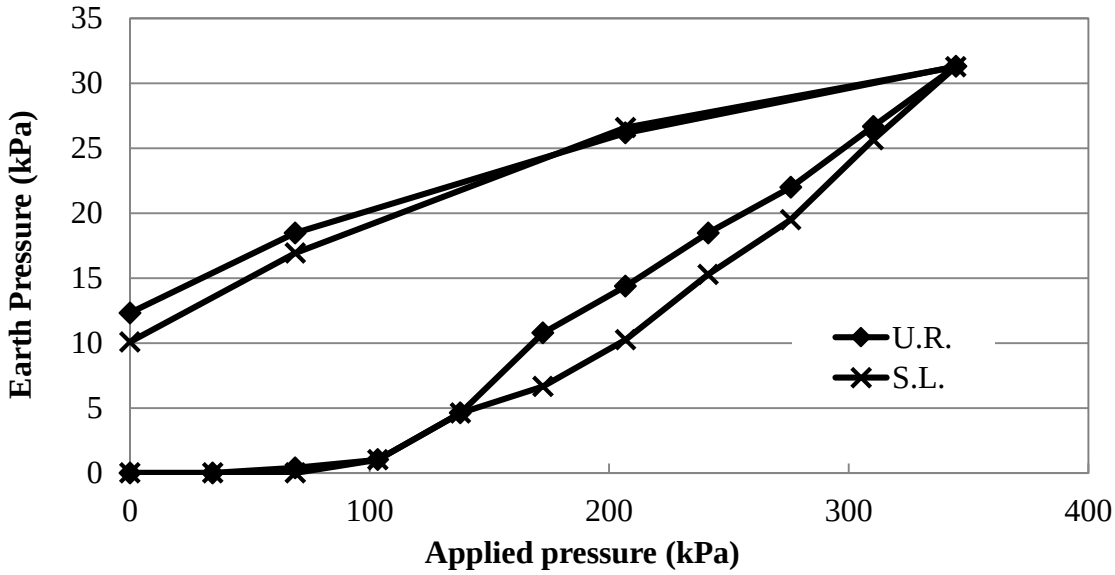

Figure 4.36 Measured Vertical Earth Pressures at Pipe Crown (C_2) with Sand Backfill (Tests 2 and 3)

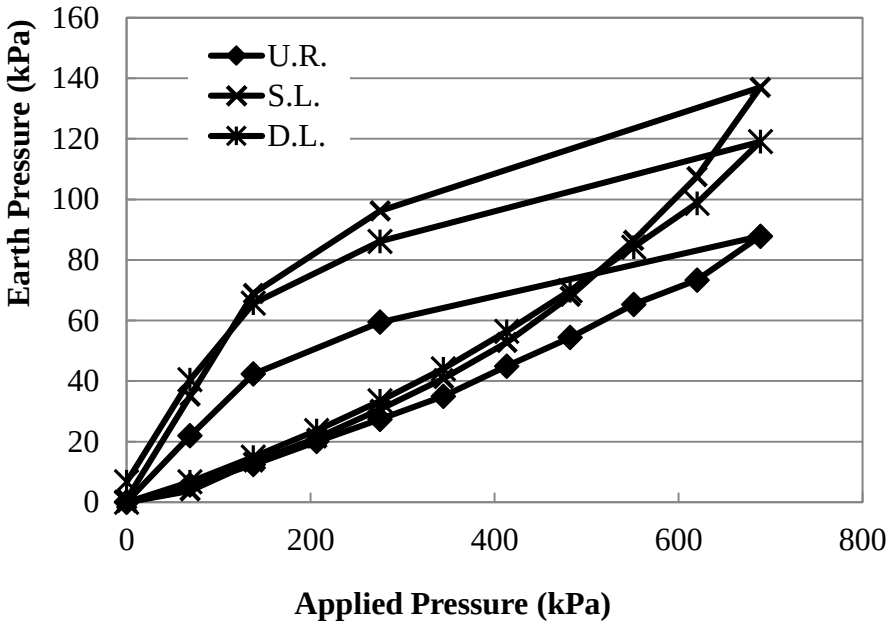

Figure 4.37 Measured Vertical Earth Pressures at Pipe Crown (C_2) (Tests 5, 7, and 9)

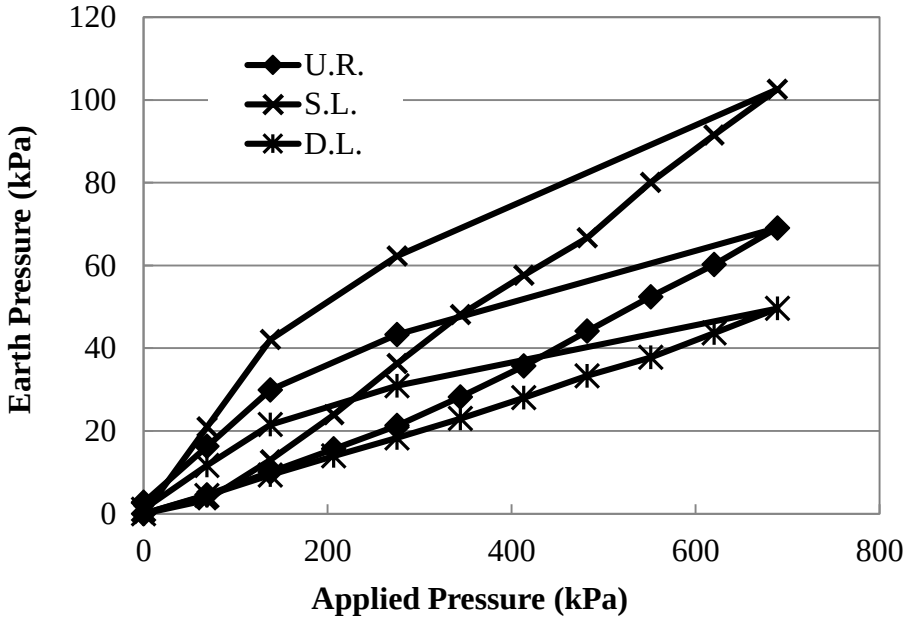

Figure 4.38 Measured Vertical Earth Pressures at Pipe Crown (C_3) (Tests 5, 7, and 9)

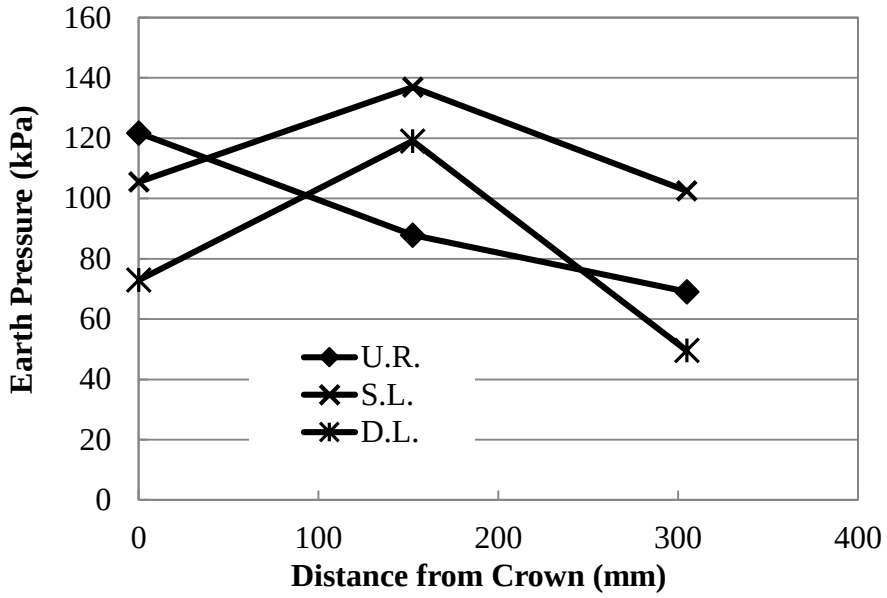

Figure 4.39 Pressure Distribution at Pipe Crown at Applied Pressure of 689 kPa (Tests 5, 7, and 9)

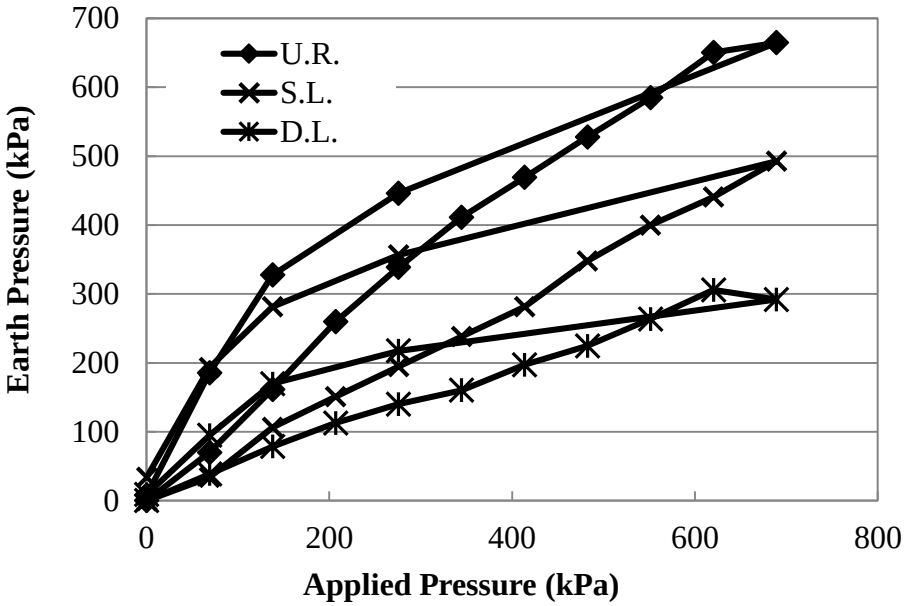

Figure 4.40 Measured Vertical Pressure at Pipe Crown (C_4) (Tests 5, 7, and 9)

4.5 Pipe Strain

4.5.1 Strain Gauge Layout

Pipe strains were recorded during the test with 17 strain gauges located at the spring line, the invert, and the crown for each test. Some strain gauges failed or exceeded the allowable range of measureable strains by the gauge. The strains of the failed strain gauges were not included in the following plots. The strain gauge locations are shown here again for convenience (Figures 4.41 and 4.42). Since the strain gauge data at Lp5 and Lp6 were almost identical to the strain gauge readings at Lp1 and Lp2, they were not included in this report to minimize the amount of data. Positive strains are tensile and negative strains are compressive. Additional pipe strains for the static load tests not included in this chapter can be found in Appendix A.

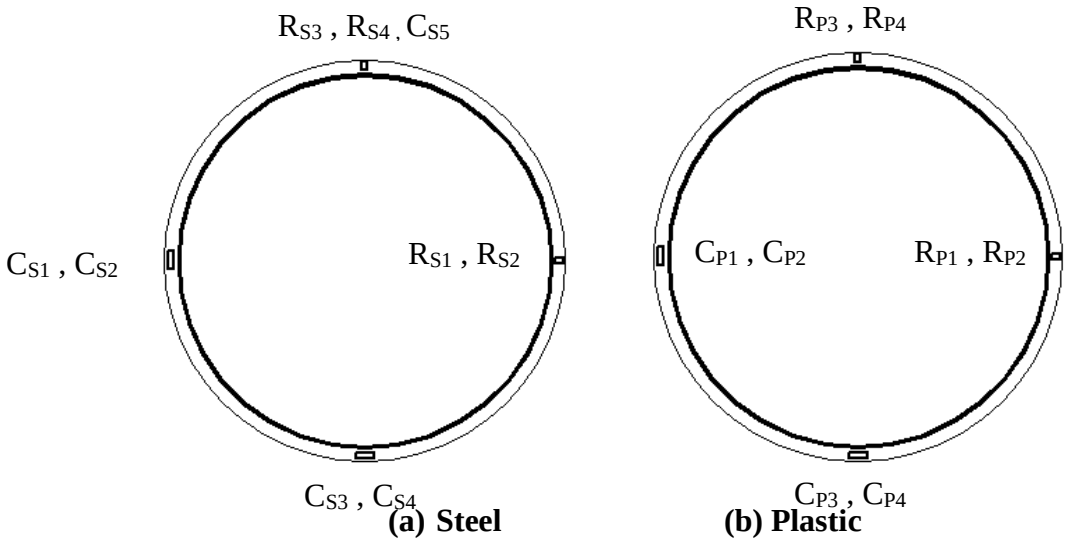

Figure 4.41 Circumferential and Radial Strain Gauge Locations

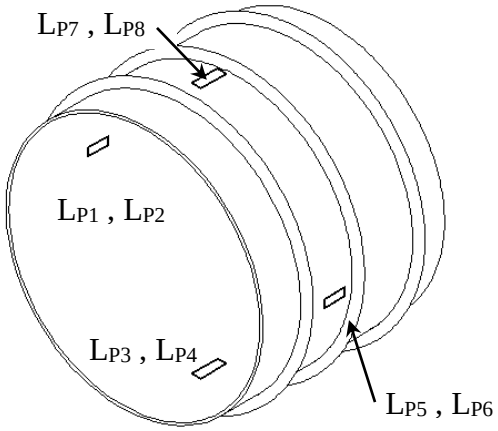

Figure 4.42 Longitudinal Strain Gauge Locations

The composite behavior of the pipe wall, and the very small recorded strains, make interpretation and analysis of the strain results difficult. In some cases, it is difficult to draw definite conclusions from the strain gauge responses. Therefore, the analysis was done to examine the general trend of these data. The initial strains for all strain gauges were set to zero before loading.

4.5.2 Pipe in Sand Backfill

To investigate possible effects of geogrid and backfill material on the strains in the steel ribs and the plastic, some test results are presented below. In this study, test sections without a geogrid, with single geogrid, and double layers of geogrid were evaluated. In addition, pipes were installed in sand or aggregate backfill. In this section, the measured pipe strains of the pipes in sand backfill are discussed.

Figure 4.43 shows that on the pipe crown, the strain gauges on the opposite sides of the plastic cover of the steel strip in the radial direction had opposite values (i.e., negative vs. positive),

which indicate the steel ribs under bending. Figure 4.43 also shows that the single layer of geogrid reduced the maximum strain under loading but increased the rebound strain under unloading.

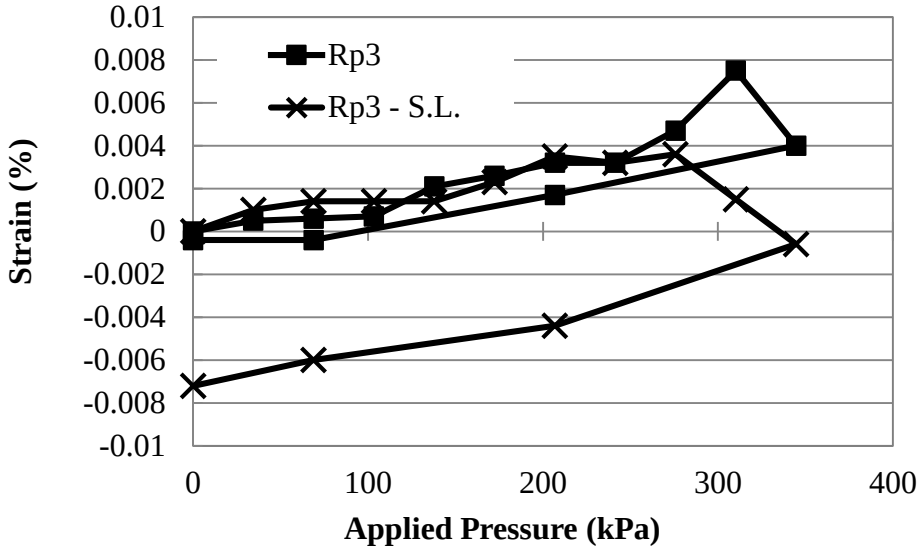

(a) R_{p3}

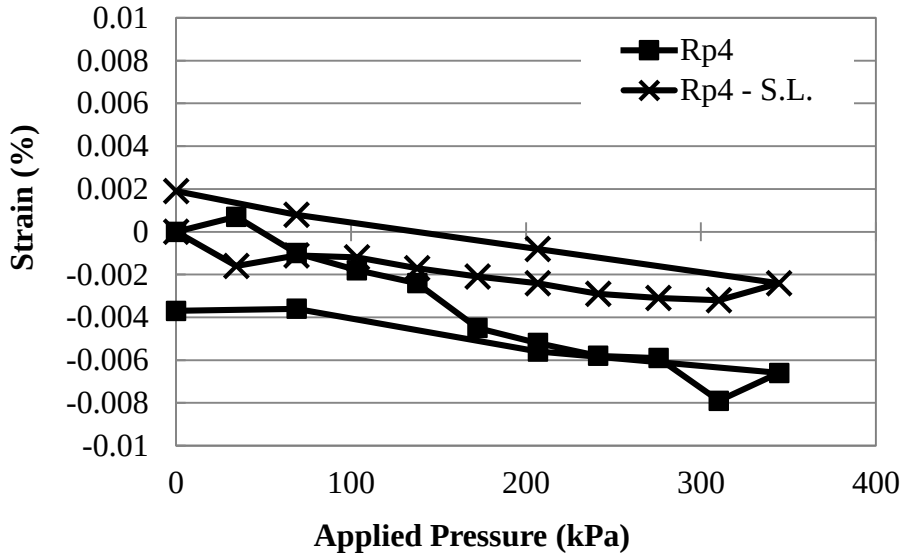

(b) R_{p4}

Figure 4.43 Radial Strains on the Plastic at Pipe Crown with Sand Backfill (Tests 2 and 3)

Figure 4.44 shows the measured strains on the plastic liner (L_{p7} outside the pipe and L_{p8} inside the pipe) on the crown in the longitudinal direction. Clearly most of the strains were tensile, indicating that there was outward movement of soil particles under loading, which induced tension in the plastic liner. In addition, the strain gauge outside the pipe (i.e., L_{p7}) had larger strains than that inside the pipe (i.e., L_{p8}). In general, the single layer of geogrid reduced the strains on the plastic cover in the longitudinal direction. In the unreinforced test section, there was a sudden reduction of the measured strain when the last load was applied. This phenomenon might result from the yielding of the sand backfill and the stress in the sand was re-distributed.

Figure 4.45(a) shows that the strain recorded at Cs1, which was one rib away at the same location, on the steel, shows only an increase in the compressive strain with the increase of the applied plate pressure. However, the strain gauge C_{p1}, on the plastic at the spring line as shown in Figure 4.45(b), shows a distinct and smooth transition of strain as the plate pressure was applied. The strain on the plastic shell began as a compression strain and transitioned to a tensile stain. The strain data indicates that the strain gauge was placed on the outside of the neutral axis of the pipe wall, and that as bending occurred at the spring line, the strain gauge went into tension. Figure 4.45 also shows that double layers of geogrid had a minor effect on the measured strains but reduced the strains on the plastic obviously.

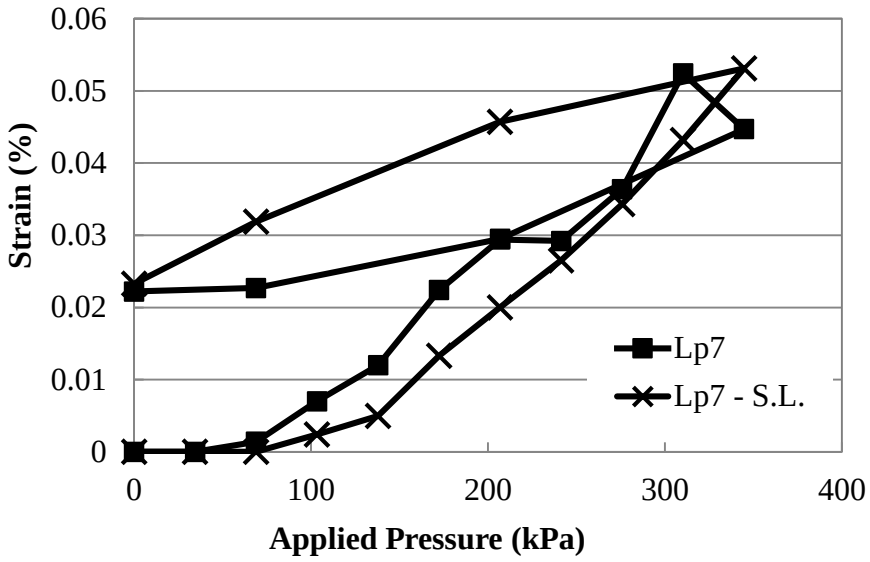

(a) L_{p7}

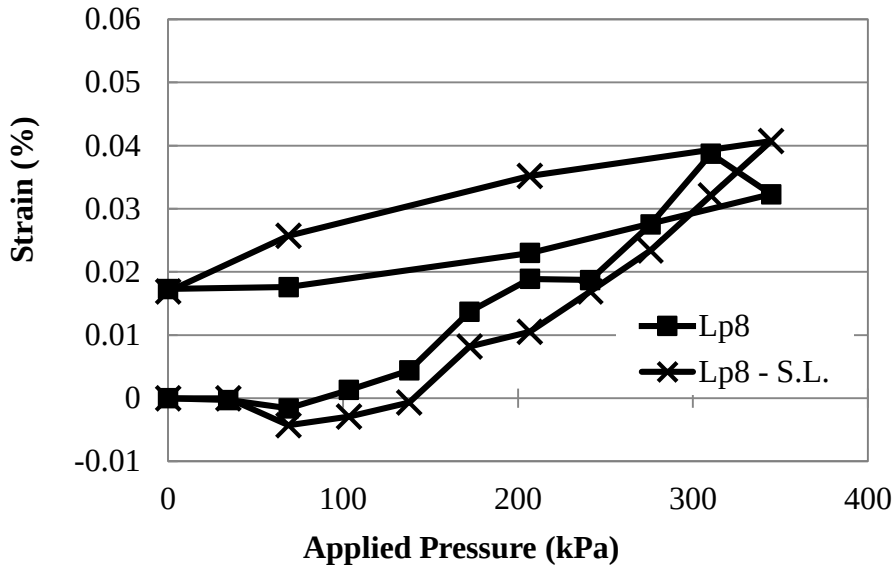

(b) L_{p8}

Figure 4.44 Longitudinal Strains at Crown with Sand Backfill (Tests 2 and 3)

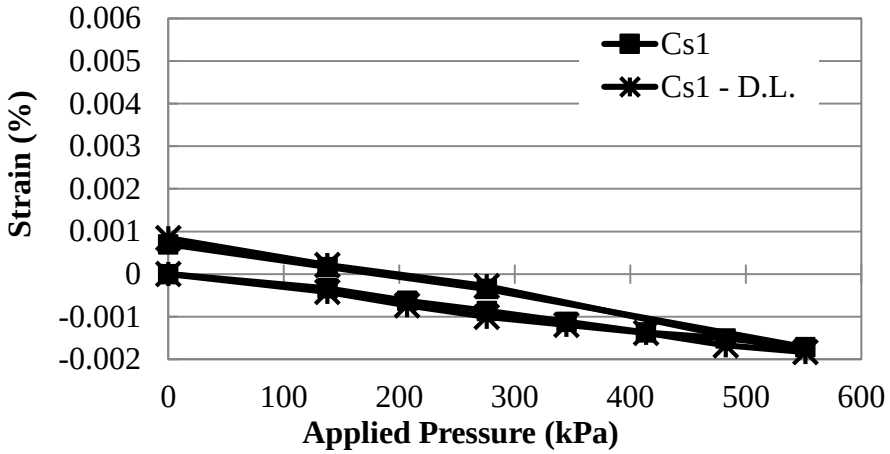

(a) C_{s1}

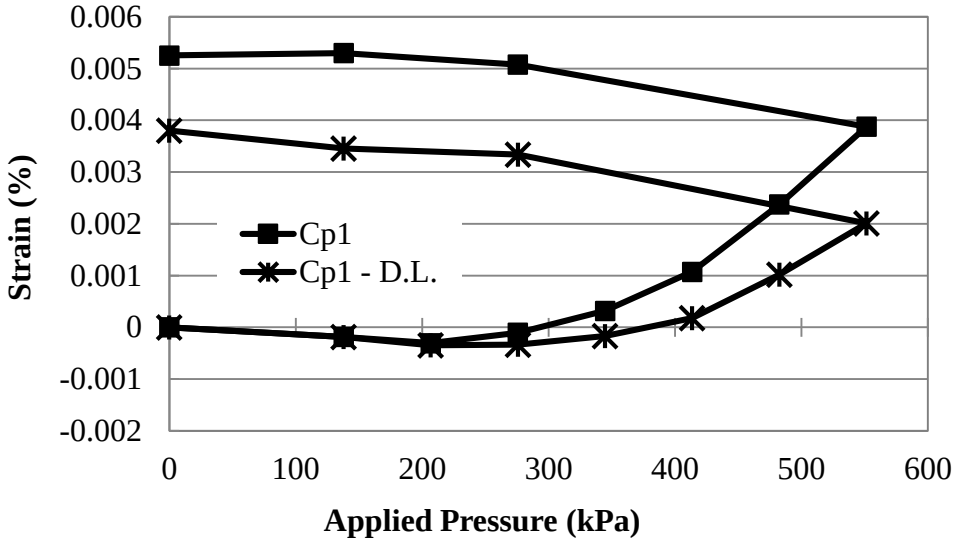

(b) C_{p1}

Figure 4.45 Circumferential Strains at Spring Line with Sand Backfill (Tests 1 and 4)

The radial strain gauges on the plastic cover of the steel ribs at the crown (R_{p3} and R_{p4}) without any geogrid show opposite, compressive and tensile strains, on either side of the rib (Figure 4.46). This result indicates that the steel ribs and the plastic cover at the crown under the loading plate were subjected to bending. Double layers of geogrid resulted in the strain gauges on both sides of the rib deformed in the similar way. In other words, they minimized the bending effect.

Figure 4.47 shows the longitudinal strains on the plastic liner outside and inside the pipe. With an increase of the applied pressure, tensile strains developed both outside and inside the pipe without or with double layers of geogrid. The outside strain gauge (L_{p7}) had larger strains than the inside one (L_{p8}). Double layers of geogrid reduced the tensile strains on the plastic linear during loading. The geogrid layers also prevented the reduction of the strains under the last load due to the yielding of sand. The reduction of the strains during unloading were similar for the test sections without and with geogrid.

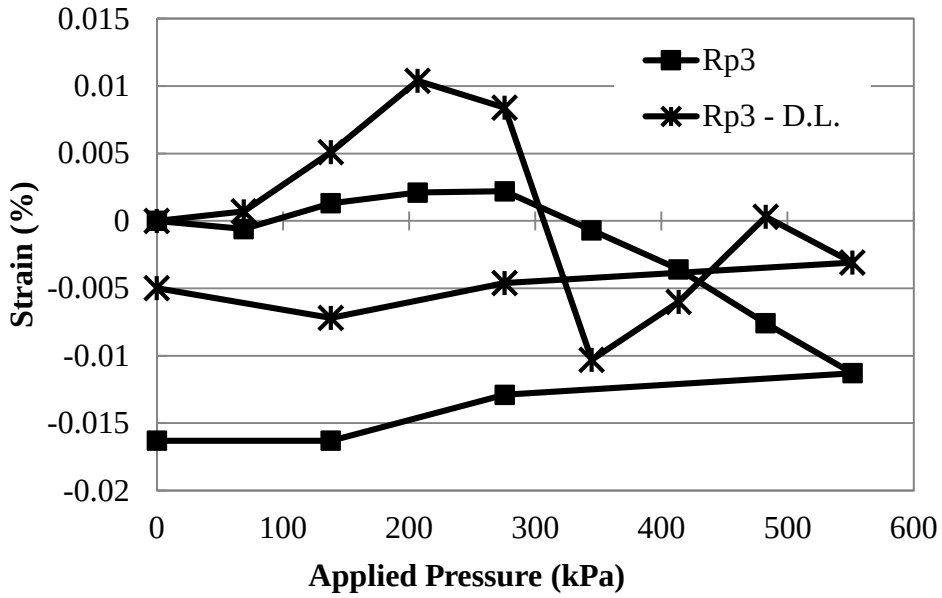

(a) R_{p3}

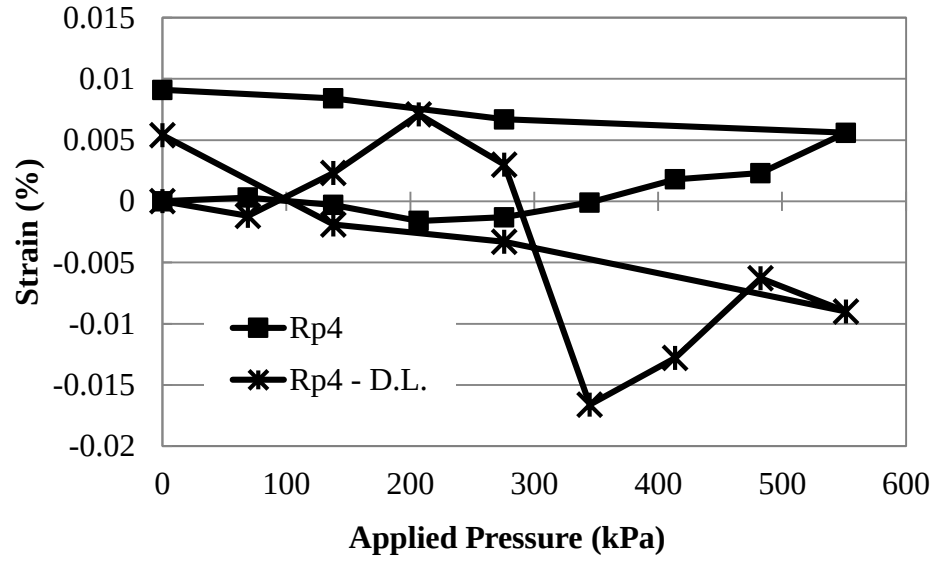

(b) R_{p4}

Figure 4.46 Radial Strains at Crown with Sand Backfill (Tests 1 and 4)

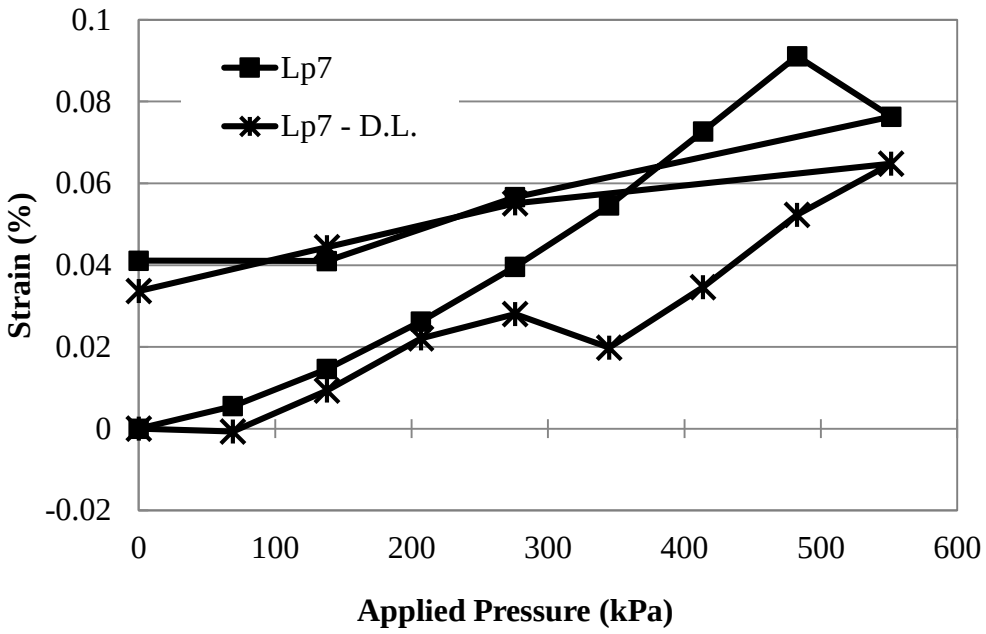

(a) L_{p7}

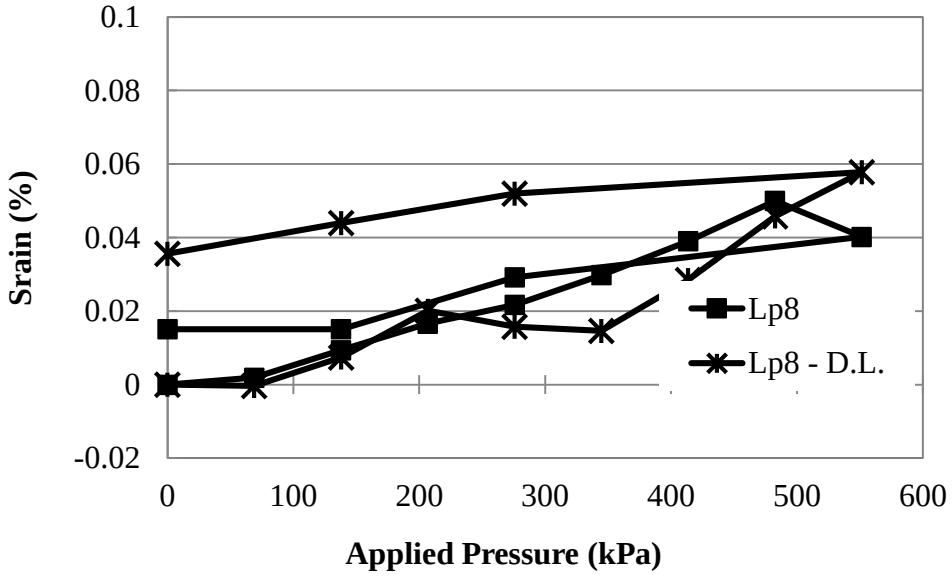

(b) L_{p8}

Figure 4.47 Longitudinal Strain at Crown with Sand Backfill (Tests 1 and 4)

4.5.3 Pipe in Aggregate Backfill

The measured pipe strains of the pipes in aggregate backfill are evaluated in this section. Figures 4.48 and 4.49 show that some strain gauges measured compressive strains while other strain gauges measured tensile strains. The measured strains also show clear rebound during unloading. Figures 4.48 and 4.49 also show that the use of the single geogrid layer slightly reduced the strains in the steel ribs and the plastic as compared those in the unreinforced section.

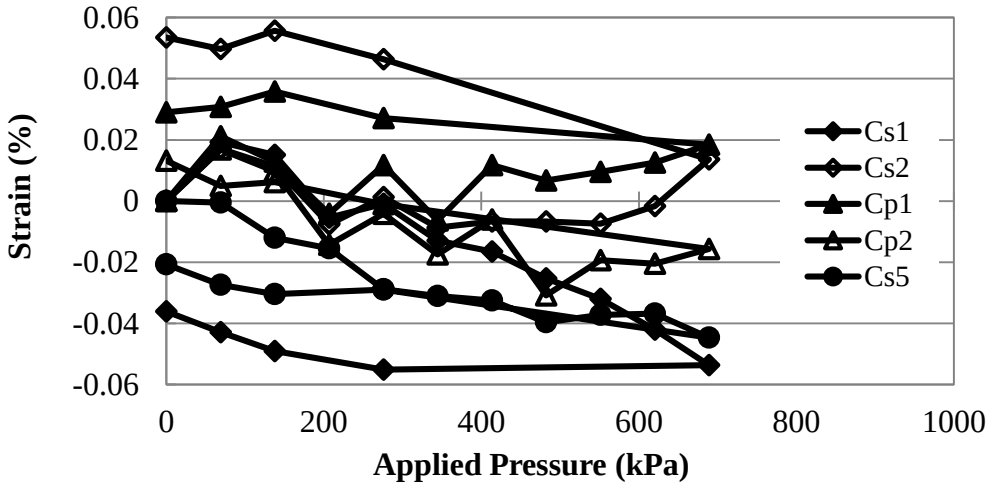

Figure 4.48 Circumferential Strains at Pipe Spring Line with Aggregate Backfill (Test 5)

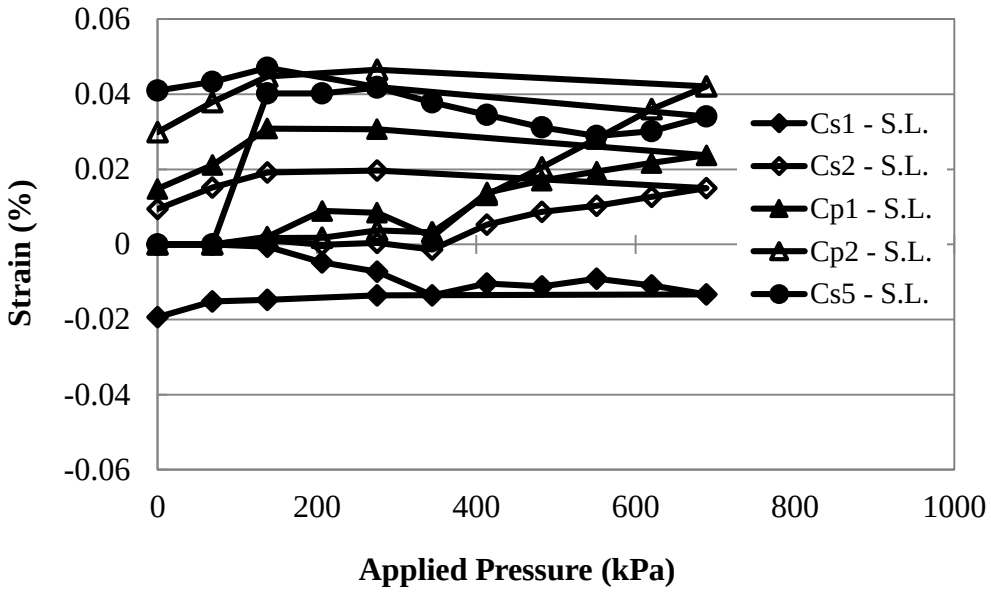

Figure 4.49 Circumferential Strains at Pipe Spring Line with Aggregate Backfill (Test 7)

Figure 4.50 shows that in the test section with double geogrid layers, most of the measured strains in the steel ribs and the plastic were tensile. The maximum strains in this test section were smaller than those in the single geogrid layer section and the unreinforced section.

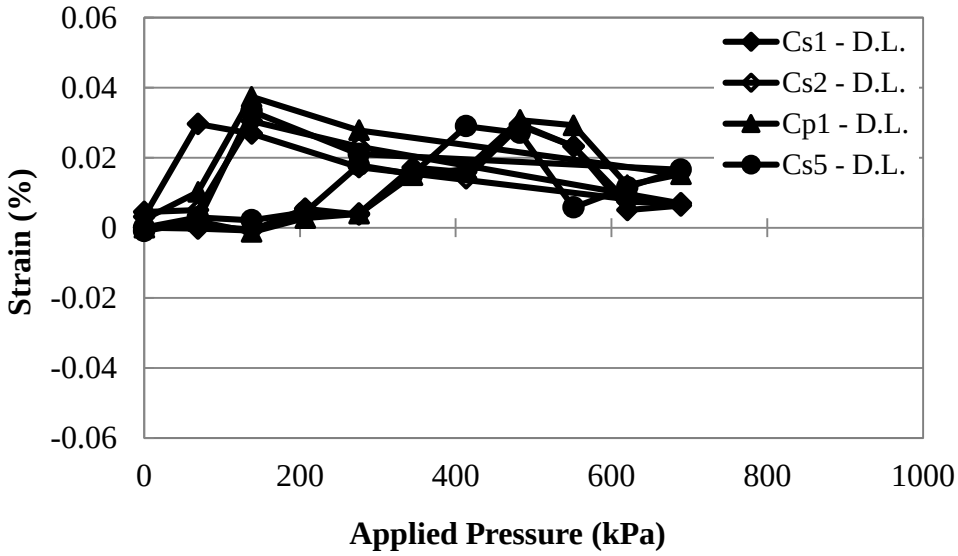

Figure 4.50 Circumferential Strains at Pipe Spring Line with Aggregate Backfill (Test 9)

When the pipes were installed in the aggregate backfill, the measured radial strains on the plastic cover of the steel ribs without a geogrid or single geogrid as shown in Figure 4.51 were compressive on side but tensile on another side, indicating bending action on the ribs. The single geogrid layer reduced the strains on the plastic cover as compared with that without a geogrid. However, the radial strains on the plastic cover of the steel ribs with double geogrid layers were compressive on both sides of the ribs.

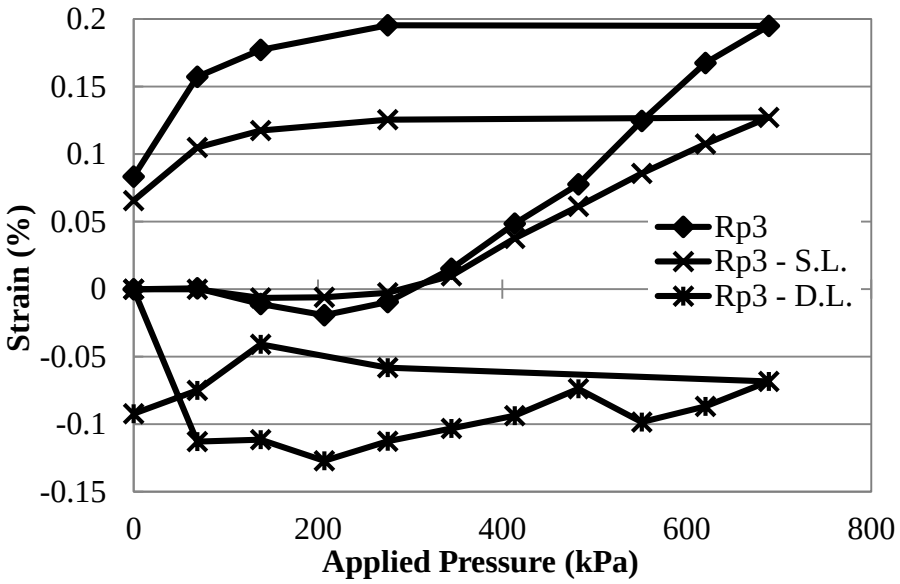

(a) R_{p3}

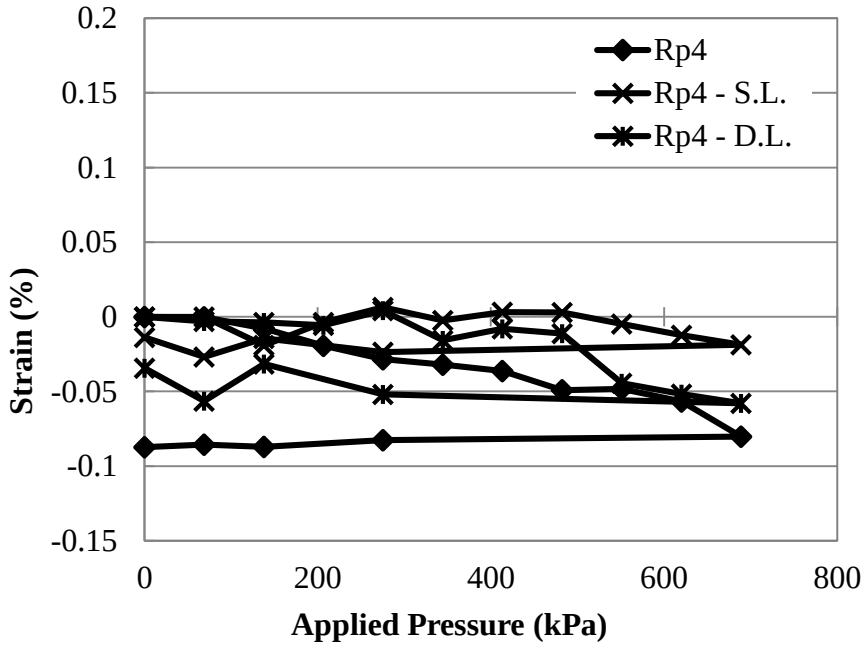

(b) R_{p4}

Figure 4.51 Radial Strains of the Plastic Cover with Aggregate Backfill

When the pipes were installed in the aggregate backfill, the measured longitudinal strains on the outside and inside plastic liners as shown in Figure 4.52 were most tensile. The strains on the outside plastic liners (L_{p7}) were smaller than those on the inside ones. This result is different from that for the pipes installed in the sand backfill. Under this condition, the aggregate might have less lateral spreading than the sand and the bending effect for the pipe in the aggregate backfill was more significant than that in the sand backfill. Figure 4.52 also shows that the use of single or double geogrid layers significantly reduced the tensile strains on the plastic liner in the longitudinal direction.

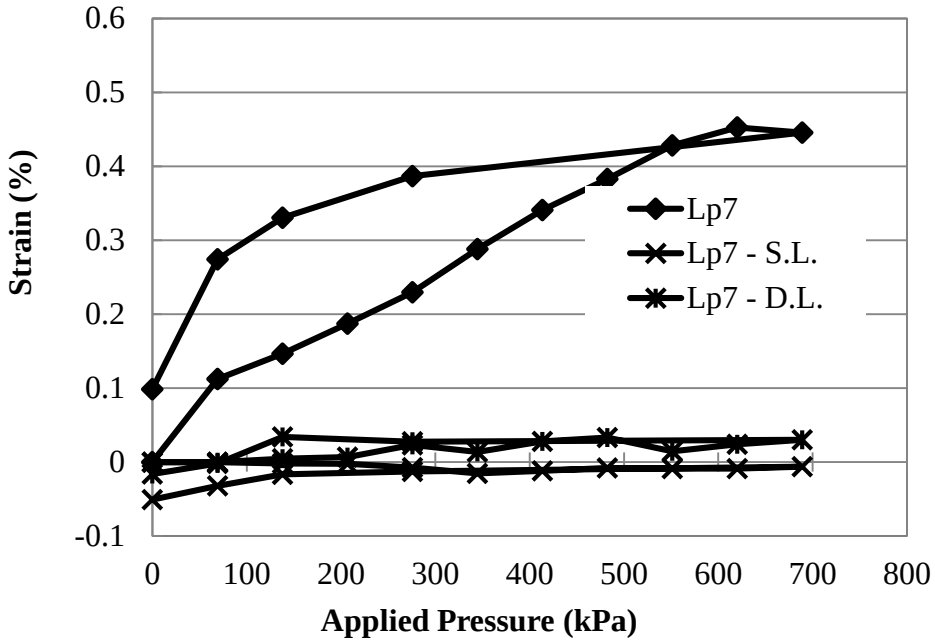

(a) L_{p7}

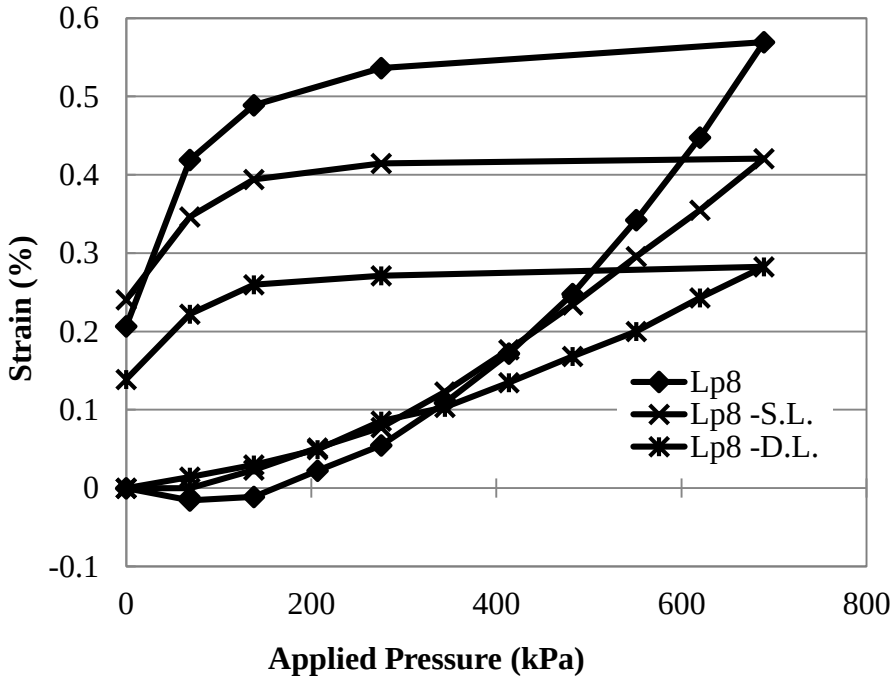

(b) L_{p8}

Figure 4.52 Longitudinal Strains on the Plastic Cover with Aggregate Backfill

4.6 Geogrid Strain

4.6.1 Strain Gauge Layout

Strain gauges were placed on the geogrid to determine the response of the geogrid to the applied load and the pipe system. The strain gauge locations which were shown in Chapter 3 are shown here again for convenience (Fig. 4.53). The strain gauges were placed on the top of the geogrid in either the single or double layers. For a single layer, only the lower layer was used. The measured strains on the geogrid(s) were grouped as follows: (1) double layers of geogrid in the sand backfill covered by the well-graded aggregate base course (Test 3), (2) a single layer of geogrid in the sand backfill covered by the sand base course (Test 4), and (3) single and double layers of geogrid in the aggregate backfill covered by well-graded aggregate base course (Tests 7 and 9). All the strain data are plotted with the applied plate pressure or with the distance at the maximum applied pressure.

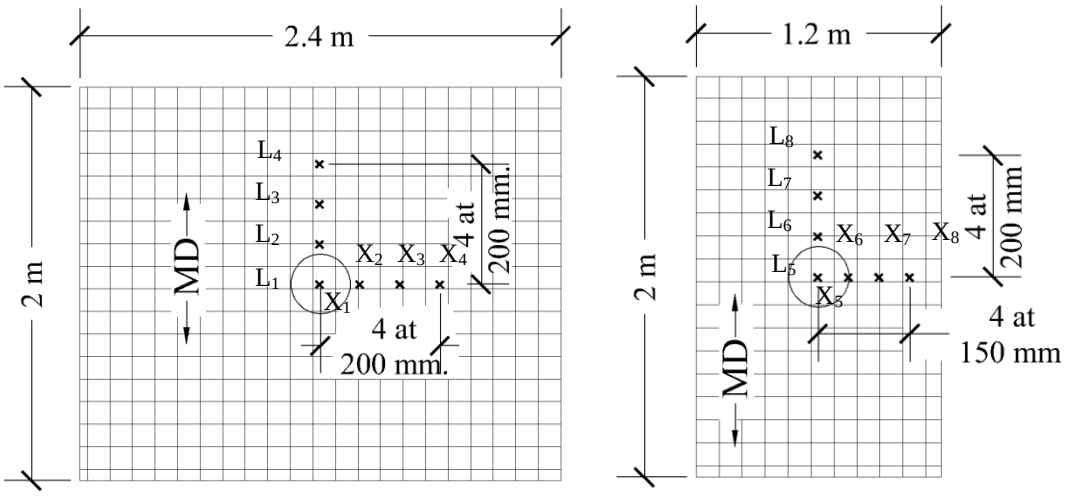

A. Upper Layer **B. Lower Layer**

Figure 4.53 Geogrid Strain Gauges on Single and Double Layers of Geogrid

4.6.2 Geogrid Strains in Test 3

In this test the a single layer of geogrid was placed at 152 mm above the pipe along the entire length of the pipe and with the width of the trench. The geogrid was instrumented with strain gauges and the strains were recorded with each applied load. The machine direction of the geogrid was the same as the longitudinal direction of the pipe while the cross-machine direction of the geogrid was perpendicular to the pipe. Figure 4.45 shows the measured geogrid strains in the machine and cross-machine directions. The strains in the machine direction were larger than those in the cross-machine direction. This is because the biaxial geogrid had higher tensile stiffness in the cross-machine direction than that in the machine direction. Figure 4.45 also shows that the geogrid strain increased with the applied plate pressure.

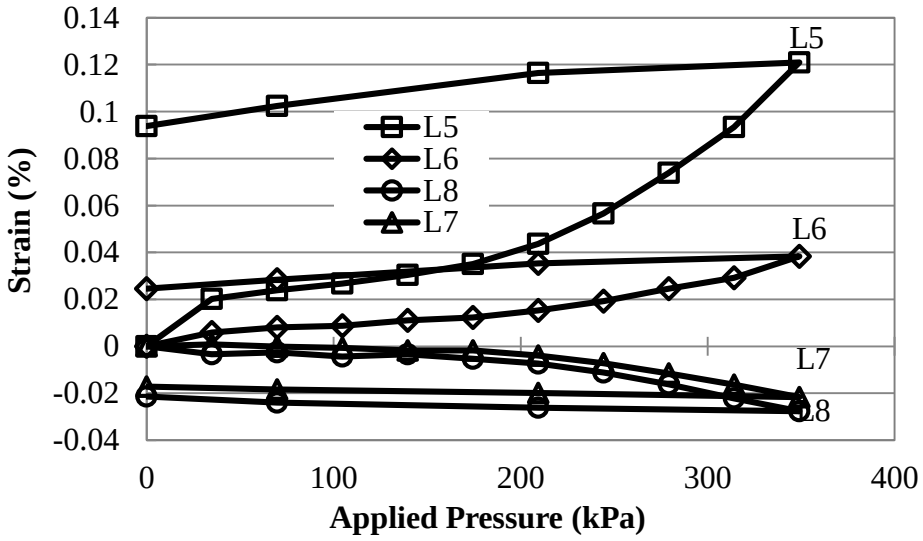

(a) Machine direction

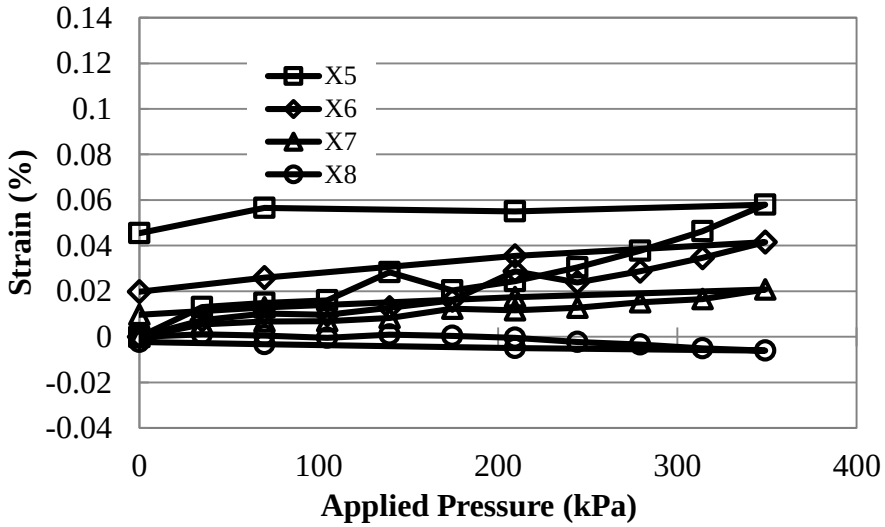

(b) Cross-machine direction

Figure 4.54 Measured Strains in the Lower Geogrid Layer in Test 3

Figure 4.55 shows that the maximum tensile strains happened at the center of the geogrid layer and the magnitude of the strain decreased with the distance. At a certain distance, the strains became compressive. These strain results resulted from lateral spreading of sand under the applied pressure. In other words, the geogrid provided lateral restraint to soil particle movement.

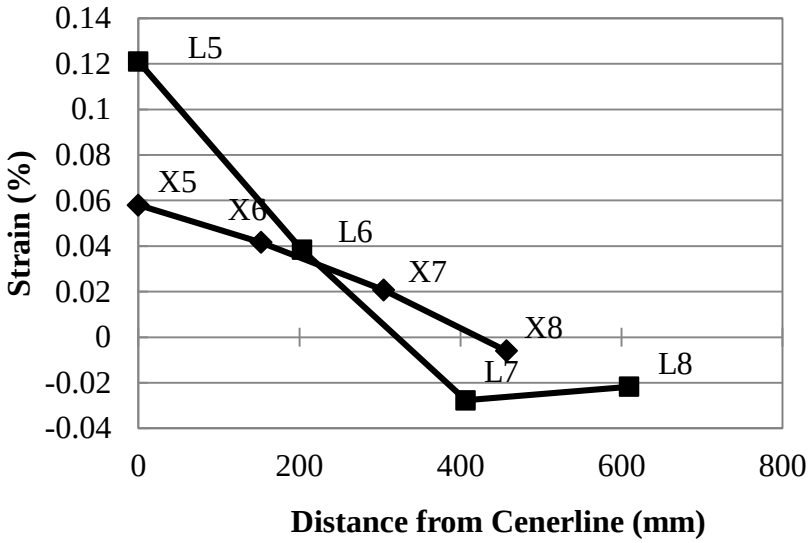

Figure 4.55 Distribution of Geogrid Strain with the Distance at the Maximum Applied Pressure of 345 kPa in Test 3

4.6.2 Geogrid Strains in Test 4

In this test a layer of geogrid was laid at 152 mm above the pipe with a width equal to the trench. An additional layer of geogrid was placed at 229 mm above the lower geogrid layer. This elevation coincided with the bottom of the base course. The upper geogrid layer like the lower geogrid layer was laid out over the length of the pipe (2.0 m) and the width of the geogrid was 2.4 m.

Figure 4.56 shows the measured strains in the lower geogrid layer in the machine and cross-

machine directions with the applied pressure. Clearly the measured strains in the machine direction were much larger than those in the cross-machine direction. The measured strains in the upper layer of geogrid had the similar behavior as shown in Figures 4.57; however, the upper geogrid layer had much larger strains than the lower geogrid layer because the upper layer was close to the applied loading plate.

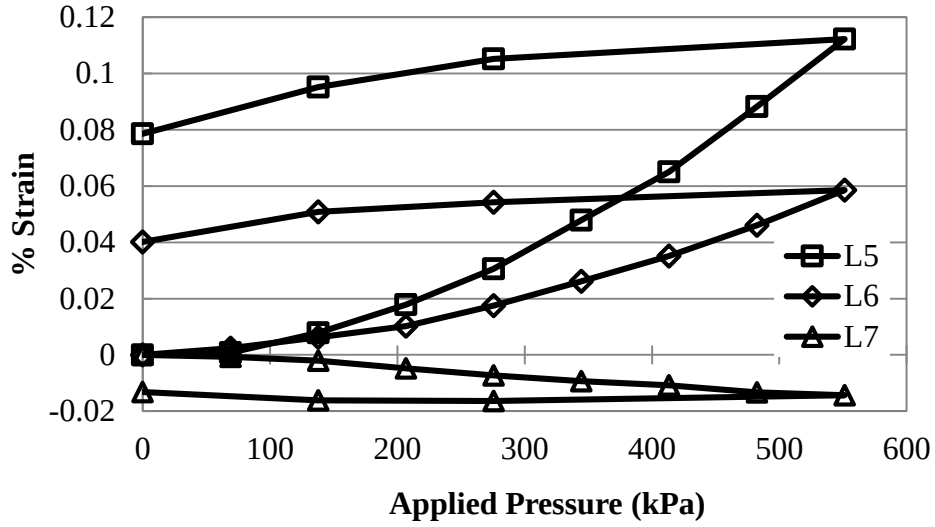

(a) Machine direction

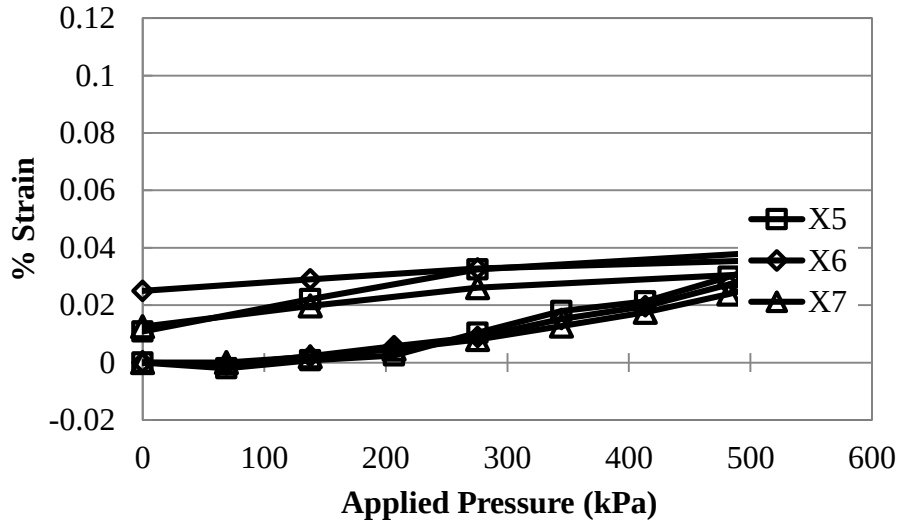

(b) Cross-machine direction

Figure 4.56 Measured Strains in the Lower Geogrid Layer in Test 4

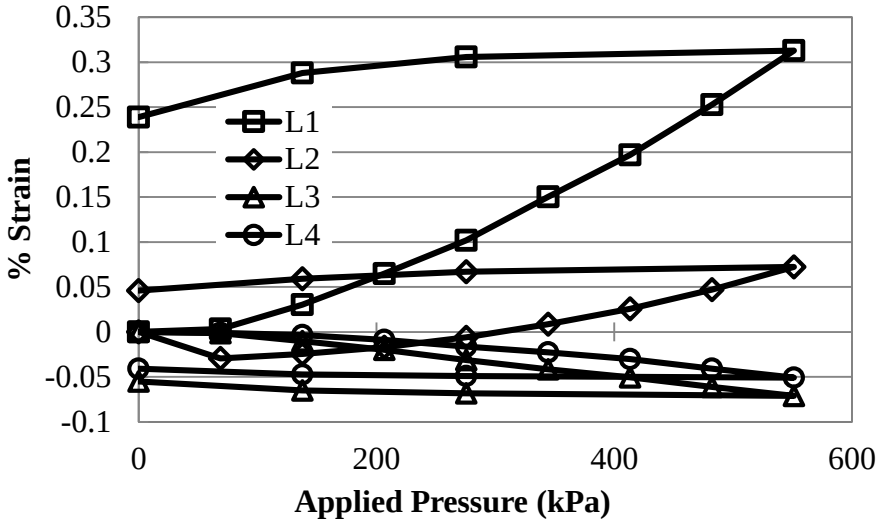

(a) Machine direction

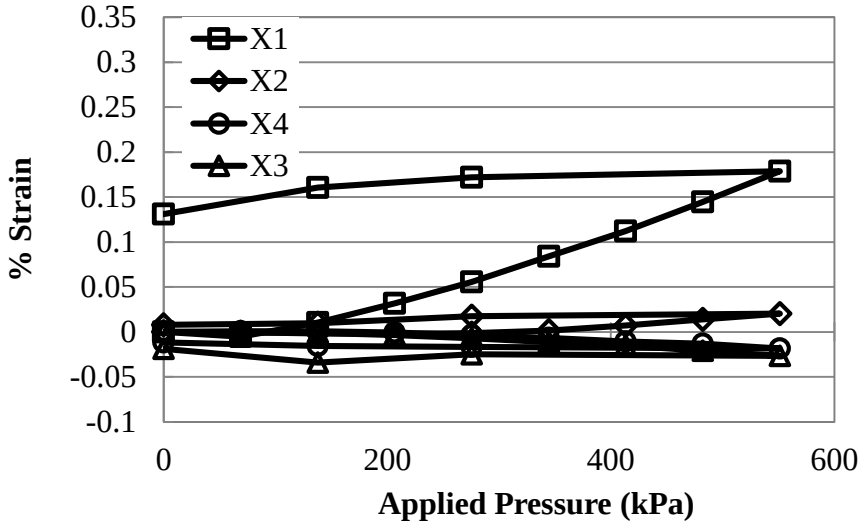

(b) Cross-machine direction

Figure 4.57 Measured Strains in the Upper Geogrid Layer in Test 4

Figures 4.58 and 4.59 show the distributions of the measured strains in the upper and lower geogrid layers with the distance at the maximum applied pressure. They have similar distributions but the upper geogrid layer had much larger strains than the lower geogrid layer.

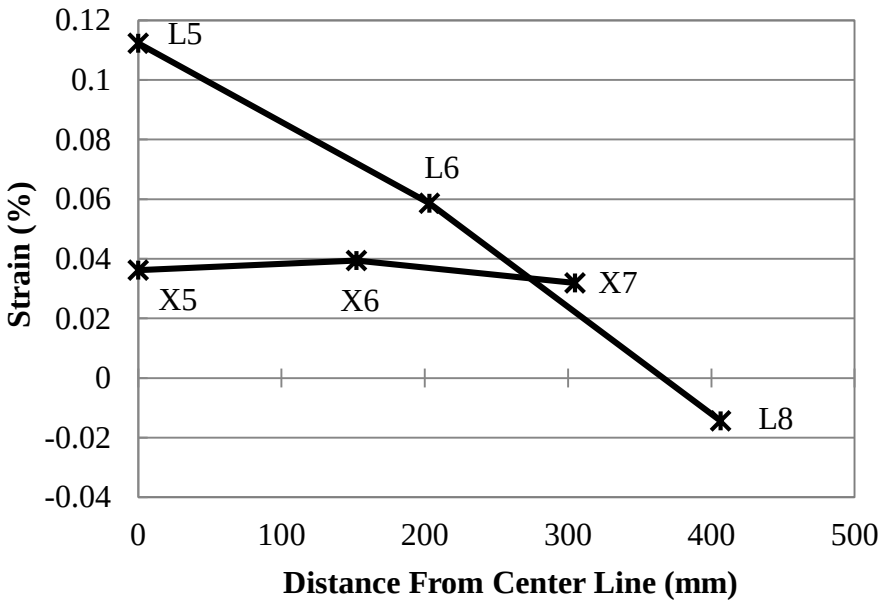

Figure 4.58 Distribution of Measured Strains in the Lower Geogrid Layer at Maximum Applied Pressure of 689 kPa in Test 4

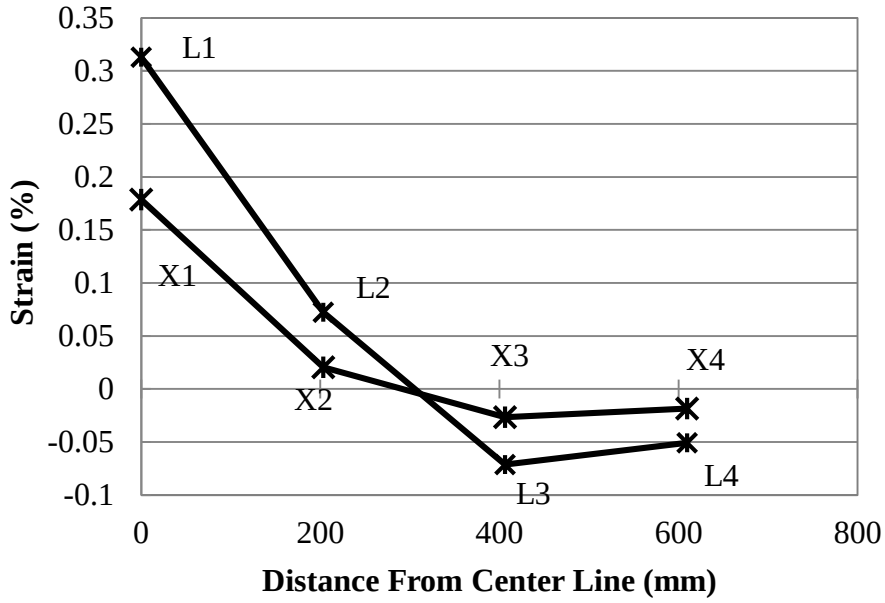

Figure 4.59 Distribution of Measured Strains in the Upper Geogrid Layer at Maximum Applied Pressure of 689 kPa in Test 4

4.6.3 Geogrid Strains in Tests 7 and 9

In Tests 7 and 9, pipes were installed in aggregate backfill. In Test 7, only one lower geogrid layer was placed while in Test 9, double geogrid layers (one lower and one upper layer) were installed.

Figure 4.60 shows the measured strains in the lower geogrid layer in Test 7. Among four strain gauges in each direction, two strain gauges failed to record strains during the tests; therefore, they are not included in the figures. Figure 4.60 shows that higher strains developed in the machine direction.

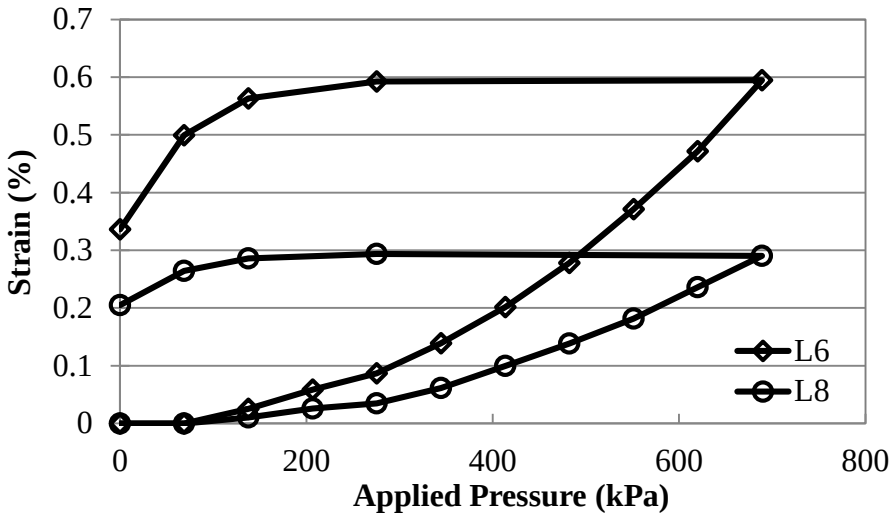

(a) Machine direction

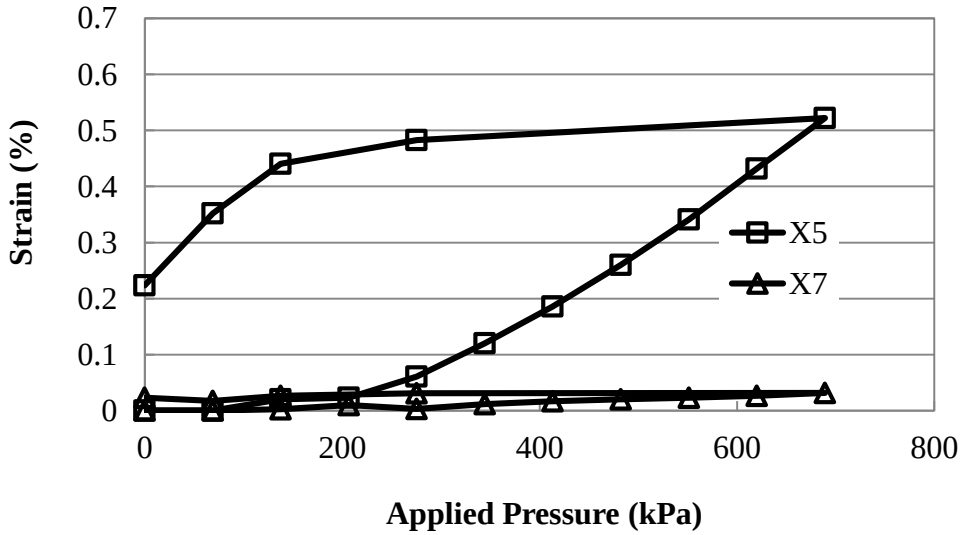

(b) Cross-machine direction

Figure 4.60 Measured Strains in the Lower Geogrid Layer in Test 7

Figure 4.61 presents the measured strains in the lower geogrid layer while Figure 4.62 shows the measured strains in the upper geogrid layer in Test 9. The lower geogrid layer had much larger measured strains in the machine direction than those in the cross-machine direction. However, the upper geogrid layer had larger measured strains in the cross-machine direction than that in the machine direction. This result is different from those in other tests. The reason for this difference is not known.

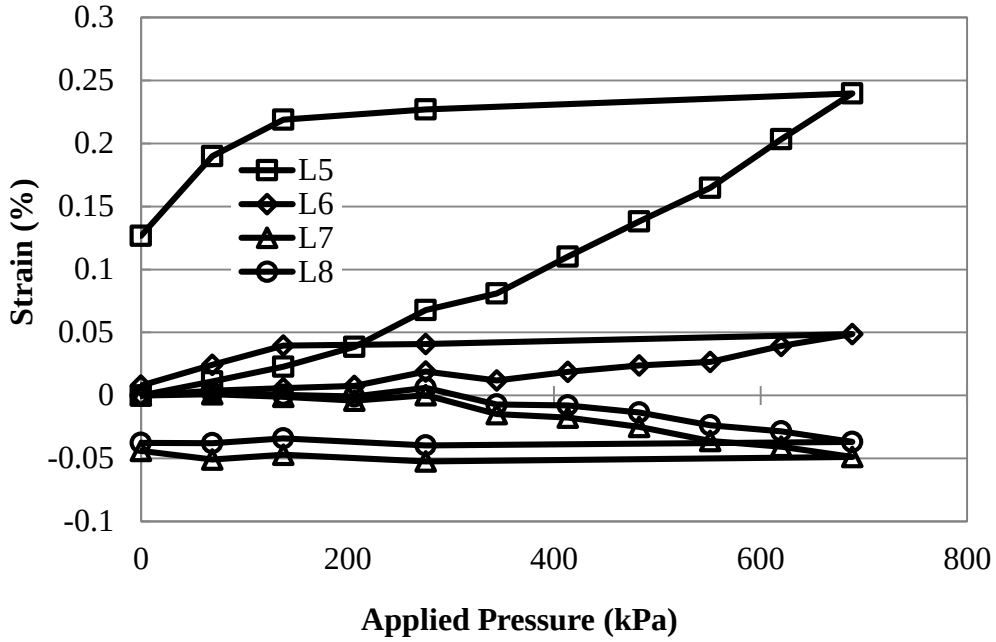

(a) Machine direction

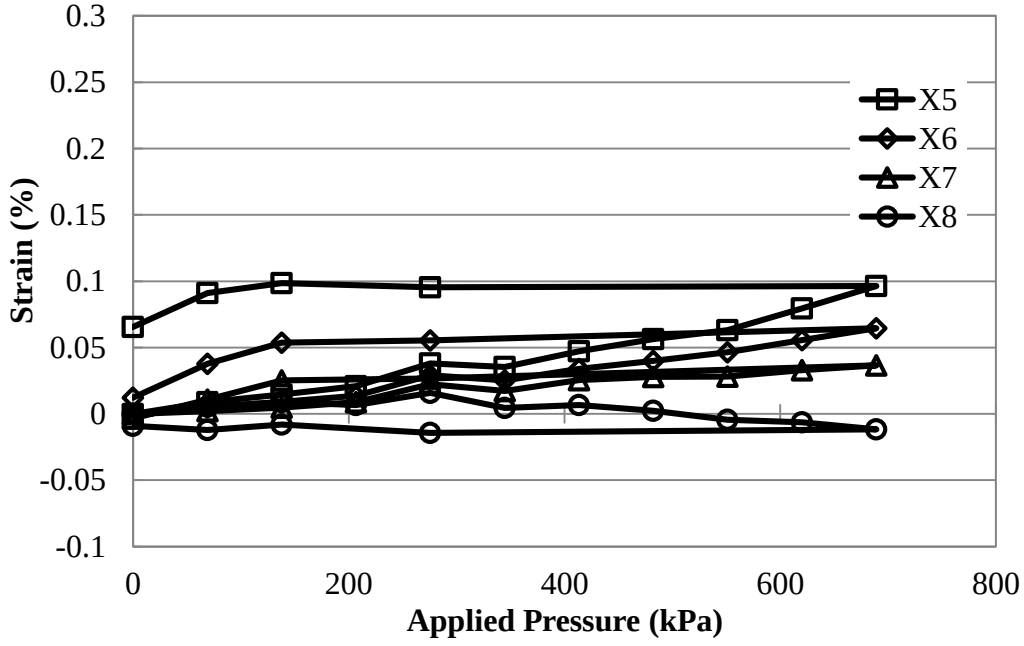

(b) Cross-machine direction

Figure 4.61 Measured Strains in the Lower Geogrid Layer in Test 9

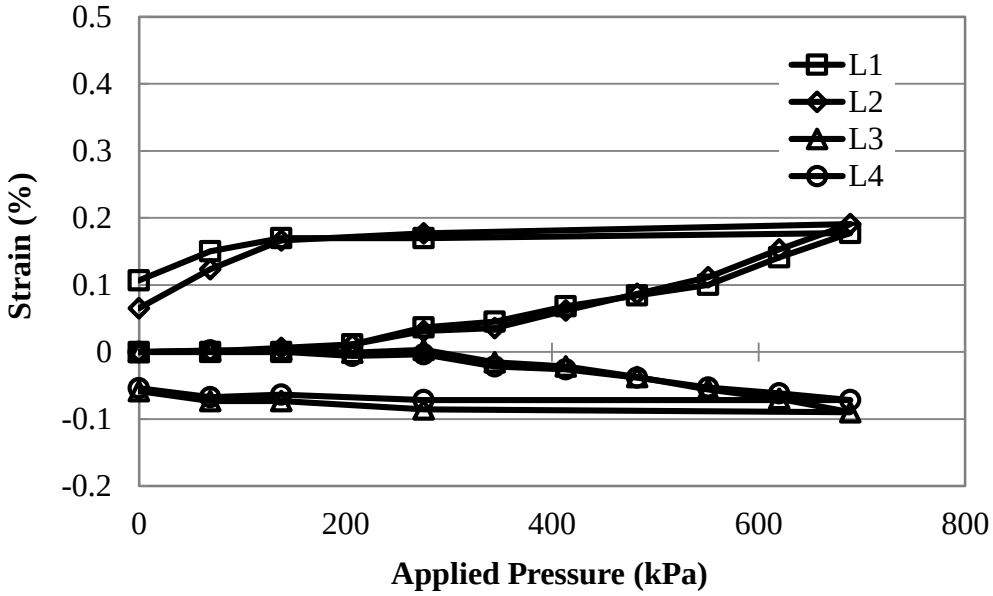

(a) Machine direction

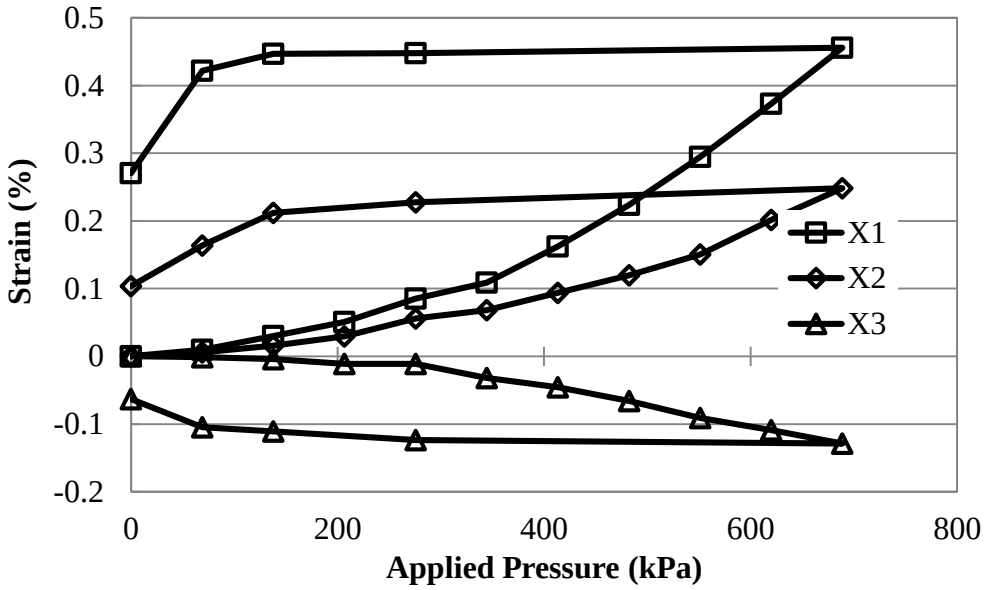

(b) Cross-machine direction

Figure 4.62 Measured Strains in the Upper Geogrid Layer in Test 9

Since Test 7 only had two strain data in each direction, no distribution of measured strains with the distance is provided here. Figures 4.63 and 4.64 show the distributions of the measured strains in the lower and upper geogrid layers with the distance to the center at the maximum applied pressure. It is shown that the maximum strains mostly occurred at the center and decreased with the distance. In addition, the upper layer had larger measured strains than the lower layer.

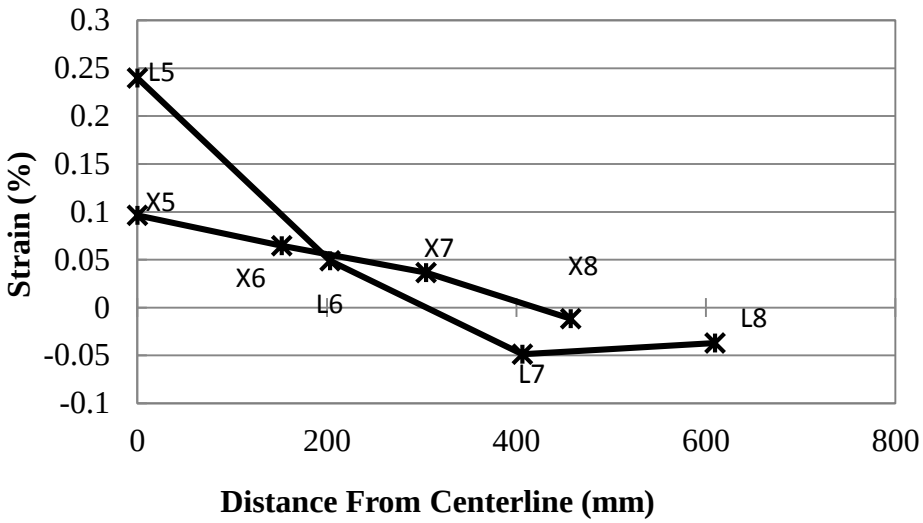

Figure 4.63 Distribution of Measured Strains in the Lower Geogrid Layer at Maximum Applied Pressure of 689 kPa in Test 9

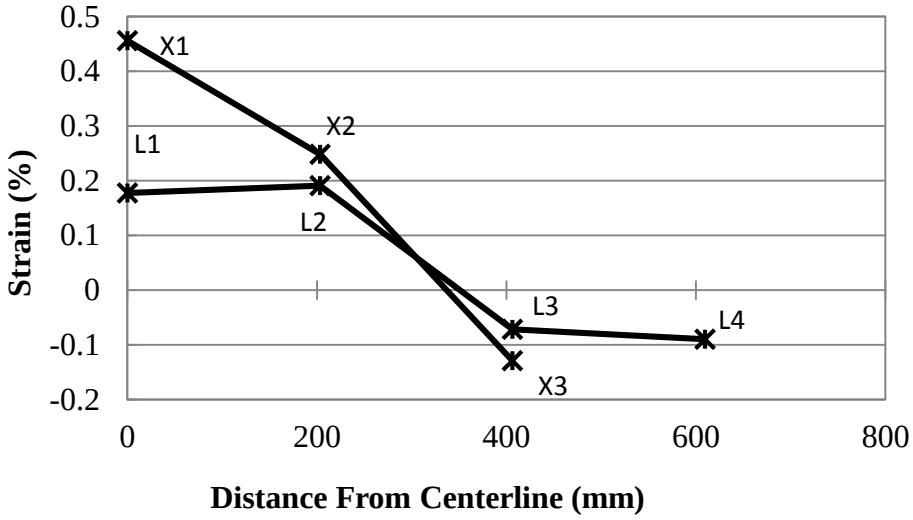

Figure 4.64 Distribution of Measured Strains in the Upper Geogrid Layer at Maximum Applied Pressure of 689 kPa in Test 9

Chapter 5 Cyclic Plate Load Tests

5.1 Introduction

After each static plate loading test with the aggregate backfill (Tests 5, 7, and 9), a cyclic load plate test was run on the same test section without changing the pipe, the backfill, the reinforcement, or the base course. Each cyclic load test consisted of applying cyclic loads to simulate the traffic loading with the same 0.3 m diameter loading plate as the static loading test. Each cyclic plate pressure had a trough value of 7 kPa, which was applied to keep the plate in contact with the surface and to prevent impact loading on the surface. The peak pressure was increased after a set number of cycles until the maximum peak pressure was reached. The loading wave frequency was 0.77 Hz. Table 5.1 provides a table of the cyclic load test parameters. The visual representation of the number of load cycles and the peak pressure is shown in Figure 5.1.

Table 5.1 Cyclical Load Tests

Test no	Description	Static pressure (kPa)		Cyclic loading	
		Increment	Max.	Increment peak (each 200 cycles)	Max. peak (cycles)
Tests 6, 8, and 10	Crushed aggregate as bedding and	68.9	689	20	100 (1000 cycles)

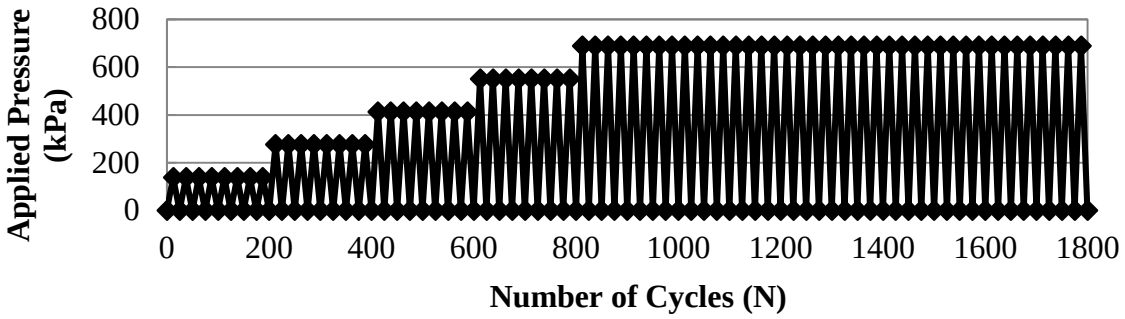

Figure 5.1 Cyclic loading used in Tests 6, 8, and 10

5.2 Plate Vertical Displacement

Minimum and maximum plate vertical displacements were monitored and recorded during each cyclic loading test. The data recorders took data every one tenth of a second continuously. The minimum displacement corresponds to the permanent deformation of the test section after unloading while the maximum displacement corresponds to the maximum deformation of the test section under loading. Due to a large number of data points, the data points will be presented at the beginning and the end of the load step after every 40 cycles except for the last load under which the data points will be plotted every 200 cycles.

Figure 5.2 shows that the plate vertical displacements of the unreinforced section increased gradually with each increase in the applied peak pressure. At approximately 600 to 800 cycles, and at a peak pressure of 276 kPa, there was a large increase in the plate vertical displacement with each cycle. After hundreds of cycles it appeared that the plate vertical displacement was stabilizing and had a slower rate of increase with additional load cycles.

The reinforced sections as shown in Figs. 5.3 and 5.4 followed the similar behavior. However, the test section with a single layer of geogrid had slightly larger vertical displacements

than those without any geogrid as shown in Fig. 5.3. This phenomenon also happened under static loading. This difference might result from the variability of the material properties in these two test sections. In other words, the geogrid within the trench did not have any positive effect in reducing the plate vertical displacement. The test section with double layers of geogrid as shown in Fig 5.4 reduced the maximum vertical displacement by 43 percent as compared with the unreinforced test section. This result implies that the upper geogrid layer was much more effective than the lower geogrid layer in reducing the plate vertical displacement. Figure 5.4 also shows that percentage of the elastic rebound to the total vertical displacement was much larger than that in other two test sections. This result suggests that the upper geogrid layer made the test section more resilient.

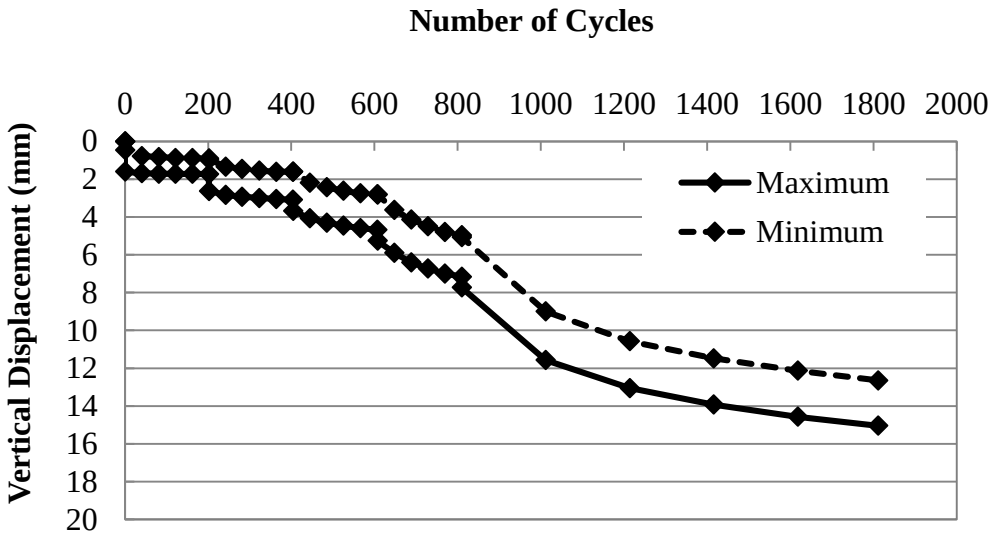

Figure 5.2 Plate Vertical Displacements in the Unreinforced Section (Test 6)

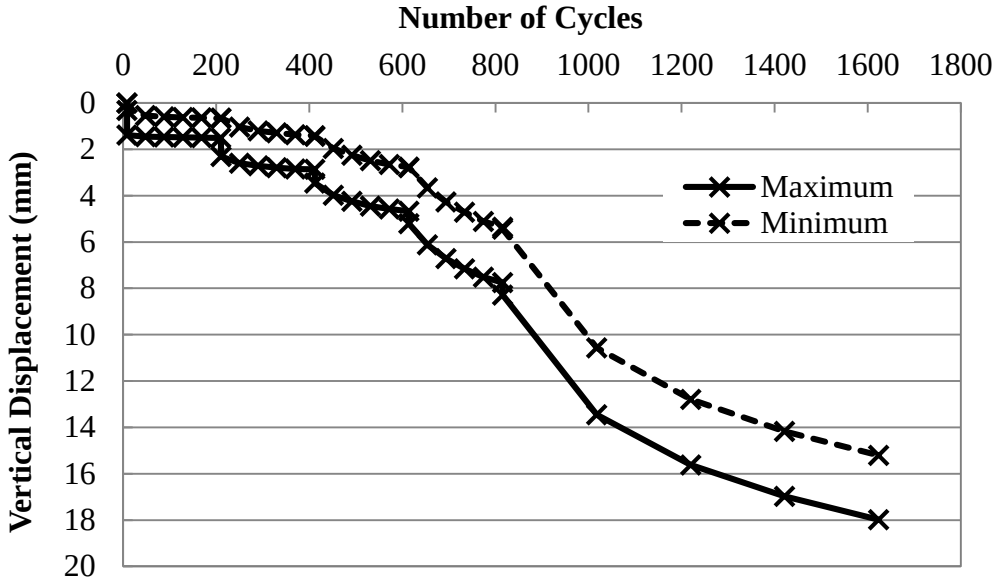

Figure 5.3 Plate Vertical Displacements in the Single Geogrid-Reinforced Section (Test 8)

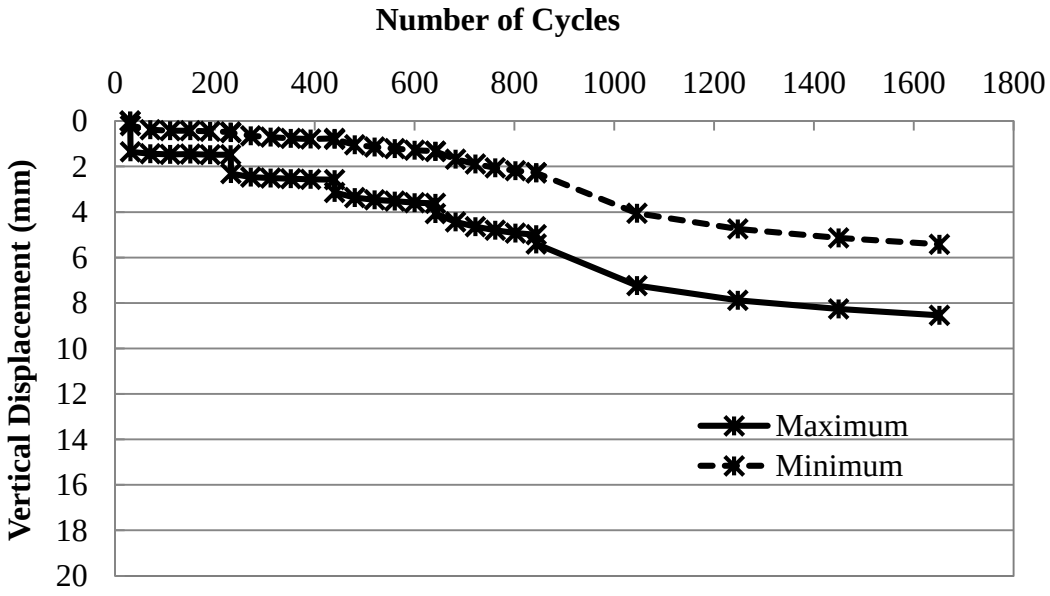

Figure 5.4 Plate Vertical Displacements in the Double Geogrid-Reinforced Section (Test 10)

5.3 Pipe Deflection

Pipe deflection is referred to as the change of the pipe diameter under loading. Pipe vertical deflection is the reduction of the pipe diameter in the vertical direction while pipe horizontal deflection is the increase of the pipe diameter in the horizontal direction. Pipe vertical displacement at the crown is the pipe vertical deflection plus the pipe vertical displacement at the invert. Pipe vertical deflections were measured under the loading plate and at a distance of 305 mm away from the center of the plate in the longitudinal direction of the pipe. Pipe horizontal deflections and vertical displacements were also monitored during the application of cyclic loading in these three test sections. The vertical displacements of the pipe crown were measured using tell-tales installed on the pipe crown against a stationary datum. Due to a large number of data points, the data points will be presented at the beginning and the end of the load step after every 40 cycles except for the last load under which the data points will be plotted every 200 cycles.

5.3.1 Pipe Vertical Deflection

Figures 5.5, 5.6, and 5.7 show the measured vertical deflections of the pipes in these three tests, which had a deflection pattern similar to those of the plate vertical displacements. Consistent with the test results discussed earlier, the double geogrid-reinforced section had the least pipe vertical deflection, followed by the unreinforced section and then the single geogrid-reinforced section. Again, the upper geogrid layer had an apparent benefit in reducing the pipe vertical deflection.

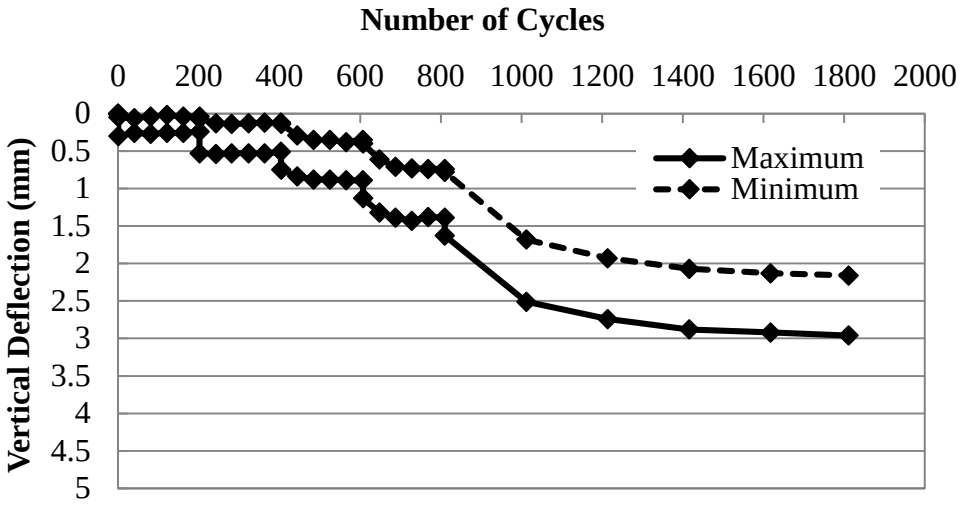

Figure 5.5 Pipe Vertical Deflections in the Unreinforced Section (Test 6)

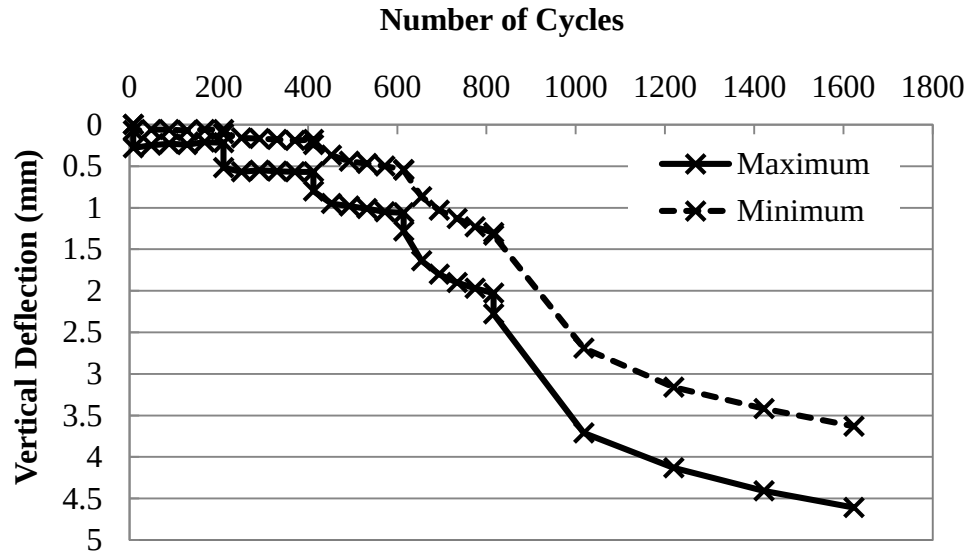

Figure 5.6 Pipe Vertical Deflections in the Single Geogrid-Reinforced Section (Test 8)

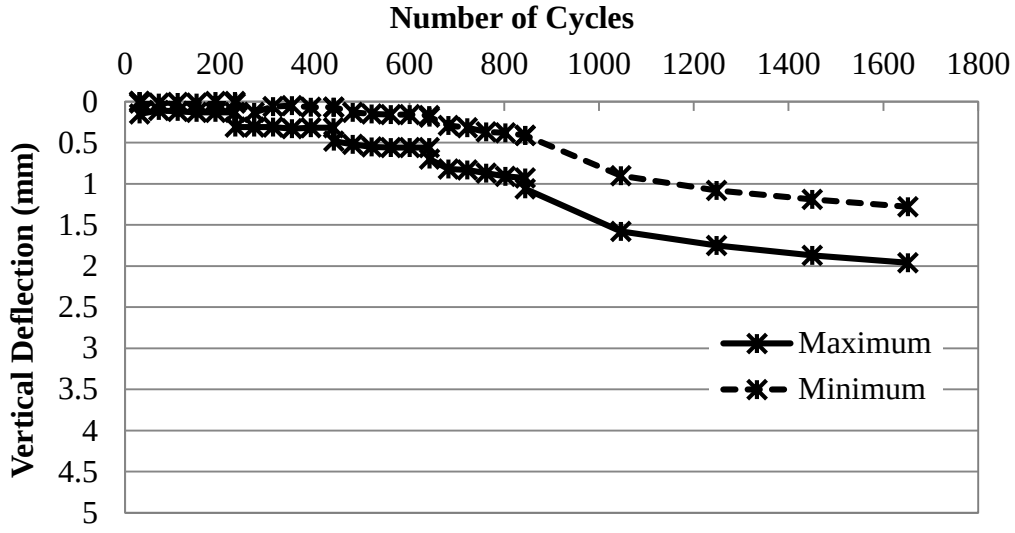

Figure 5.7 Pipe Vertical Deflections in the Double Geogrid-Reinforced Section (Test 10)

Figures 5.8, 5.9, and 5.10 show the measured vertical deflections of the pipes at 305 mm from the center of the pipe in these three tests. As expected, the deflections at these locations are similar to those directly under the loading plate, but with a smaller magnitude of deflection.

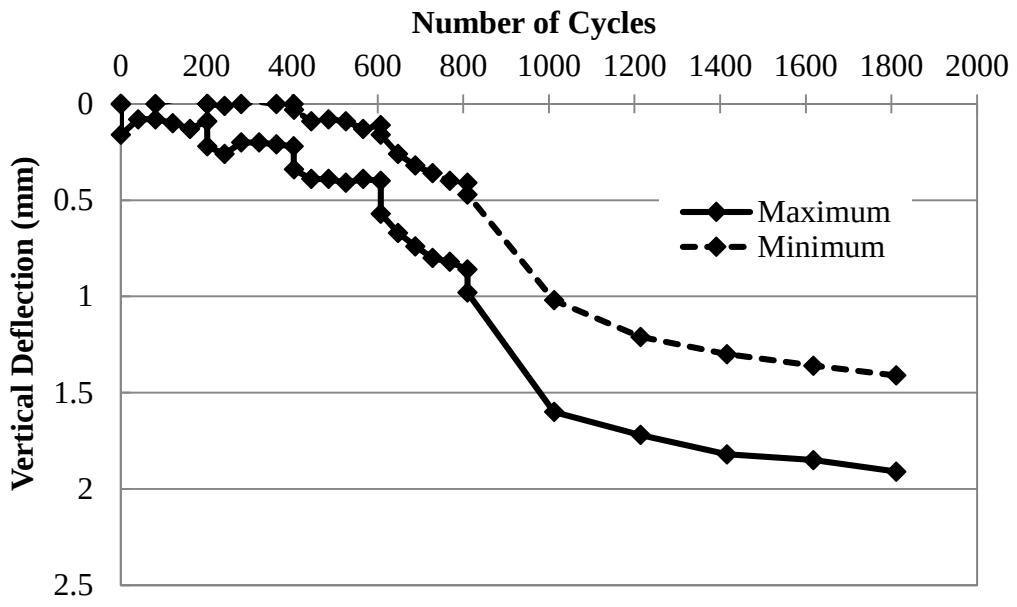

Figure 5.8 Pipe Vertical Deflection at 305 mm from the Center of the Plate in the Unreinforced Section (Test 6)

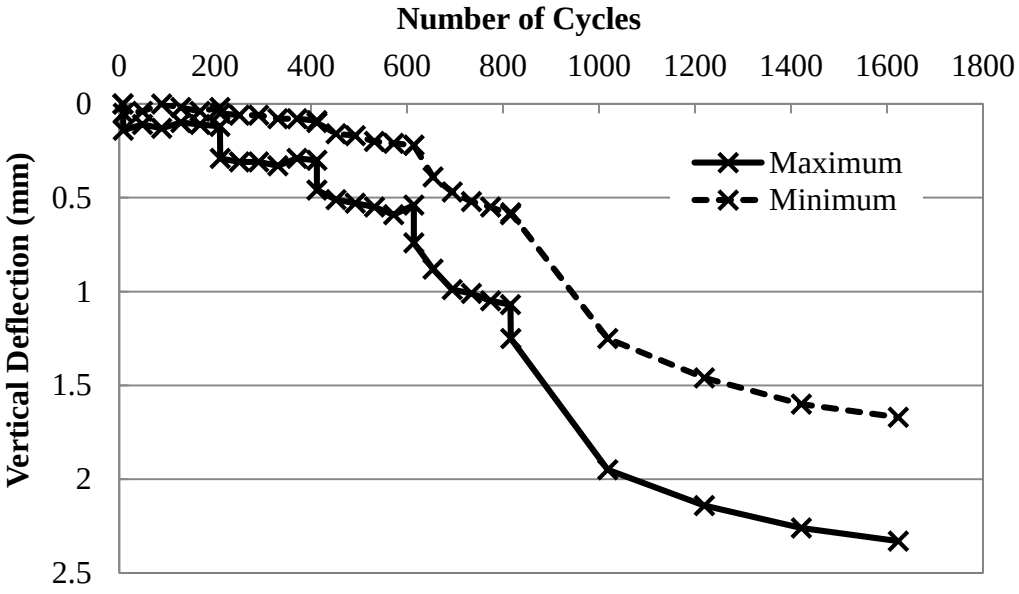

Figure 5.9 Pipe Vertical Deflection at 305 mm from the Center of the Plate in the Single Geogrid-Reinforced Section (Test 8)

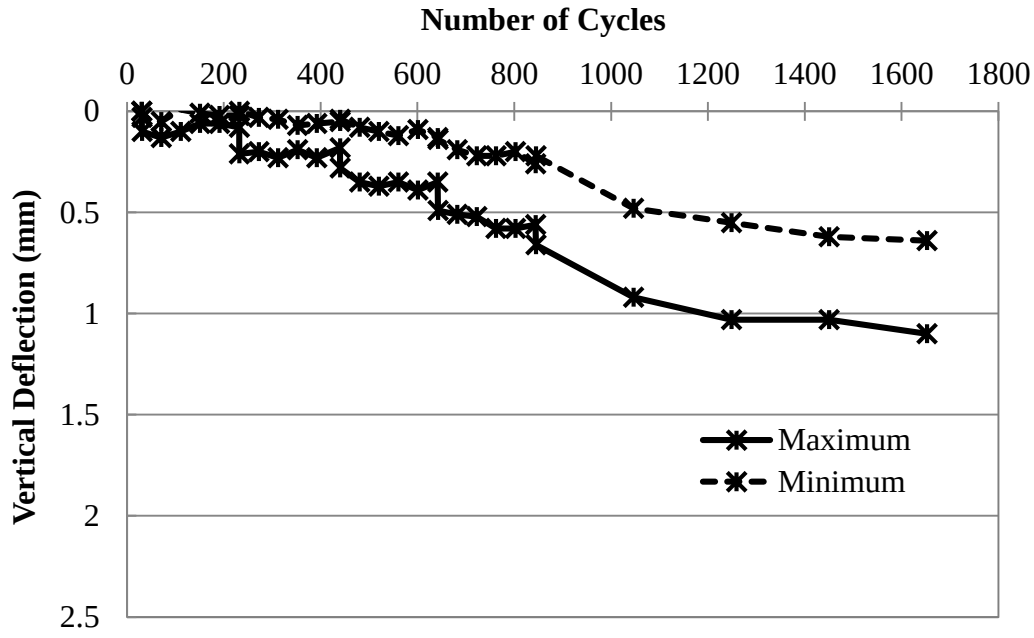

Figure 5.10 Pipe Vertical Deflection at 305 mm from the Center of the Plate in the Double Geogrid-Reinforced Section (Test 10)

Figures 5.11, 5.12, and 5.13 show the measured vertical displacements at the pipe crown under the loading plate with the number of loading cycles. Similar to other test results, the double geogrid-reinforced section had the least vertical displacement at the pipe crown, followed by the unreinforced section and then the single geogrid-reinforced section.

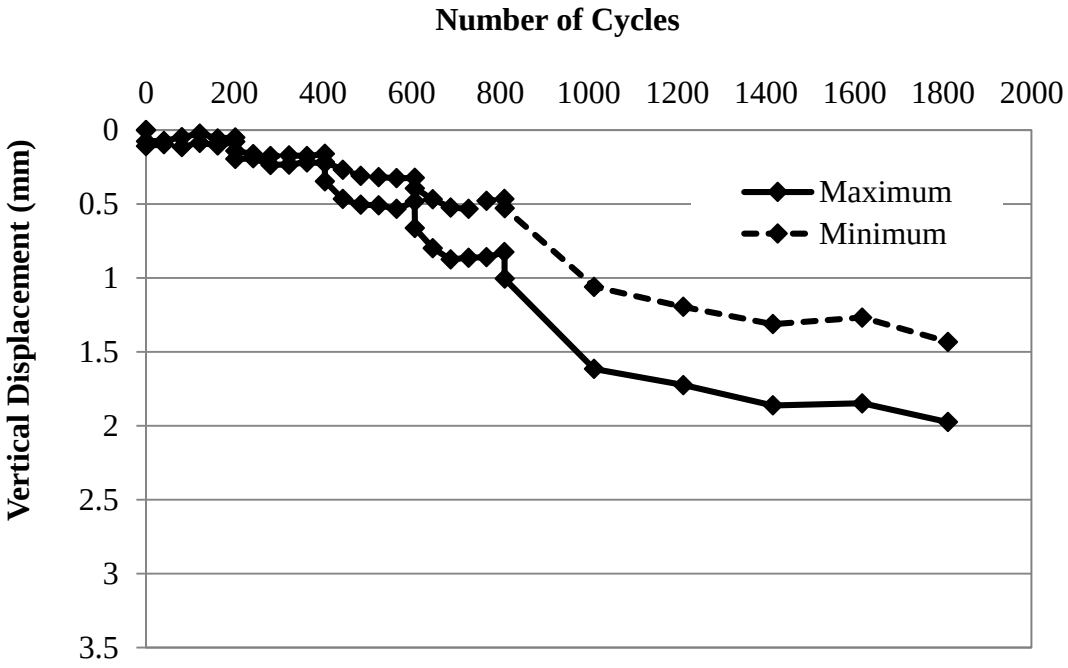

Figure 5.11 Vertical Displacement at the Pipe Crown in the Unreinforced Section (Test 6)

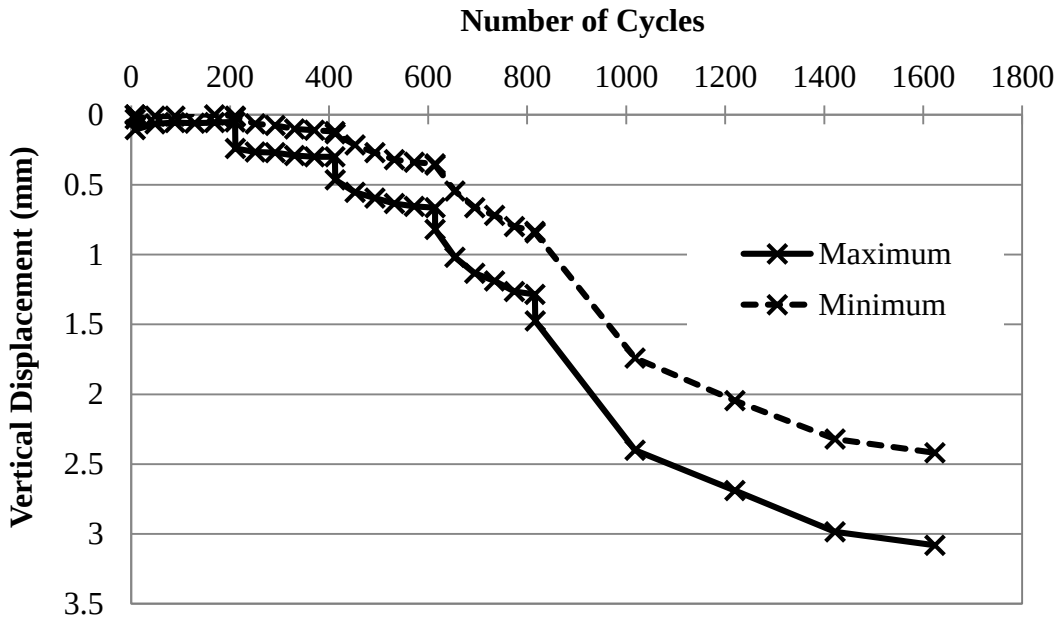

Figure 5.12 Vertical Displacement at the Pipe Crown in the Single Geogrid-Reinforced Section (Test 8)

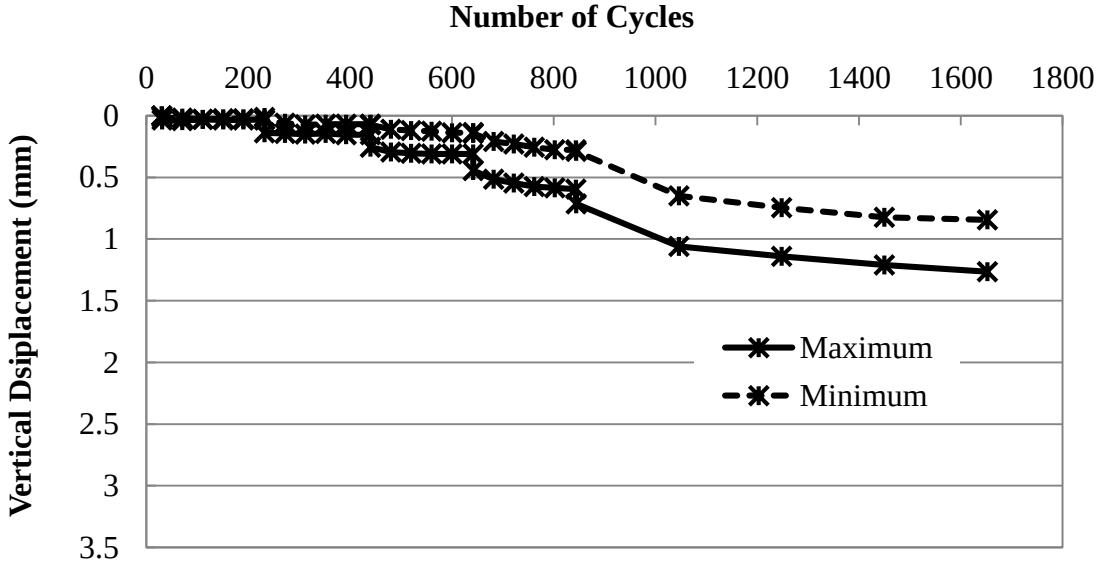

Figure 5.13 Vertical Displacement at the Pipe Crown in the Double Geogrid-Reinforced Section (Test 10)

5.3.2 Pipe Horizontal Deflection

Figures 5.14, 5.15, and 5.16 show the measured horizontal deflections of the pipes under cyclic loading. The increase of the pipe horizontal deflection implies the increase of the pipe diameter in the horizontal direction. The pattern of the increase in the pipe horizontal deflection follows the same pattern as the pipe vertical deflection and the plate vertical displacement. There was an increase in the pipe horizontal deflection due to the single geogrid layer, as compared to the unreinforced case, but a decrease due to the double geogrid layers.

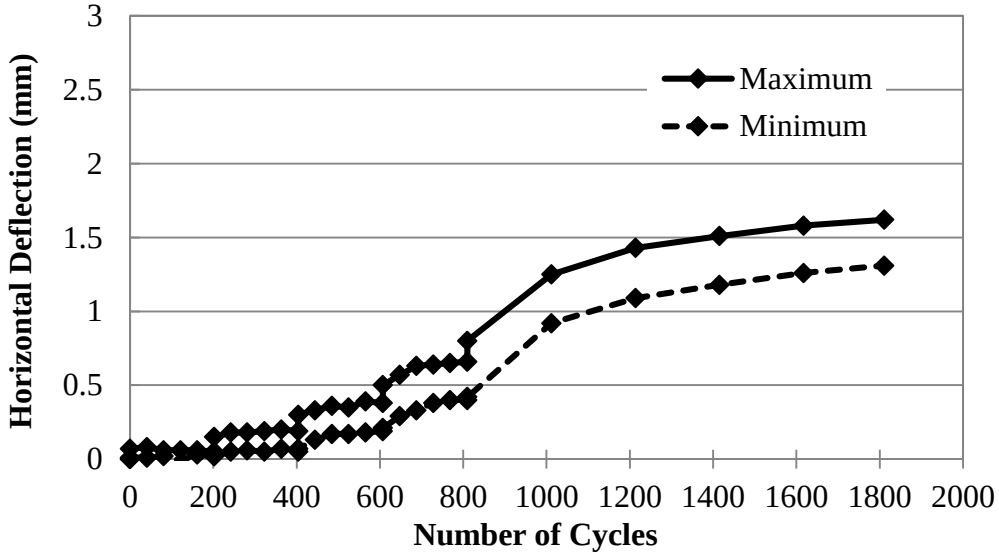

Figure 5.14 Pipe Horizontal Deflection in the Unreinforced Section (Test 6)

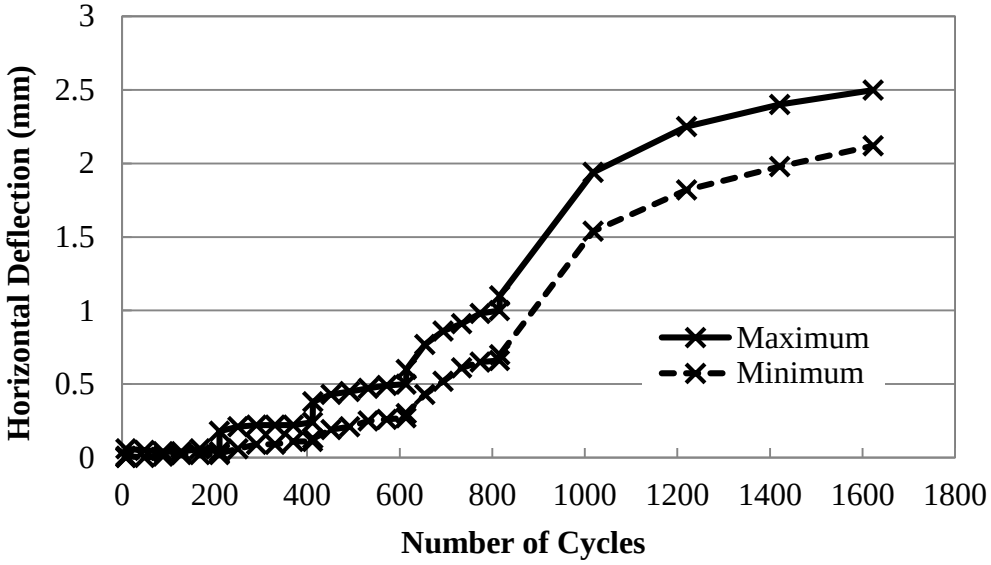

Figure 5.15 Pipe Horizontal Deflection in the Single Geogrid-Reinforced Section (Test 8)

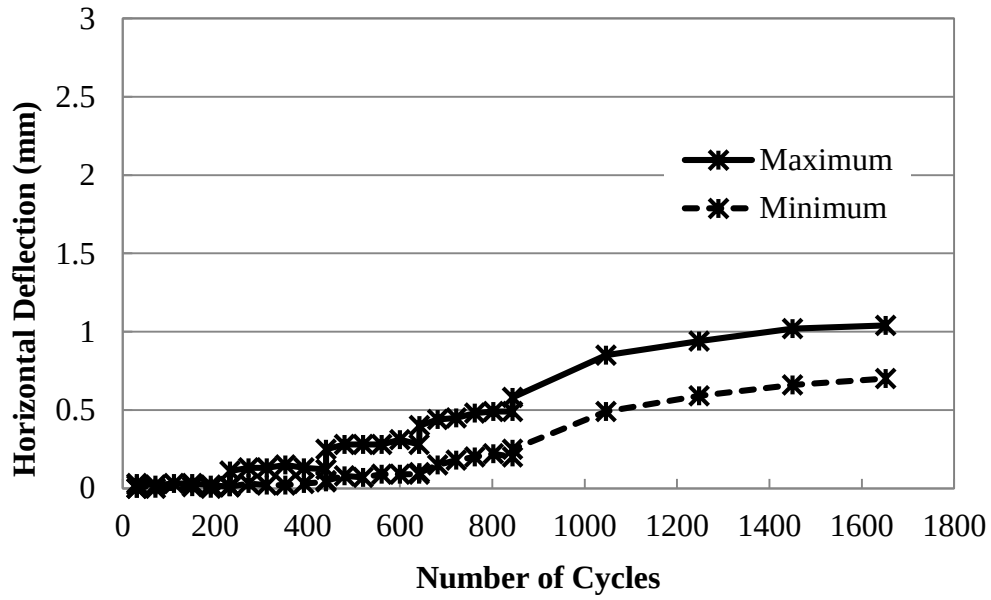

Figure 5.16 Pipe Horizontal Deflection in the Double Geogrid-Reinforced Section (Test 10)

5.4 Earth Pressure

The earth pressure cells placed in the backfill were used to monitor and record the measured pressures every one tenth of a second. Due to a large number of data points, the measured pressures will be presented at the beginning and the end of the load step after every 40 cycles except for the last load under which the measured pressures will be plotted every 200 cycles. The measured pressure cell results will be discussed in terms of their pressures at the invert, the spring line, and the crown of the pipe. Additional earth pressure data are shown in Appendix B. Before the cyclic loading, all the earth pressure readings were set to zero; therefore, all the measured pressures were induced by cyclic loading.

5.4.1 Earth Pressure at Pipe Invert

Figures 5.17, 5.18, and 5.19 show the measured vertical earth pressures under the pipes at the invert with the number of loading cycles. Clearly, the earth pressures in the single geogrid-reinforced section were much lower than those in the unreinforced section and the double geogrid-reinforced section. This result implies that the bedding layer under the pipe in the single geogrid-reinforced section was looser than those in other two sections. This result may also explain why the single geogrid-reinforced section had larger deformations than the unreinforced section. A similar general relationship between the earth pressure at the pipe invert and the geogrid reinforcement was seen in the static load tests (Fig. 4.19).

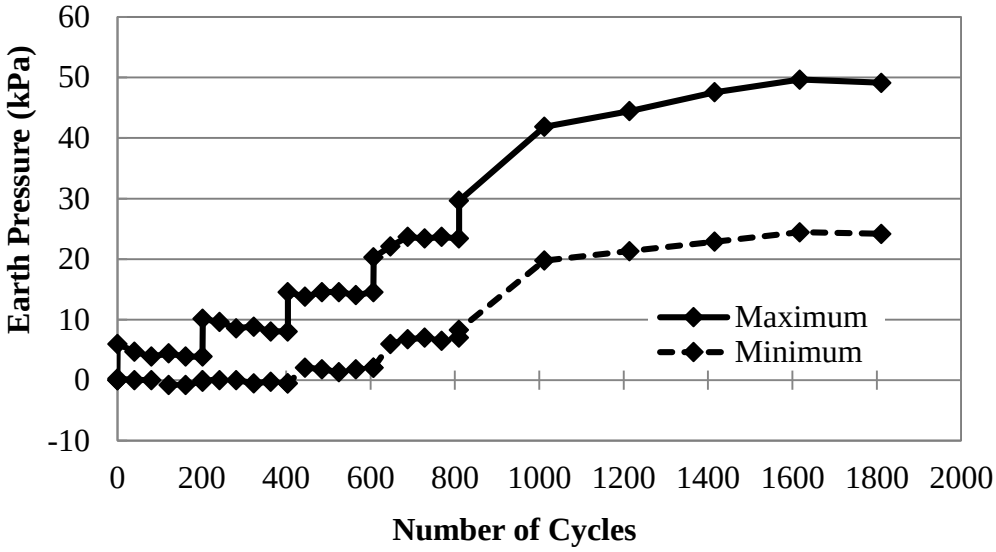

Figure 5.17 Measured Vertical Pressure at the Invert (I_1) in the Unreinforced Section (Test 6)

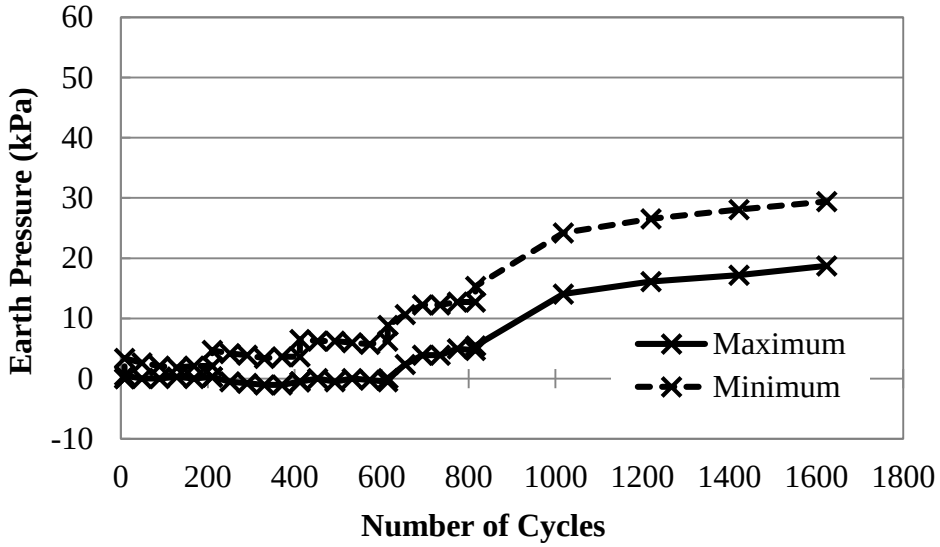

Figure 5.18 Measured Vertical Pressure at the Invert (I_1) in the Single Geogrid-Reinforced Section (Test 8)

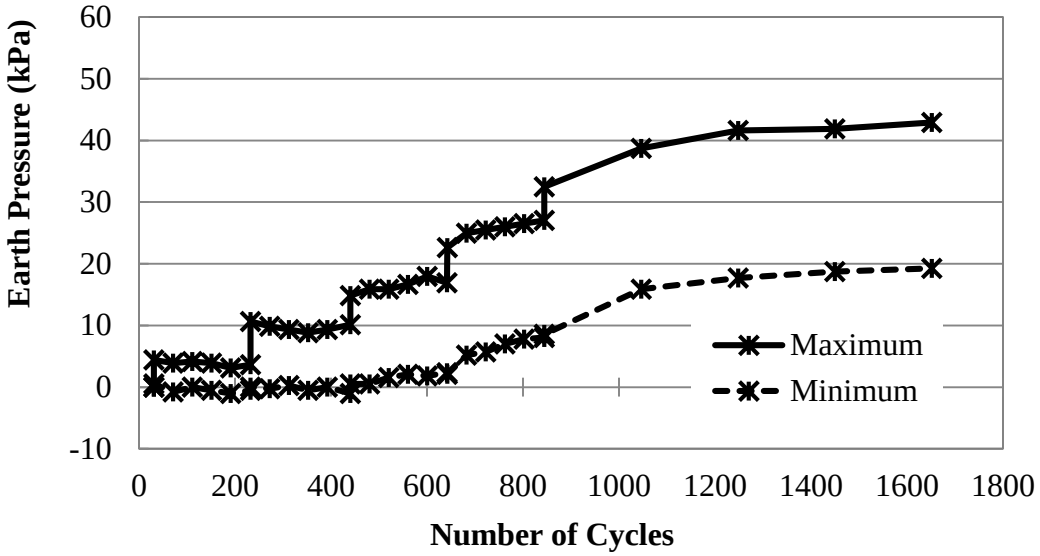

Figure 5.19 Measured Vertical Pressure at the Invert (I_1) in the Double Geogrid-Reinforced Section (Test 10)

5.4.2 Earth Pressure at Pipe Spring Line

Figures 5.20, 5.21, and 5.23 show the measured vertical earth pressures at the pipe spring line with the number of loading cycles in the unreinforced, single geogrid-reinforced, and double geogrid-reinforced sections, respectively. The minimum earth pressure after unloading was close to zero. The maximum earth pressure increased with the magnitude of the applied pressure. The measured earth pressures were highest in the single geogrid-reinforced section, followed by the double geogrid-reinforced section and then the unreinforced section. This result is reasonable as compared with that for the earth pressure at the pipe invert. When the pipe invert carried less load, more load was transferred to the soil in the trench. As a result, the vertical earth pressure at the spring line was higher.

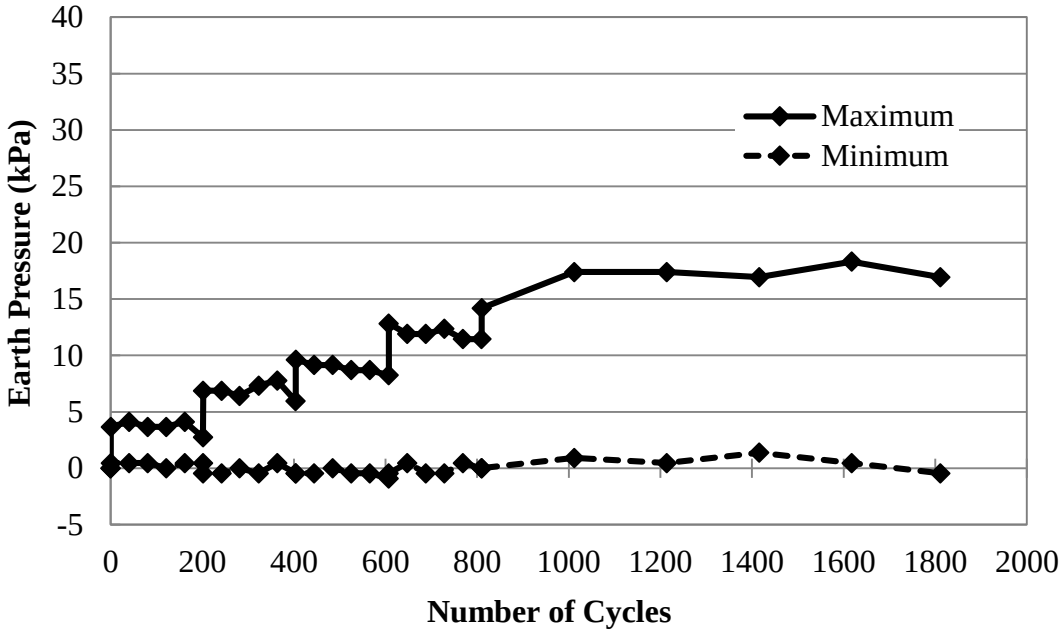

Figure 5.20 Measured Vertical Earth Pressures at the Spring Line (S_4) in the Unreinforced Section (Test 6)

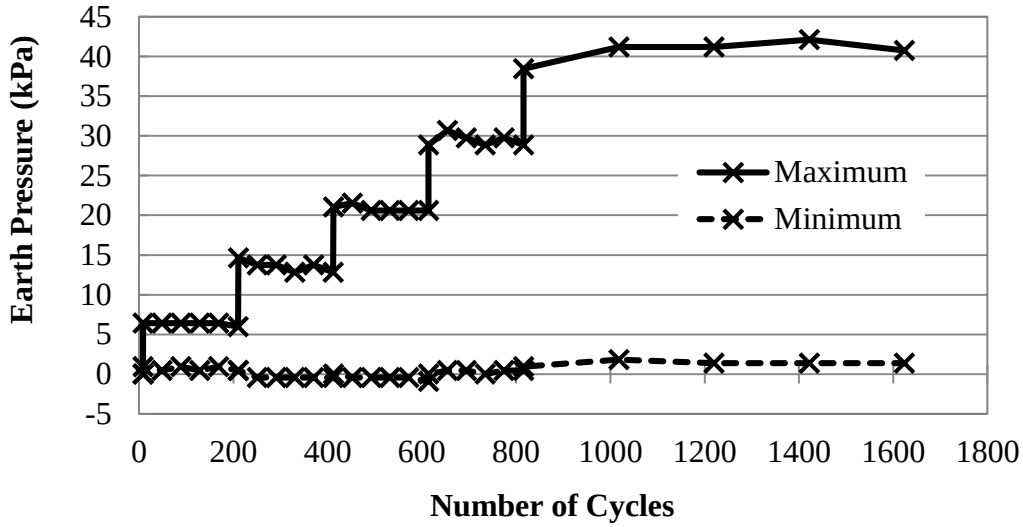

Figure 5.21 Measured Vertical Earth Pressures at the Spring Line (S_4) in the Single Geogrid-Reinforced Section (Test 8)

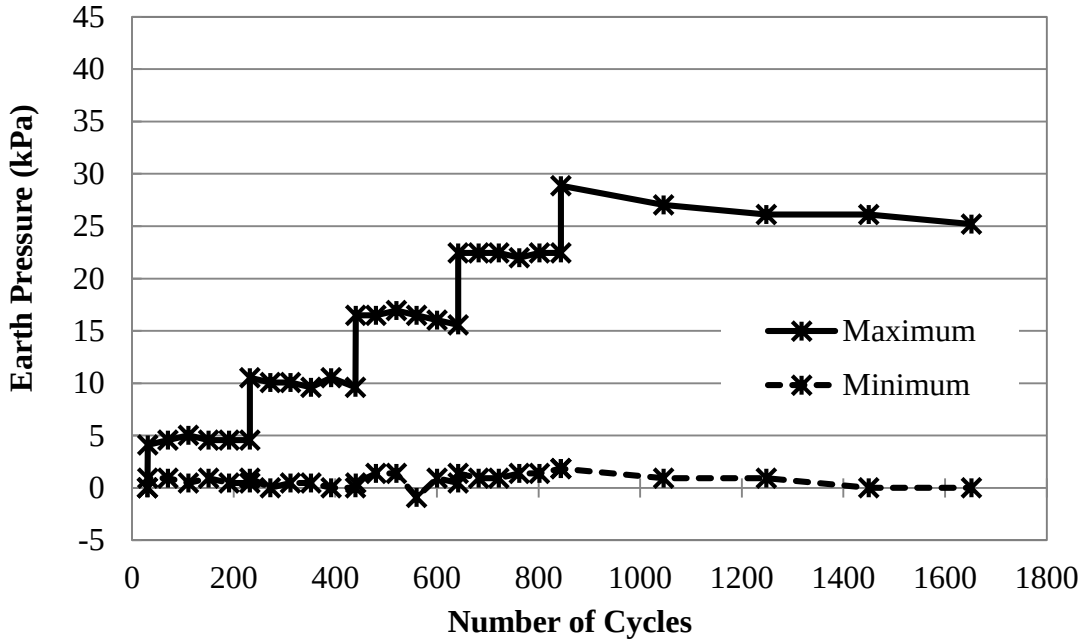

Figure 5.22 Measured Vertical Earth Pressure at the Spring Line (S_4) in the Double Geogrid-Reinforced Section (Test 10)

Figures 5.23, 5.24, and 5.25 show the measured horizontal earth pressures at the pipe shoulder with the number of loading cycles in the unreinforced, single geogrid-reinforced, and double geogrid-reinforced sections, respectively. Similar to the measured vertical earth pressures at the pipe spring line, the measured horizontal earth pressures at the pipe shoulder were highest in the single geogrid-reinforced section, followed by the double geogrid-reinforced section and then the unreinforced section. This result is due to the same reason that the pipe invert in the single geogrid-reinforced section carried the least load and the unreinforced section carried the most load. This same phenomenon was observed in the static load tests.

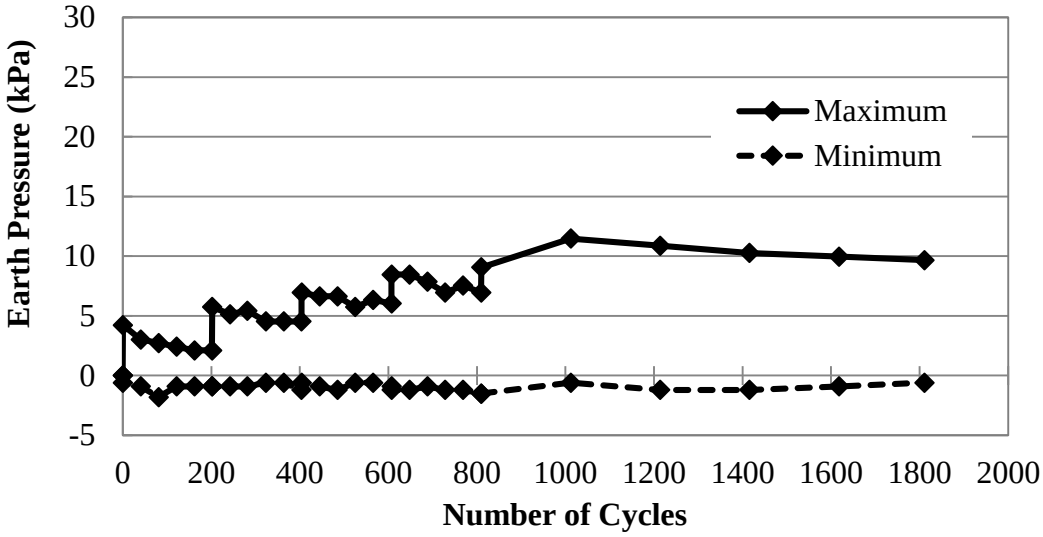

Figure 5.23 Measured Horizontal Earth Pressure at the Shoulder (S_2) in the Unreinforced Section (Test 6)

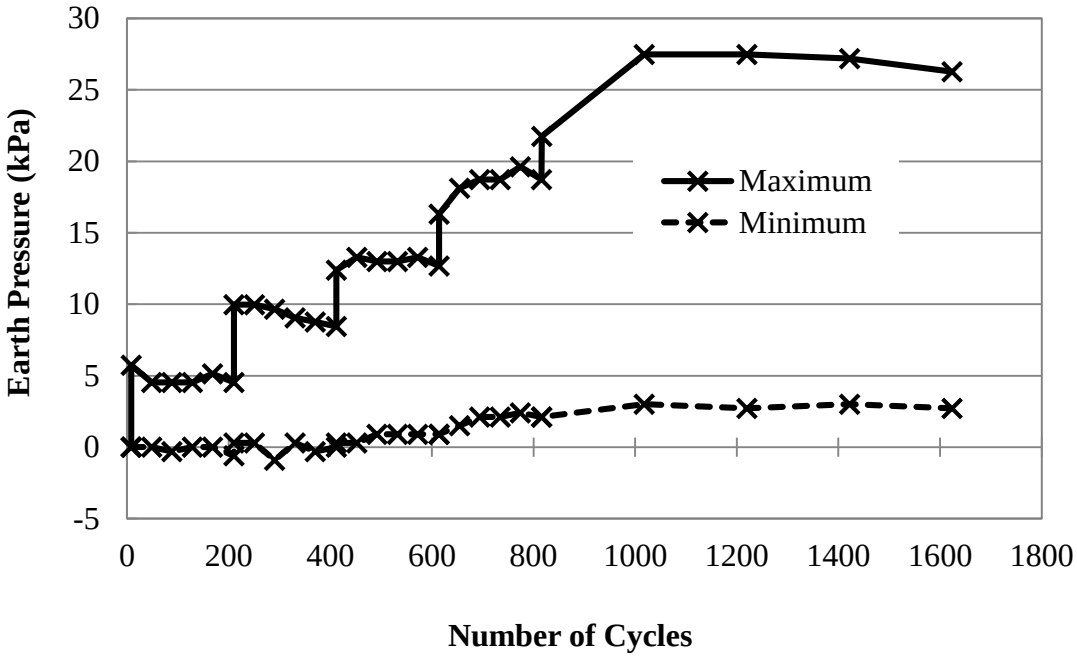

Figure 5.24 Measured Horizontal Earth Pressure at the Shoulder (S_2) in the Single Geogrid-Reinforced Section (Test 8)

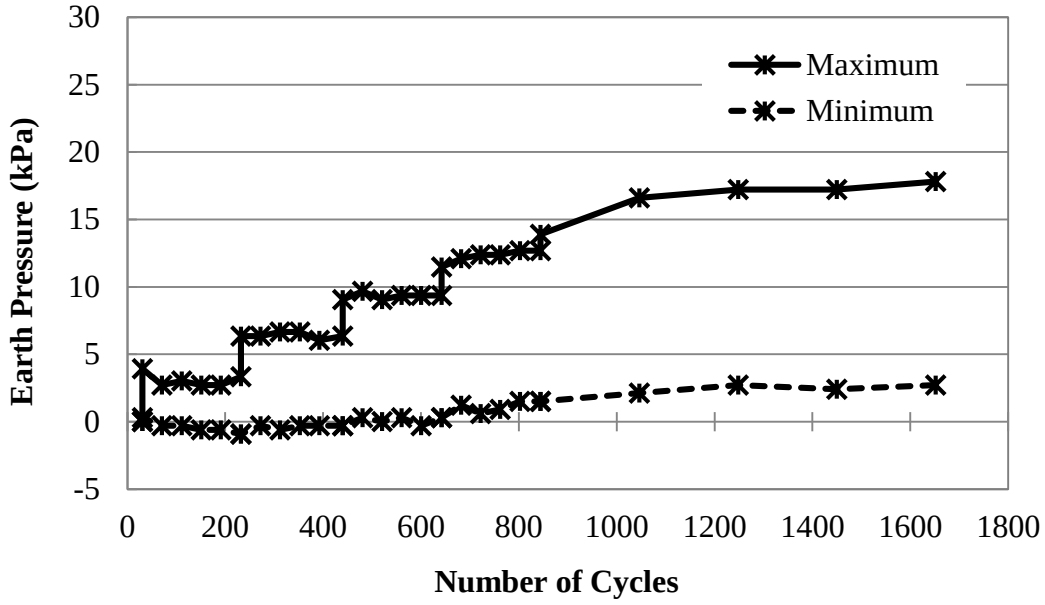

Figure 5.25 Measured Horizontal Earth Pressure at the Shoulder (S_2) in the Double Geogrid-Reinforced Section (Test 10)

Figure 5.26 shows the distribution of the horizontal earth pressures around the spring line at the maximum applied peak pressure of 689 kPa. Figure 5.26 shows that the single geogrid-reinforced section had the highest horizontal earth pressure at the pipe shoulder and the pipe haunch, followed by the double geogrid-reinforced section and then the unreinforced section. The reason is that the pipe invert in the single geogrid-reinforced section carried the least load, followed by the double geogrid-reinforced section and then the unreinforced section. If the pipe invert carried less load, more load was transferred to the backfill in the trench. This distribution of earth pressures is similar to that in the static load tests (Fig. 4.28).

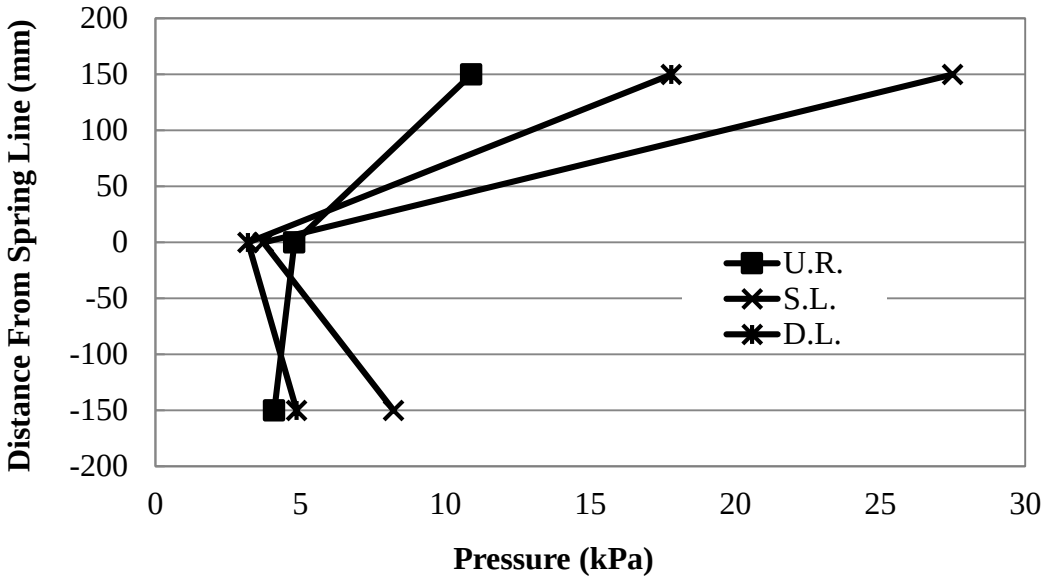

Figure 5.26 Distribution of Horizontal Earth Pressure around the Spring Line at Applied Peak Pressure of 689 kPa (Test 6, 8, and 10)

5.4.3 Earth Pressure at Pipe Crown

Figures 5.27, 5.28, and 5.29 show the measured vertical earth pressures directly above the crown of the pipe with the number of loading cycles in the unreinforced section, the single geogrid-reinforced section, and the double geogrid-reinforced section, respectively. Up to the third applied plate pressure (i.e., 413 kPa), the measured vertical earth pressures were approximately the same in the unreinforced and reinforced sections. There was a significant increase in the measured earth pressures in the single geogrid-reinforced section at the applied plate pressure of 551 kPa and 689 kPa.

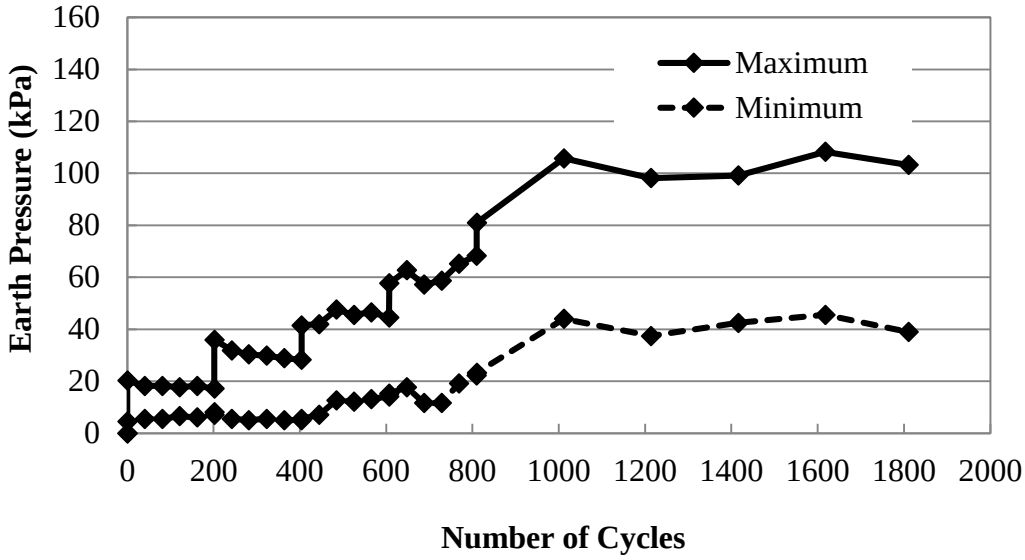

Figure 5.27 Measured Vertical Earth Pressure at the Pipe Crown (C_1) in the Unreinforced Section (Test 6)

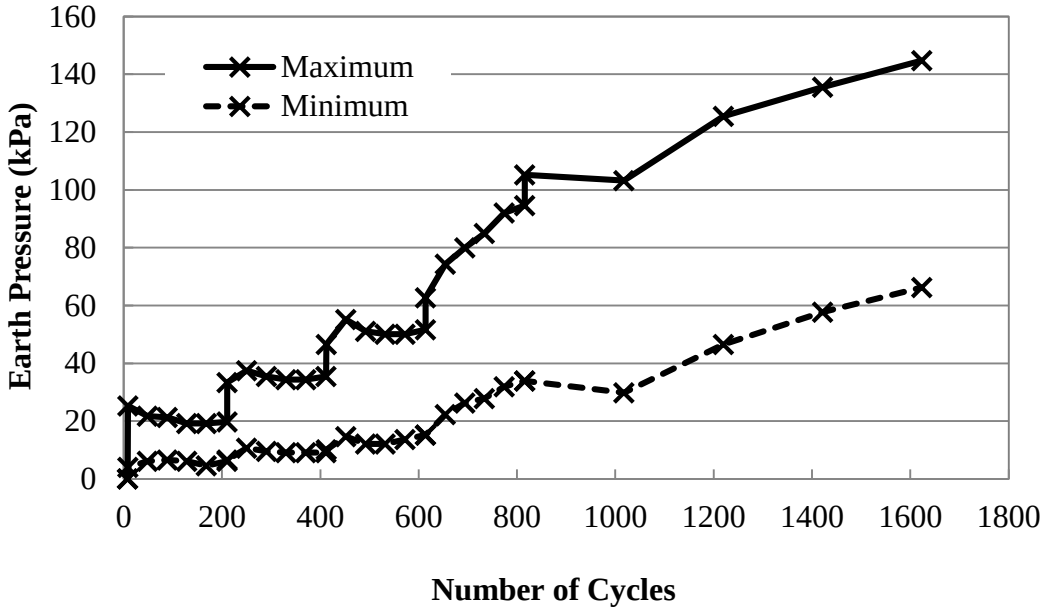

Figure 5.28 Vertical Earth Pressures at the Pipe Crown (C_1) in the Single Geogrid-Reinforced Section (Test 8)

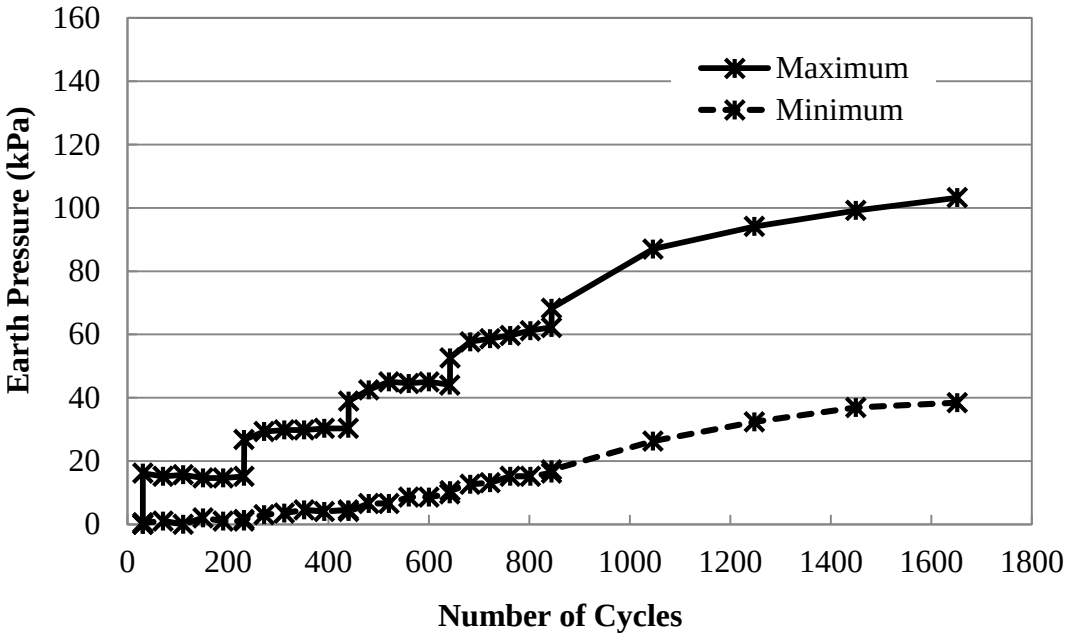

Figure 5.29 Vertical Earth Pressure at the Pipe Crown (C_1) in the Double Geogrid-Reinforced Section (Test 10)

Figure 5.30 shows the distributions of the measured earth pressures at the crown in these three test sections. These distributions are different from those in the static load tests (Fig. 4.39). The single geogrid-reinforced section had the highest vertical earth pressure at the crown.

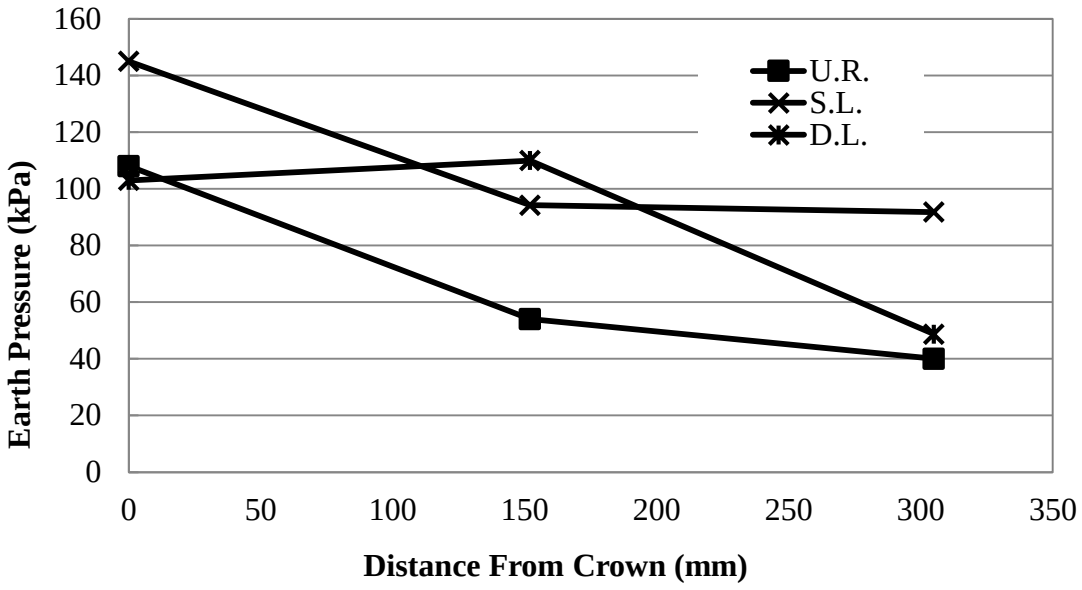

Figure 5.30 Distribution of Vertical Earth Pressure at the Pipe Crown at Applied Peak Pressure of 689 kPa (Tests 6, 8, and 10)

5.5 Pipe Strain

Pipe strains were measured during the test with 17 strain gauges located at the spring line, the invert, and the crown for each cyclic loading test. Some strain gauges failed or exceeded the allowable range of measureable strains by the gauge. The strains of the failed strain gauges are not included. The strain gauge locations are shown in Figures 5.31 and 5.32 again for convenience. Positive strains are tensile while negative strains are compressive. Limited strain gauge data are discussed in this chapter. Other pipe strains for the cyclic load tests are provided in Appendix C.

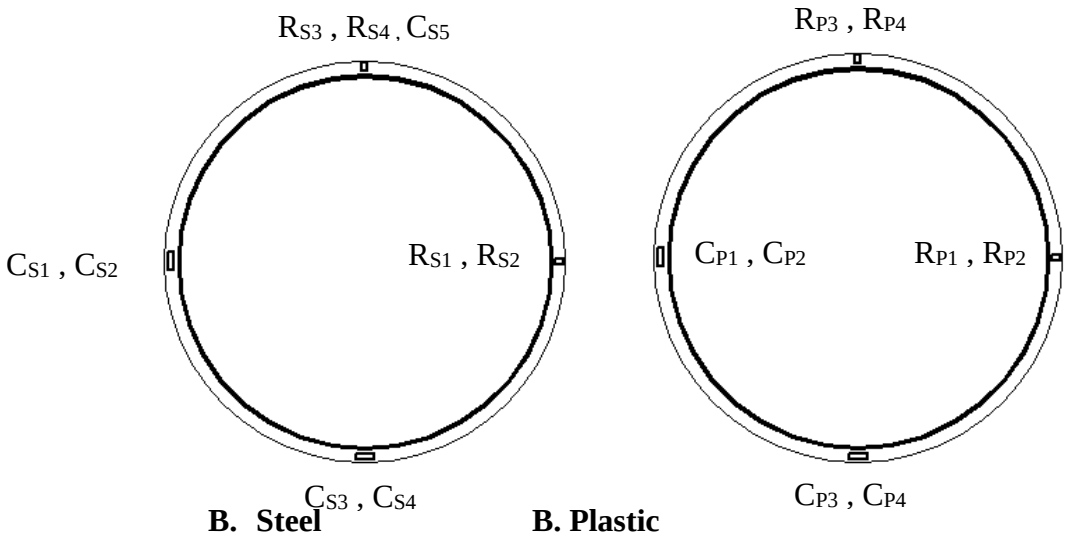

Figure 5.31 Circumferential and Radial Strain Gauge Locations

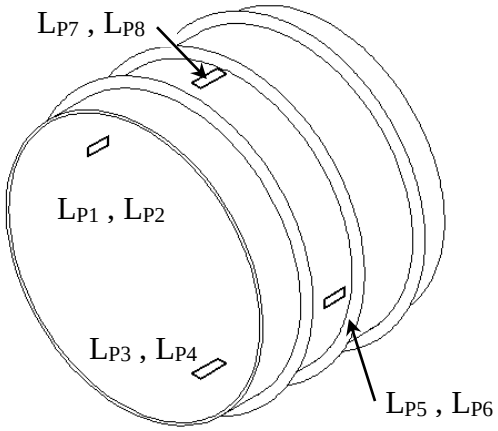

Figure 5.32 Longitudinal Strain Gauge Locations

Since there are a large number of strain gauge data, the measured strains at the end of cyclic loading at each load increment as shown in Figure 5.1 are plotted in the figures to be discussed in the following section.

Although the measured strains were small, the inclusion of the geogrid above the pipe did appear to reduce the overall strains in the pipe. For instance the circumferential strains on the steel rib (Fig. 5.33) and on the plastic (Fig. 5.34) at the pipe spring line decreased by the geogrid while the strains on the steel rib at the pipe crown increased (Fig. 5.35).

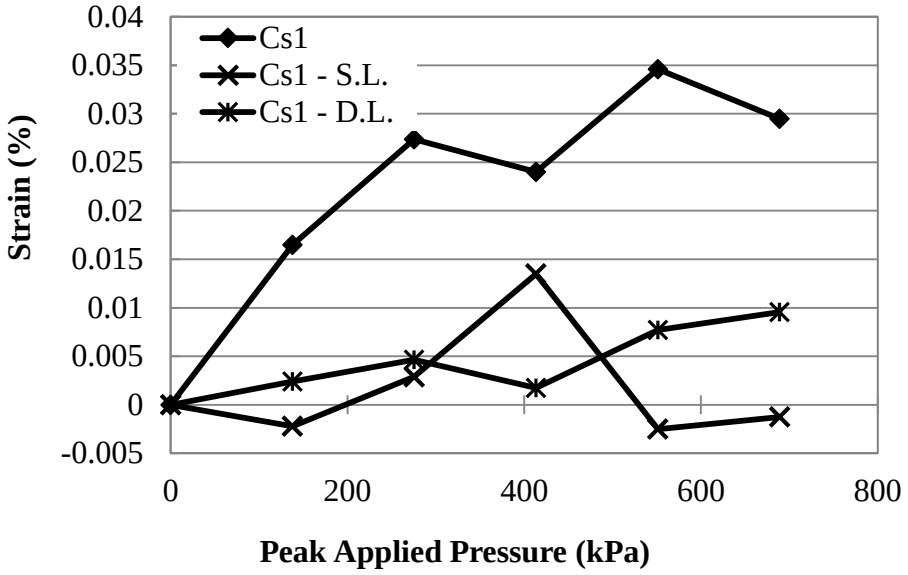

Figure 5.33 Maximum Circumferential Strains on the Steel Ribs at the Pipe Spring Line (C_{s1})

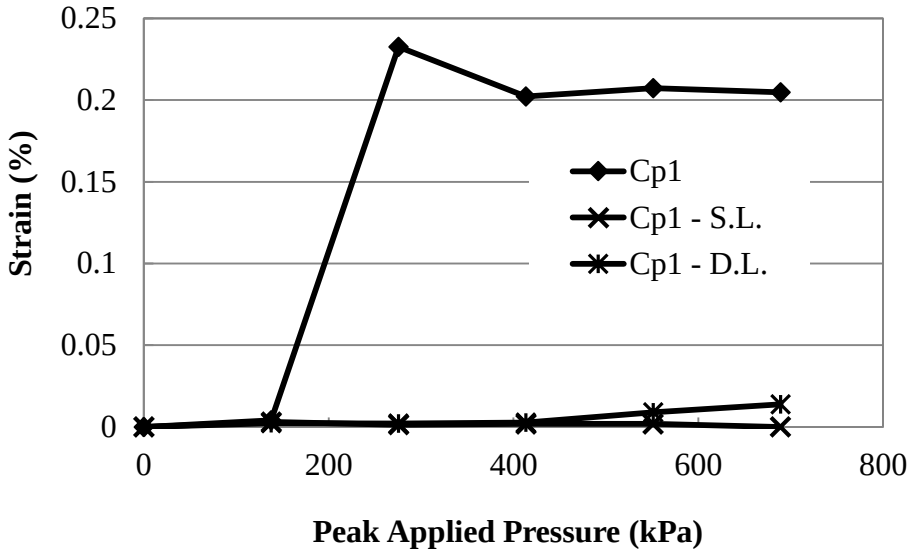

Figure 5.34 Maximum Circumferential Strains on the Plastic Cover around the Steel Ribs at the Pipe Spring Line (C_{p1})

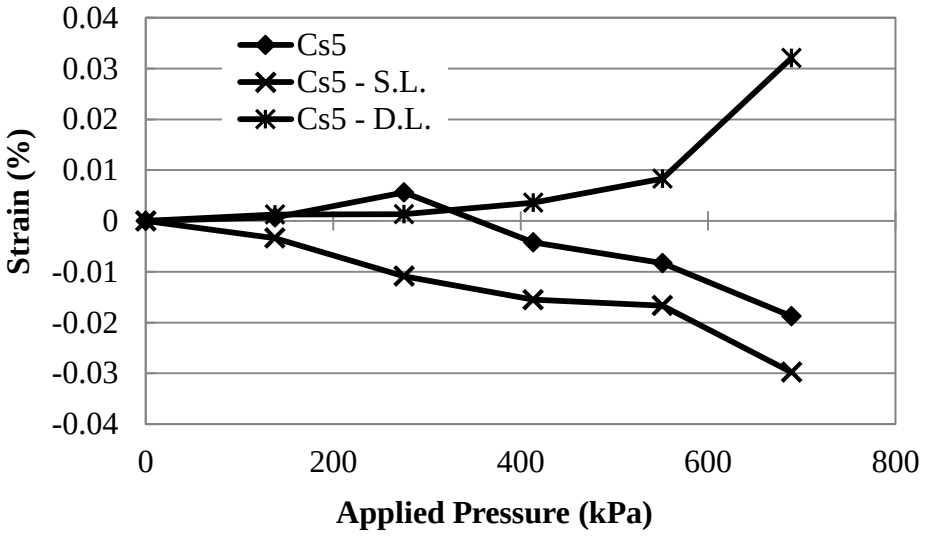

Figure 5.35 Maximum Circumferential Strains on the Steel Ribs at the Pipe Crown (C_{s5})

Similar to the static load tests, the largest strains in the cyclic plate load tests were in the longitudinal direction of the pipe wall (Fig 5.36 and 5.37). In the unreinforced section at the pipe crown both inside and outside pipe walls were in tension. When the peak applied pressure was increased to 551 kPa, there appeared to be a loss of interaction between the backfill and the pipe wall in the unreinforced section, and the tension in the pipe wall began to decrease. The pipes in the reinforced sections seemed to perform more as typical plate bending as the bottom of the pipe wall was in tension and the top of the pipe wall was in compression or slightly in tension.

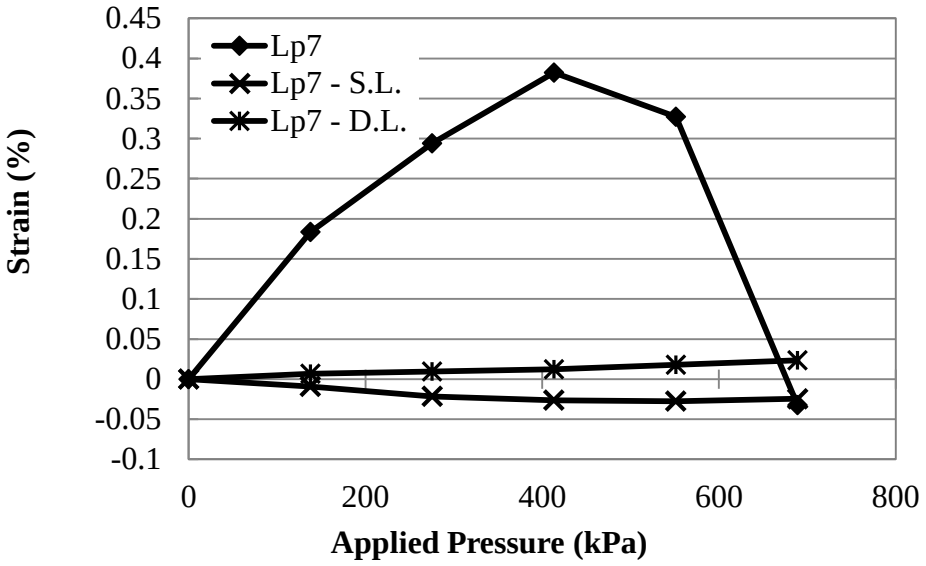

Figure 5.36 Maximum Longitudinal Strains on the Plastic Liner at the Pipe Crown (L_7)

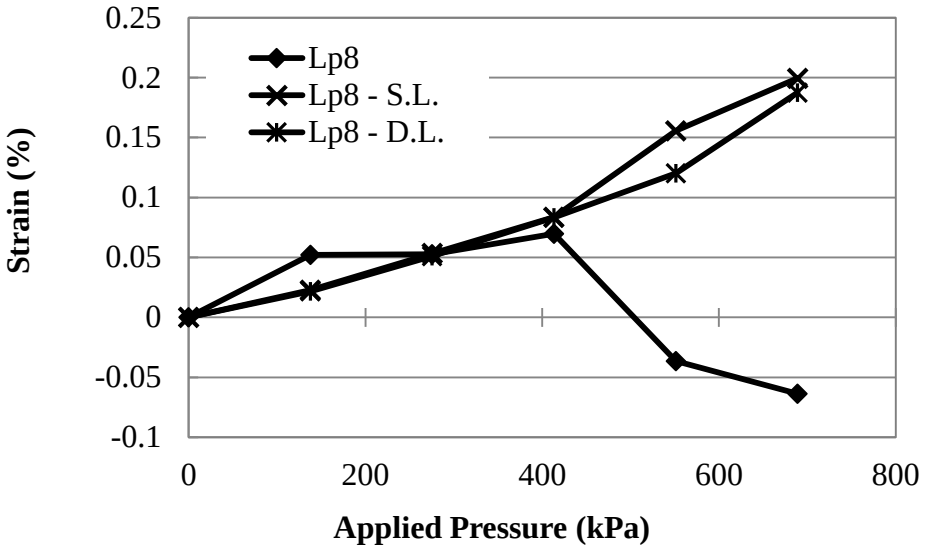

Figure 5.37 Maximum Longitudinal Strains on the Plastic Liner at the Pipe Crown (L_8)

5.6 Geogrid Strains in Tests 8 and 10

Strain gauges were placed on the geogrid to determine the response of the geogrid to the applied load and the pipe system. The strain gauge locations which were shown in Chapter 3 are shown in Fig. 5.38 again for convenience . Strain data presented in the following section are based on the single geogrid-reinforced section (Test 8) and the double geogrid-reinforced section (Test 10).

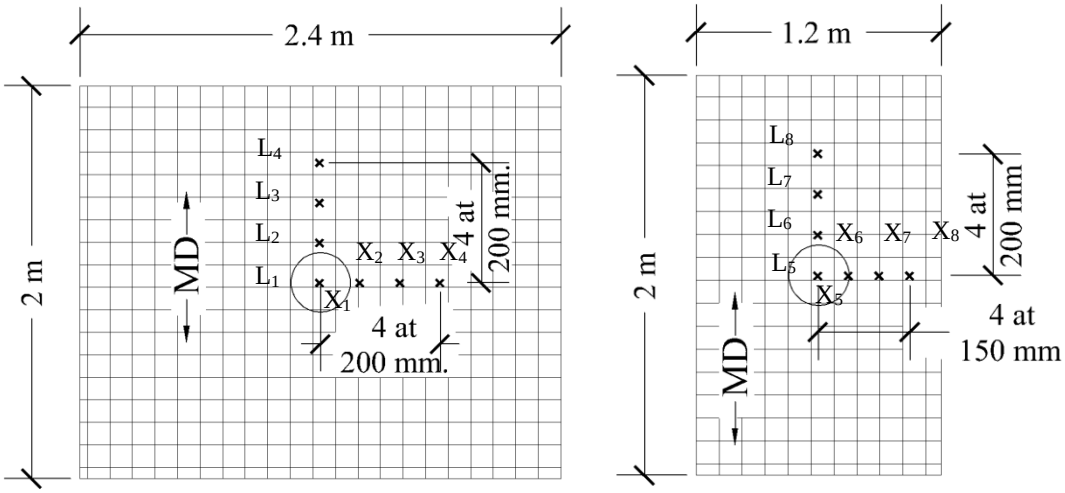

B. Upper Layer **B. Lower Layer**

Figure 5.38 Strain Gauges on Single and Double Geogrid Layers

A large number of strain gauges on the geogrids failed during the cyclic tests, therefore only a few strain gauge data will be presented in the following section to show the geogrid behavior under cyclic loading. The maximum strains on the geogrid under each load increment are reported.

Figure 5.39 show the maximum geogrid strains in the machine and cross-machine directions in the single geogrid-reinforced section under applied pressure. These figures show that the gauges close to the center of the plate measured larger strains than those away from the center. The measured maximum geogrid strains in the machine direction were lower than those in the static load tests while the measured maximum geogrid strains in the cross-machine direction were similar to those in the static load tests as shown in Fig. 4.60.

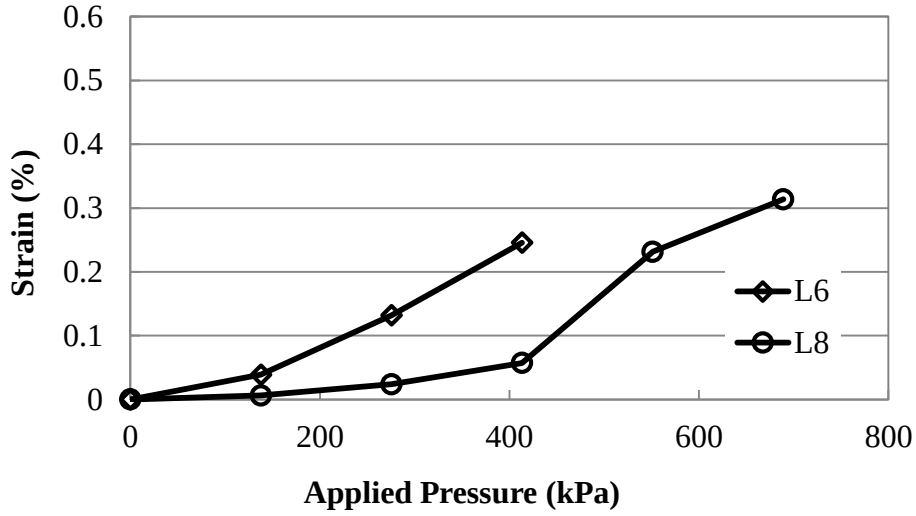

(a) Machine direction

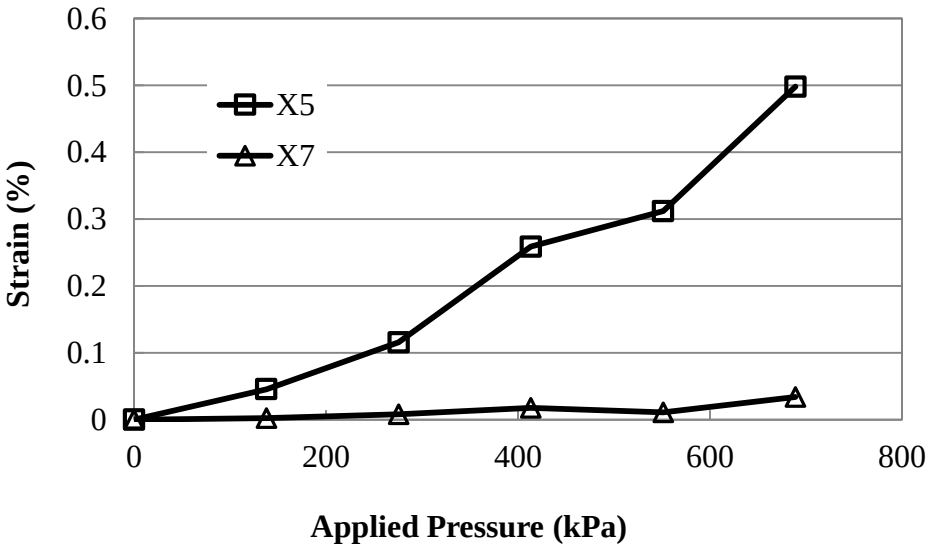

(b) Cross-machine direction

Figure 5.39 Maximum Geogrid Strain in the Single Geogrid-Reinforced Section under Applied Pressure

In the double geogrid-reinforced section, the maximum strains in the geogrids due to the cyclic loads were different from those recorded during the static loads. On the lower geogrid layer as shown in Fig. 5.40, the maximum strains were smaller in magnitude than those in the static load test, but exhibited the same pattern of strains. The largest strains were at the center of the geogrid, while the smaller strains occurred at the distances away from the center of the loading plate. The measured geogrid maximum strain in the machine direction was larger than that in the cross-machine direction.

However, in the cyclic loading test, the upper geogrid layer had the maximum recorded strain at the distance of 400 mm from the center of the plate as shown in Fig. 5.41. The geogrid was even in compression directly under the plate. These results can also be seen in the distribution of the geogrid strains at the peak applied pressure of 689 kPa as shown in Fig. 5.42.

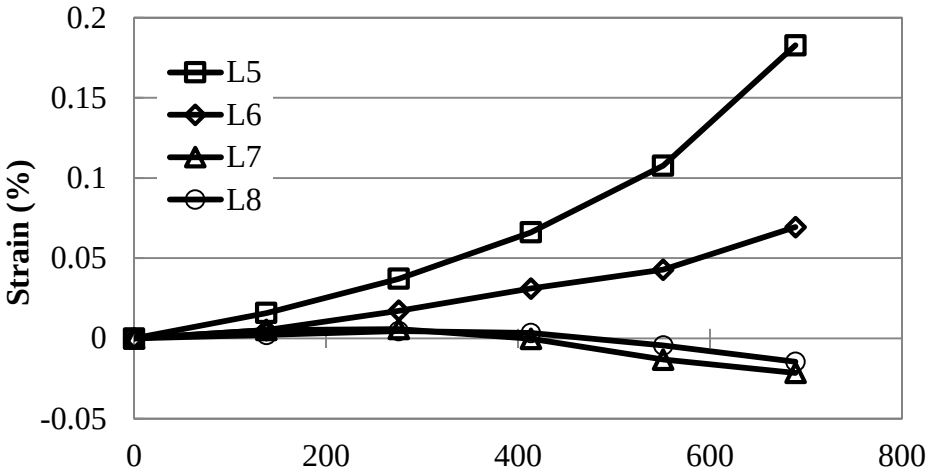

(a) Machine Direction

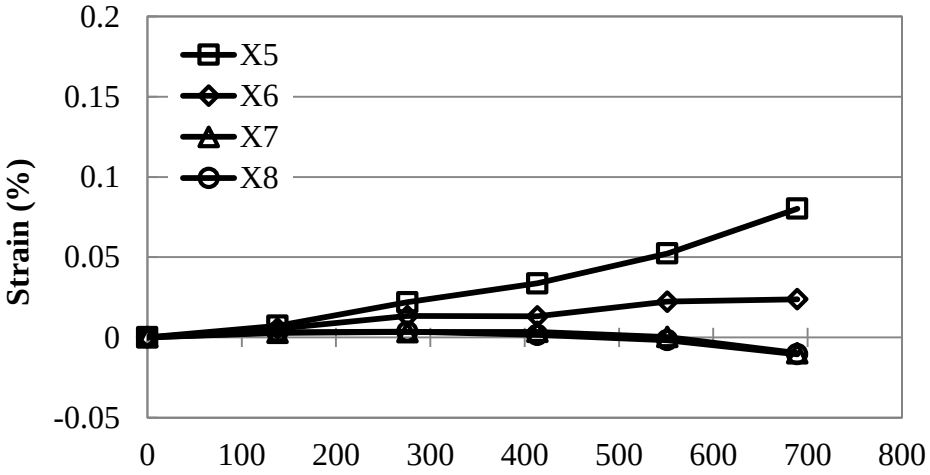

(b) Cross-machine direction

Figure 5.40 Maximum Geogrid Strain in the Lower Layer in the Double Geogrid-Reinforced Section

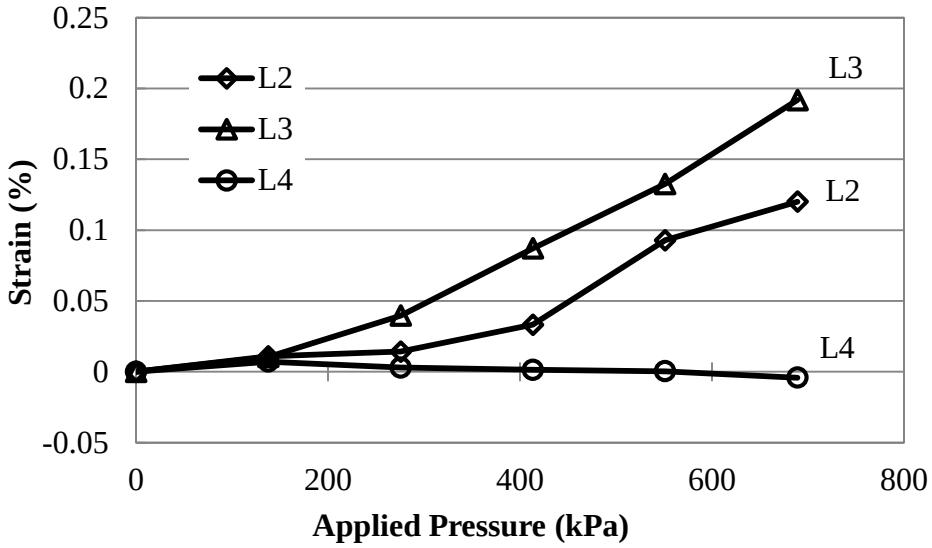

(a) Machine Direction

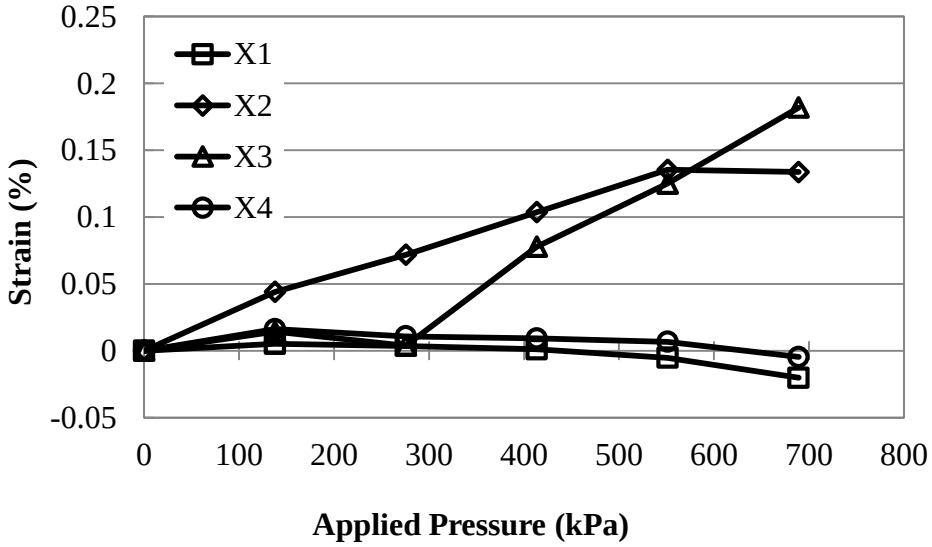

(b) Cross-machine direction

Figure 5.41 Maximum Geogrid Strain in the Upper Layer in the Double Geogrid-Reinforced Section

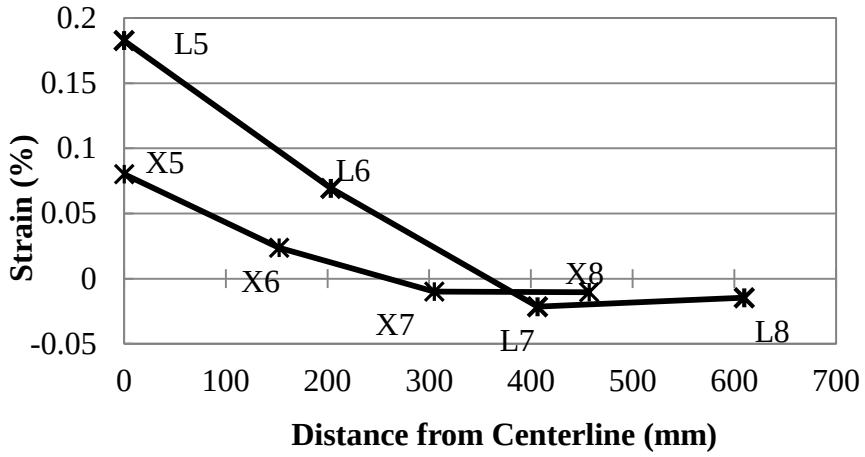

Figure 5.42 Distribution of the Geogrid Strains in the Lower Layer at the Maximum Applied Pressure of 689 kPa on the Double Geogrid-Reinforced Section

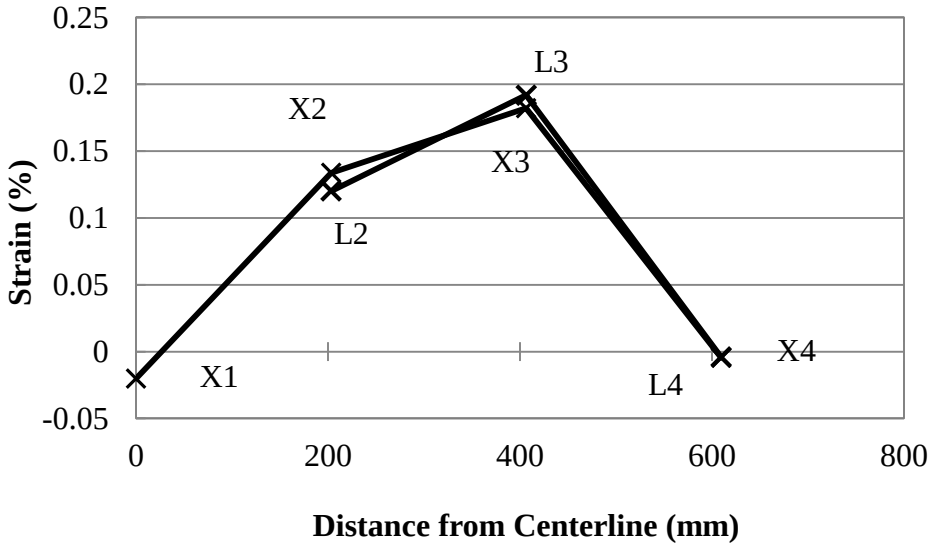

Figure 5.43 Distribution of the Geogrid Strains in the Upper Layer at the Maximum Applied Pressure of 689 kPa on the Double Geogrid-Reinforced Section

Chapter 6 Penetration Test Results

6.1 Introduction

To simulate a construction equipment accident, a 102 mm diameter by 356 mm long steel round rod was connected to the actuator to penetrate the test sections vertically using the hydraulic actuator. The penetration test was performed using the displacement control method. The steel rod was pushed into the soil at a displacement interval of 12.7 mm up to the maximum penetration of 305 mm. The force was monitored during and after each penetration. In all the penetration tests, the backfill was un-compacted aggregate and the base course was AB-3 aggregate.

Figure 6.1 shows the geogrid location and orientation that were used during each test, not including the unreinforced condition. For the tests with the single and double geogrid layers (i.e., Tests 16 and 17), the machine direction of the geogrid was placed in the longitudinal axis of the pipe while in the 270 degree and 360 degree wrapped tests, the machine direction of the geogrid was placed perpendicular to the longitudinal axis of the pipe.

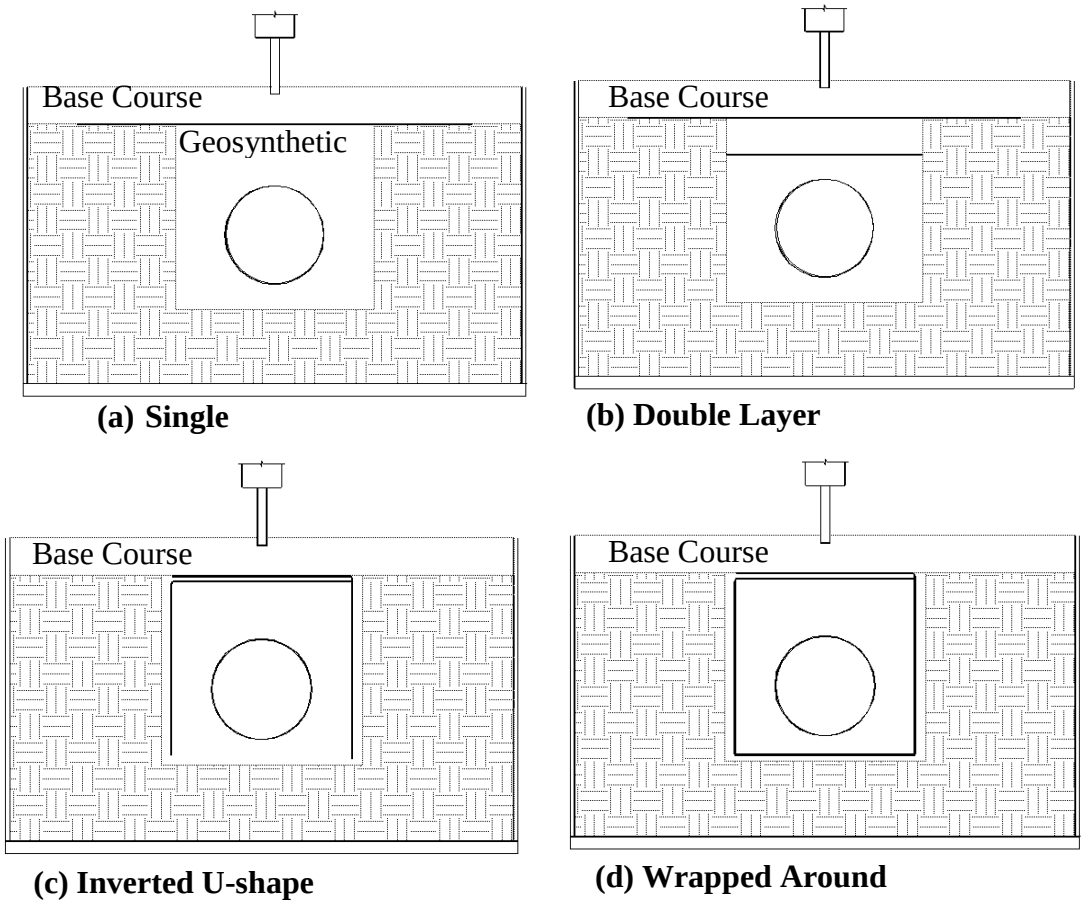

Figure 6.1 Geogrid Layout

6.2 Pipe Penetration

The effectiveness of the geogrid in reducing the penetration of the rod can most easily be demonstrated by plotting the applied force needed to meet the constant penetration steps of 12.7 mm as shown in Figure 6.2. Adding the geogrid reinforcement increased the required force necessary to push the 102 mm diameter steel rod into the soil. The maximum force for the unreinforced section was approximately 21 kN. Adding the single and double horizontal geogrid layers increased the maximum force to approximately 26 kN. Wrapping the pipe with an inverted

U-shape geogrid or a full 360 degree wrapped-around geogrid increased the maximum force to approximately 35 kN.

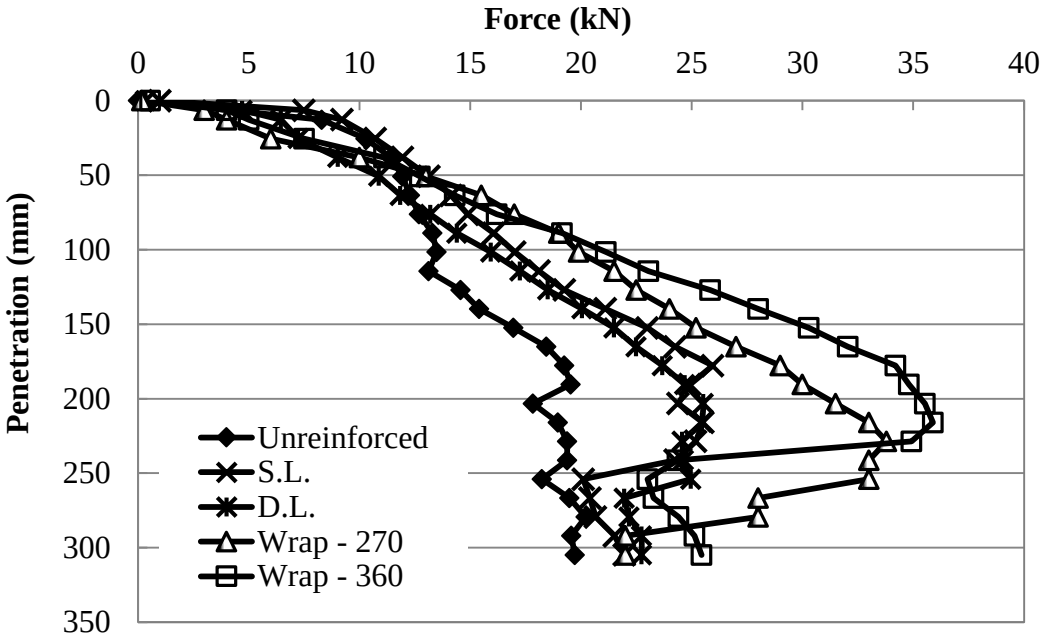

Figure 6.2 Applied Force vs. Rod Penetration

In the cases with horizontal geogrid reinforcement, the maximum force was reached when the geogrid was ruptured and the rod passed through the geogrid layer. After the rod penetrated through the geogrid, the applied force dropped to a value close to that for the unreinforced case.

For the inverted U-shape reinforcement (also referred to as Wrap 270 in the figure) and the wrapped-around reinforcement (also referred to as Wrap 360 in the figure), there appeared to be a secondary strengthening effect of the backfill due to the confinement of the backfill even after the geogrid was penetrated. When the geogrid was exhumed after the completion of the test it was visually confirmed that the geogrid was ruptured and had been penetrated. The ruptured area was

equal to the cross sectional area of the 102 mm diameter rod and only those ribs within this area were broken.

6.3 Pipe Deflection

6.3.1 Vertical Pipe Deflection

Figures 6.3 and 6.4 present the vertical deflection of the pipe versus the penetration of the steel rod and the applied force on the steel rod. When the vertical pipe deflection was negative, it indicates shortening of the vertical diameter of the pipe. Figure 6.3 indicates that additional layers of geogrid actually increased the vertical pipe deflection under the same rod penetration. This is because that the inclusion of geogrid distributed the load to a deeper depth. Figure 6.4 reveals that significantly more force was needed to induce the same vertical pipe deflection for the reinforced sections than the unreinforced section. Figure 6.4 also shows that after the rod penetrated through the geogrid, the required force rapidly decreased and the vertical pipe deflection quickly increased.

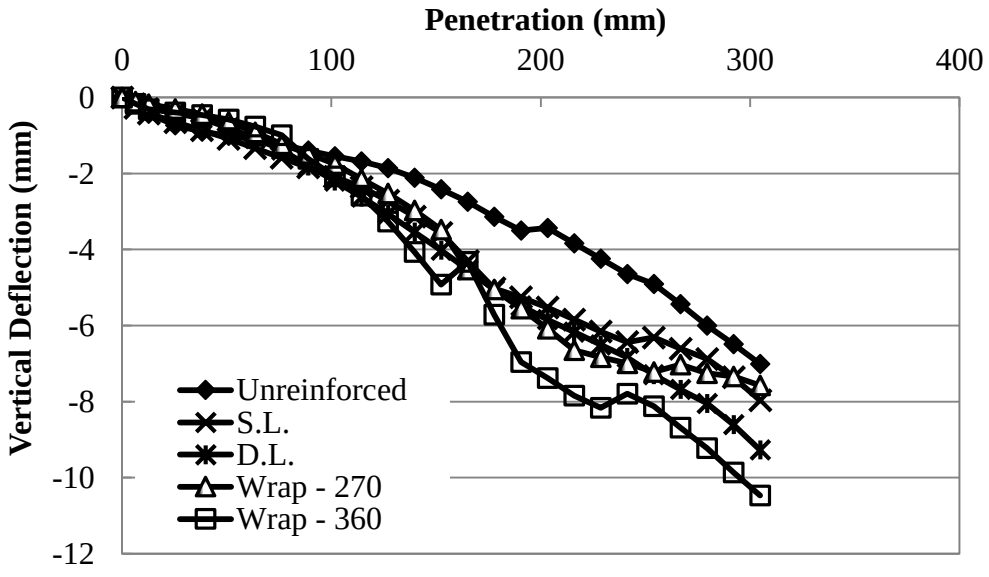

Figure 6.3 Rod Penetration vs. Vertical Pipe Deflection at the Center of Rod Penetration

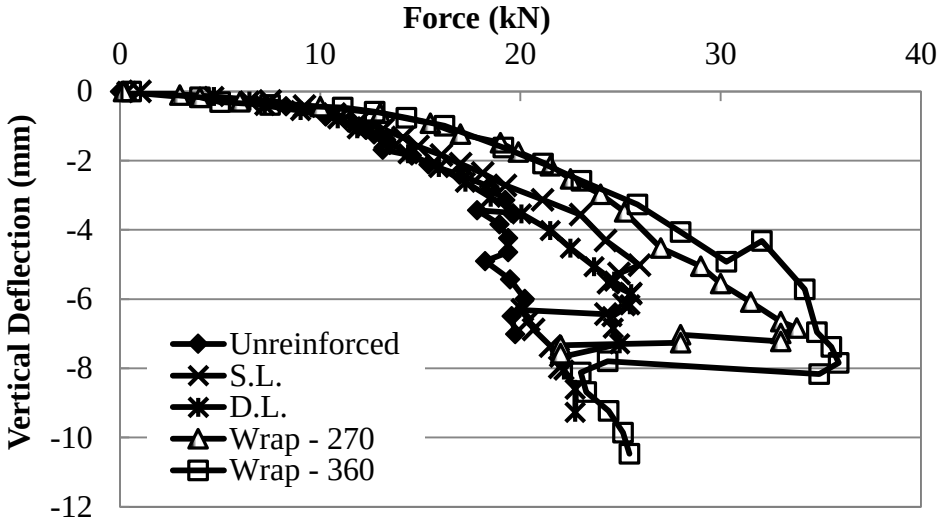

Figure 6.4 Applied Force vs. Vertical Pipe Deflection at the Center of Rod Penetration

Figure 6.5 shows the vertical deflection of the pipe at 305 mm from the center of the penetration along the centerline of the pipe during rod penetration. It can be seen that the vertical deflection of the pipe at 305 mm from the center of penetration was similar to that at the center of penetration but with smaller magnitude, as expected. In addition, it can be seen that the rate of vertical pipe deflection decreased with the rod penetration. Once the rod penetrated through the geogrid, less force was distributed to the pipe and therefore the rate of vertical pipe deflection decreased with the rod penetration.

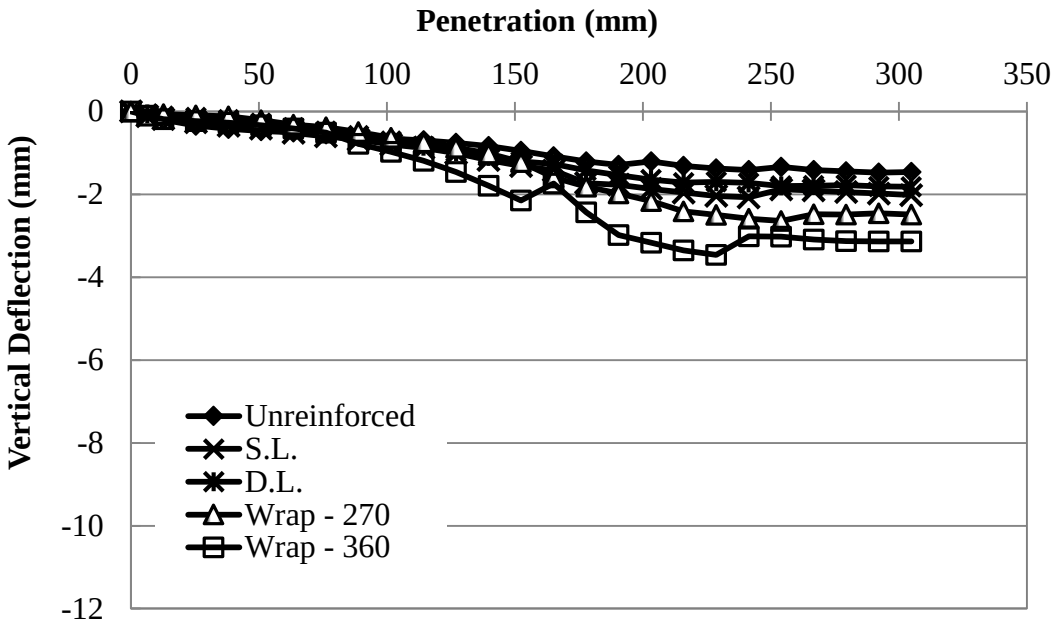

Figure 6.5 Rod Penetration vs. Vertical Pipe Deflection at 305 mm from the Center of Penetration along the Centerline of the pipe

In addition to the displacement transducers installed inside the pipe, tell-tales were used to measure the relative locations of the pipe crown to a stationary datum, at the center of rod penetration and at 305 mm from the center of rod penetration along the centerline of the pi. The tell-tales did not work during the penetration test in the unreinforced section. Figures 6.6 and 6.7 show the displacements of the pipe crown at the center of penetration and at 305 mm from the center of penetration along the centerline of the pipe, respectively. When the crown displacement was larger than the vertical deflection of the pipe, there was some displacement at the pipe invert. Again, a reduction in the crown displacement rate can be seen, at around 200 mm, after the rod penetrated through the geogrid.

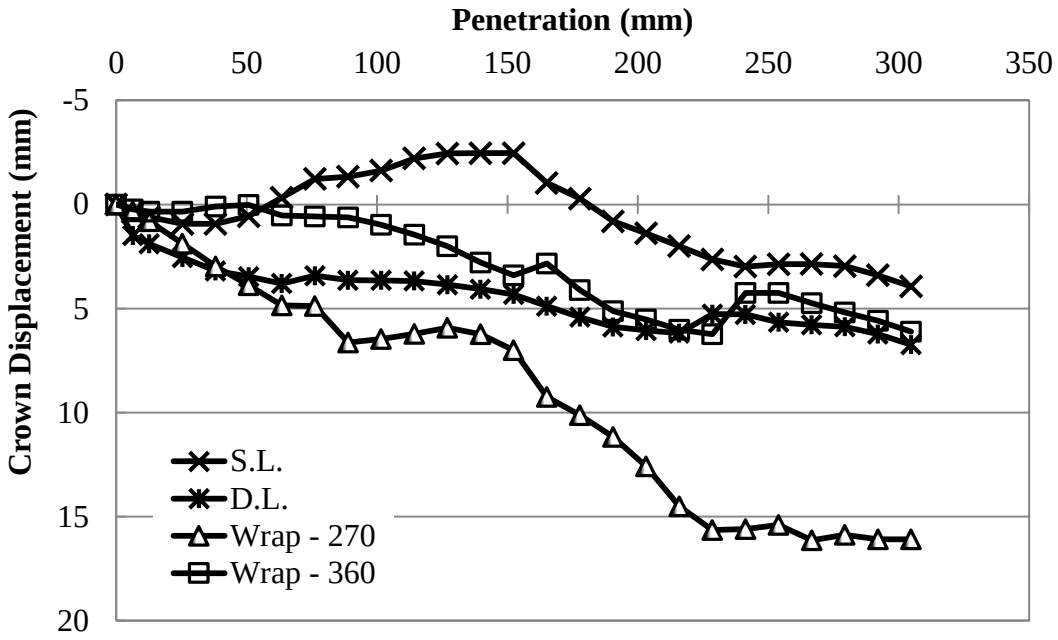

Figure 6.6 Rod Penetration vs. Crown Displacement at the Center of Penetration

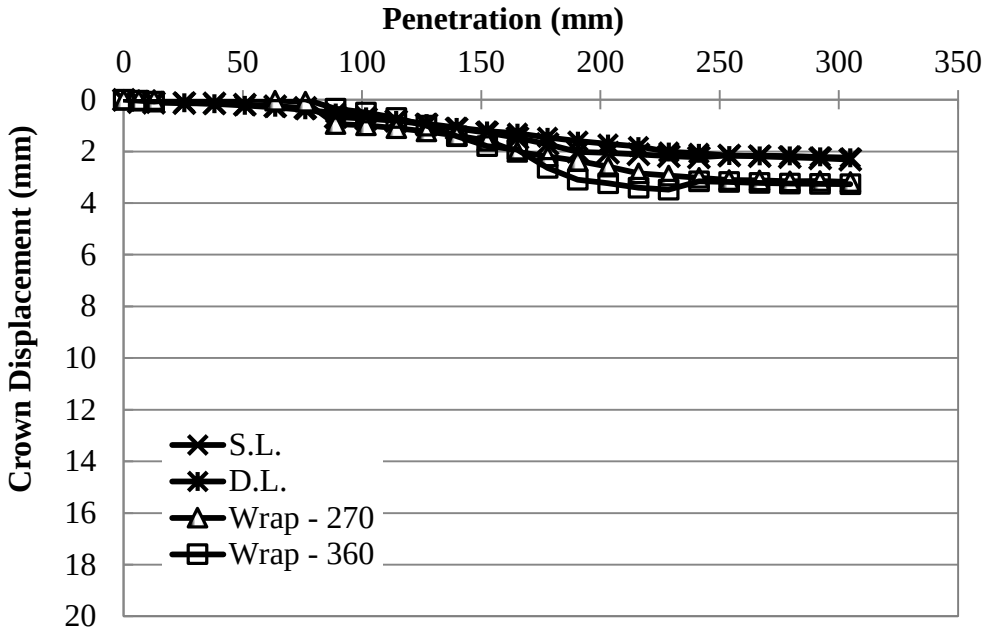

Figure 6.7 Rod Penetration vs. Crown Displacement at 305 mm from the Center of Penetration along the Centerline of the Pipe

6.3.2 Horizontal Pipe Deflection

The horizontal deflection of the pipe is the change of the pipe diameter in the horizontal direction, designated positive for the increase of the pipe diameter along the horizontal axis. Figure 6.8 shows the relationship between the horizontal deflection of the pipe and the vertical penetration of the steel rod. It is shown that the inclusion of the geogrid increased the horizontal deflection of the pipe. There was almost no difference in the responses when single and double geogrid layers were used. The inverted U-shape geogrid and the wrapped-around geogrid resulted in large horizontal deflections.

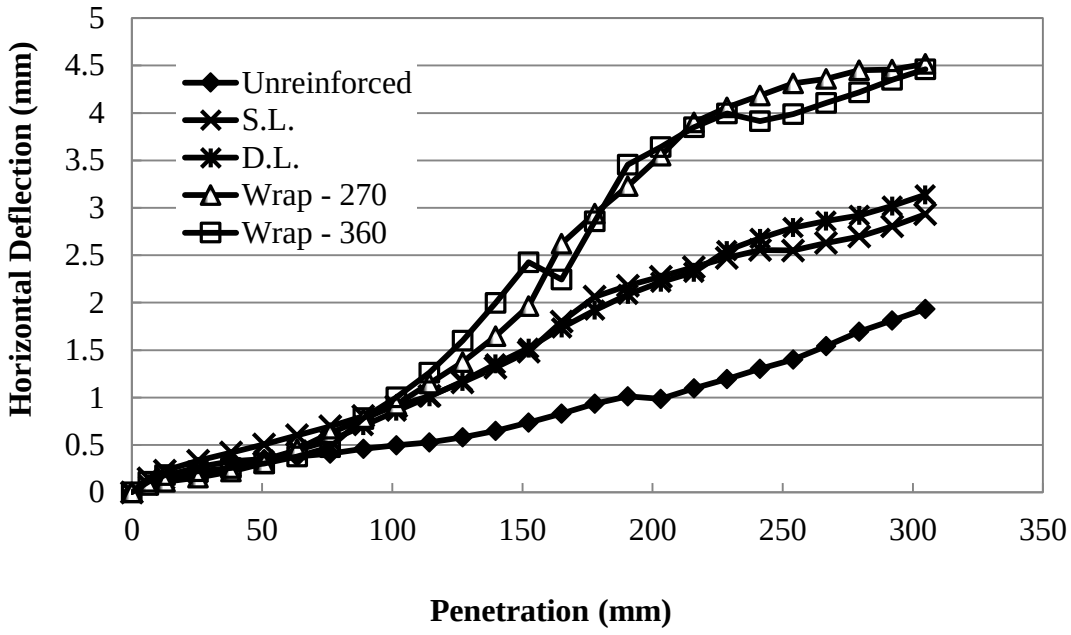

Figure 6.8 Rod Penetration vs. Horizontal Deflection of the Pipe

Assuming that a pipe is deflected to a prototypical elliptical shape, the ratio of vertical to horizontal deflection would be equal to or nearly equal to 1.0. Figure 6.9 shows that the vertical to horizontal deflection ratio of the pipe ranged from approximately 1.5 to 3.7, indicating a non-uniform distortion of the pipe. Generally, the geogrid reinforcement reduced the ratio of vertical to horizontal deflection. In other words, rod penetration induced more local deflection of the pipe in the unreinforced section than in the reinforced section. The inverted U-shape geogrid and the wrapped-around geogrid resulted in more uniform deflection of the pipe.

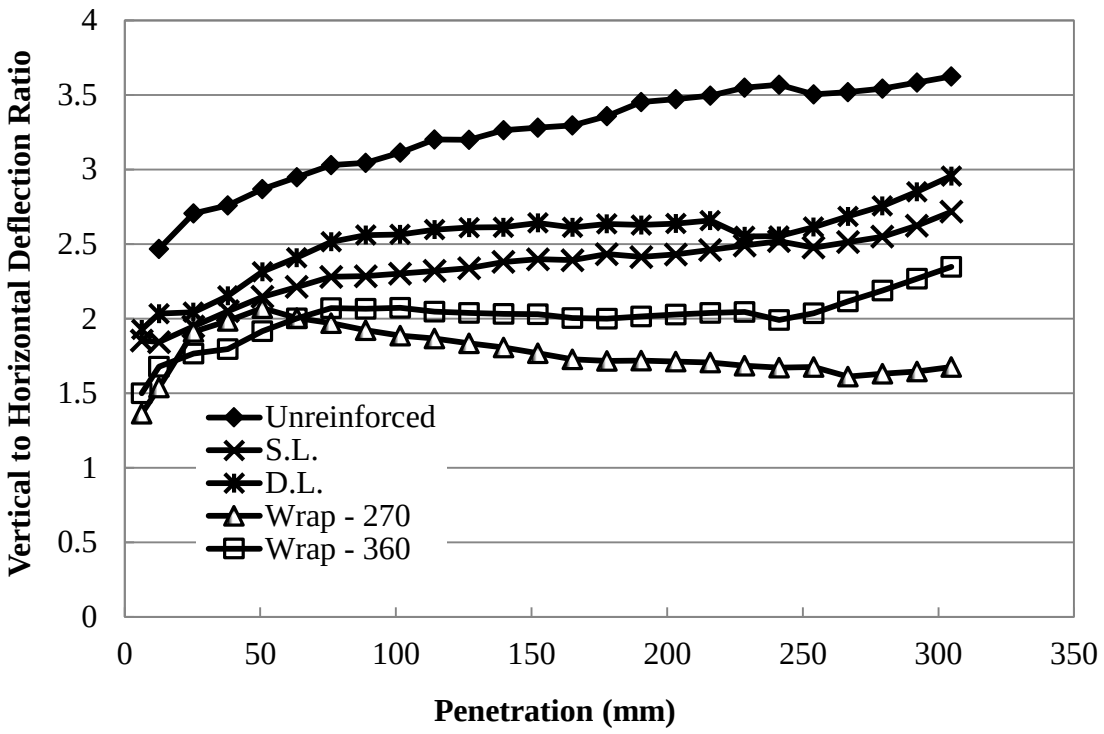

Figure 6.9 Rod Penetration vs. Vertical to Horizontal Deflection Ratio of the Pipe

6.4 Earth Pressure

During the penetration of the steel rod the earth pressure cells were monitored and recorded. It is clear from the recorded earth pressures that for each individual reinforcement condition the distribution of earth pressures was greatly affected by the geosynthetic. The locations of the earth pressure cells, shown in Chapter 3, are shown in Fig. 6.10 again for convenience. Earth pressure cell C4 was not included in these penetration tests. Some pressure cells failed to measure data or malfunctioned, therefore, they are not included in the following discussion. For the wrapped-around geogrid case, the earth pressure cell I_1 was placed above the geogrid. For the inverted U-shape and wrapped-around cases, the earth pressure cells (S_1, S_2, S_3, S_4, and S_5) were placed between the pipe and the vertically-oriented geogrid.

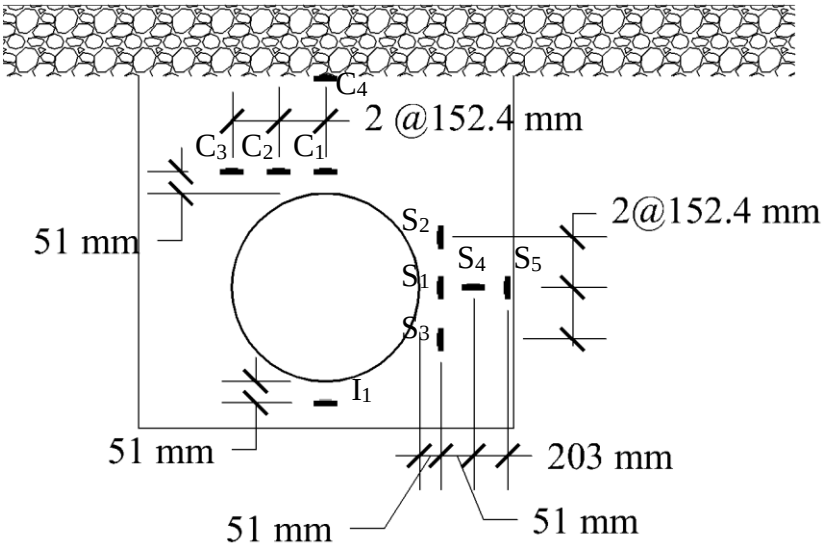

Figure 6.10 Earth Pressure Cell Locations

6.4.1 Earth Pressure at Pipe Invert

Figure 6.11 shows that measured vertical earth pressures at the pipe invert during rod penetration. For the unreinforced condition, the vertical pressures at the invert were nearly linear with respect to the penetration of the steel rod, increasing with each successive penetration step. Similarly, the vertical pressures at the invert, for the single and double layers of reinforcement, had a linear relationship with respect to the penetration. This linear relationship changed when the penetration reached the reinforcing layer (i.e., the geogrid was at 229 mm below the surface of the base course) and ruptured the geogrid, after which the rate of pressure increase with respect to penetration decreased. . With respect to the single and double layers of reinforcement, the inclusion of the geogrid caused a slightly increased earth pressure at the invert because higher force was required to make the same penentration. The wrap reinforcement condition greatly reduced the vertical pressures at the pipe invert.

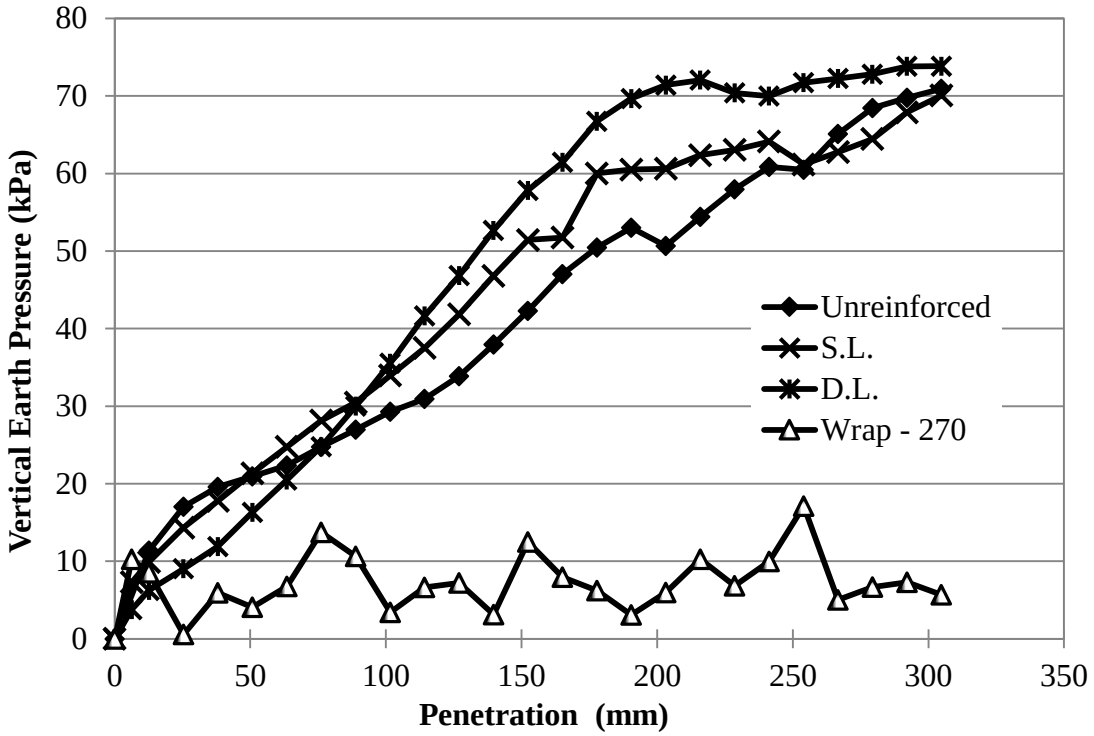

Figure 6.11 Vertical Earth Pressure at Pipe Invert (I_1)

6.4.2 Earth Pressures at Pipe Spring Line, Shoulder, and Haunch

Figures 6.12, 6.13, and 6.14 present the measured horizontal earth pressures at the pipe spring line, shoulder, and haunch in the five conditions during rod penetration. In general, the single layer and double layers of reinforcement resulted in higher horizontal earth pressures at the spring line, shoulder, and haunch of the pipe as compared to those in the unreinforced condition, while the 270 degree and 360 degree wrap conditions resulted in similar or slightly lower horizontal earth pressures at these locations. In addition, the measured horizontal earth pressures at the pipe shoulder were much higher than those at the pipe spring line and haunch.

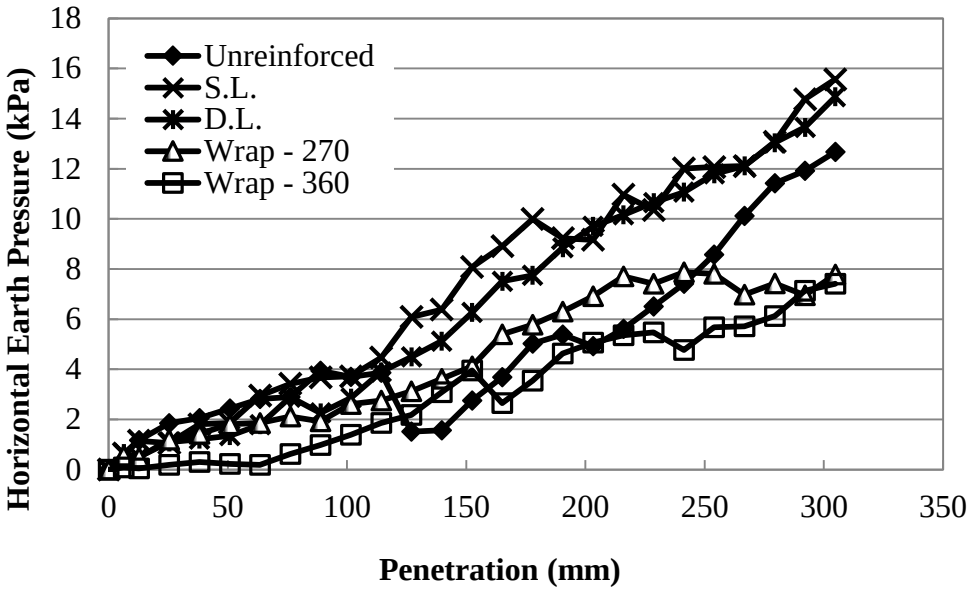

Figure 6.12 Horizontal Earth Pressure at Pipe Spring Line (S_1)

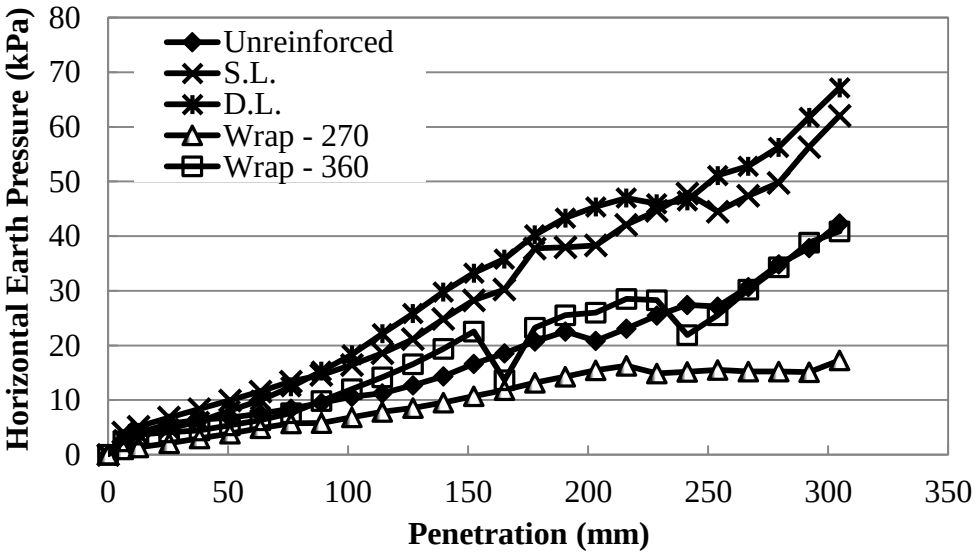

Figure 6.13 Horizontal Earth Pressure at Pipe Shoulder (S_2)

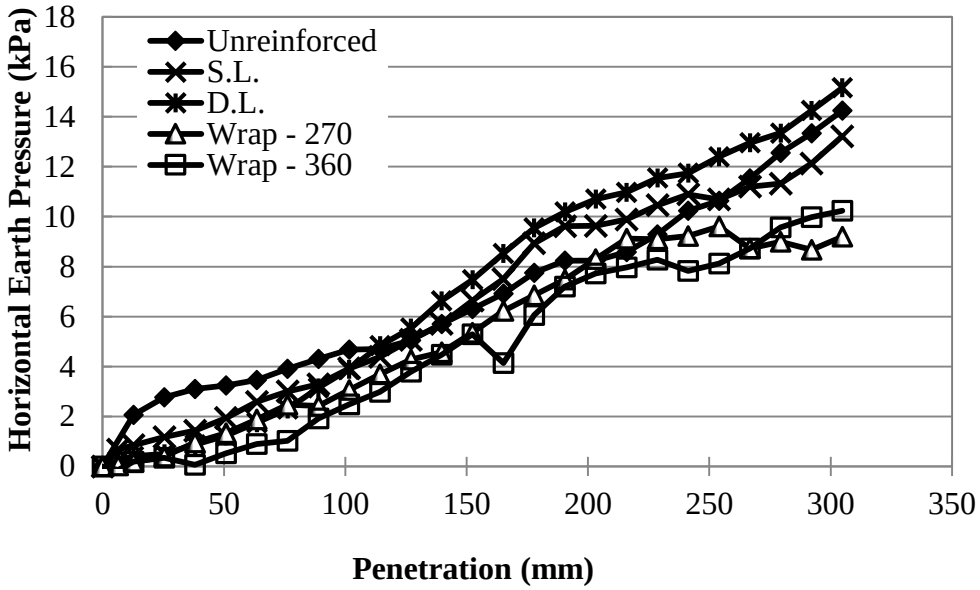

Figure 6.14 Horizontal Earth Pressure at Pipe Haunch (S_3)

Figure 6.15 shows the distribution of horizontal earth pressures around the pipe spring line, which reveals that the earth pressures did not form the assumed parabolic shape of an elliptically distorted buried pipe. However, higher horizontal earth pressures were located at the shoulder of the pipe. The use of the single or double geogrid layers increased the horizontal earth pressures at the same rod penetration. However, the inverted U-shape and wrapped-around geogrids did not change the distribution that much as compared with the unreinforced case even though the required penetration forces were much higher in the reinforced cases.

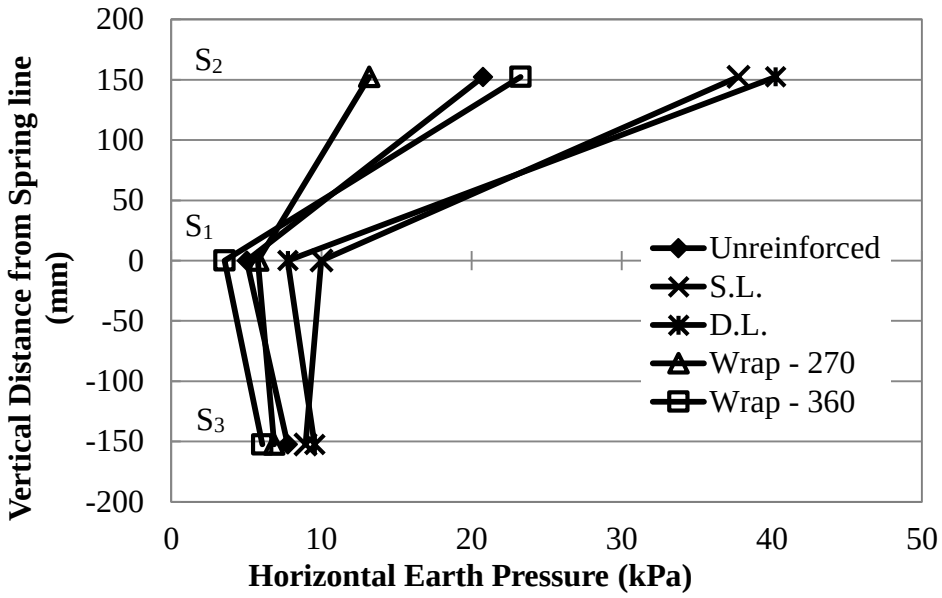

Figure 6.15 Distribution of Horizontal Earth Pressure around the Pipe Spring Line at Rod Penetration of 178 mm

Figure 6.16 shows the measured horizontal earth pressure at the trench wall and at the elevation of the spring line. Clearly, the geogrid reinforcement increased the horizontal pressure. This increase had also something to do with the increased required force to have the same penetration.

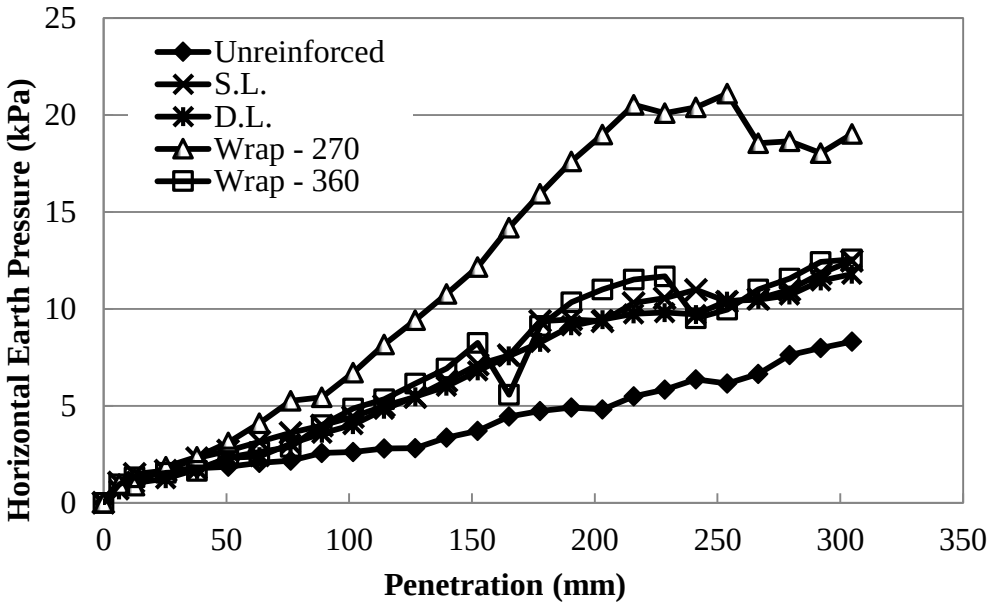

Figure 6.16 Horizontal Earth Pressure at the Trench Wall (S_5)

Figure 6.17 presents the measured vertical earth pressures at the pipe spring line in all five conditions. Clearly the vertical earth pressures increased with the inclusion of the geogrid reinforcement. The inverted U-shape and wrapped-around cases had the highest vertical earth pressures. The reason for this increase is that the required force to penetrate the rod was increased in the reinforced conditions, especially for the inverted U-shape and wrapped-around cases.

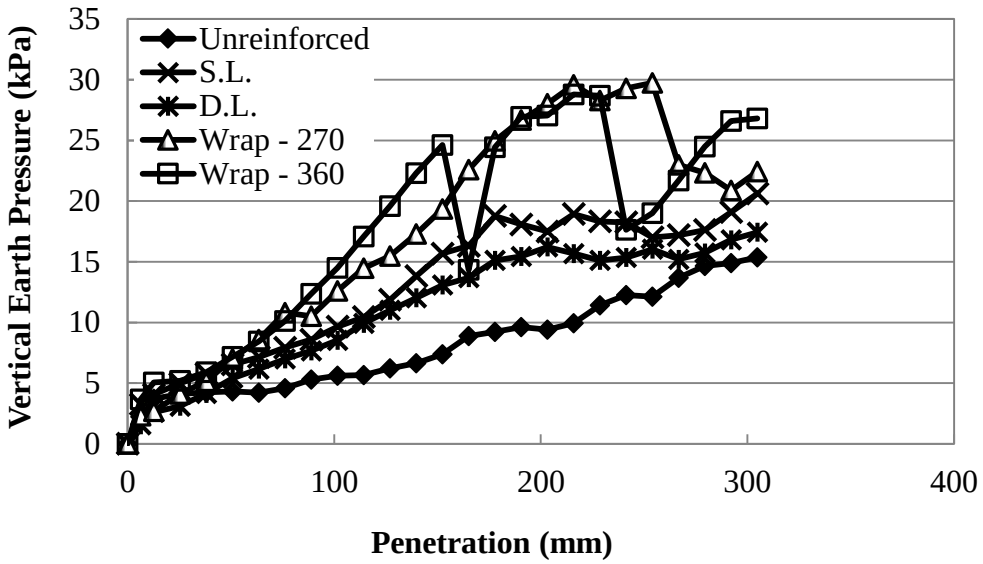

Figure 6.17 Vertical Earth Pressure at the Pipe Spring Line (S_4)

Figure 6.18 shows the ratios of vertical to horizontal earth pressures at the pipe spring-line in all five conditions. The layers of reinforcement, particularly the inverted U-shape and wrapped-around geogrids, significantly reduced the ratio of horizontal to vertical earth pressures, suggesting more redistribution of earth pressure through the backfill and less redistribution through the distortion of the pipe.

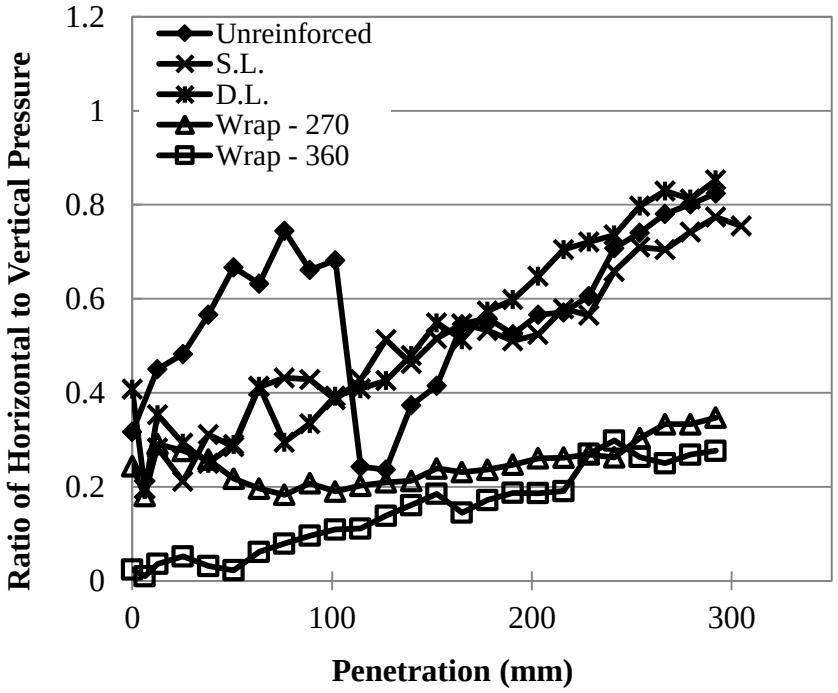

Figure 6.18 Ratio of Horizontal to Vertical Earth Pressures at the Pipe Spring Line

6.4.3 Vertical Earth Pressure at Pipe Crown

Figure 6.19 presents the measured vertical earth pressure directly over the pipe crown, and directly under the penetrating rod, which shows the vertical earth pressure increasing with the rod penetration. The pressure increase accelerated after the rod penetrated though the geogrid in the reinforced cases. There are a combined effect of the geogrid reinforcement on the vertical earth pressure at the pipe crown: (1) the geogrid reinforcement increased the required force to make the same rod penetration, which increased the vertical earth pressure and (2) the geogrid reinforcement distributed the force to a wider area, which reduced the vertical earth pressure. The final result depends on which one is more dominated.

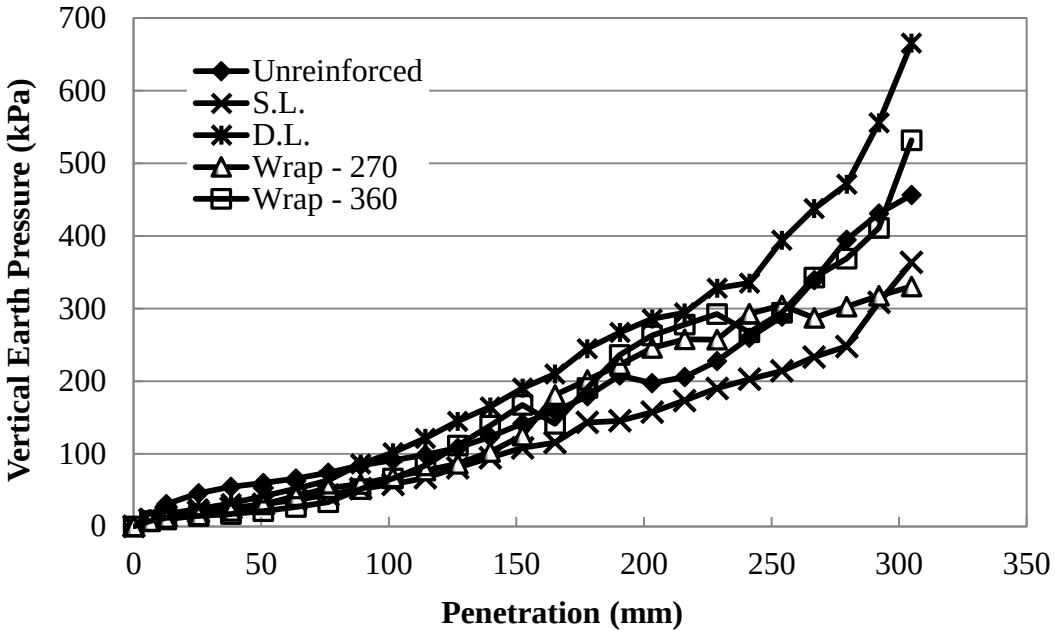

Figure 6.19 Vertical Earth Pressure at the Pipe Crown (C_1)

Figures 6.20 and 6.21 presents the measured vertical earth pressures at the distance of 152 and 305 mm from the pipe crown. It can be seen that the geogrid had a significant effect on reducing the vertical earth pressures at the distance of 152 mm from the pipe crown, while increasing the pressures at the distance of 305 mm from the crown.

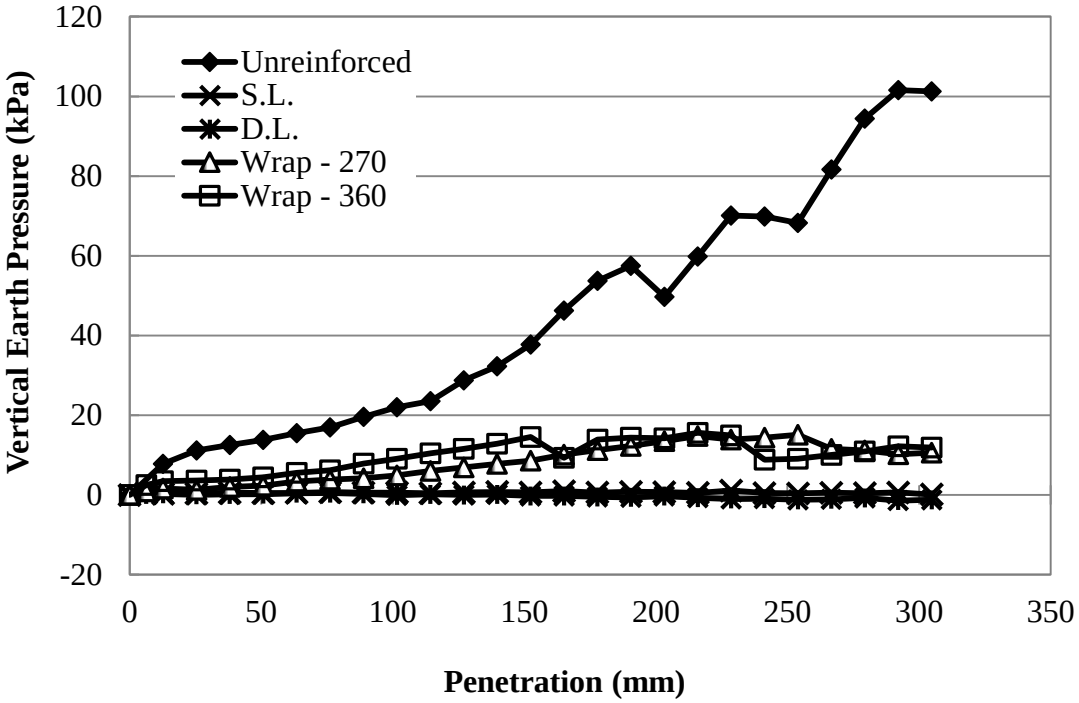

Figure 6.20 Vertical Earth Pressure at the Distance of 152 mm from the Pipe Crown (C_2)

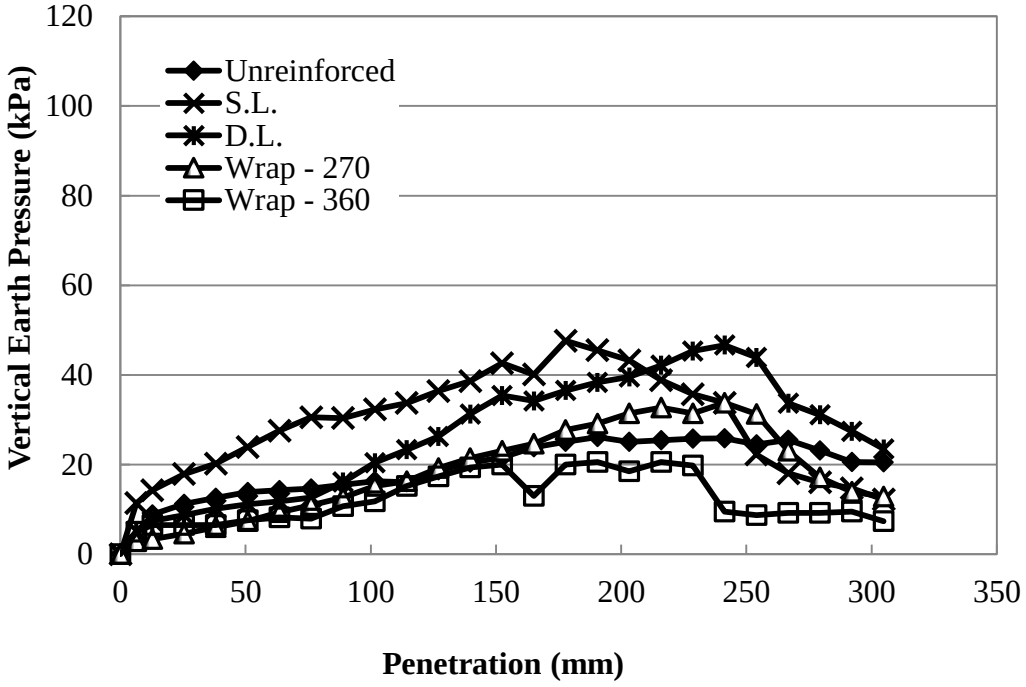

Figure 6.21 Vertical Earth Pressure at the Distance of 305 mm from the Pipe Crown (C_3)

The vertical earth pressure distributions at the elevation of the pipe cro can be seen in Figures 6.22 and 6.23 at the rod penetration of 178 mm and 203 mm. In general, the vertical earth pressure decreased with the distance from the pipe crown and the large penetration induced higher vertical earth pressure.

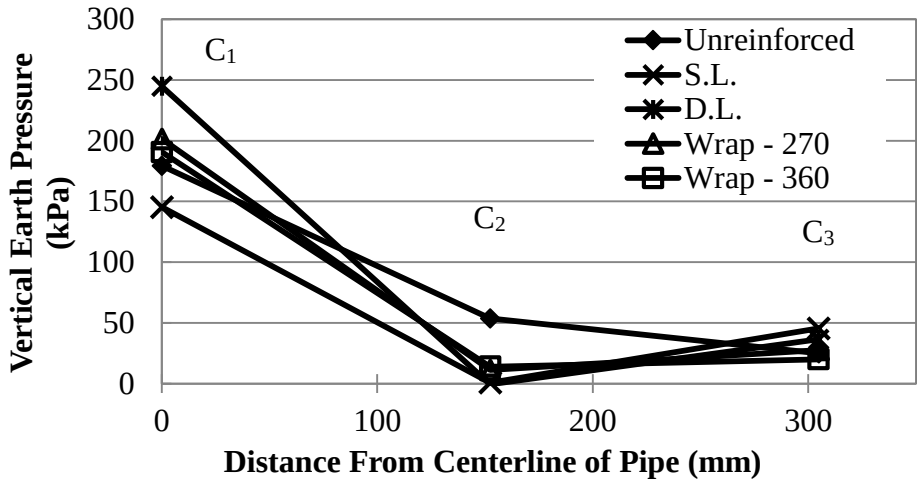

Figure 6.22 Distribution of Vertical Earth Pressures at the Elevation of the Pipe Crown under the Penetration of 178 mm

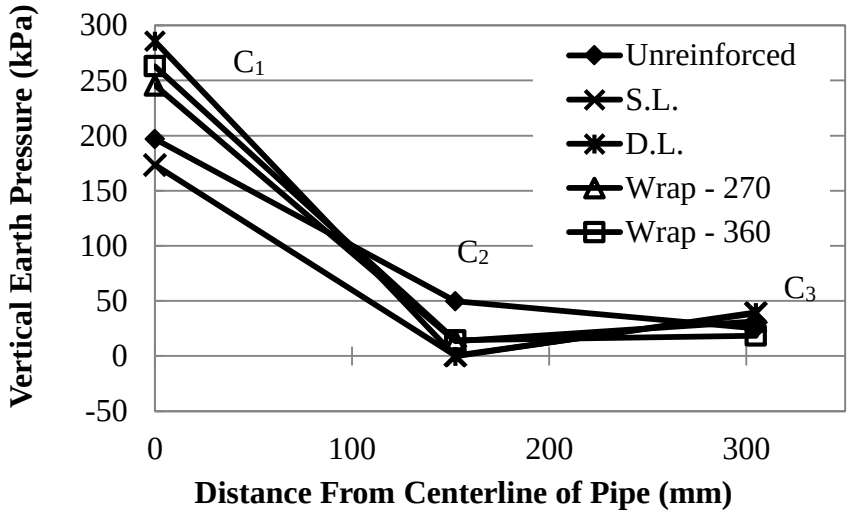

Figure 6.23 Distribution of Vertical Earth Pressures at the Elevation of the Pipe Crown under the Penetration of 203 mm

6.5 Pipe Strain

Strain gauges were installed on the pipes to monitor the deformations of the pipes during rod penetration. As noted in the earlier sections of this report, some pipe strains were very small and appeared to be influenced more by localized movement in the backfill and noise than by bending and compression of the pipe. Some strain gauges failed or exceeded the allowable range of measureable strains by the gauge. These factors and the composite behavior of the pipe wall made interpretation and analysis of the pipe strains difficult. The strains of the failed strain gauges are not included in the following discussion. The strain gage locations are shown in Figures 6.24 and 6.25 again for convenience of presentation. A limited number of strain gauge data are discussed in the following sections, other pipe strains are included in Appendix D. The pipe strain data can be analyzed based on different test sections and different locations in the same test.

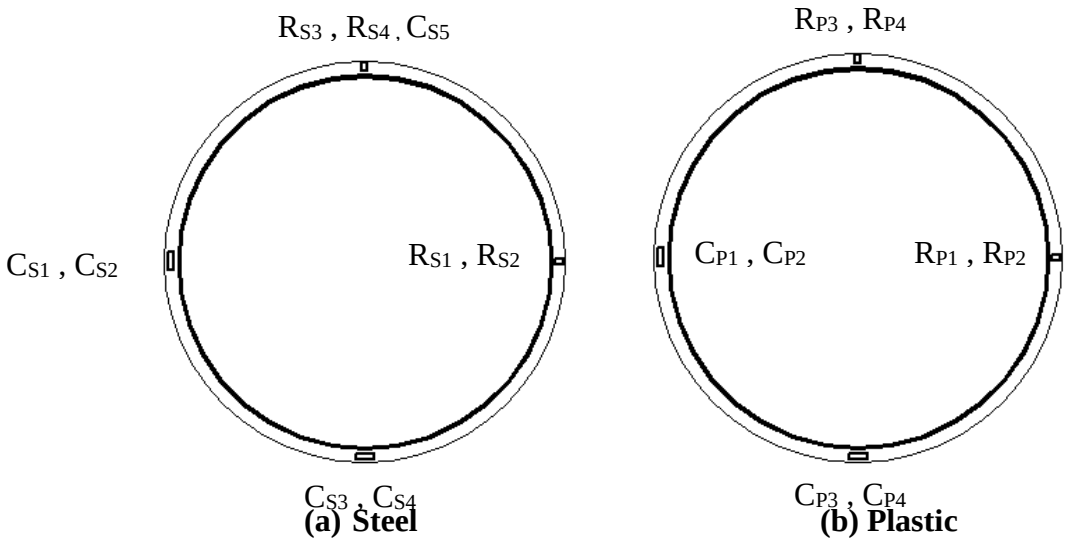

Figure 6.24 Circumferential and Radial Strain Gauge Locations

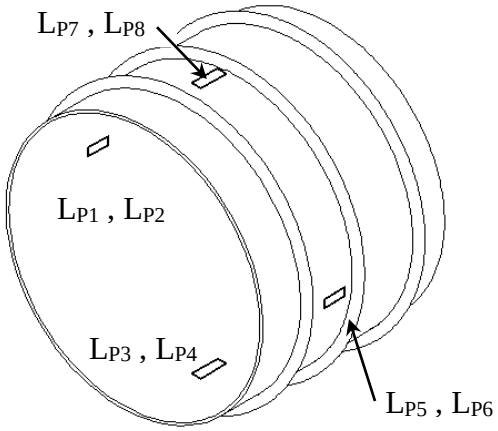

Figure 6.25 Longitudinal Strain Gauge Locations

6.5.1 Pipe Strains in Different Test Sections

Figure 6.26 shows the measured circumferential strains on the steel ribs at the pipe spring line. Although there were variations in the measured pipe strains, Fig. 6.26 shows that the unreinforced section had lower strains on the steel ribs than those in the reinforced cases. There

are two reasons which might contribute to this result: (1) more force was required to penetrate the rod to the same depth and (2) geogrid reinforcement helped distribute the load to a deeper depth. There was a sudden reduction in the measured strain or switch of the sign of the measured strain after the rod penetrated through the geogrid. The measured strains in the penetration tests were an one order of magnitude higher than those in the previous static and cyclic plate loading tests. Similar behavior was obtained for the measured circumferential strains at other locations (i.e., pipe invert and crown) as shown in Figures 6.26 to 6.30.

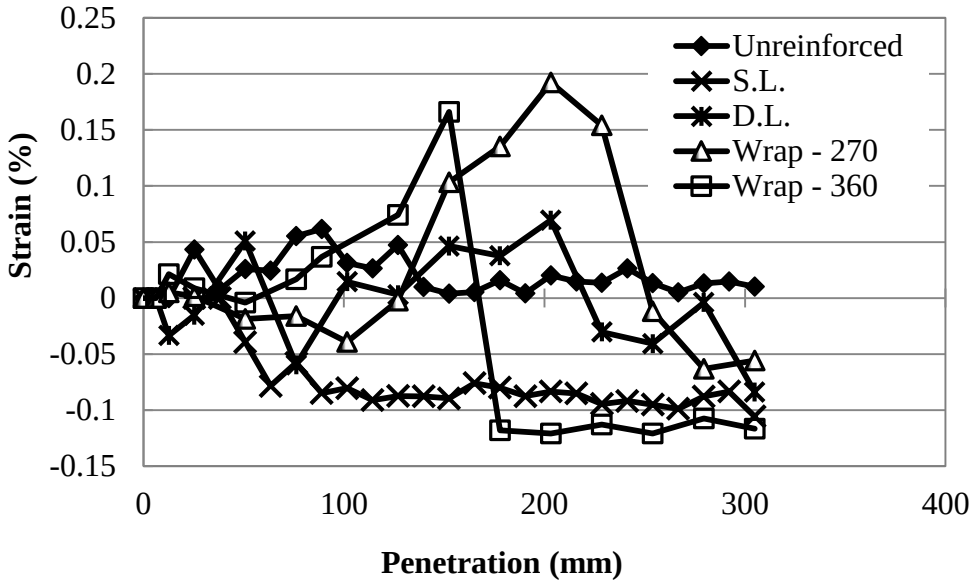

Figure 6.26 Circumferential Strains on the Steel Ribs at the Pipe Spring Line (C_{s1})

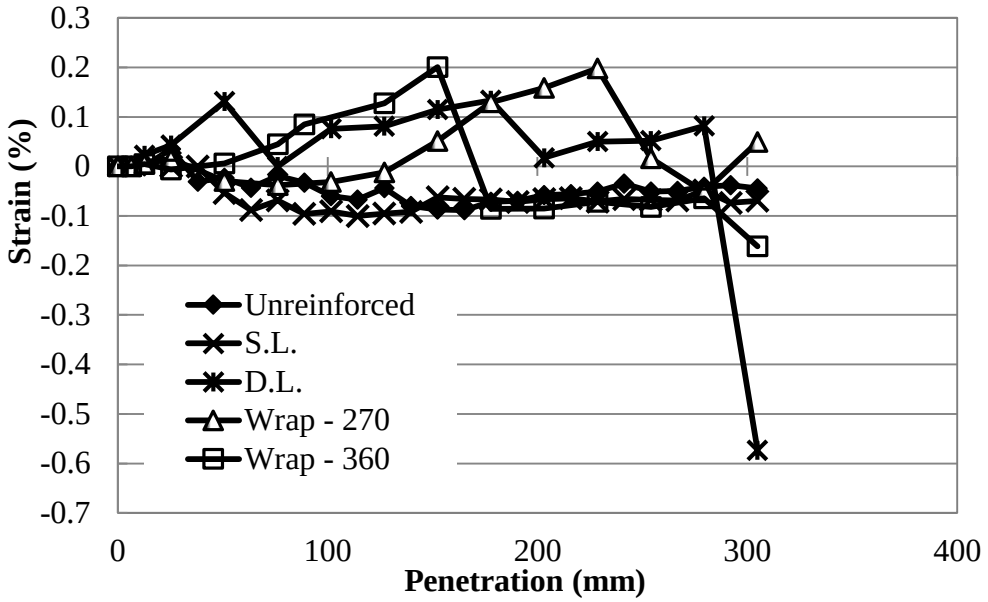

Figure 6.27 Circumferential Strains on the Plastic Cover on the Steel Ribs at the Pipe Spring Line (C_{p1})

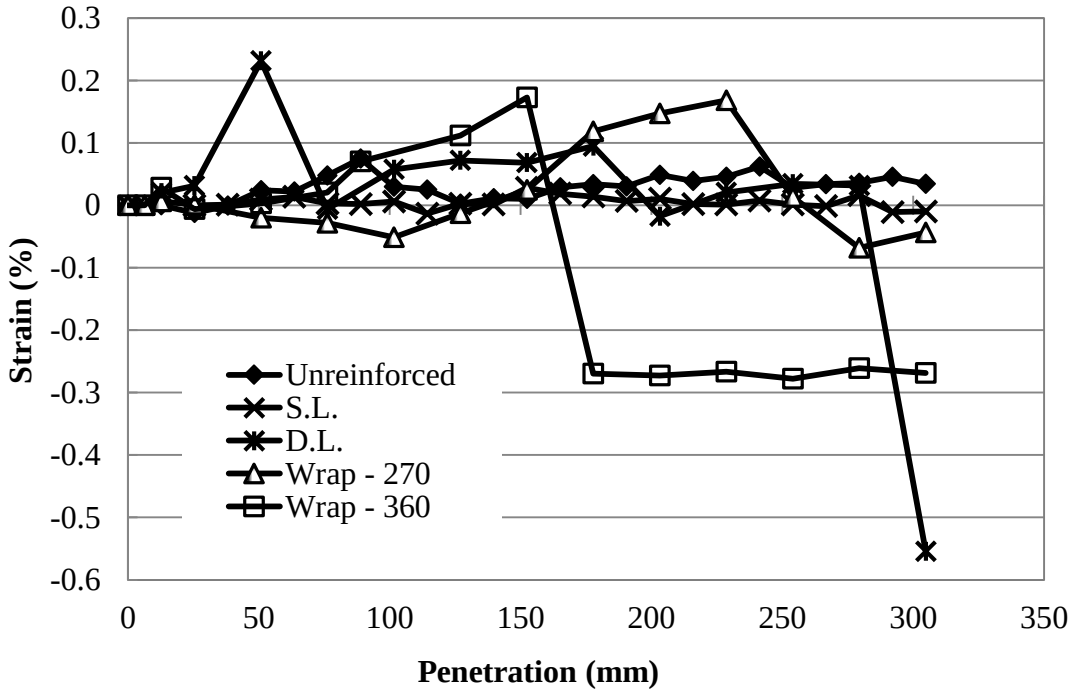

Figure 6.28 Circumferential Strains on the Steel Ribs at the Pipe Invert (C_{s3})

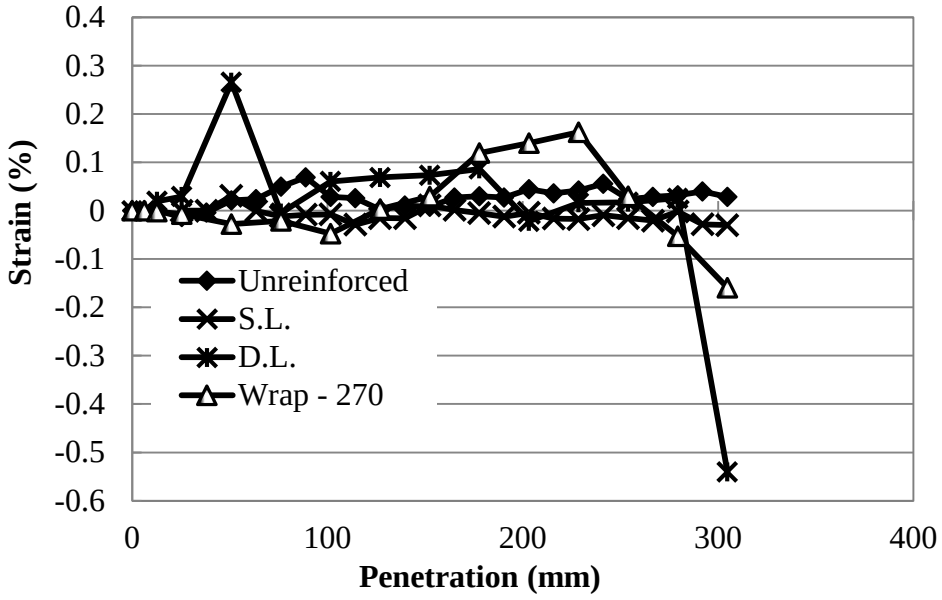

Figure 6.29 Circumferential Strains on the Plastic Cover on the Steel Ribs at the Pipe invert (C_{p3})

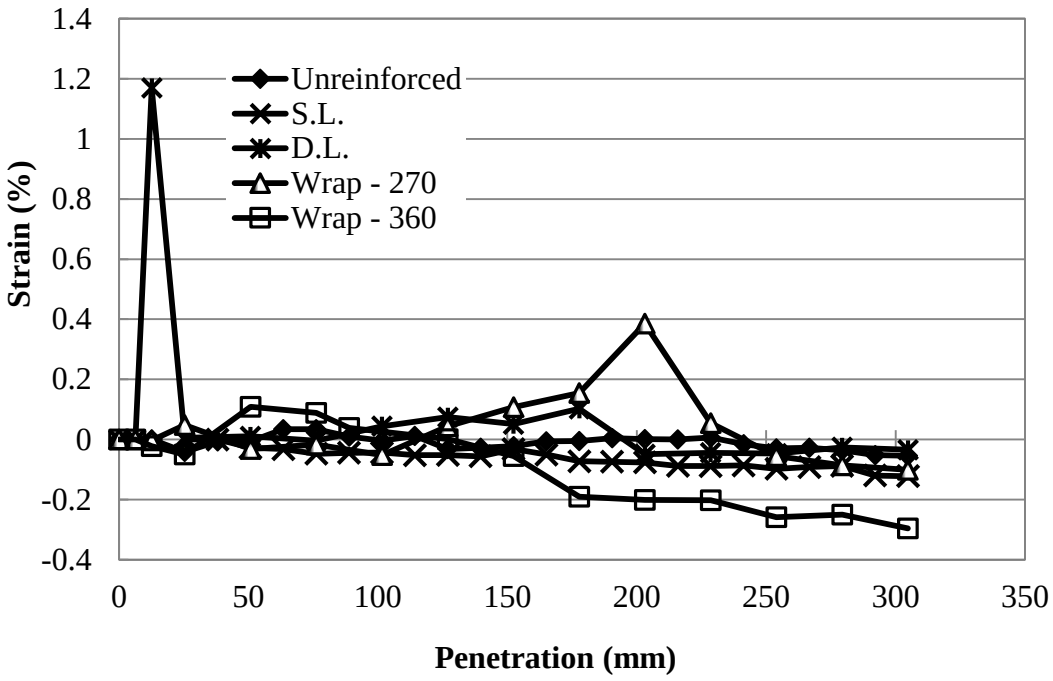

Figure 6.30 Circumferential Strains on the Steel Ribs at the Pipe Crown (C_{s5})

As noted in the plate loading tests, the highest pipe strains in the pipe wall were those in the shell in the longitudinal direction, specifically at the pipe crown as shown in Figs. 6.31 and Fig 6.32. In the penetration tests, the inside of the plastic liner at the pipe crown was in tension while the outside of the plastic liner at the pipe crown was in compression, or in tension at a much smaller magnitude except for the inverted U-shape geogrid case, even in the unreinforced condition. The tensile strain on the outside of the plastic liner might be induced by lateral spreading of aggregate during the rod penetration.

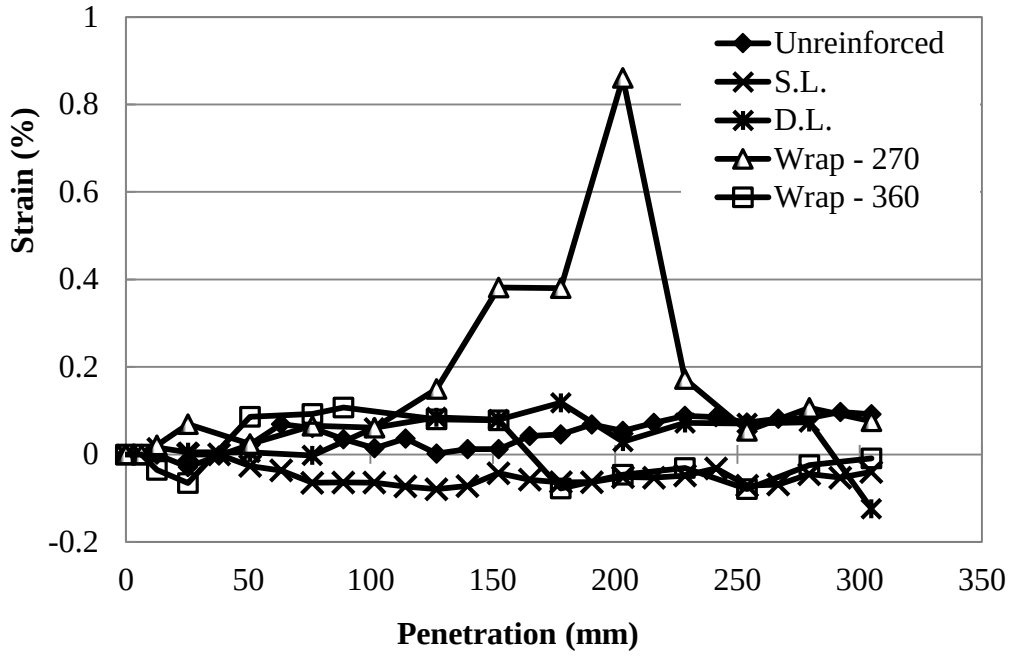

Figure 6.31 Longitudinal Strains on the Outside of the Plastic Liners at the Pipe Crown (L_7)

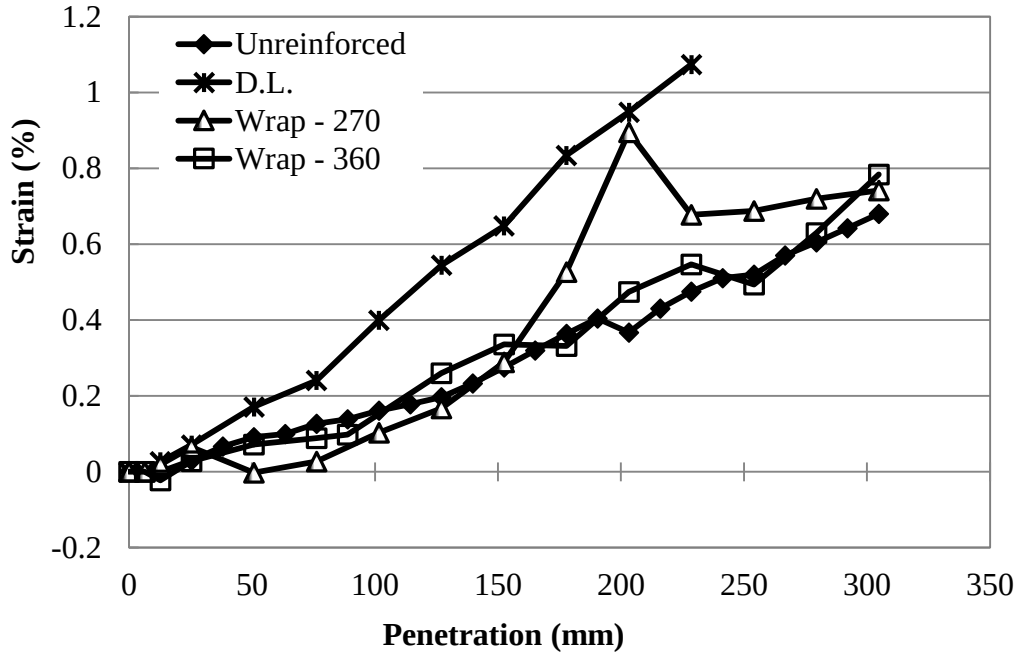

Figure 6.32 Longitudinal Strains on the Inside of the Plastic Liners at the Pipe Crown (L_8)

6.5.2 Pipe Strains at Different Locations in Same Test

Figures 6.33, 6.34, and 6.35 show the circumferential and radial pipe strains at different locations in the unreinforced section. Although they do not allow for comparisons of the reinforcement effect, they can be used to confirm overall behavior of the strain gauges at the same location. Figure 6.34 clearly shows the four strain gauges had the same response.

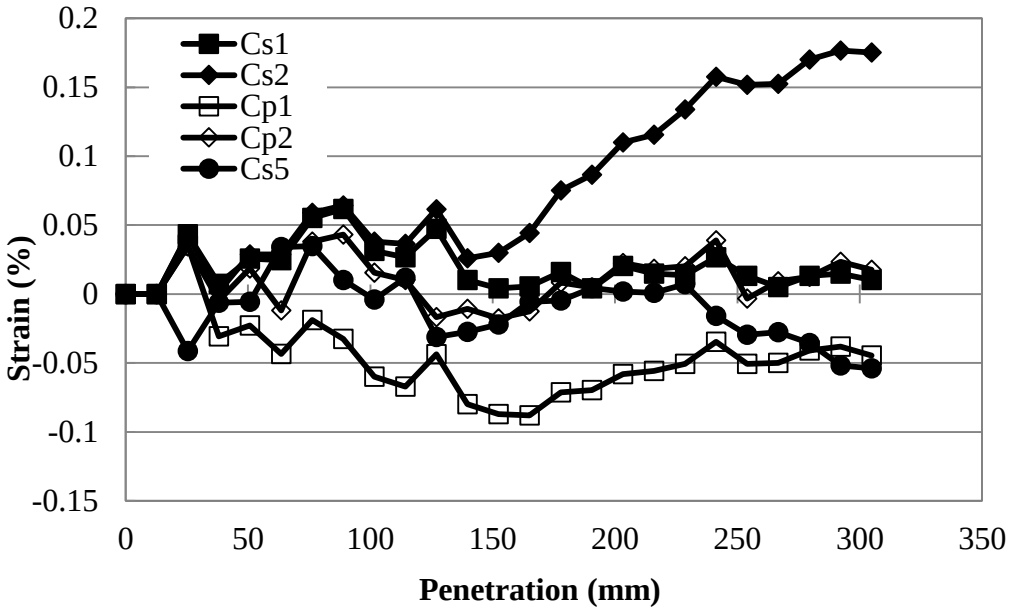

Figure 6.33 Circumferential Pipe Strains (Cs1, Cs2, Cp1, Cp2, and Cs5) in the Unreinforced Section (Test 11)

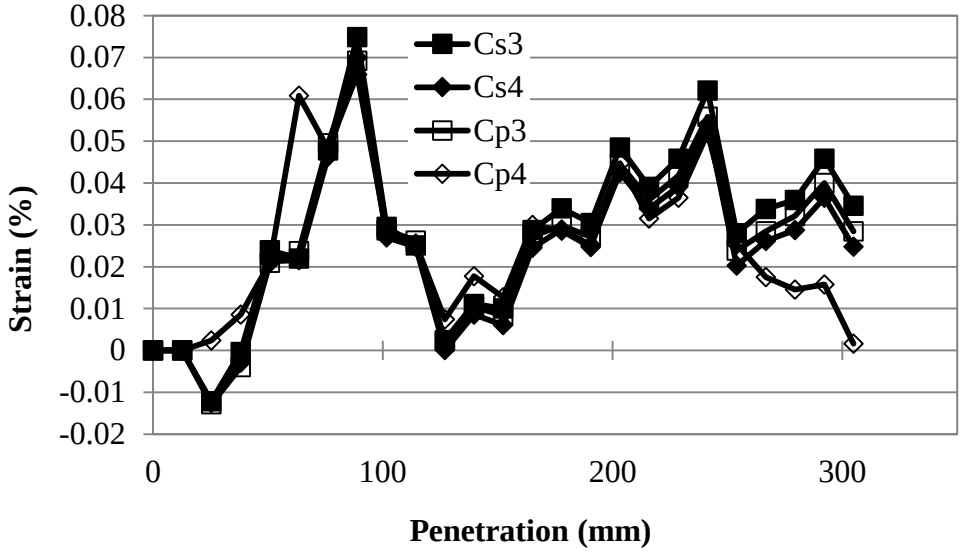

Figure 6.34 Circumferential Pipe Strains (Cs3, Cs4, Cp3, and Cp4) in the Unreinforced Section (Test 11)

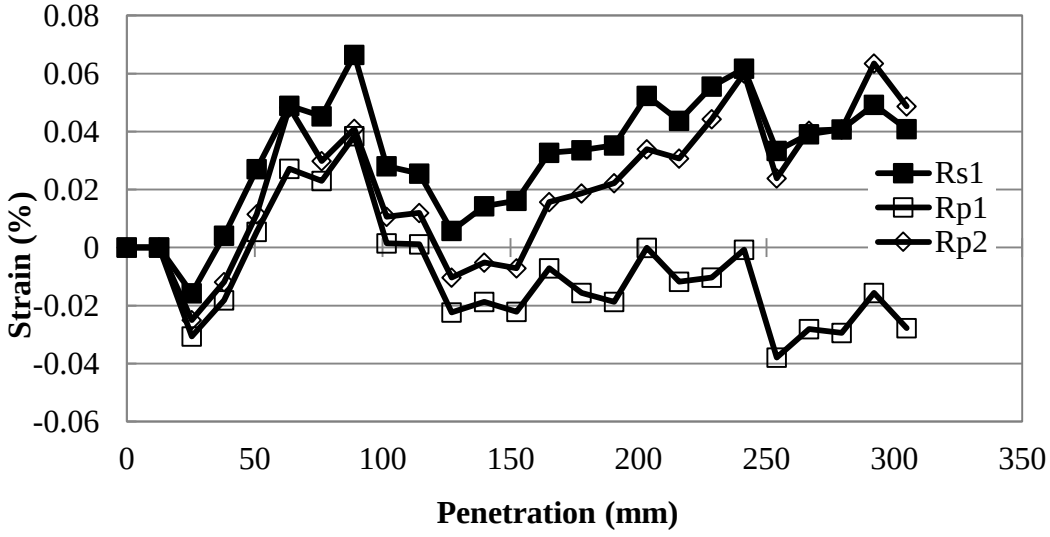

Figure 6.35 Radial Pipe Strains in the Unreinforced Section (Test 11)

6.6 Geogrid Strain

In addition to the strain gauges on the pipes, strain gauges were also placed on the geogrids and their strains were recorded during the penetration tests. A layout of the geogrid strain gauges is shown in Figures 6.36 and 6.37 again for convenience of presentation. Note that in the single and double geogrid-reinforced sections, the machine direction of the geogrid was the same as the longitudinal direction of the pipe. However, the machine direction of the geogrid was the same as the transverse direction of the pipe in the inverted U-shape and wrapped-around sections. The reason for this change considered the ease of placing the geogrid layer in the trench. In Figure 6.35, the L designation refers to the longitudinal direction of the pipe and X refers to the direction perpendicular to the pipe (or called the transverse direction of the pipe). In the single geogrid-reinforced section, only the lower geogrid layer was used.

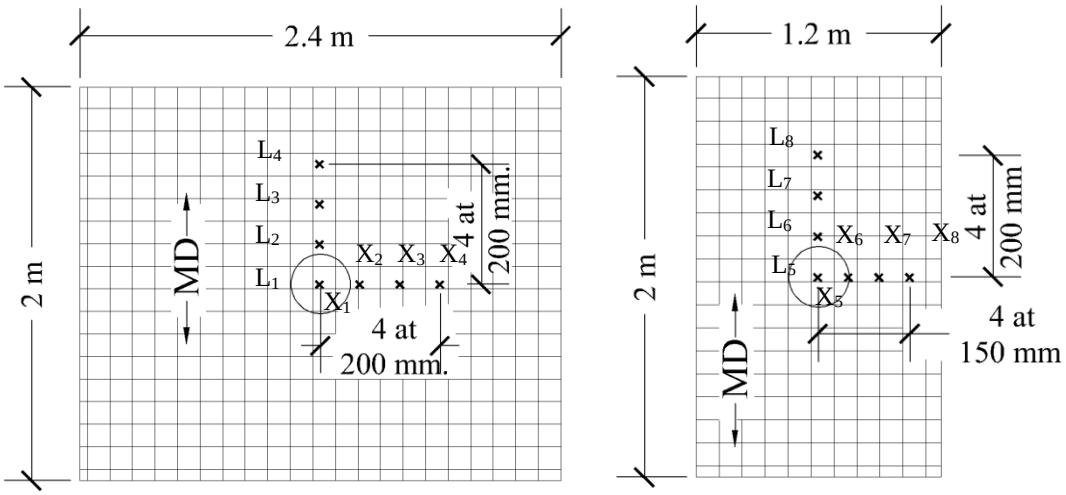

A. Upper Layer **B. Lower Layer**

Figure 6.36 Strain Gauges on Single and Double Geogrid Layers

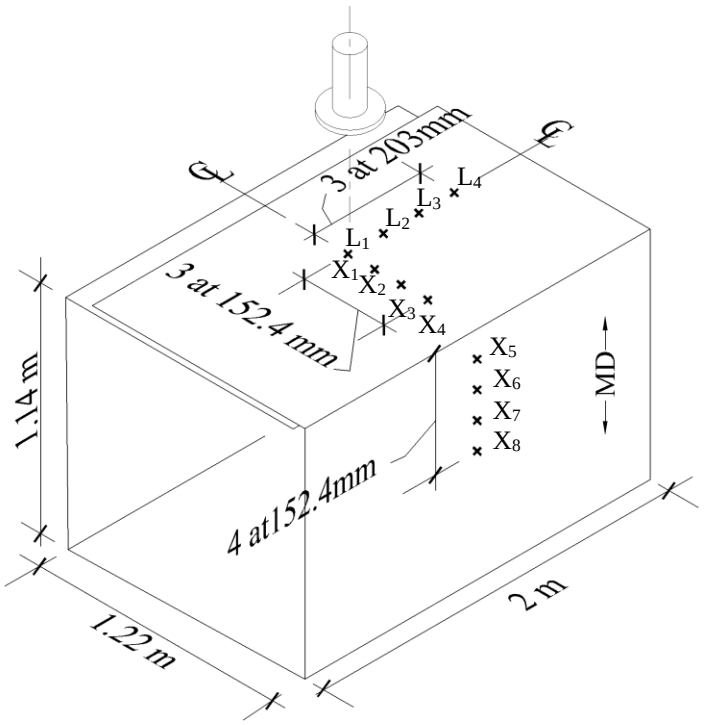

Figure 6.37 Strain Gauges on the Inverted U-shape and Wrapped-Around Geogrids

Figures 6.38 to 6.47 presents the measured geogrid strains in the machine and cross-machine directions in the geogrid-reinforced sections. The strain gage behavior was similar in all the test sections had similar strain responses to the rod penetration. As expected with a destructive test by penetrating a rod through a geogrid, some strain gauges failed during the tests. In each of the reinforcement configurations the first strain gauge directly under the penetrating rod immediately developed a tensile strain while the subsequent strain gauges along the geogrid developed much smaller tensile strains, and in some cases, developed compressive strains. In the inverted U-shape and wrapped-around geogrid conditions (Tests 14 and 15), the second strain gauge next to the center one had more tendency to go into tension as compared to those at other locations. Once the geogrid was ruptured, the strain in the geogrid appeared to be redistributed away from the ruptured area. The distribution of tensile and compressive strains along the geogrid

appears to confirm the observed distribution of earth pressures at the crown as shown in Figures 6.22 and 6.23. The geogrid over the pipe away from the penetrating rod appeared to restrain the soil from heaving up, in addition to acting as a tension membrane to carry the force of the penetrating rod.

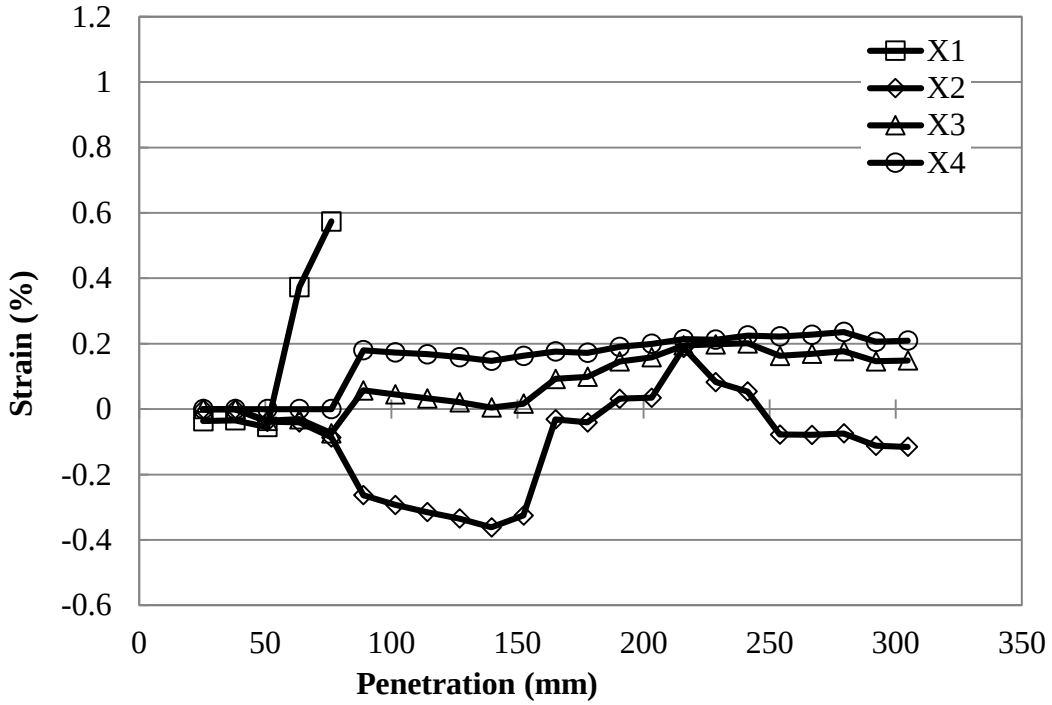

Figure 6.38 Cross-machine Direction Geogrid Strains in the Single Layer (Test 12)

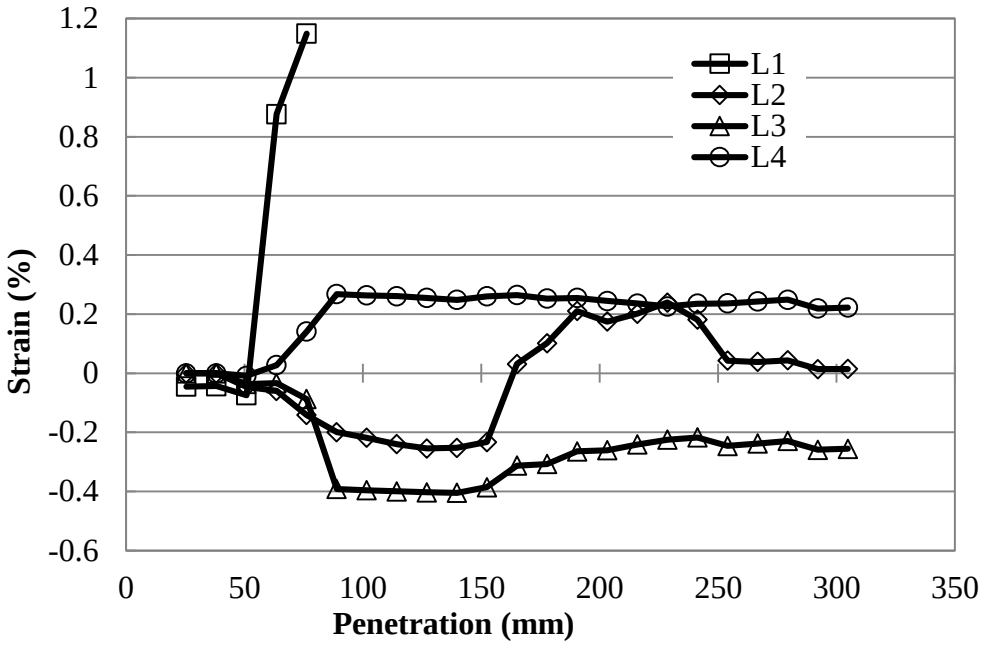

Figure 6.39 Machine Direction Geogrid Strains in the Single Layer (Test 12)

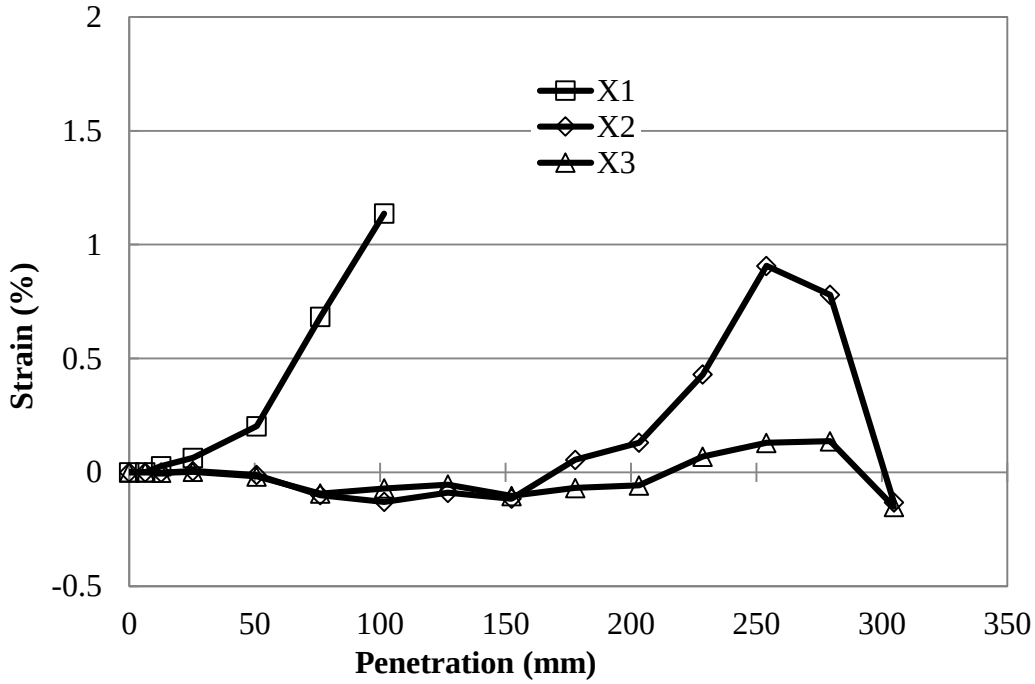

Figure 6.40 Cross-machine Direction Geogrid Strains in the Upper Layer (Test 13)

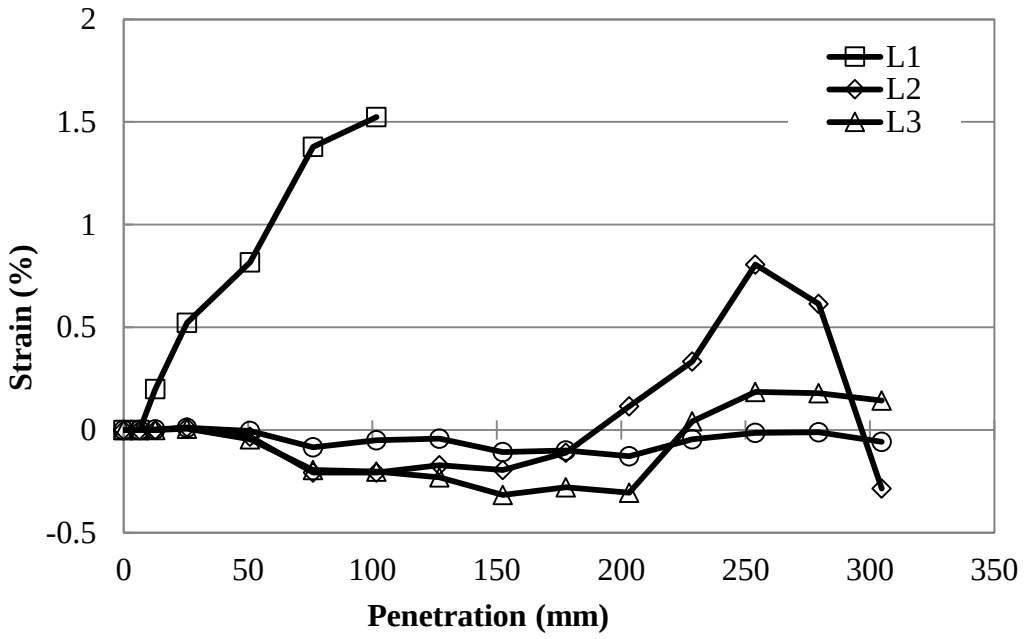

Figure 6.41 Machine Direction Geogrid Strains in the Upper Layer (Test 13)

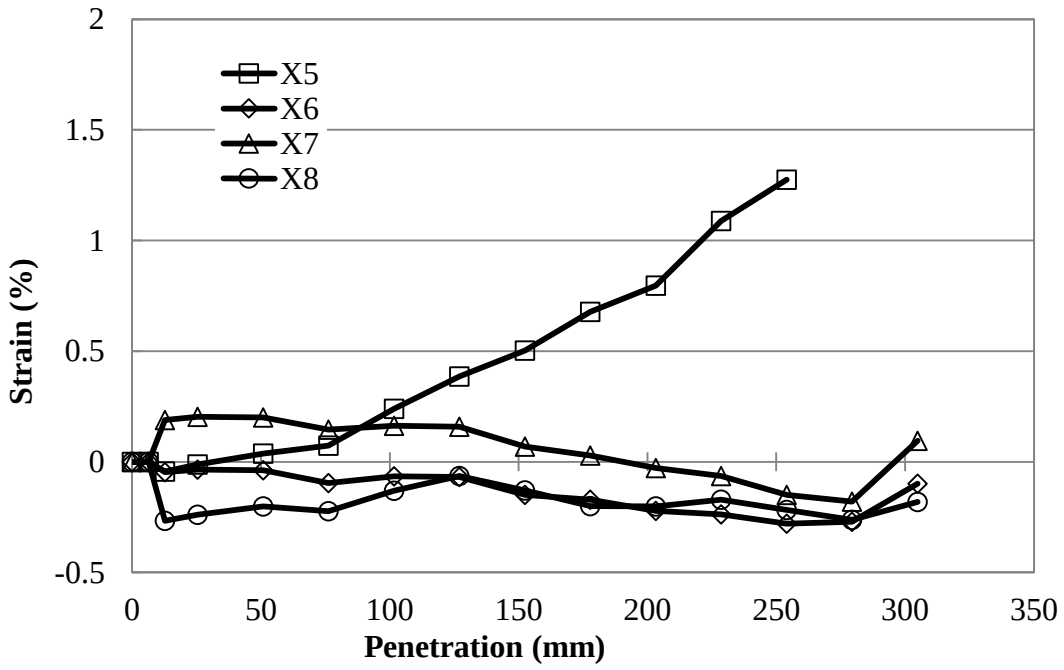

Figure 6.42 Cross-machine Direction Geogrid Strains in the Lower Layer (Test 13)

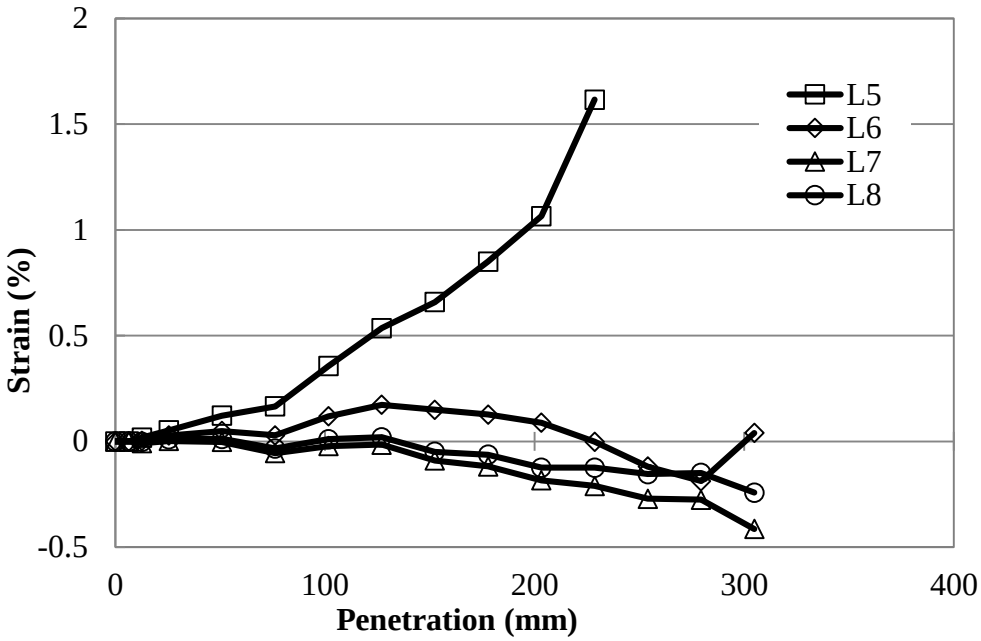

Figure 6.43 Machine Direction Geogrid Strains in the Lower Layer (Test 13)

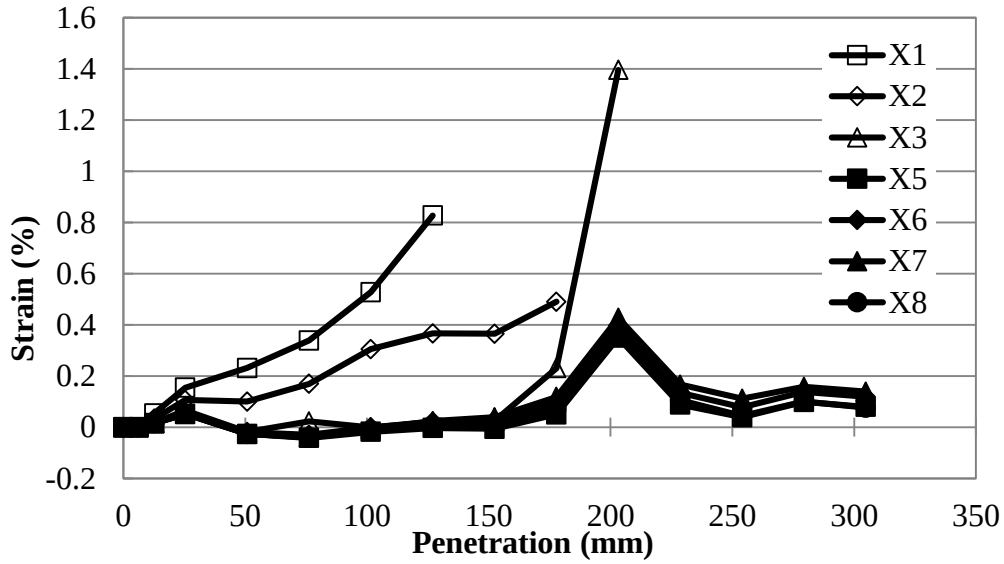

Figure 6.44 Machine Direction Geogrid Strains in the Inverted U-Shape Layer (Test 14)

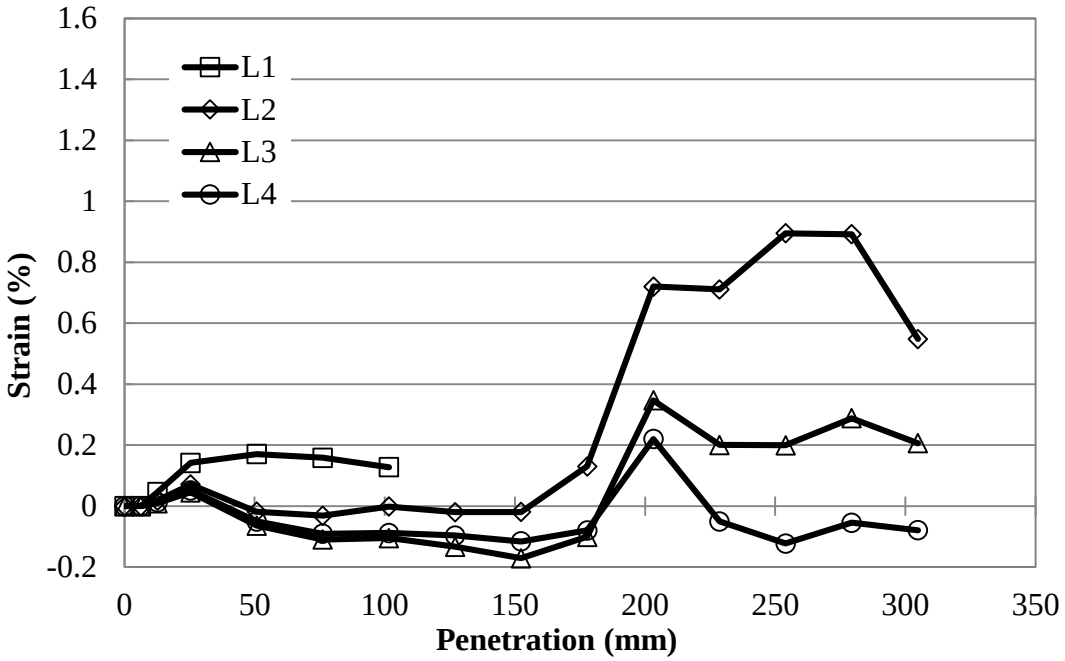

Figure 6.45 Cross-machine Geogrid Strains in the Inverted U-Shape Layer (Test 14)

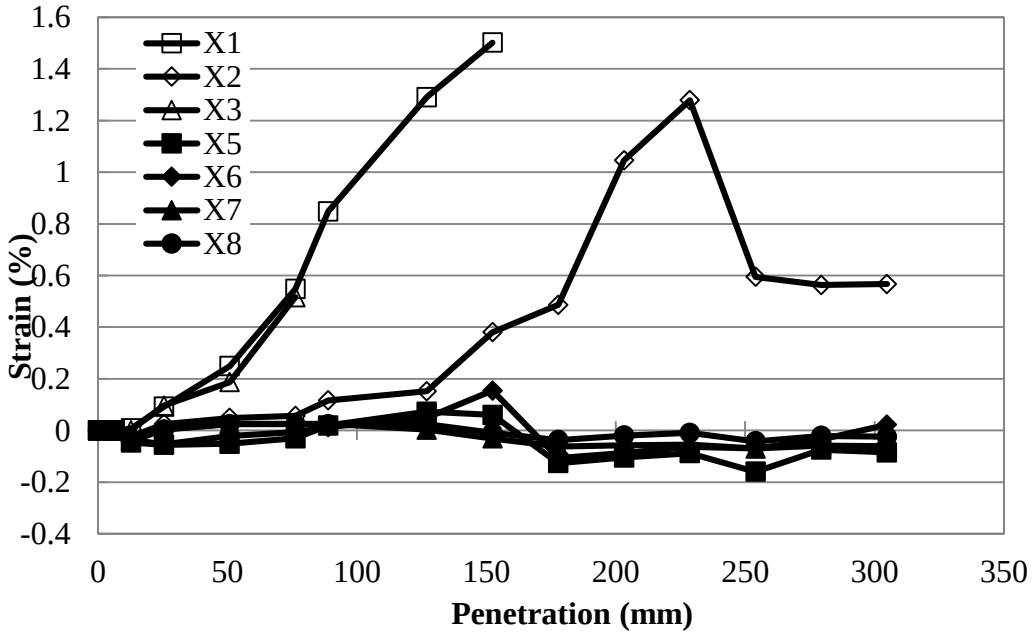

Figure 6.46 Machine Direction Geogrid Strains in the Wrapped-around Layer (Test 15)

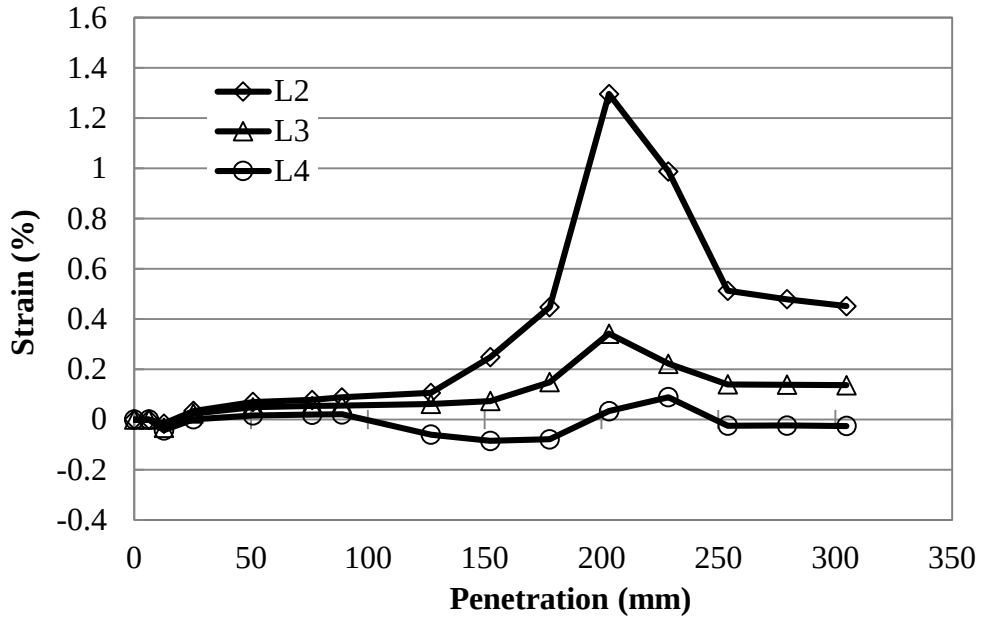

Figure 6.47 Cross-machine Direction Geogrid Strains in the Wrapped-around layer (Test 15)

Chapter 7 Conclusions and Recommendations

7.1 Summary

Seven static plate load tests, three cyclic plate load tests, and five rod penetration tests were run on shallowly-buried steel-reinforced HDPE pipes in the geotechnical box at the University of Kansas. Of the fifteen tests, five tests were run without geosynthetic as control sections for comparison to the geogrid-reinforced sections. Two backfill materials were used, which included a compacted sand backfill and a poured aggregate backfill. For all tests the in-situ soil was a fat clay. The objective of this research was to evaluate the benefits of geogrid to the protection of shallowly-buried pipes under surface loading and construction penetration and possible locations and layouts of the geogrid for its effectiveness. Through these tests, the following conclusions and recommendations can be made.

7.2 Conclusions

The following conclusions can be made after analyzing the results of these 15 large box tests.

1. The effectiveness of the geosynthetic was influenced by the stiffness of the backfill. The poured aggregate backfill, was considerably less stiff than the compacted sand backfill, which resulted in more improvement with the inclusion of the geosynthetic.
2. Under static and cyclic plate loading tests, the geogrid placed above the pipe inside the trench was not effective due to limited width and great depth. The geogrid placed underneath the base course was very effective in reducing the settlement of the plate, the vertical and horizontal deflections of the pipe, and the vertical earth pressures at the pipe crown and invert. The inclusion of geogrid improved the distribution of earth

pressures around the pipe and resulted in more uniform deformation of the pipe. The upper geogrid minimized the bending of steel ribs at pipe crown.

3. Under static and cyclic plate loading tests and rod penetration tests, the geogrid provided lateral restraint to soil particle movement and reduced the strain in the pipe liner in the longitudinal direction. The maximum tension developed under the center of the loading plate or the penetrating rod and decreased with the distance. Beyond the certain distance, the geogrid became compression. This benefit in reducing the longitudinal strain in the pipe liner is significant for the improvement of pipe performance and life.
4. Geogrid reinforcement above the pipe increased the rod penetration resistance at the constant penetration depth. In other words, more force was required to penetrate into the test section with geogrid reinforcement than that without geogrid. The inverted U-shape geogrid and wrapped-around geogrid layouts were more effective than the single and double geogrid layouts. The tensioned membrane effect played an important role in increasing the rod penetration resistance.

7.3 Recommendations for Future Research

The following recommendations can be made for future research on the protection of shallowly-buried pipes with Geosynthetics subjected to surface loading.

1. In this study, only one type and one size of pipe of one stiffness value was used. Size and stiffness of the pipe including the bending stiffness, hoop stiffness, and the long-term stiffness (especially for HDPE pipes due to creep deformation) may affect the effectiveness of the geosynthetic in protecting the pipe. Therefore, alternate pipe types with varying stiffness should be included in future research.

2. In this study, only one type of biaxial geogrid was used. Other types of geosynthetics, such as woven geotextiles, uniaxial geogrids, and triaxial geogrids, may be investigated.
3. Each full-scale test requires a significant amount of time and effort. It is recommended that the test data documented in this report or similar reports be used in numerical analyses for a future study to supplement physical testing.
4. Geogrid reinforcement appears to be an excellent way to reduce longitudinal tensile strains in the pipe wall. How this benefit may affect fatigue life of pipes in the longitudinal direction should be investigated.
5. Design methods should be developed to quantify the benefits of geosynthetics in protecting shallowly-buried pipes subjected to surface loading.

References

Bauer, G.E. (1994). “The control of settlement using geogrids.” *Vertical and Horizontal Deformations of Foundations and Embankments, Geotechnical Special Publication No. 40 Vol.1*, Albert T. Yeung and Guy Y. Félio (eds.), ASCE, New York, NY, 491-501.

Bathhurst, R.J., Knight, M.A. (1998). “Analysis of geo-cell reinforced-soil covers over large span conduits.” *Computers and Geotechnics*, 3 (22), 205-219.

Bueno, B. S., Viana, P. M. F., and Zornberg, J. G. (2005) "A novel construction method for buried pipes using geosynthetics." *Proc., Geo-Frontiers 2005*, ASCE, Austin, TX, 4155-4161.

Jeyapalan, J. K. (1983). "Geofabric stabilization of soft backfill materials for plastic sewer pipe installation." *Proc., Pipelines in Adverse Environments II*, ASCE, New York, NY, 188-198.

Kawabata, T., Uchida, K., Hirai, T., Mohri, Y., Ling, H. I., and Koyama, N. (2003) "Experiments on buried pipe using backfill of cover with geosynthetics." *Proc., Proceedings of the ASCE International Conference on Pipeline Engineering and Construction*, ASCE, Baltimore, MD, 1271-1278.

Kazemian, S., Barghchi, M., Prasad, A., Maydi, H., and Huat, B.K. (2010). "Reinforced pavement above trench under urban traffic load: Case study and finite element (FE) analysis." *Scientific Research and Essays*, 5(21), 3313-3329.

Kansas Department of Transportation (2012). *State Transportation Improvement Program Fiscal Year 2013-2016*, Kansas Department of Transportation, Topeka, KS.

Kennedy, J.B., Laba, J.T., and Shaheen H. (1988). “Reinforced Soil-Metal Structures.” *Journal of Structural Engineering*, 6 (114), 1372-1388.

Lundvall, J.F., and Turner, J.P. (1997). “Mitigation of roadway settlement above buried culverts and pipes” *Report FHWA/WY -97/01*, Wyoming Department of Transportation, Cheyenne WY.

Moghaddas Tafreshi, S. N. and Khalaj, O. (2008). "Laboratory tests of small-diameter HDPE pipes buried in reinforced sand under repeated-load." *Geotextiles and Geomembranes*, 26(2), 145-163.

Moghaddas Tafreshi, S. N. and Khalaj, O. (2010). "Analysis of repeated-load laboratory tests on buried plastic pipes in sand." *Soil Dynamics and Earthquake Engineering*, 31, 1-15.

Palmeira, E. M. and Andrade, H. K. P. A. (2010). "Protection of buried pipes against accidental damage using geosynthetics." *Geosynthetics International*, 17(4), 228-241.

Pearson, A. E. and Milligan, G.W.E. (1991). "Model tests of reinforced soil in conjunction with flexible culverts." *Proceedings of the International Reinforced Soil Conference*, Glasgow, Scotland, 365-365.

Rajkumar, R. and Ilamparuthi, K. (2008). "Experimental study on the behavior of buried flexible plastic pipe." *Electronic Journal of Geotechnical Engineering*, 13(C), 1-10.

Schaefer, V.R., Suleiman, M.T., White D.J., and Swan C. (2005). “Utility Cut Repair Techniques-Investigation of Improved Cut Repair Techniques to Reduce Settlement in Repaired Areas” *CTRE Project 03-158*, Center for Transportation Research and Education, Iowa State University, Ames Iowa

Appendix A - Measured Pipe Strains in Static Plate Load Tests

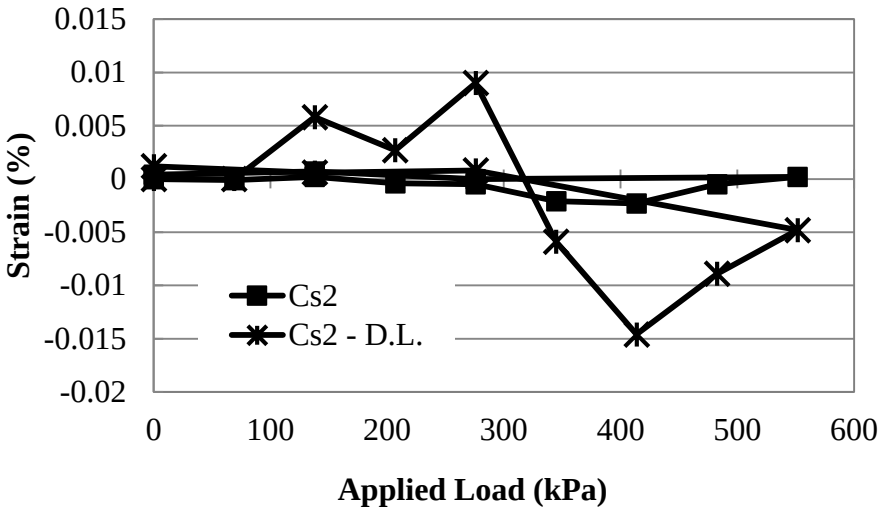

Figure A.1 Circumferential Strains at Spring Line C_{s2}

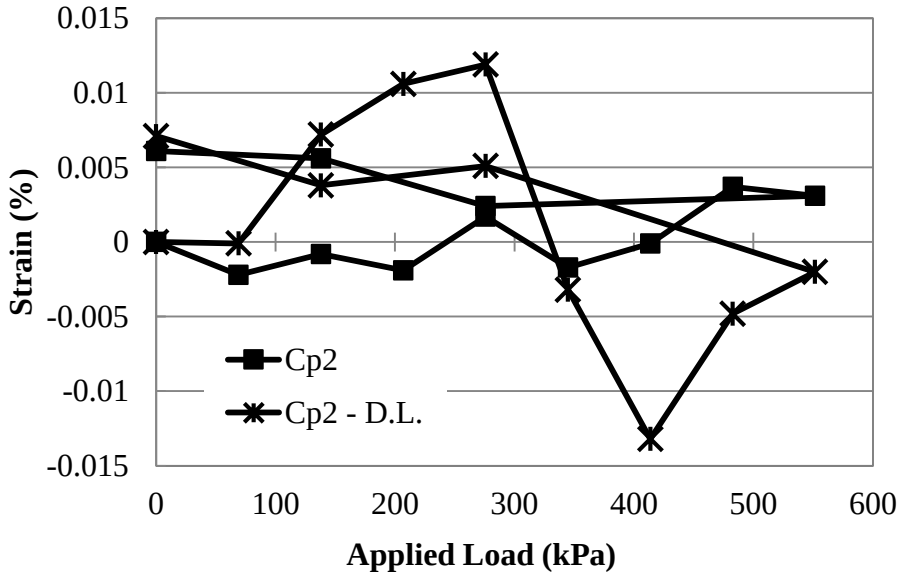

Figure A.2 Circumferential Strains at Spring Line C_{p2}

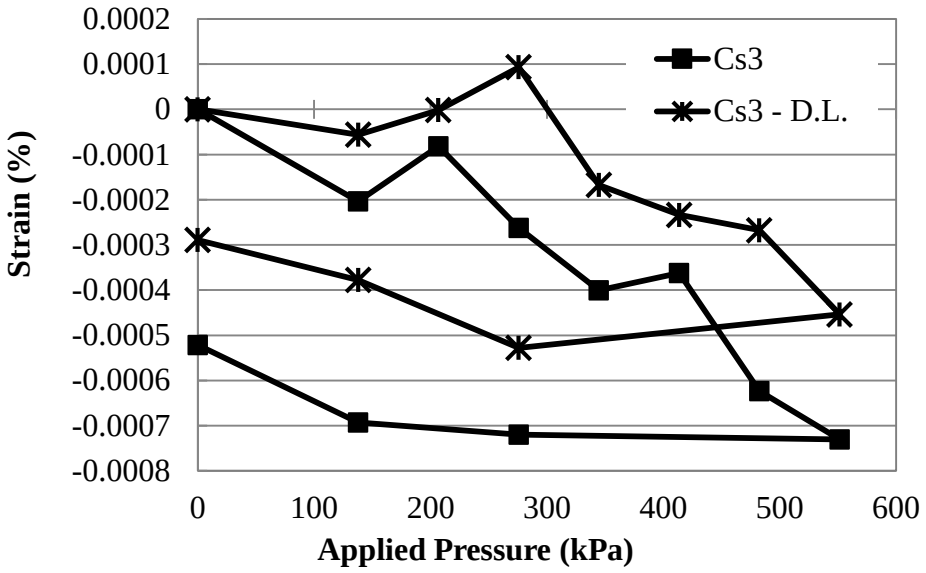

Figure A.3 Circumferential Strains at Spring Line C_{s3}

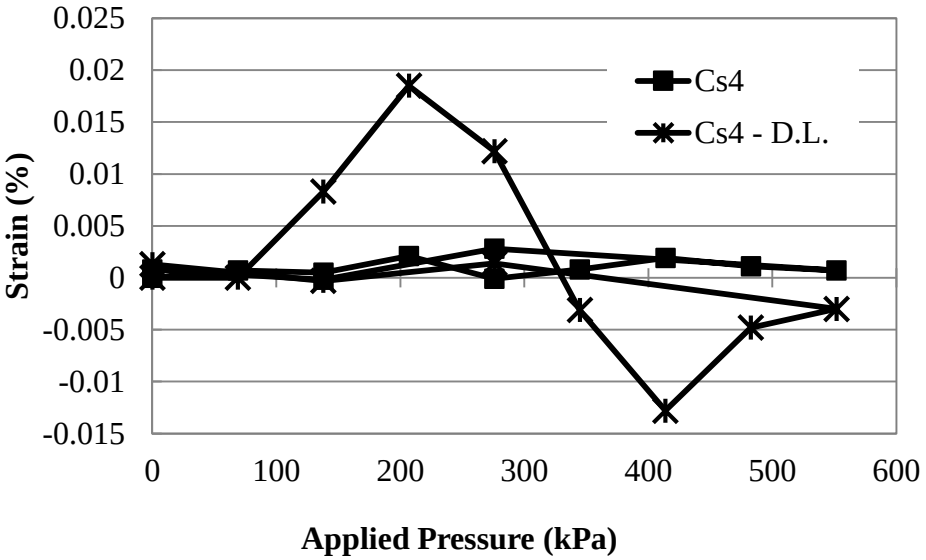

Figure A.4 Circumferential Strains at Invert C_{s4}

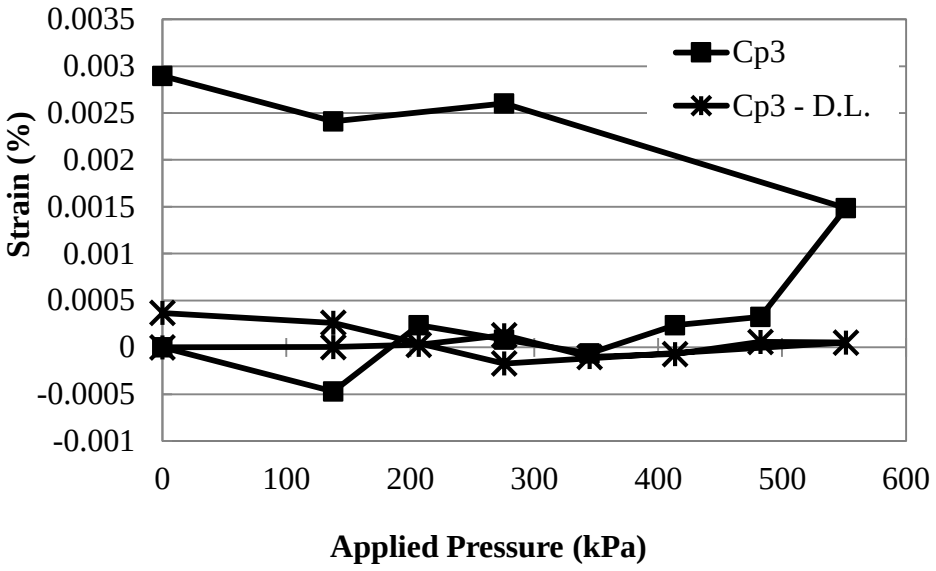

Figure A.5 Circumferential Strains at Invert C_{p3}

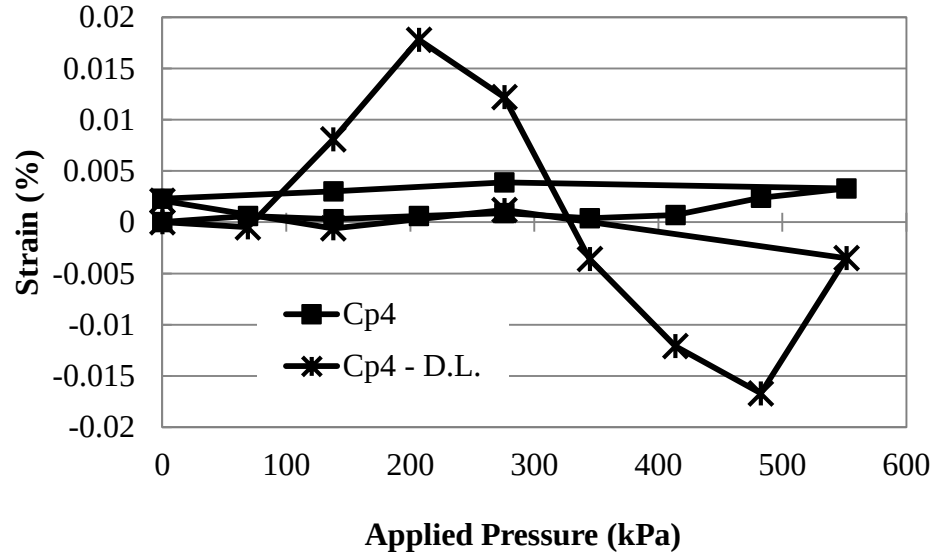

Figure A.6 Circumferential Strains at Invert C_{p4}

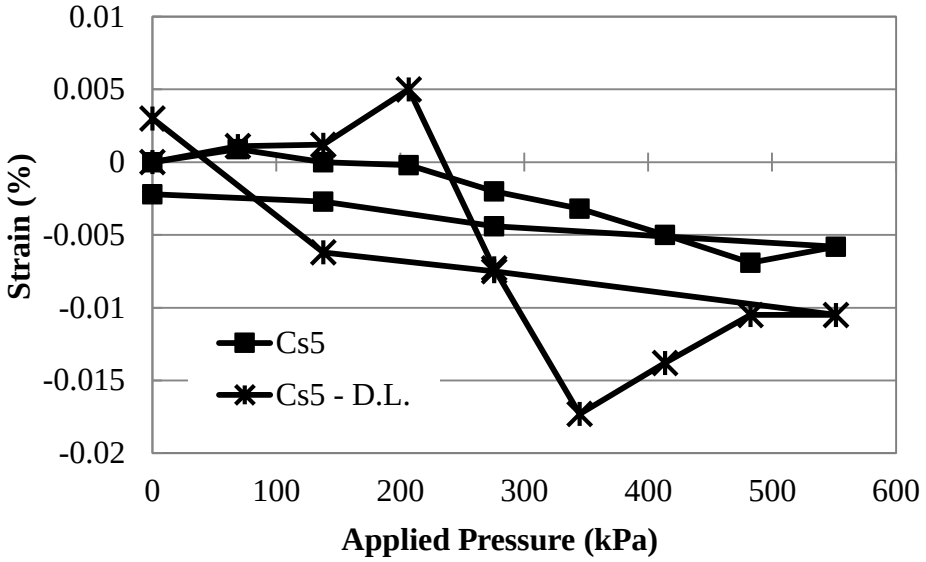

Figure A.7 Circumferential Strains at Crown C_{s5}

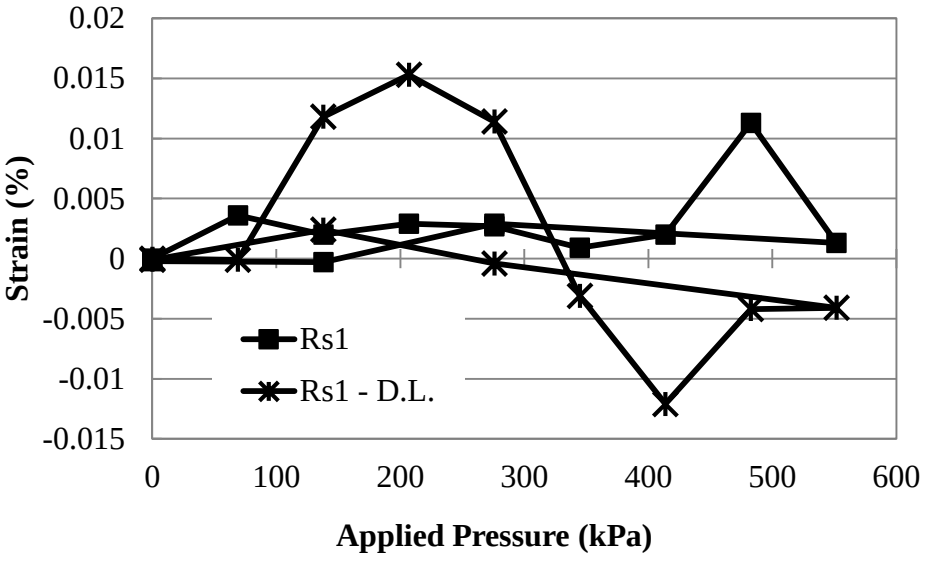

Figure A.8 Radial Strains at Spring Line R_{s1}

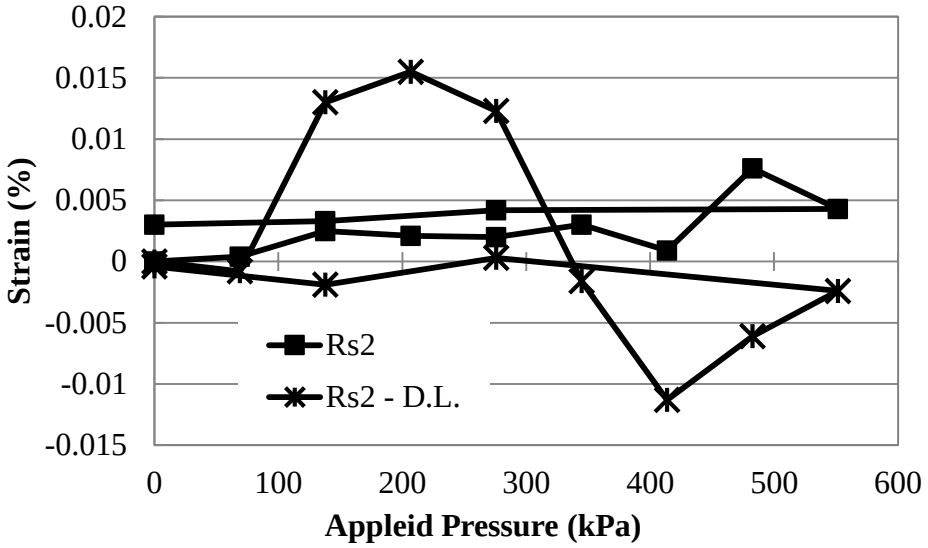

Figure A.9 Radial Strains at Spring Line R_{s2}

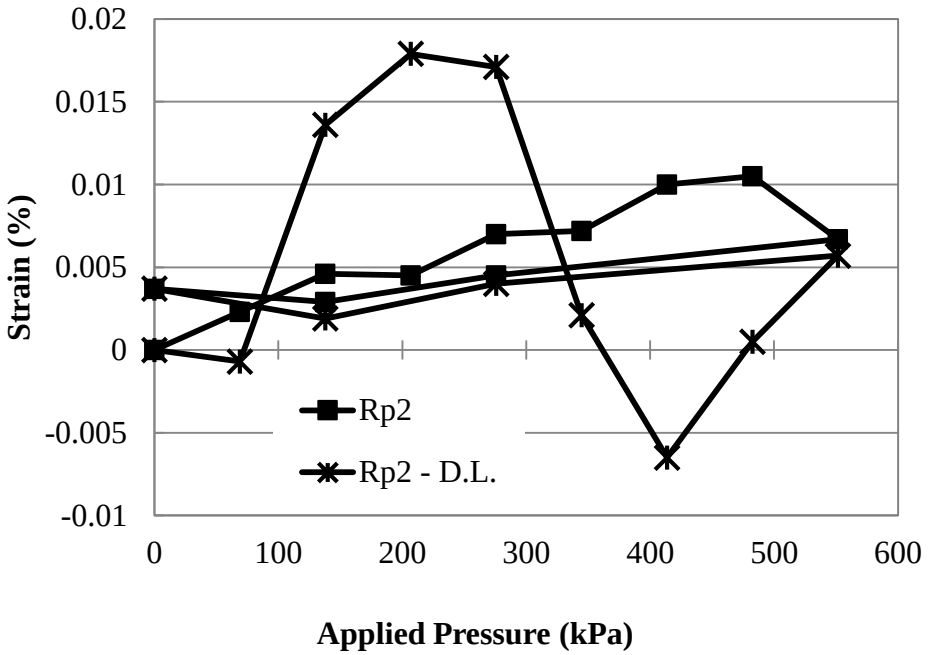

Figure A.10 Radial Strains at Spring Line R_{p2}

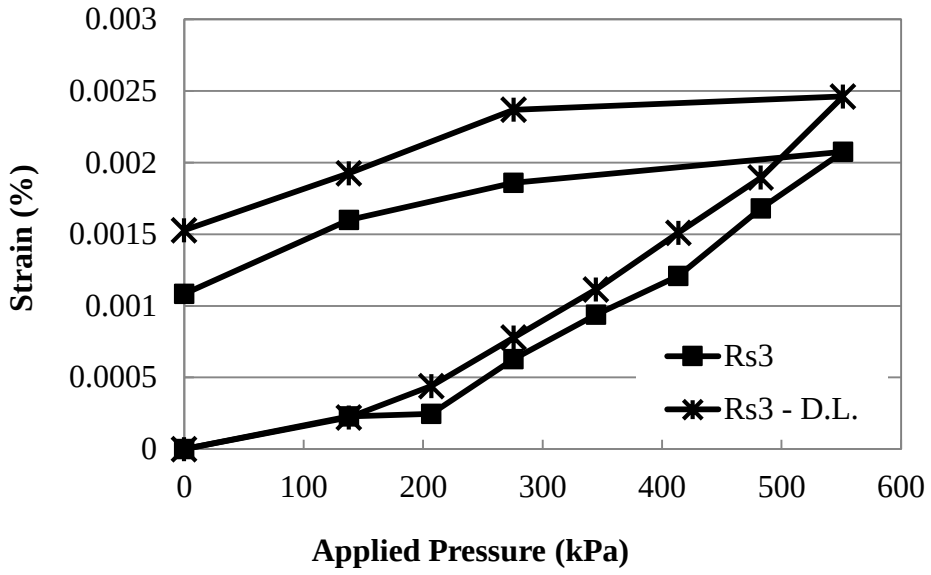

Figure A.11 Radial Strains at Crown R_{s3}

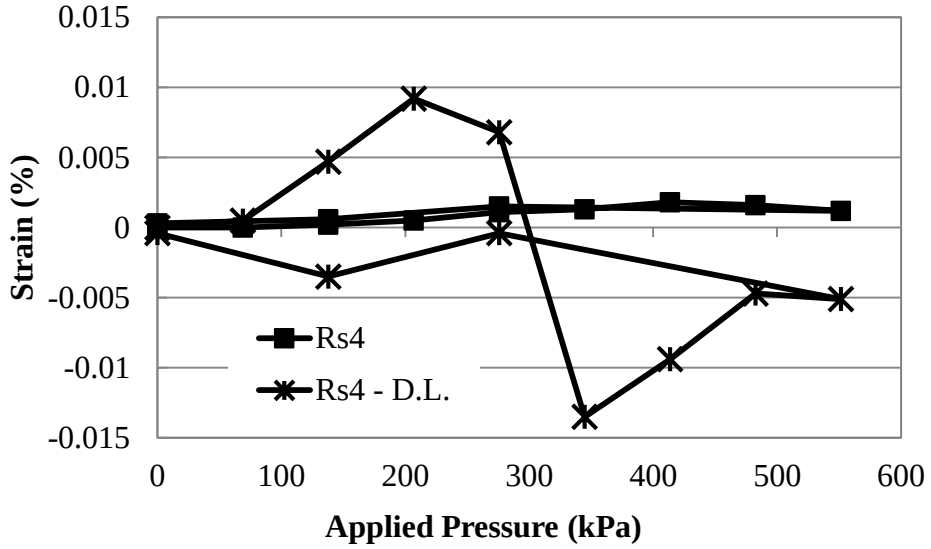

Figure A.12 Radial Strains at Crown R_{s4}

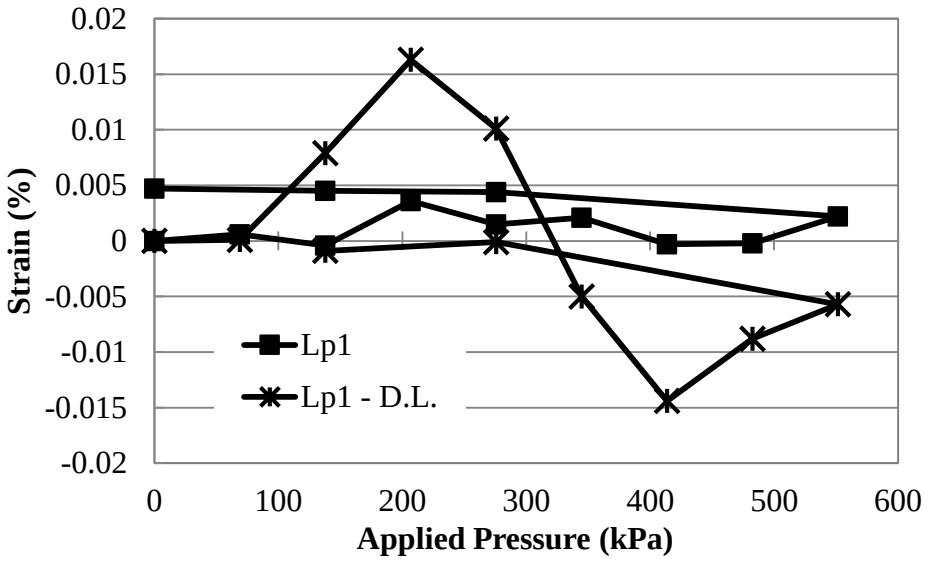

Figure A.13 Longitudinal Strain at Spring Line Lp_1

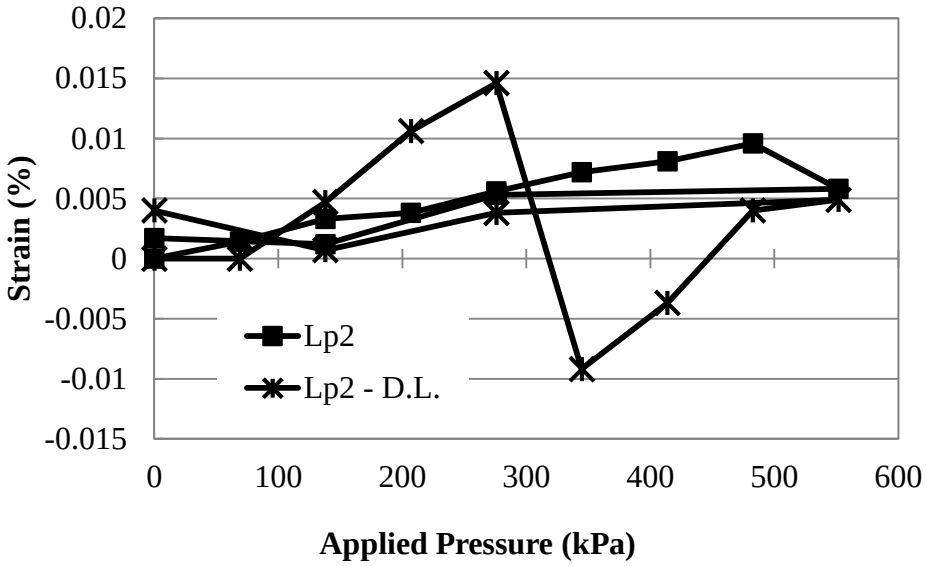

Figure A.14 Longitudinal Strain at Spring Line Lp_2

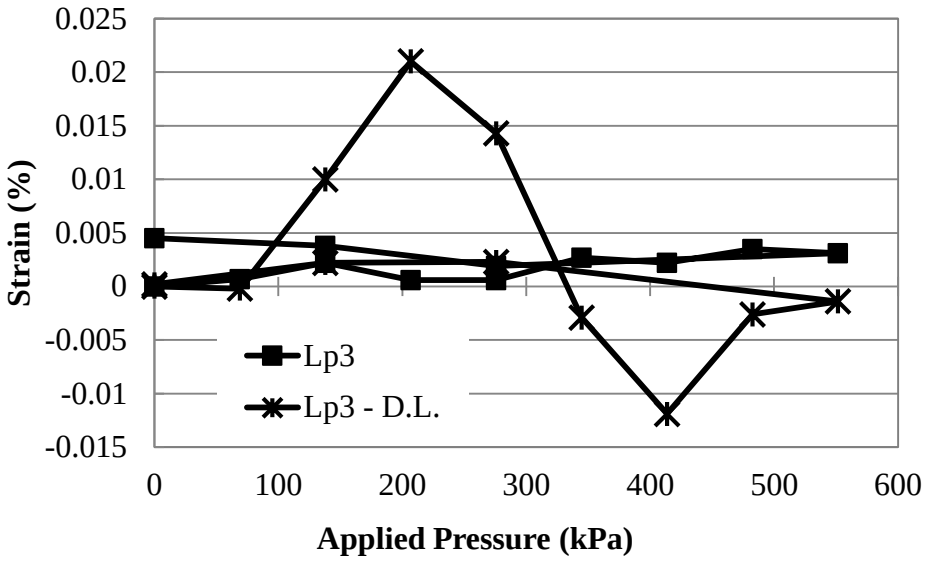

Figure A.15 Longitudinal Strain at Invert L_3

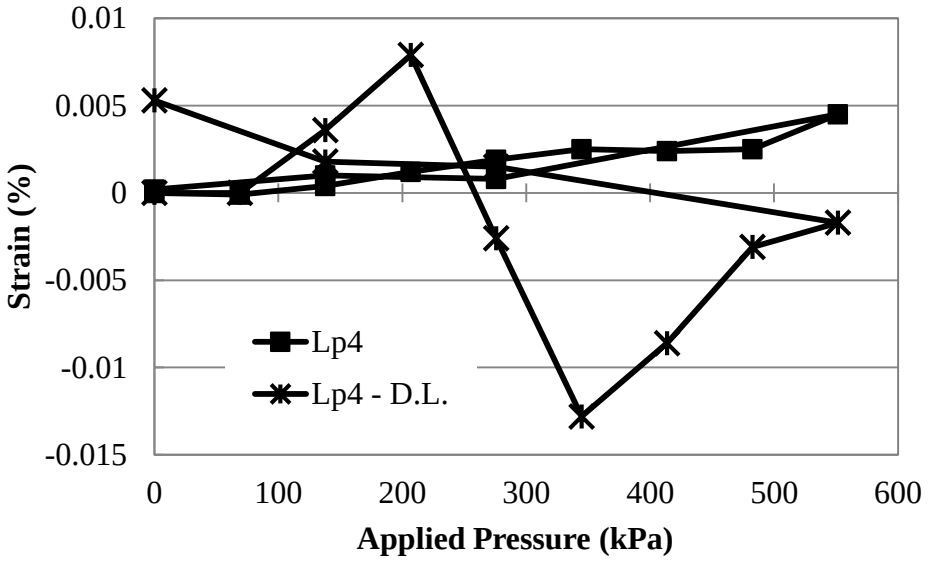

Figure A.16 Longitudinal Strain at Invert L_4

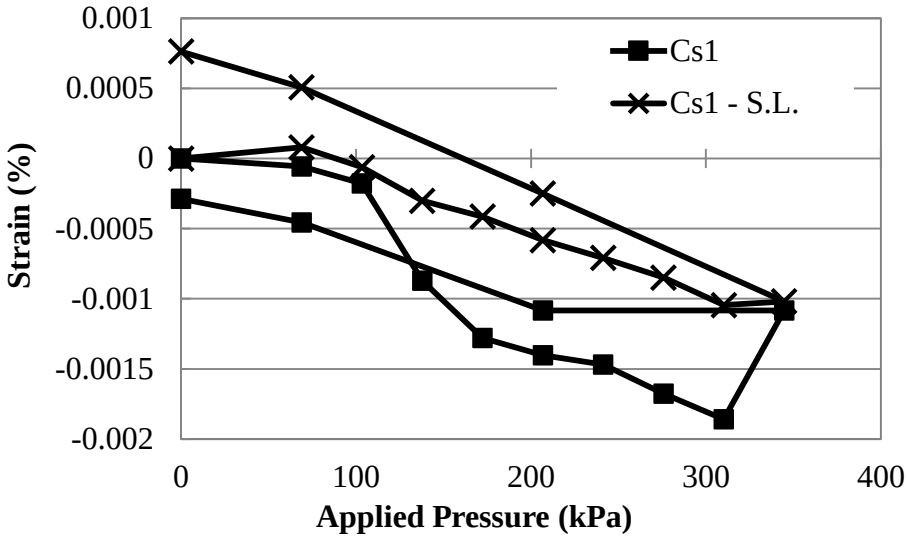

Figure A.17 Circumferential Strain at Spring Line C_{s1}

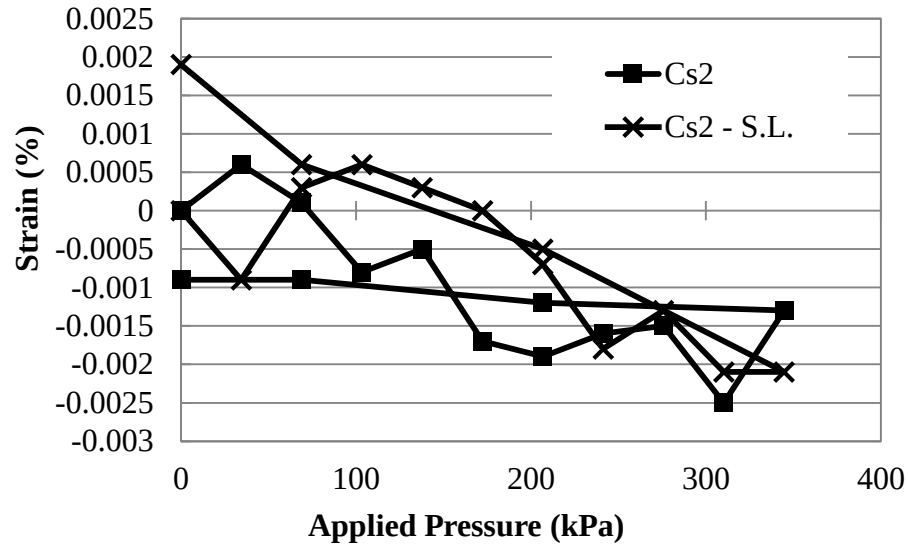

Figure A.18 Circumferential Strain at Spring Line C_{s2}

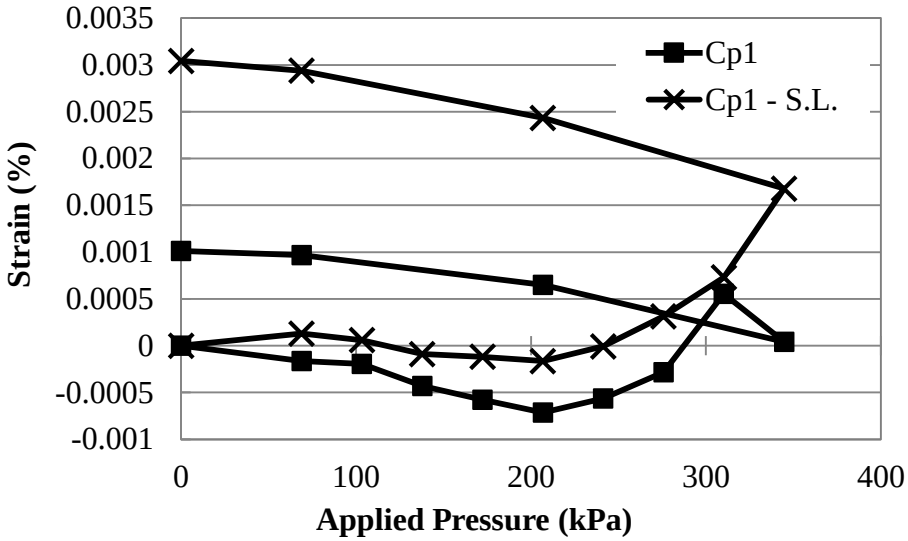

Figure A.19 Circumferential Strains at Spring Line C_{p1}

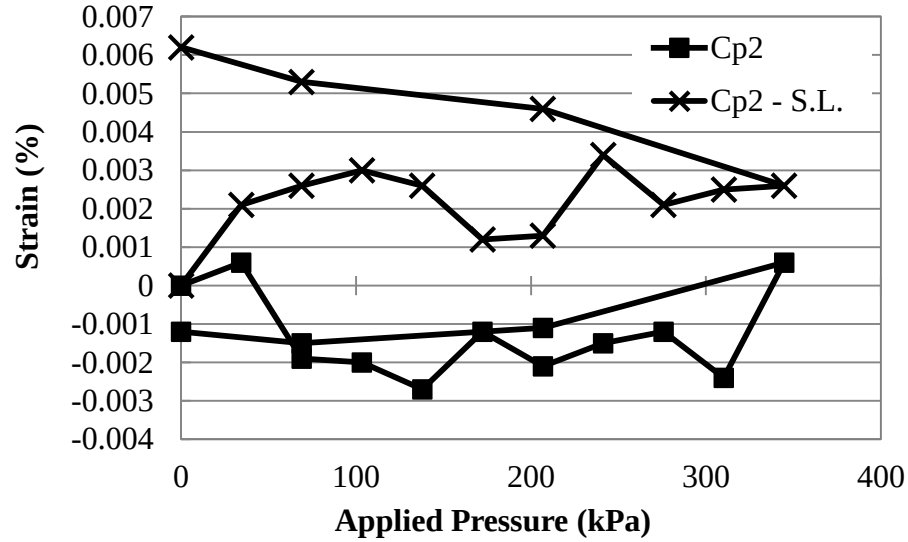

Figure A.20 Circumferential Strains at Spring Line C_{p2}

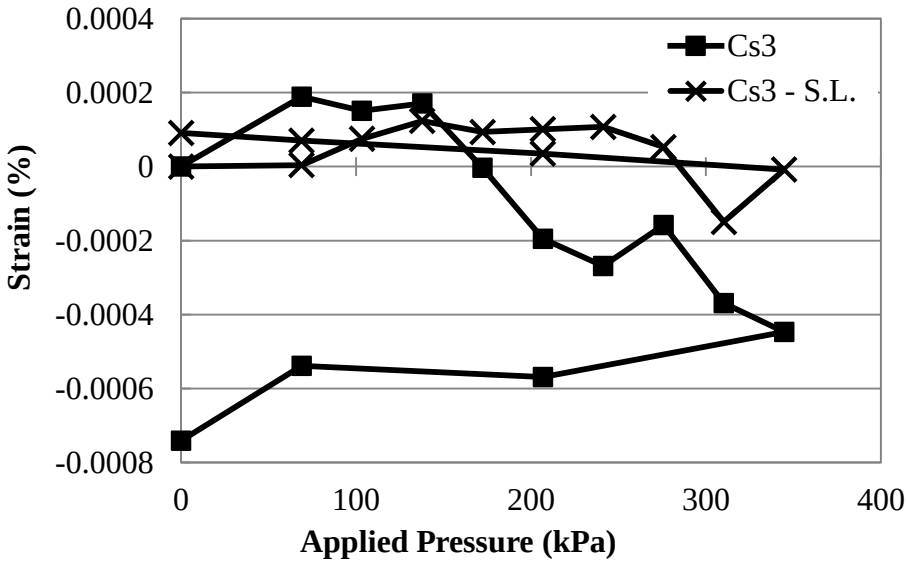

Figure A.21 Circumferential Strains at Spring Line C_{s3}

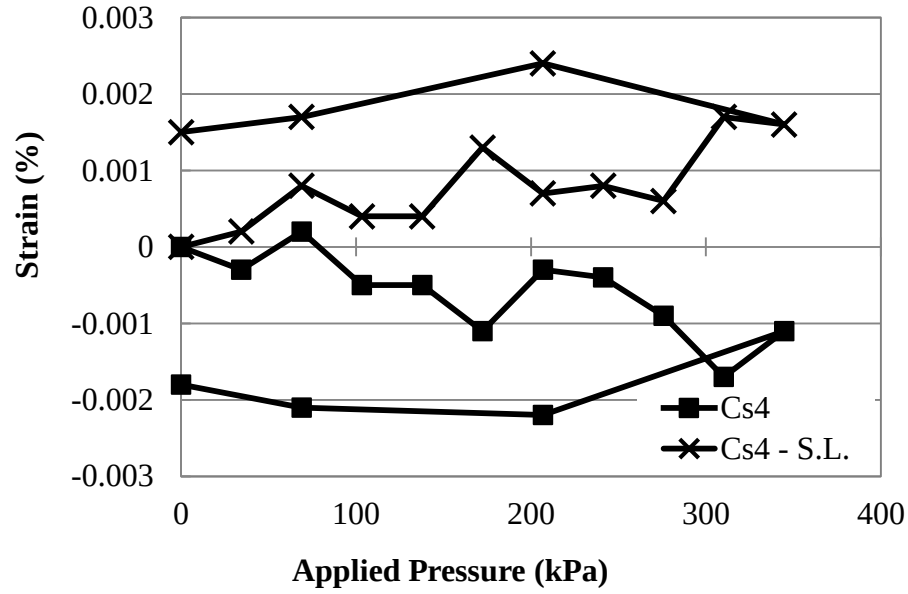

Figure A.22 Circumferential Strains at Invert C_{s4}

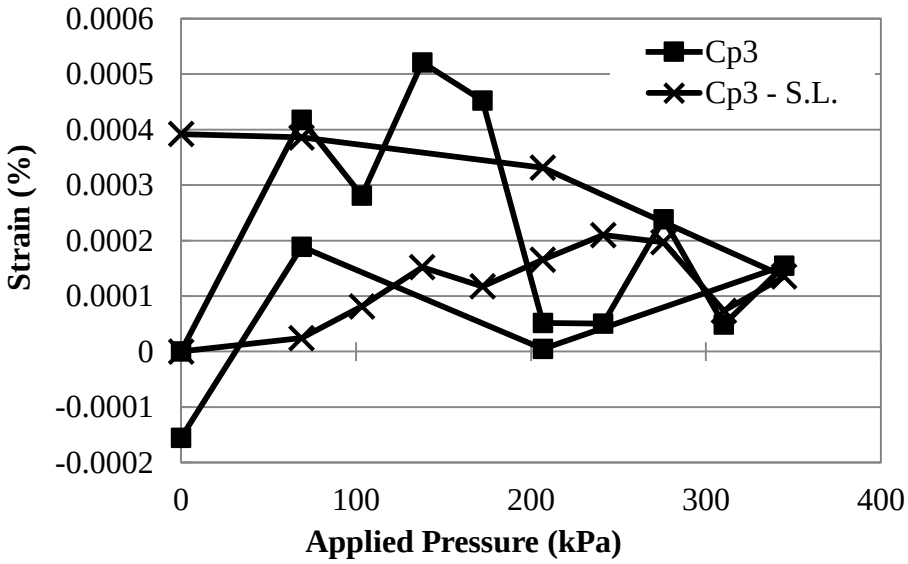

Figure A.23 Circumferential Strains at Invert C_{p3}

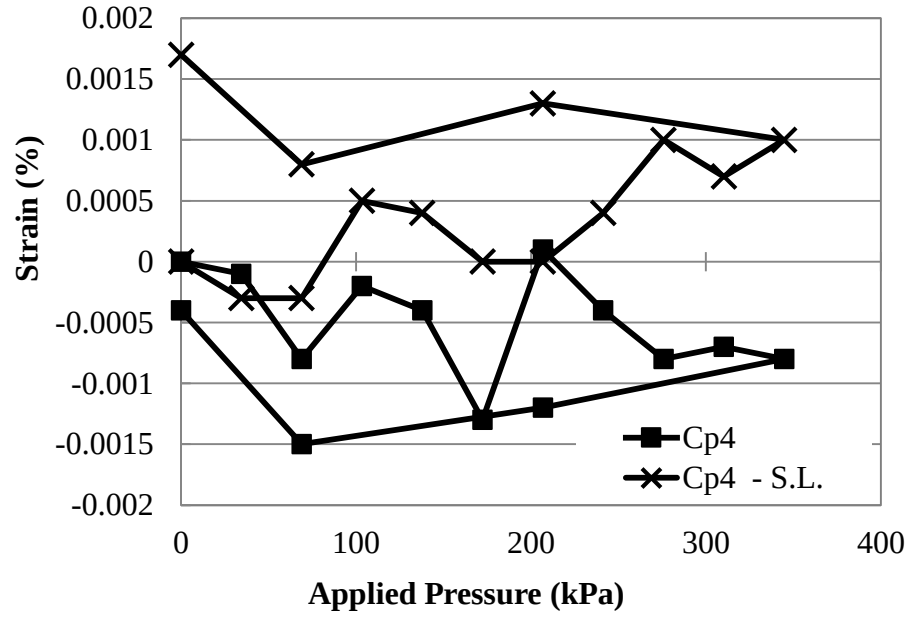

Figure A.24 Circumferential Strains at Invert C_{p4}

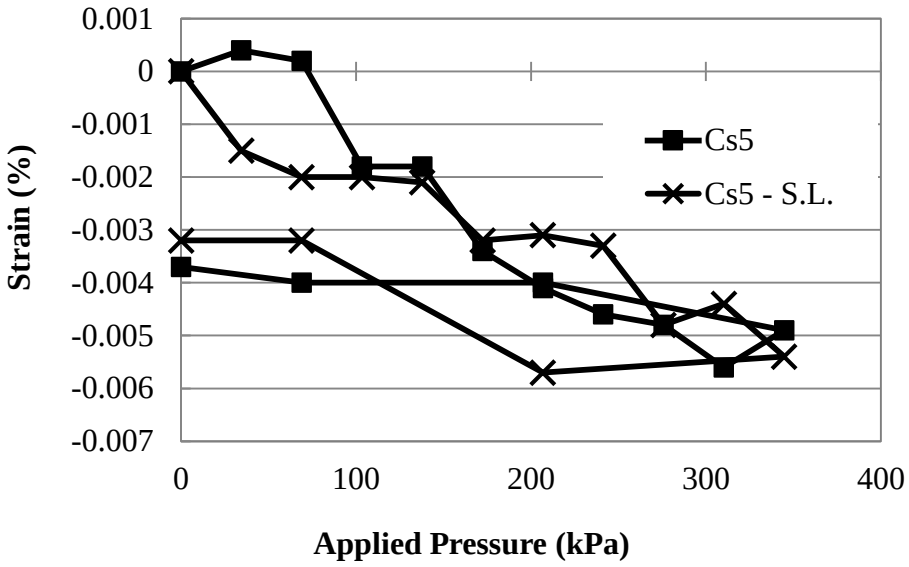

Figure A.25 Circumferential Strains at Crown C_{s5}

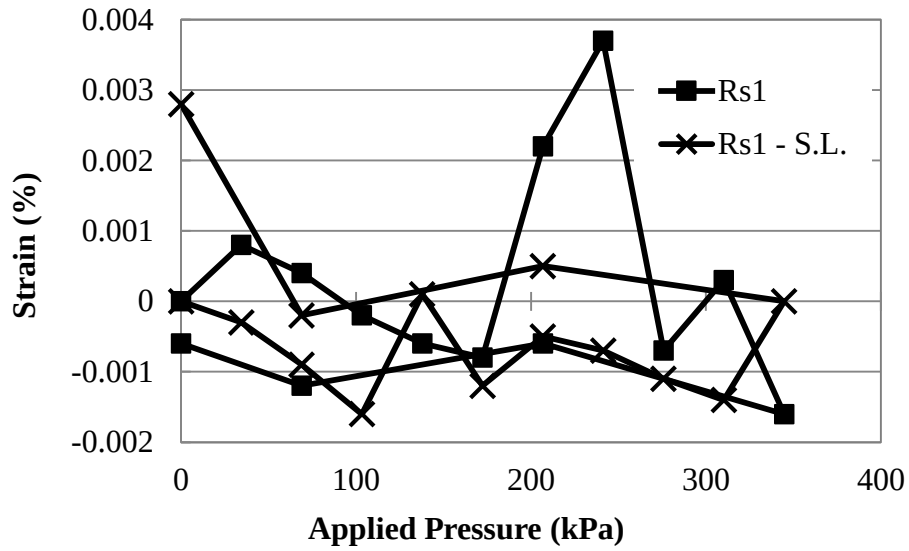

Figure A.26 Radial Strains at Spring Line R_{s1}

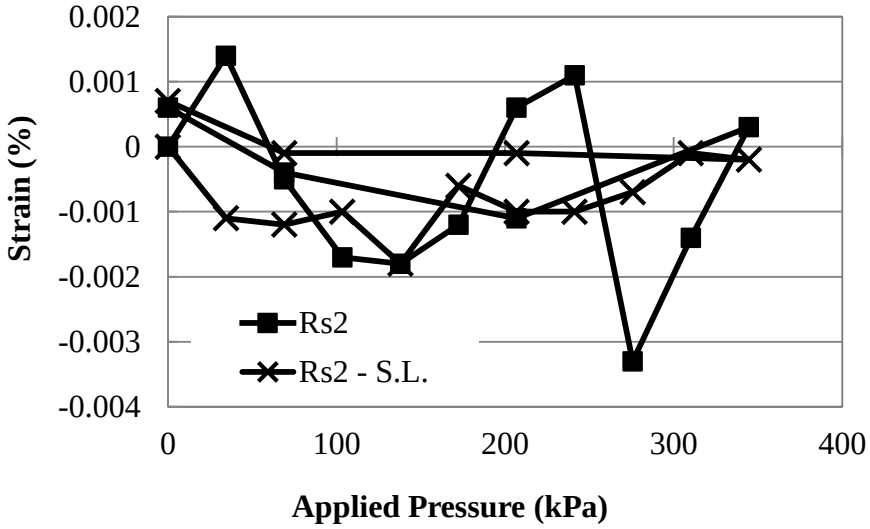

Figure A.27 Radial Strains at Spring Line R_{s1}

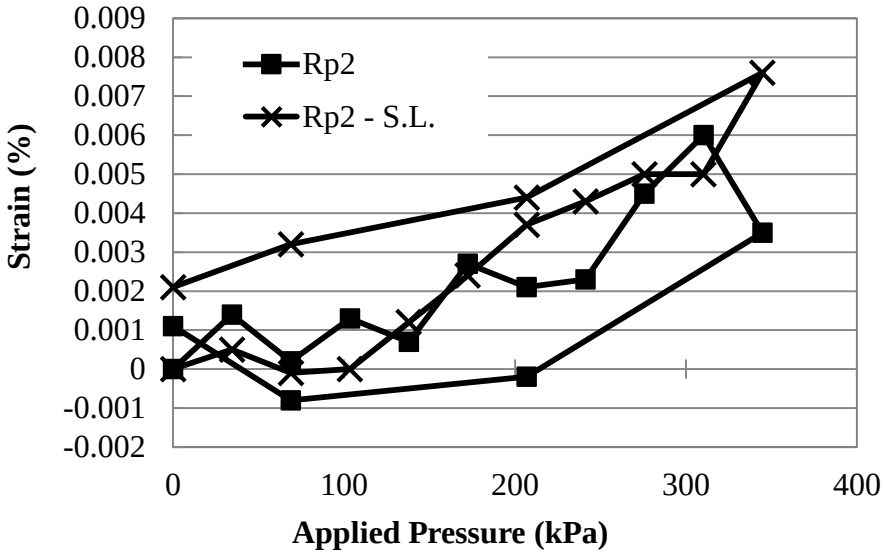

Figure A.28 Radial Strains at Spring Line R_{p2}

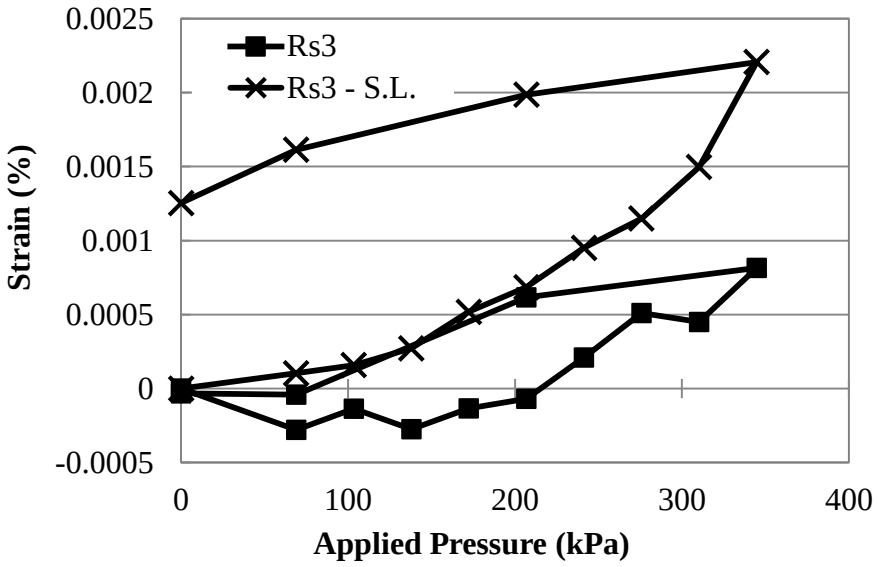

Figure A.29 Radial Strains at Invert R_{s3}

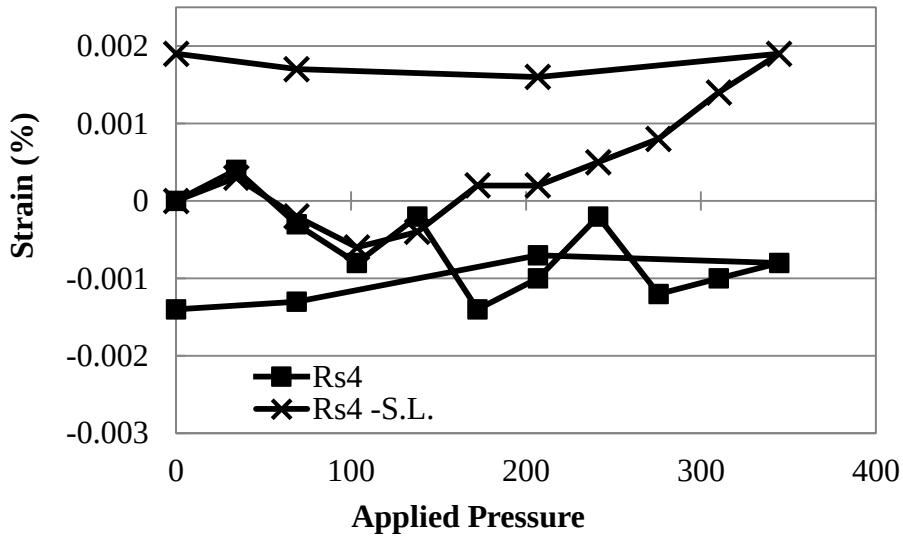

Figure A.30 Radial Strains at Crown – R_{s4}

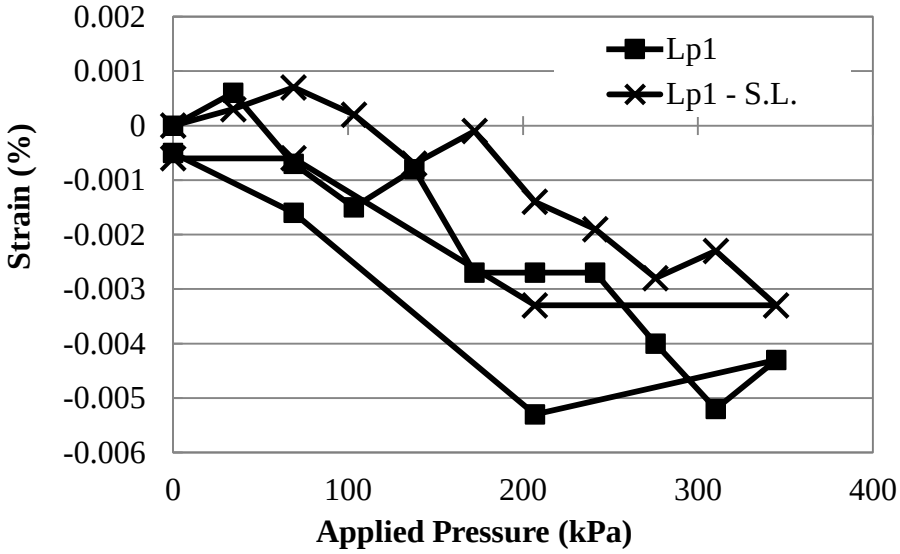

Figure A.31 Longitudinal Strains at Spring Line - L_{p1}

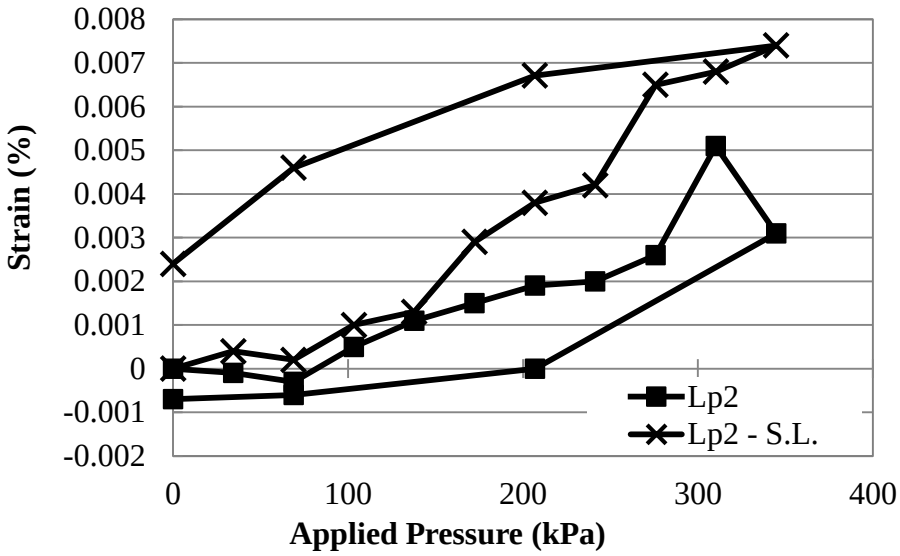

Figure A.32 Longitudinal Strains at Spring Line – L_{p2}

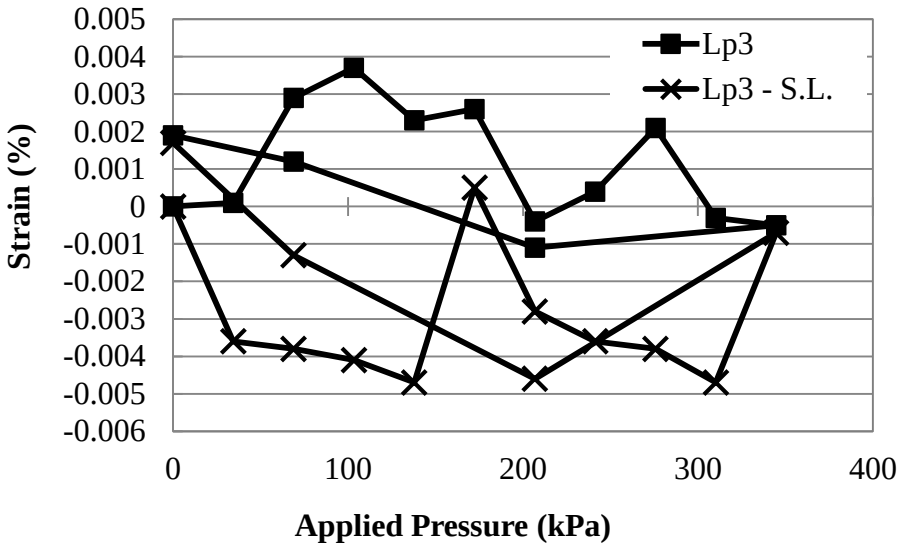

Figure A.33 Longitudinal Strains at Invert – L_{p3}

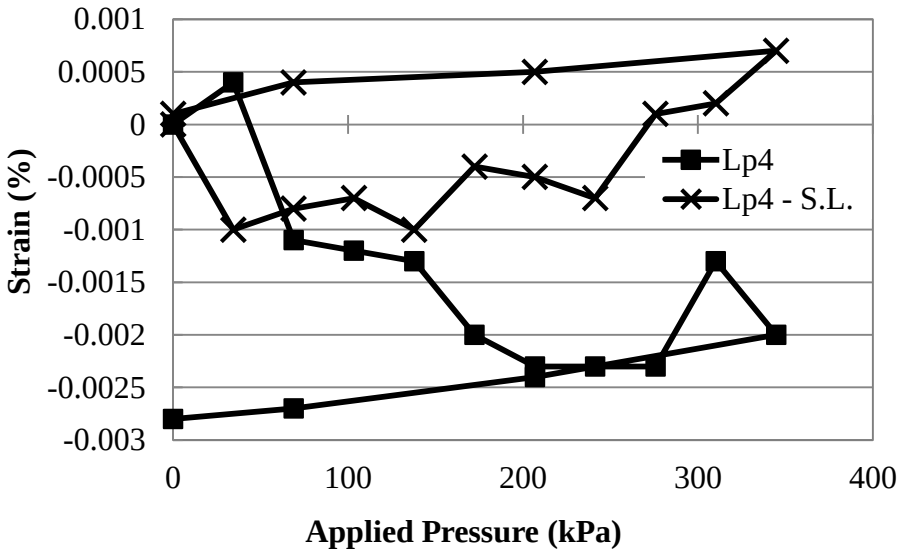

Figure A.34 Longitudinal Strains at Invert - L_{p4}

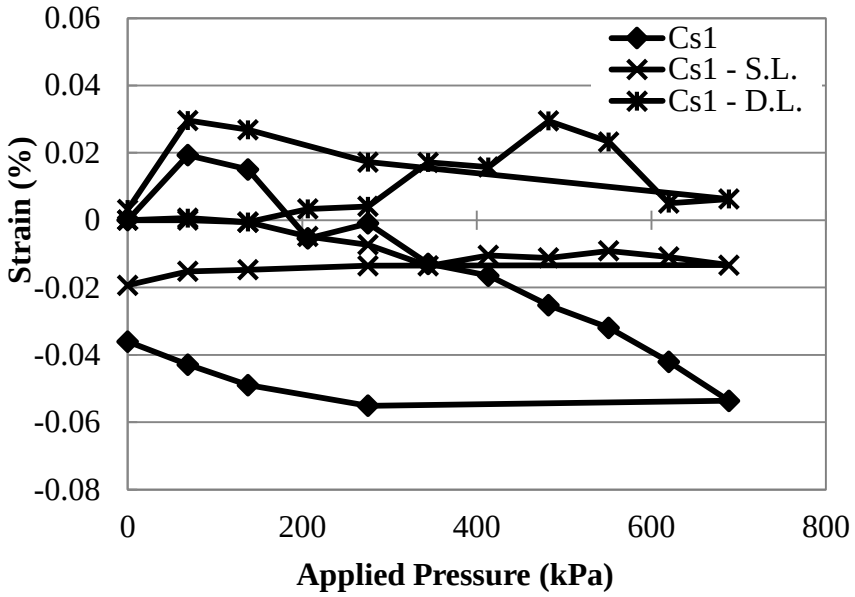

Figure A.35 Circumferential Strains at Spring Line – Steel C_{s1}

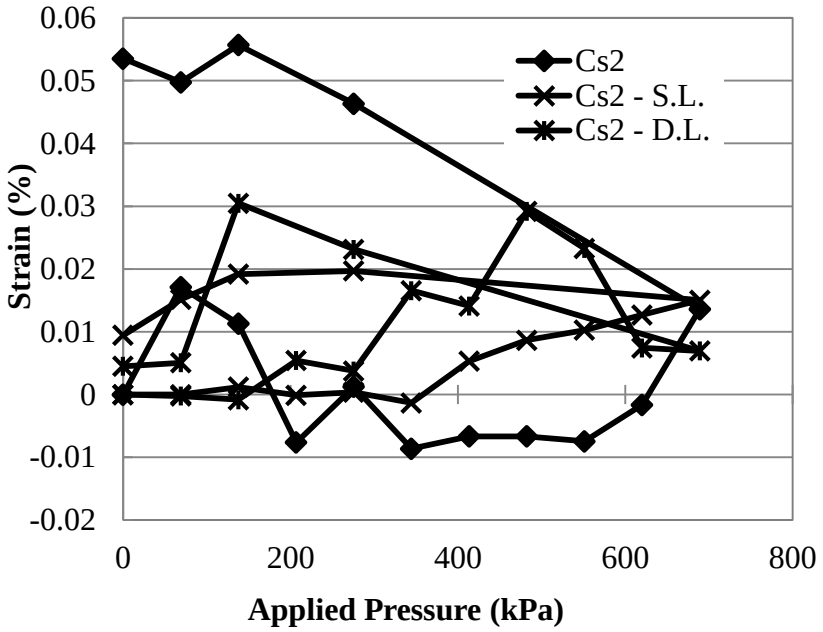

Figure A.36 Circumferential Strains at Spring Line – Steel C_{s2}

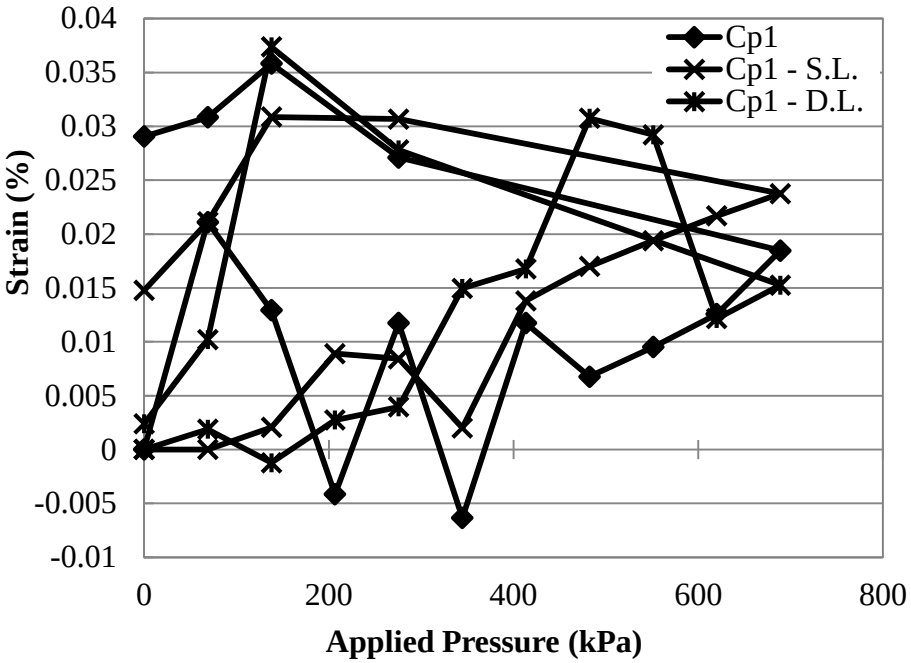

Figure A.37 Circumferential Strains at Spring Line – Plastic C_{p1}

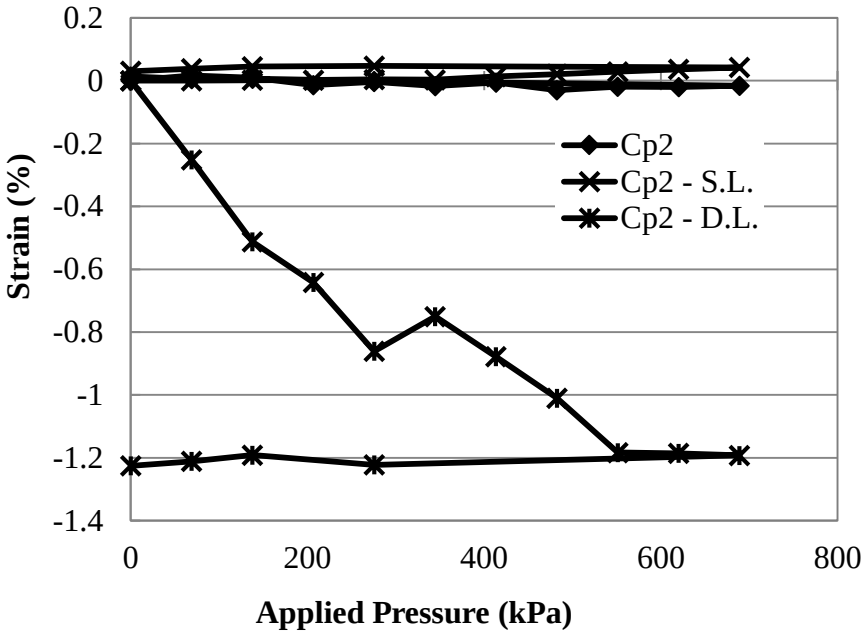

Figure A.38 Circumferential Strains at Spring Line – Plastic C_{p2}

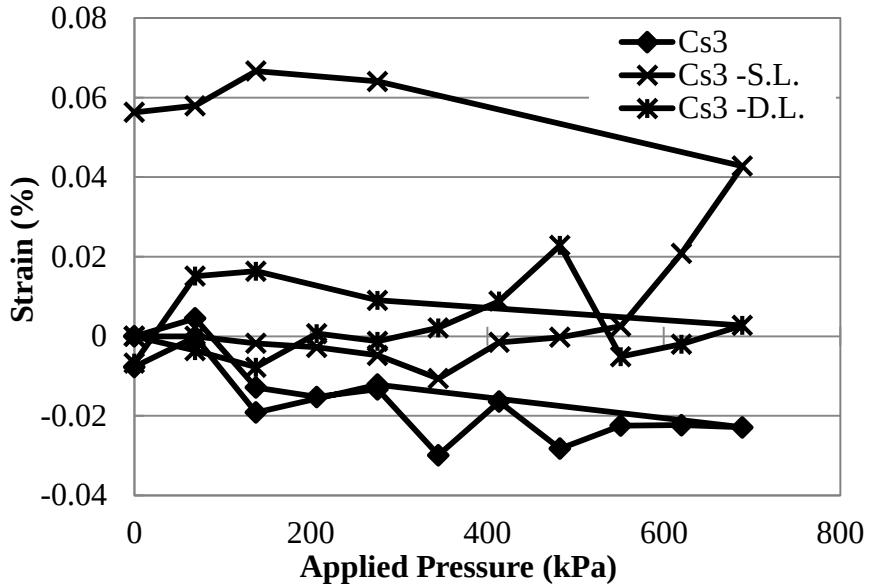

Figure A.39 Circumferential Strains – Steel C_{s3}

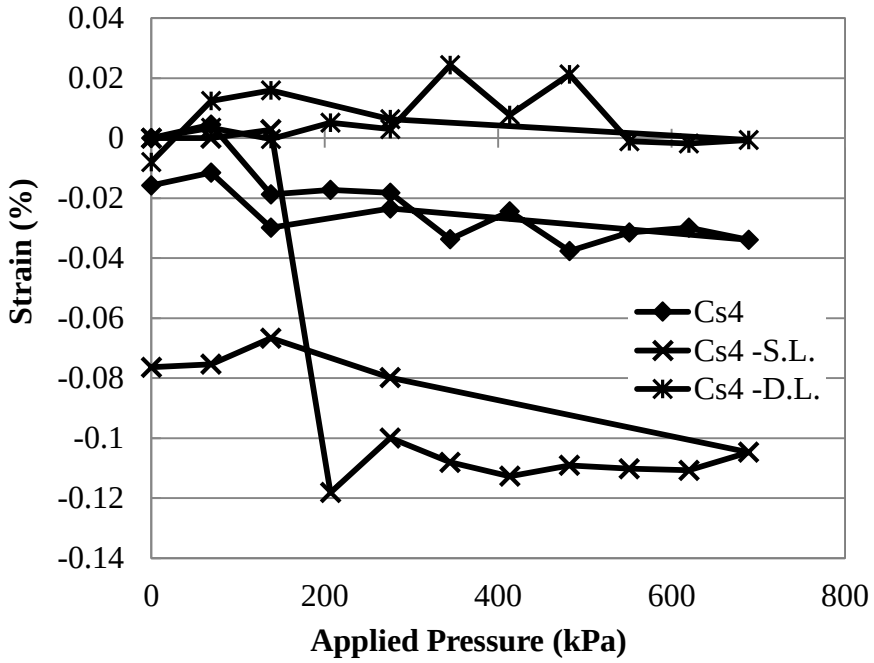

Figure A.40 Circumferential Strains – Steel C_{s4}

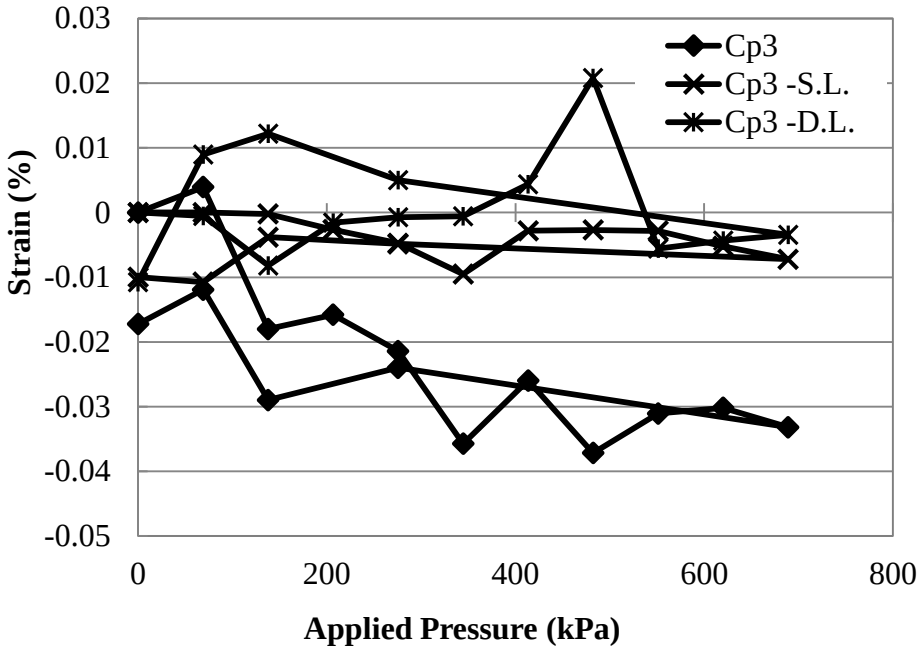

Figure A.41 Circumferential Strains – Plastic C_{p3}

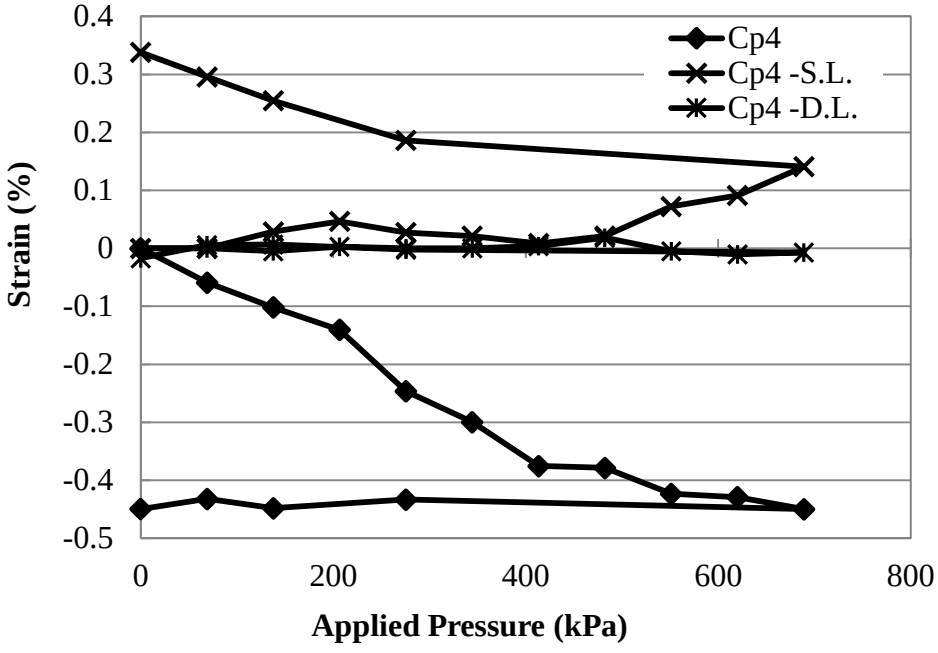

Figure A.42 Circumferential Strains – Plastic C_{p4}

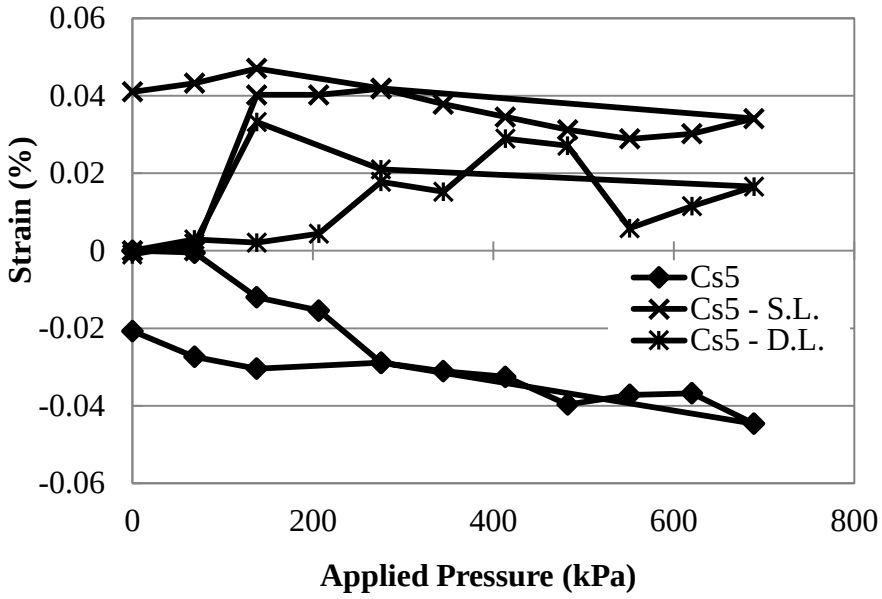

Figure A.43 Circumferential Strains – Steel C_{s5}

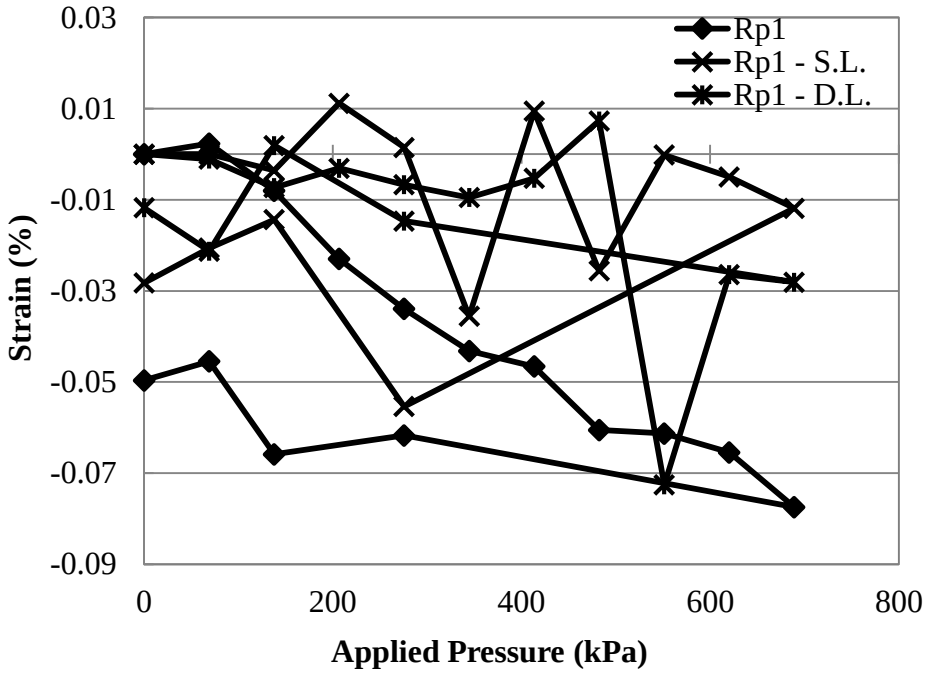

Figure A.44 Radial Strains – Plastic R_{p1}

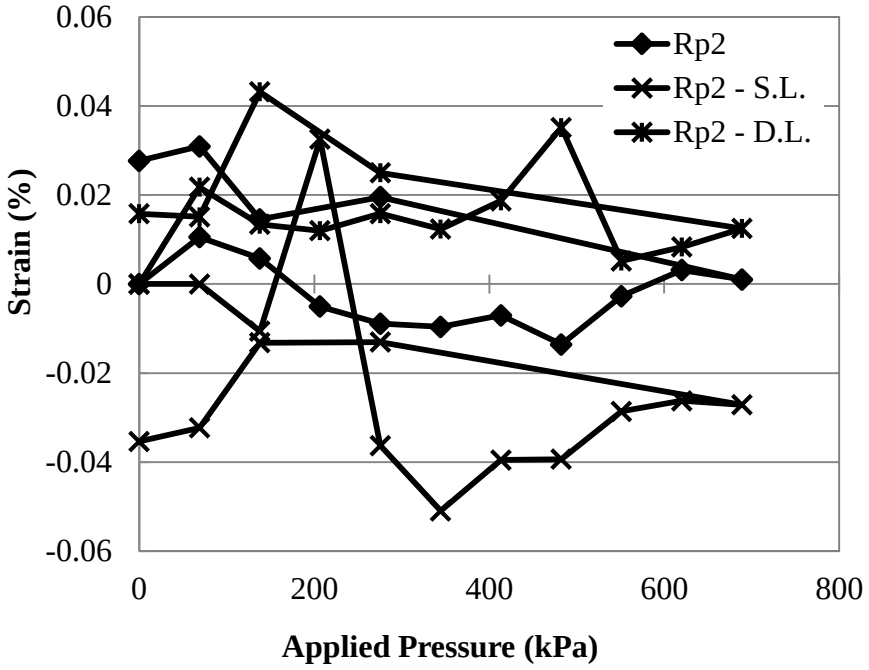

Figure A.45 Radial Strains – Plastic R_{p2}

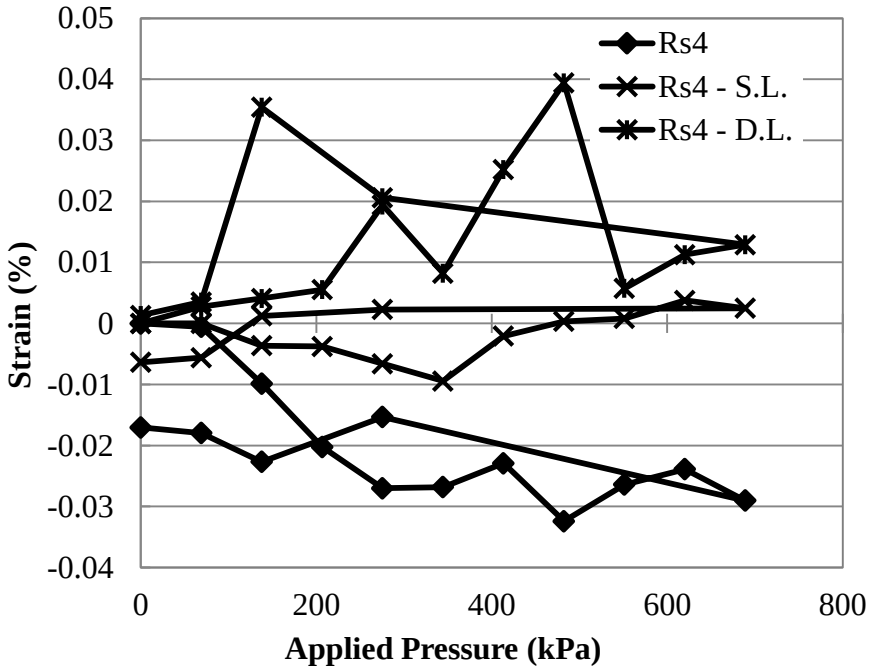

Figure A.46 Radial Strains – Steel R_{s4}

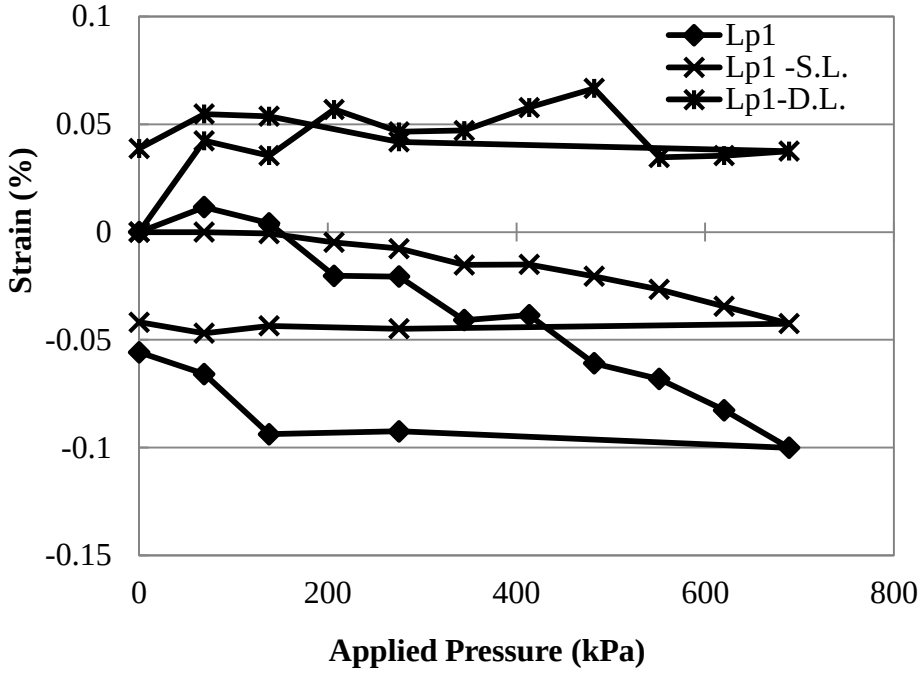

Figure A.47 Longitudinal Strains - Plastic L_{p1}

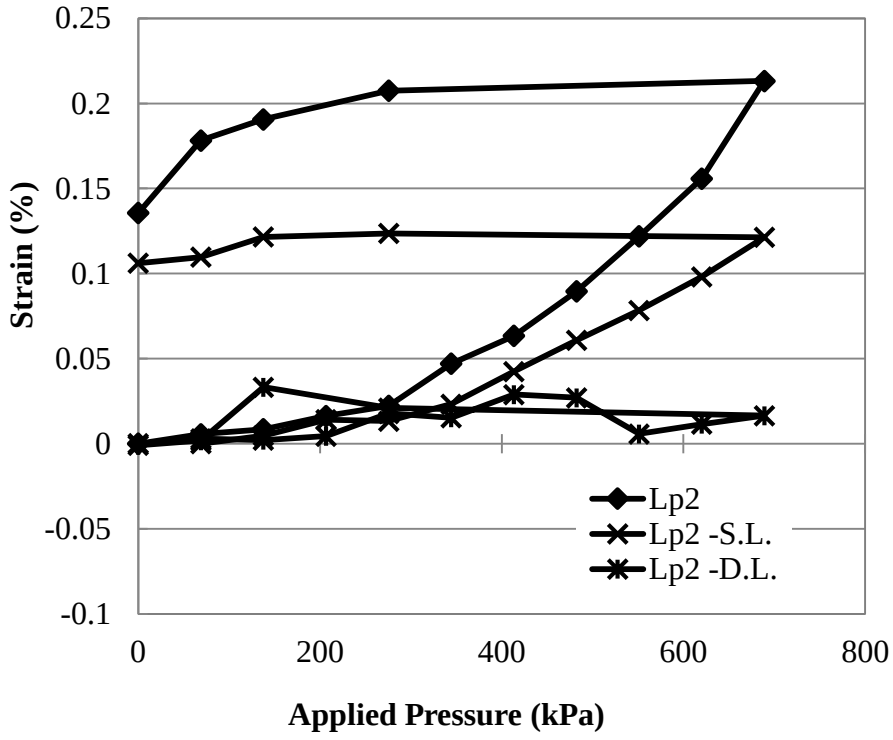

Figure A.48 Longitudinal Strains – Plastic L_{p2}

Appendix B – Measured Earth Pressures in Cyclic Plate Load Tests

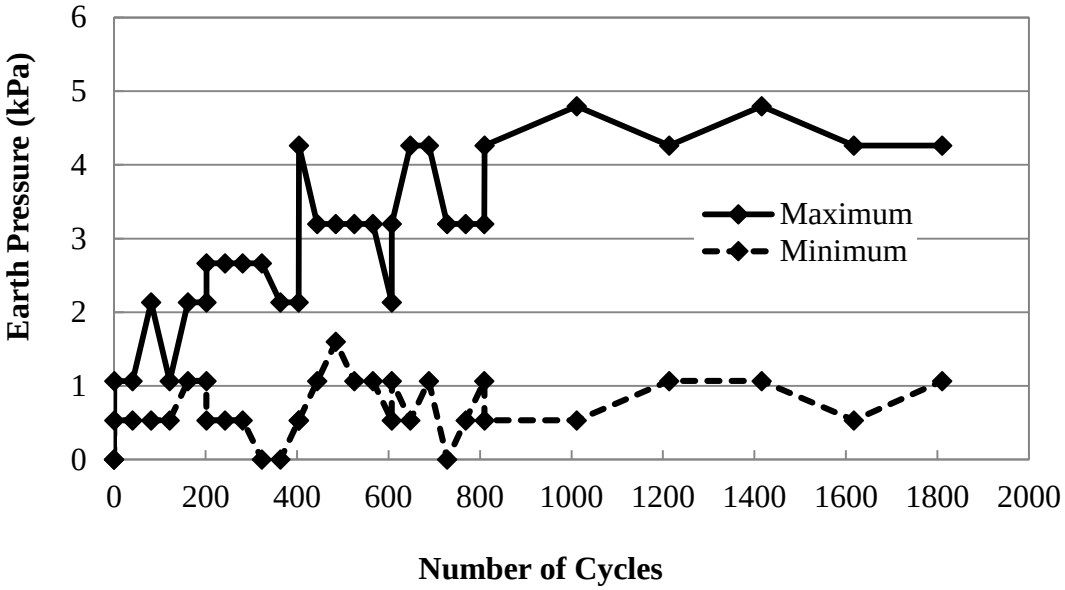

Figure B.1 Measured Horizontal Pressure at Spring Line (S_1) in the Unreinforced Section (Test 6)

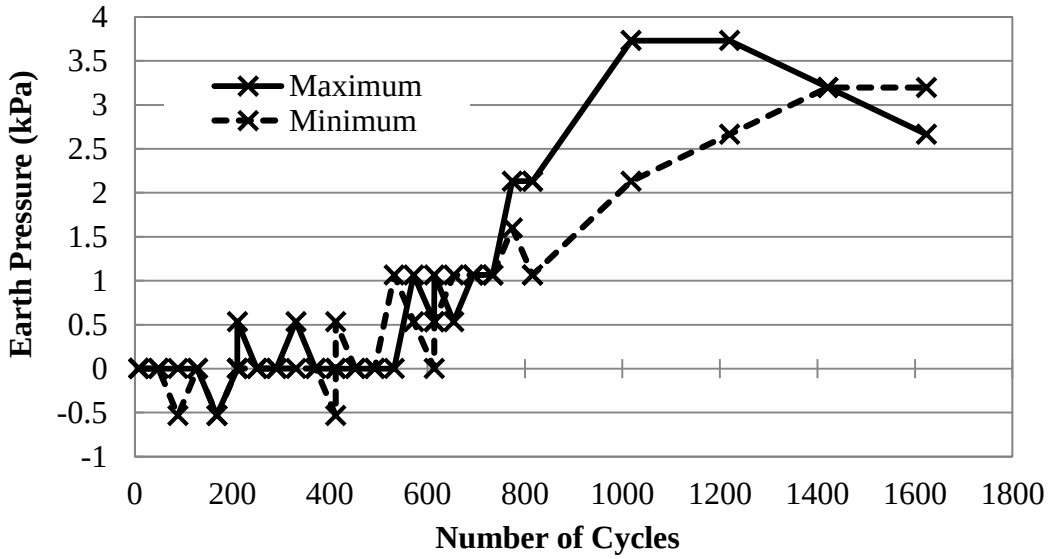

Figure B.2 Measured Horizontal Pressure at the Spring Line (S_1) in the Single Geogrid-Reinforced Section (Test 8)

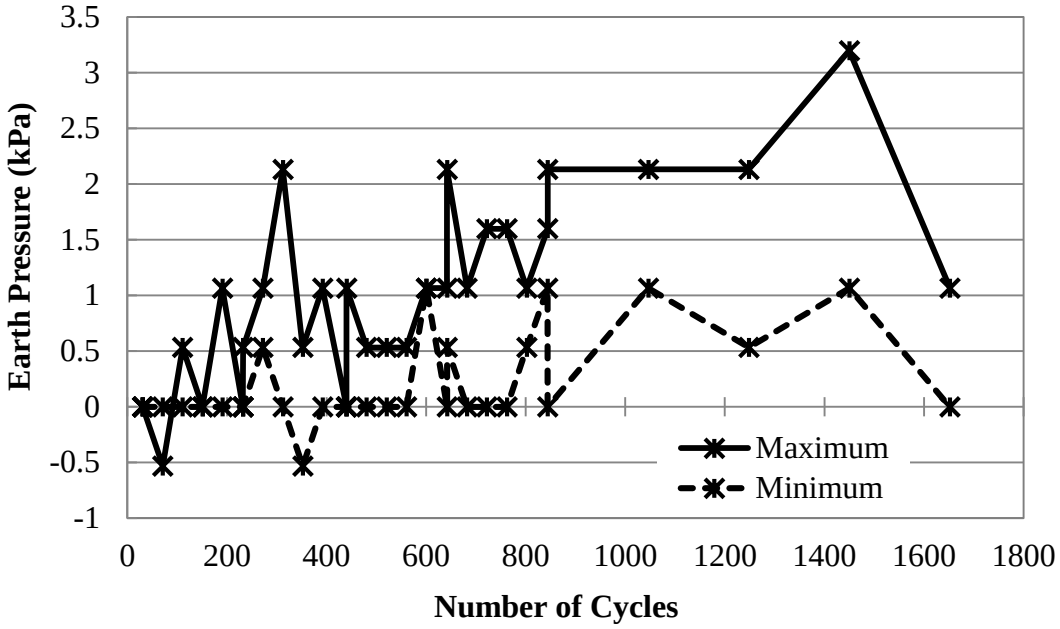

Figure B.3 Measured Horizontal Pressure at the Spring Line (S_1) in the Double Geogrid-Reinforced Section (Test 10)

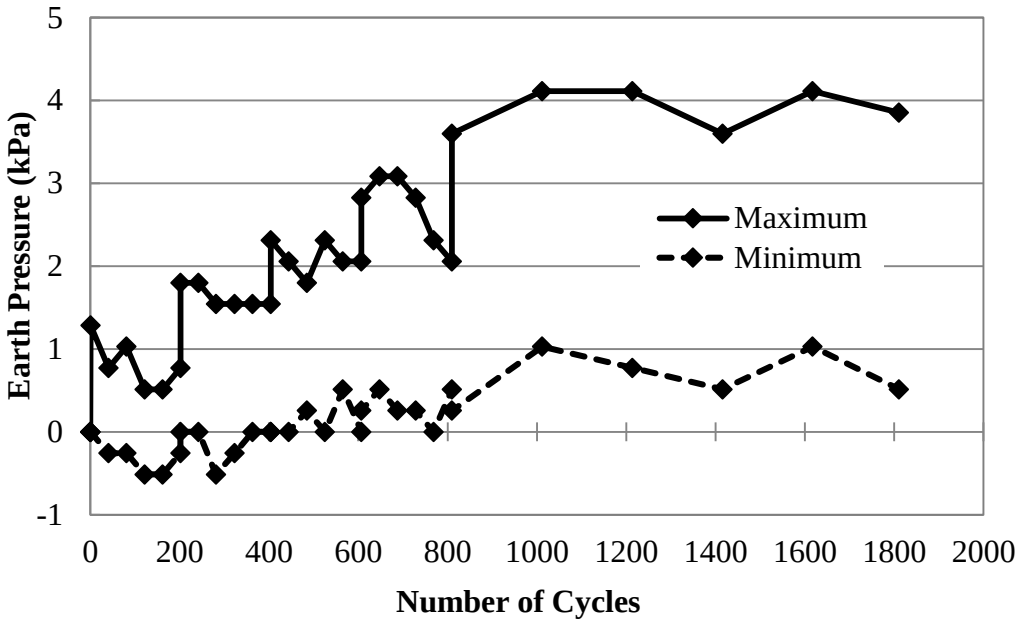

Figure B.4 Measured Horizontal Pressure at the Haunch (S_3) in the Unreinforced Section (Test 6)

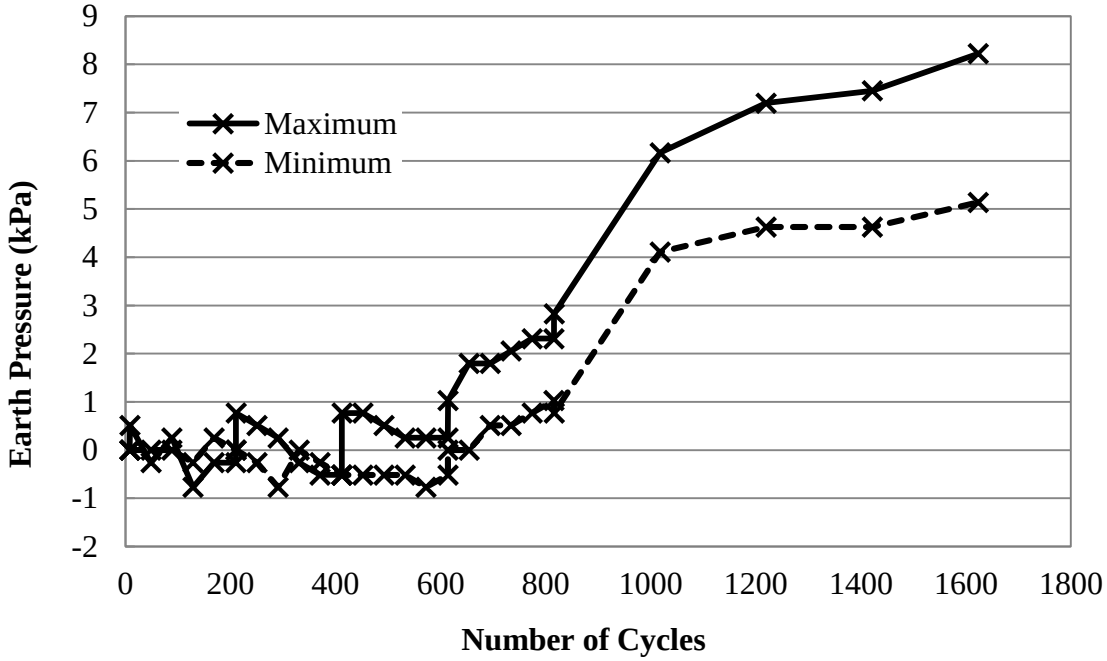

Figure B.5 Measured Horizontal Pressures at the Haunch (S_3) in the Single Geogrid-Reinforced Section (Test 8)

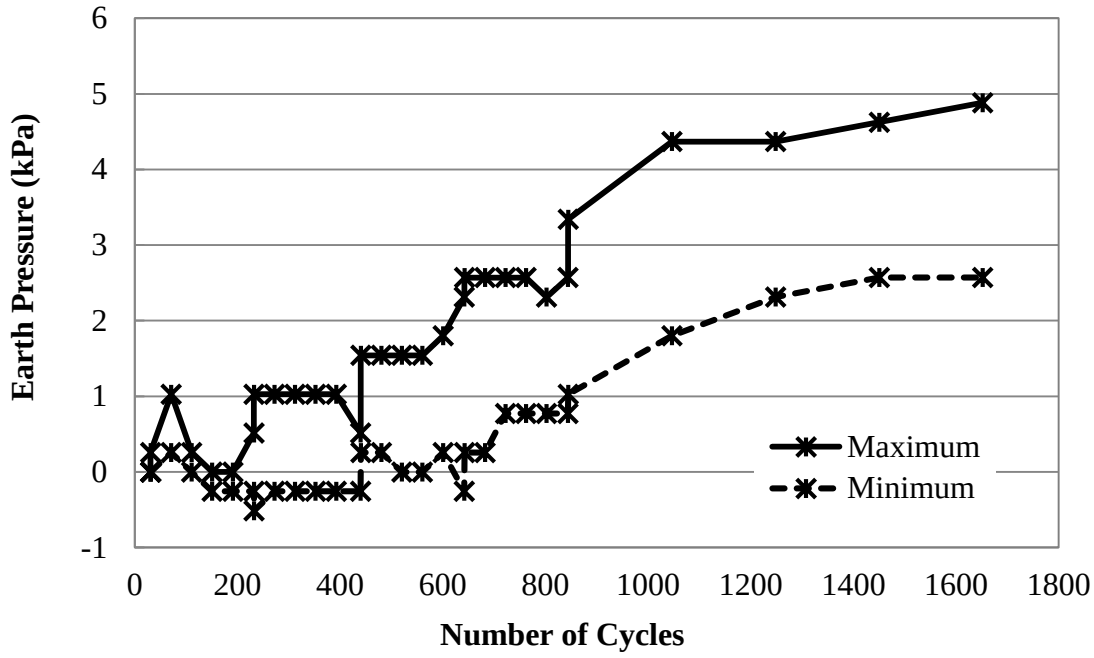

Figure B.6 Measured Horizontal Pressures at the Haunch (S_3) in the Double Geogrid-Reinforced Section (Test 10)

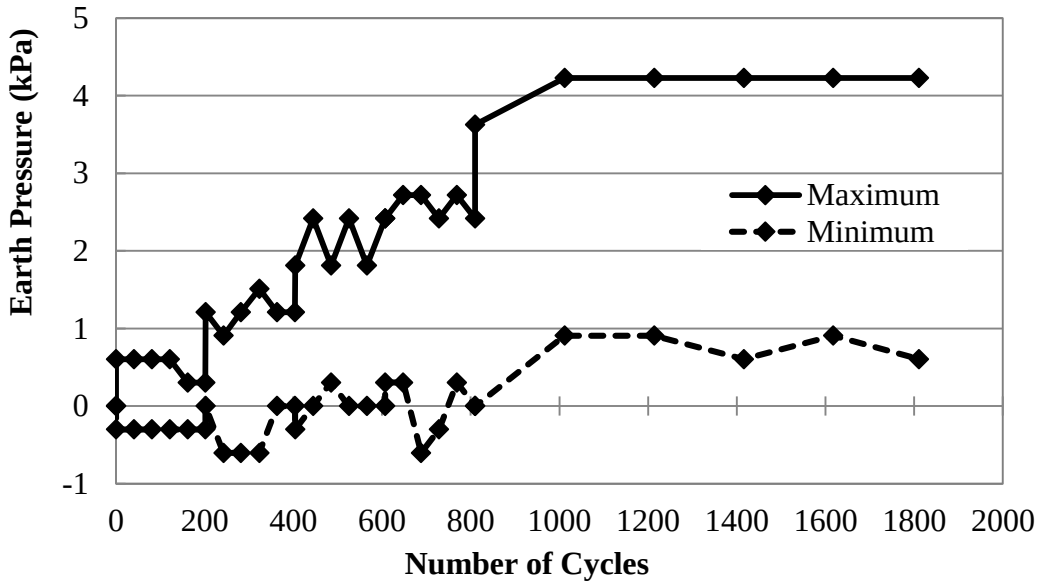

Figure B.7 Measured Horizontal Pressures at the Trench Wall (S_5) in the Unreinforced Section (Test 6)

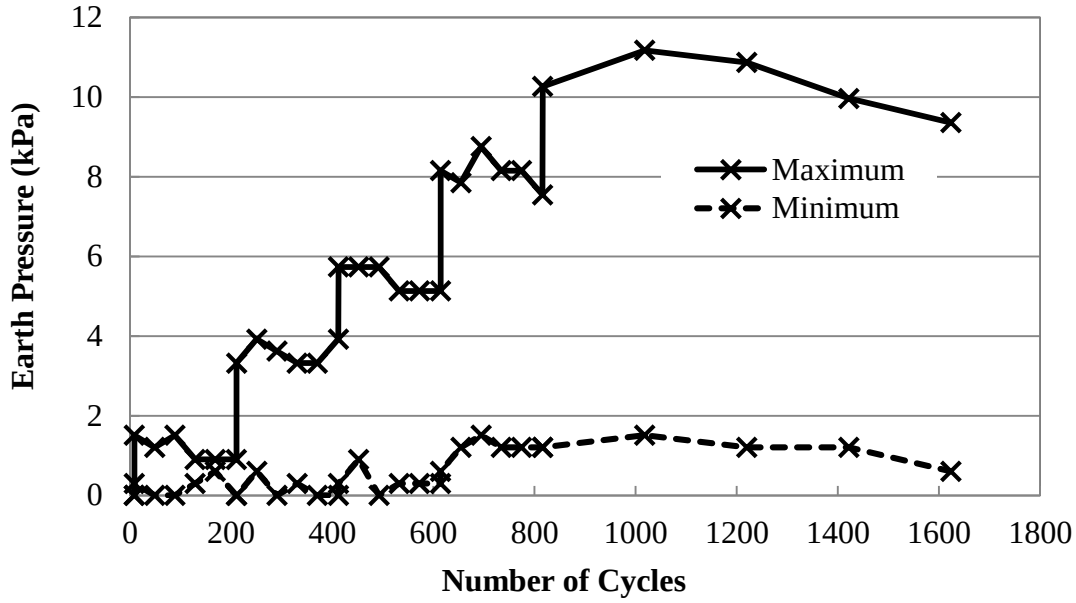

Figure B.8 Measured Horizontal Pressures at the Trench Wall (S_5) in the Single Geogrid-Reinforced Section (Test 8)

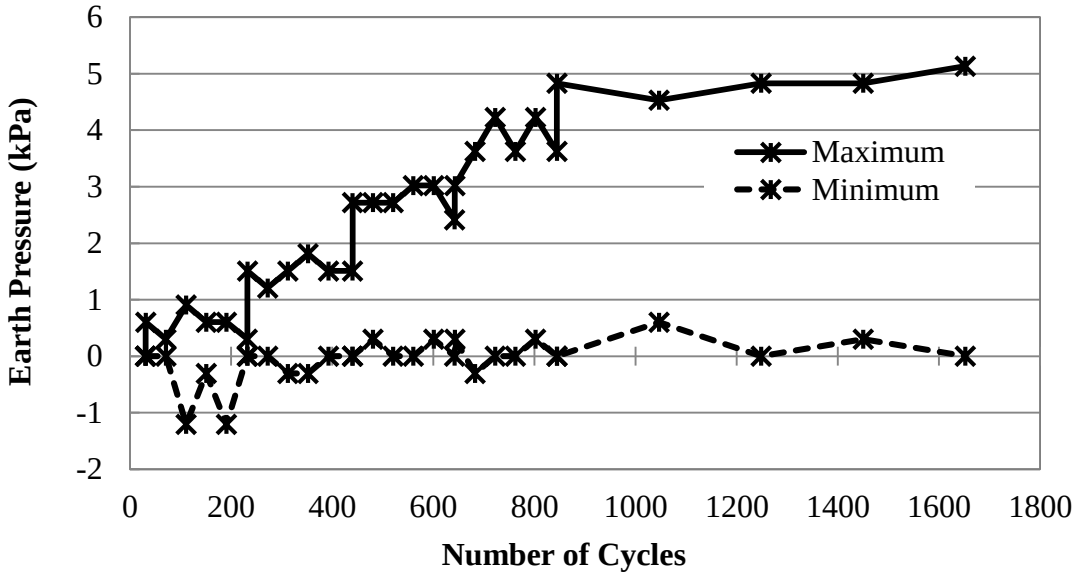

Figure B.9 Measured Horizontal Pressures at the Trench Wall (S_5) in the Double Geogrid-Reinforced Section (Test 10)

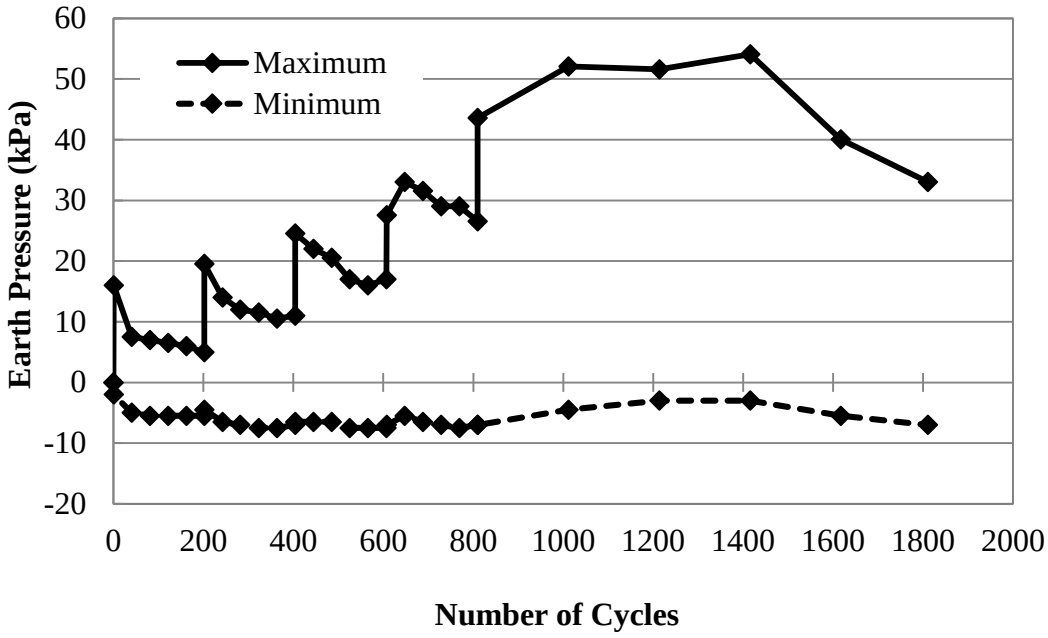

Figure B.10 Vertical Pressures at the Crown (C_2) in the Unreinforced Section (Test 6)

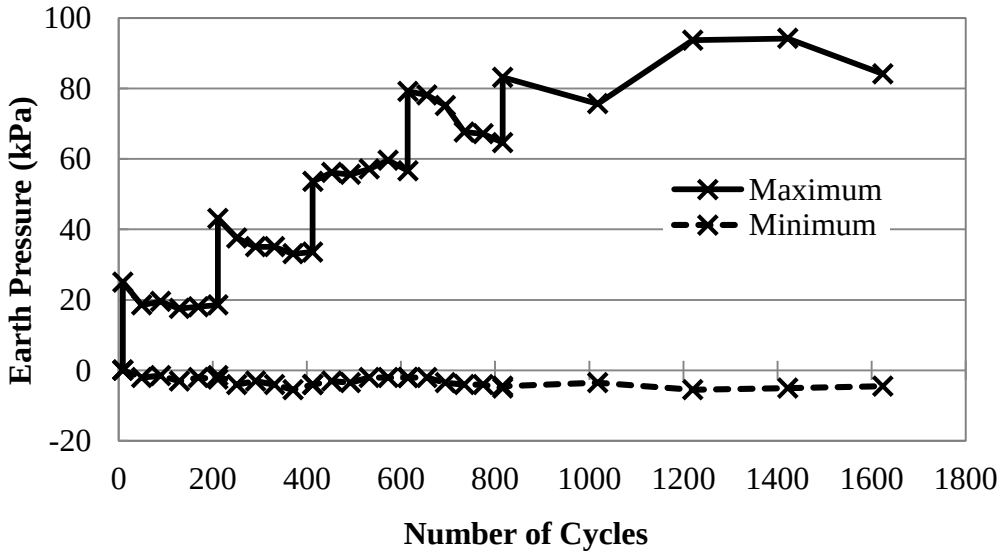

Figure B.11 Vertical Pressures at the Crown (C_2) in the Single Geogrid-Reinforced Section (Test 8)

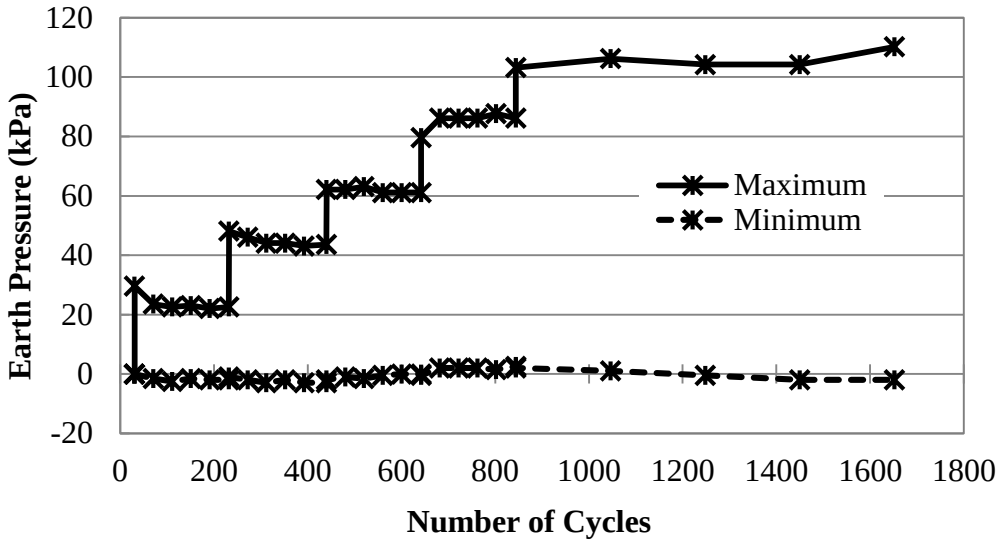

Figure B.12 Vertical Pressures at the Crown (C_2) in the Double Geogrid–Reinforced Section (Test 10)

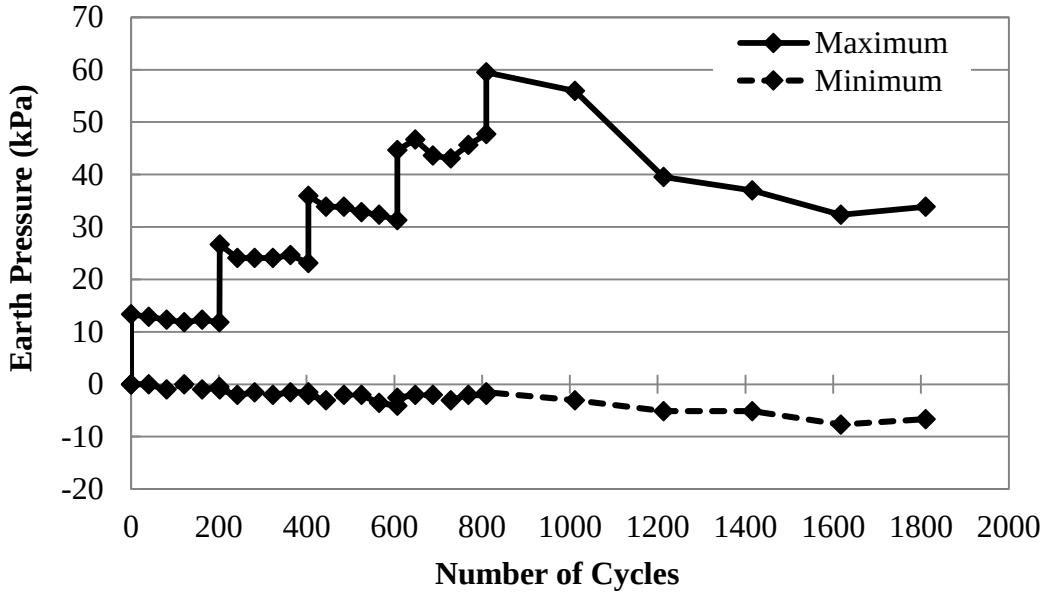

Figure B.13 Vertical Pressures at the Crown (C_3) in the Unreinforced Section (Test 6)

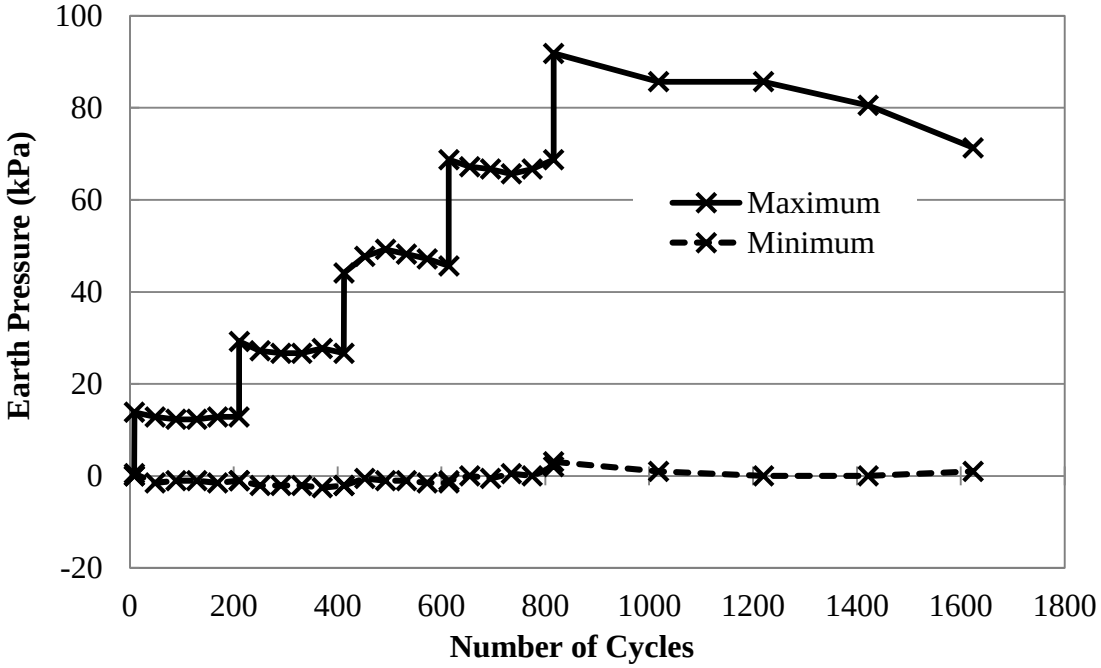

Figure B.14 Vertical Pressures at the Crown (C_3) in the Single Geogrid-Reinforced Section (Test 8)

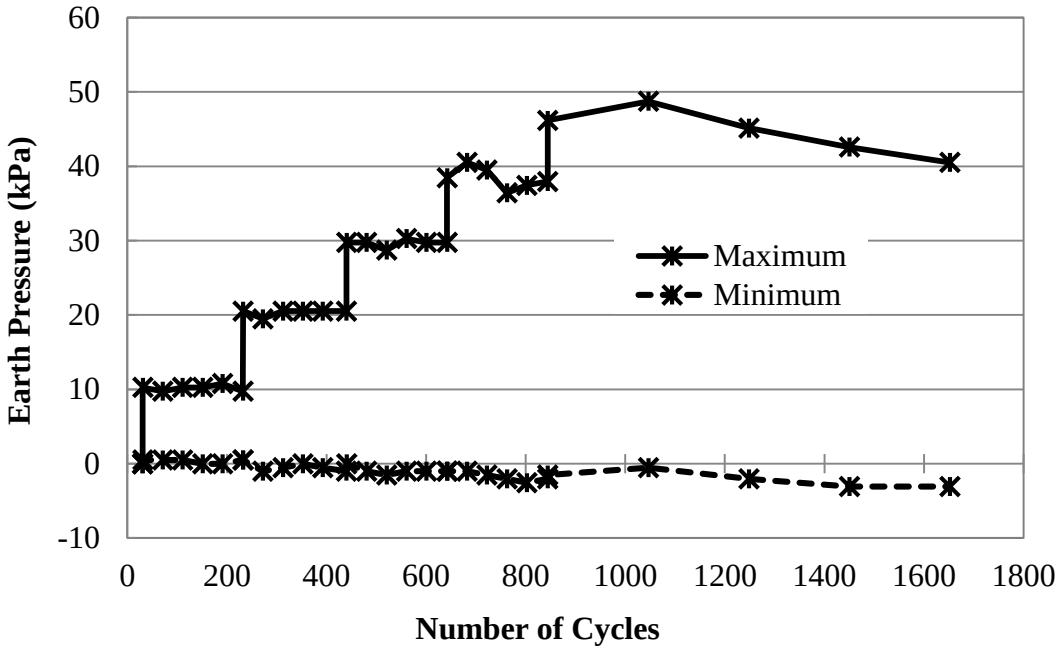

Figure B.15 Vertical Pressures at the Crown (C_3) in the Double Geogrid-Reinforced Section (Test 10)

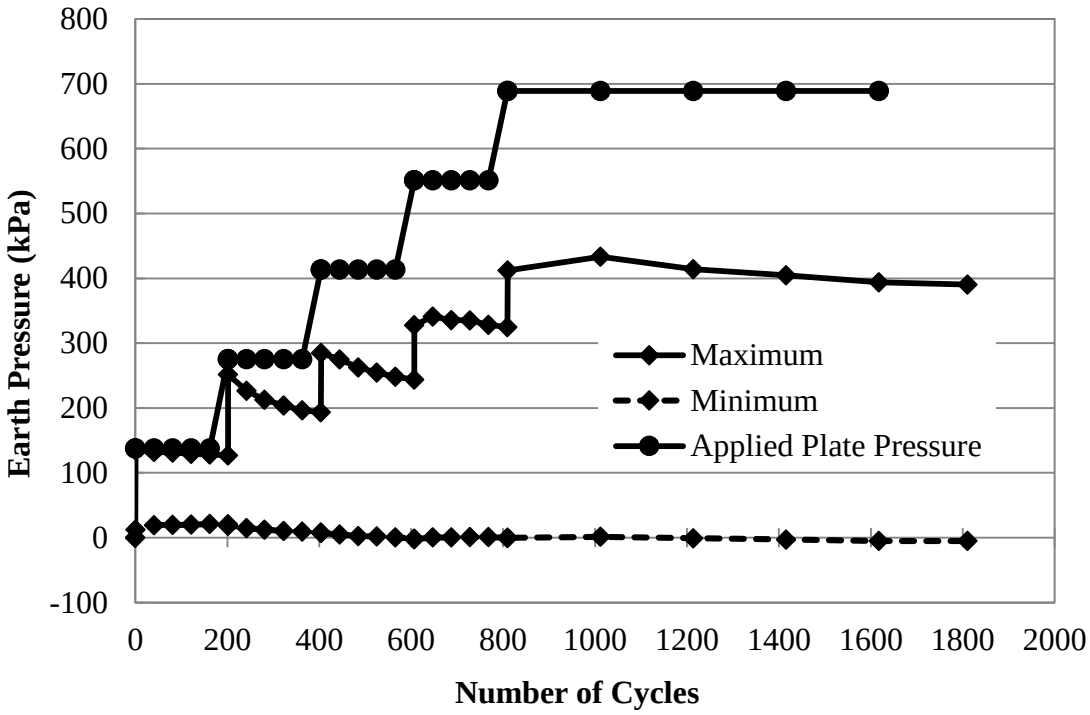

Figure B.16 Vertical Pressures under Base Course (C_4) in the Unreinforced Section (Test 6)

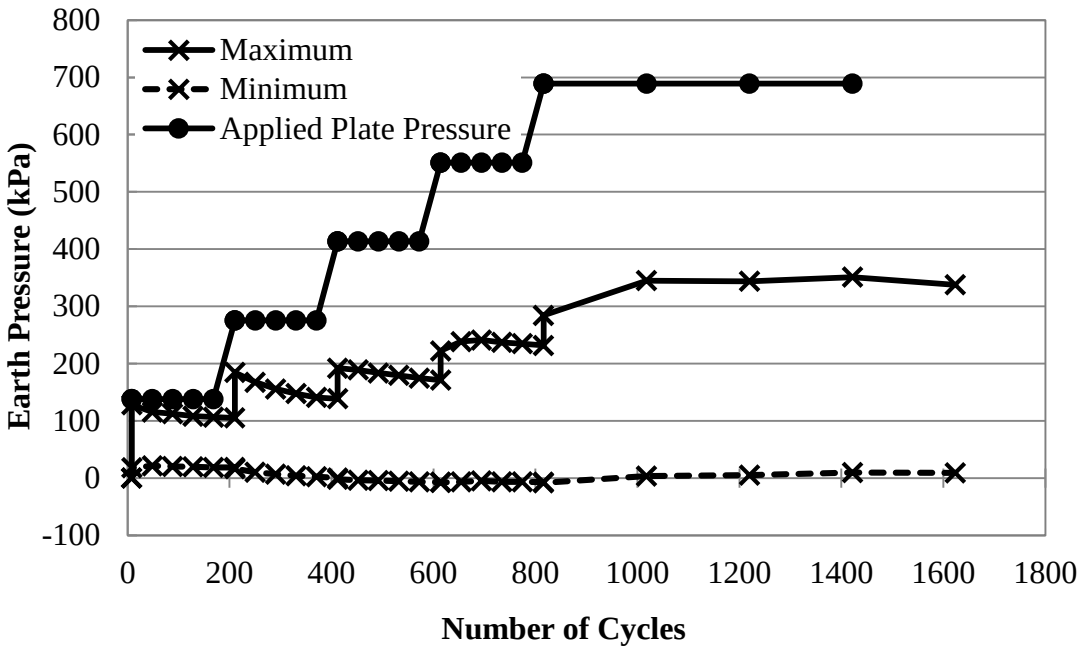

Figure B.17 Vertical Pressures under Base Course (C_4) in the Single Geogrid-Reinforced Section (Test 8)

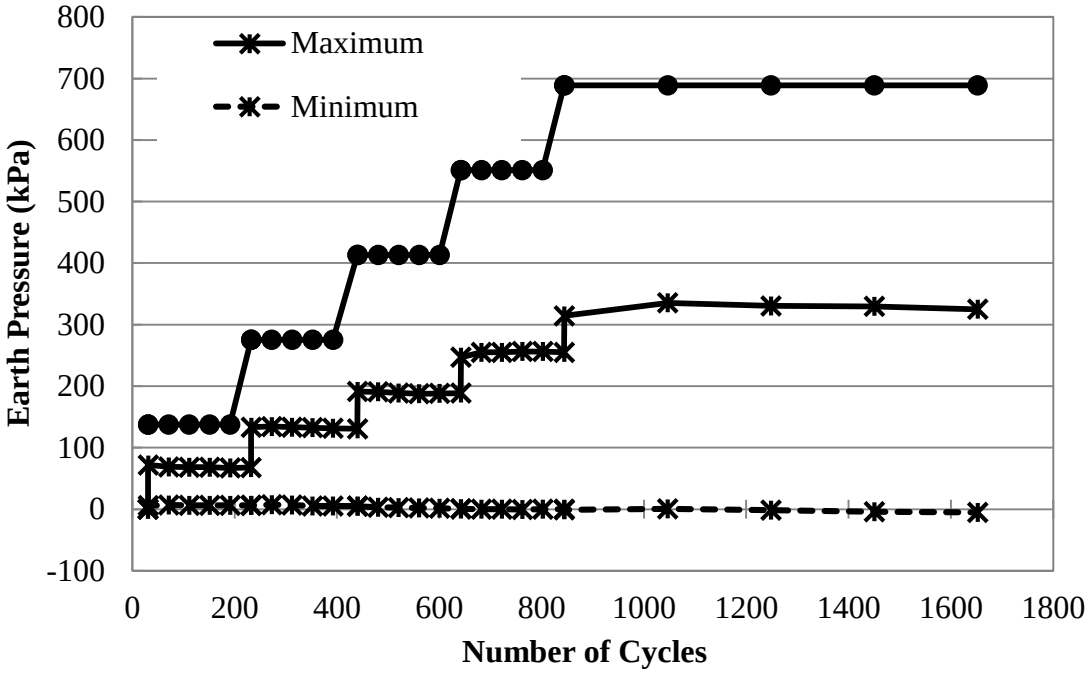

Figure B.18 Vertical Pressures under Base Course (C_4) in the Double Geogrid-Reinforced Section (Test 10)

Appendix C - Measured Pipe Strains in Cyclic Plate Load Tests

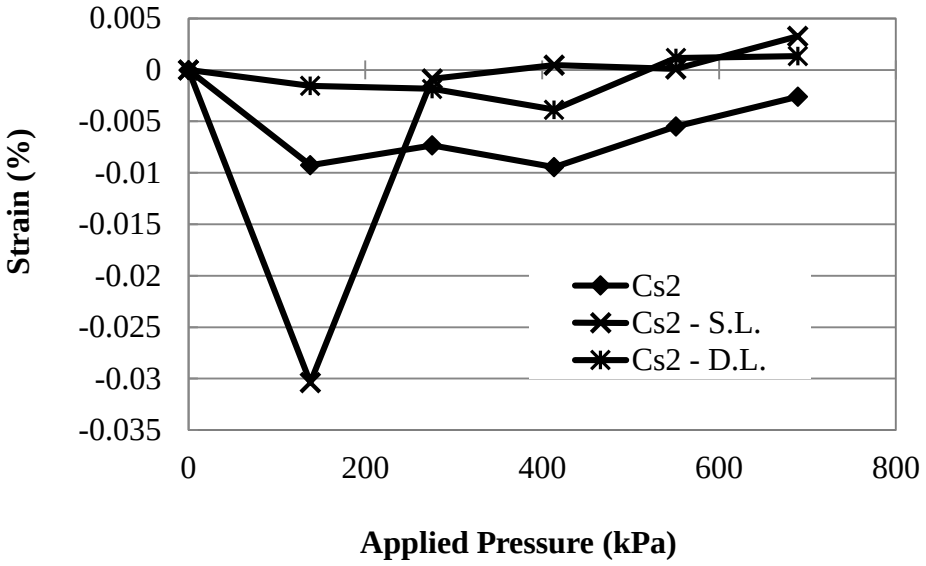

Figure C.1 Maximum Circumferential Strains at Spring Line (C_{s2})

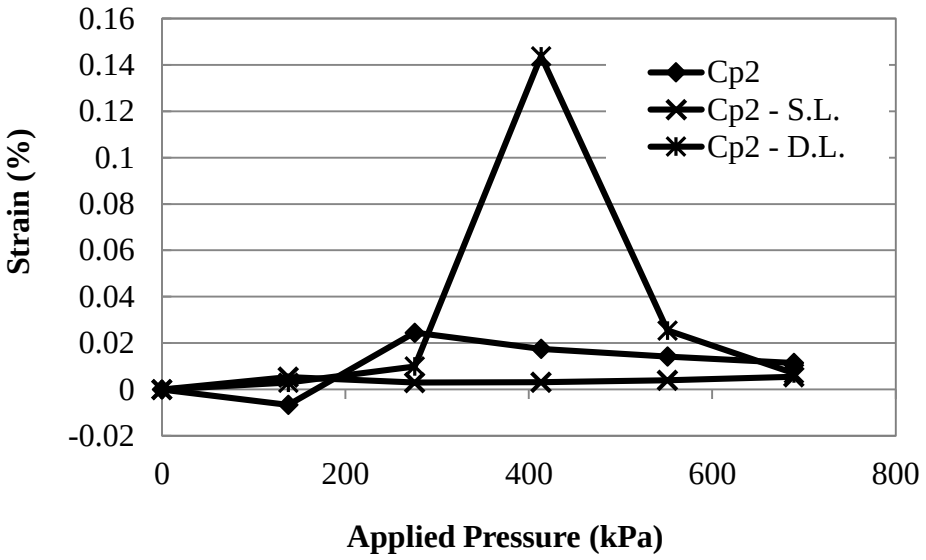

Figure C.2 Maximum Circumferential Strains at the Spring Line (C_{p2})

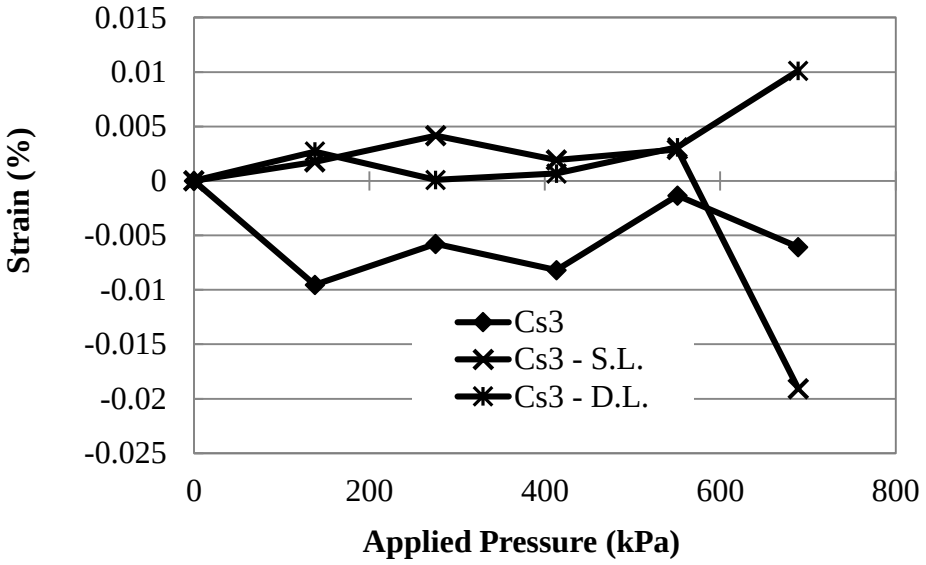

Figure C.3 Maximum Circumferential Strains at Invert (C_{s3})

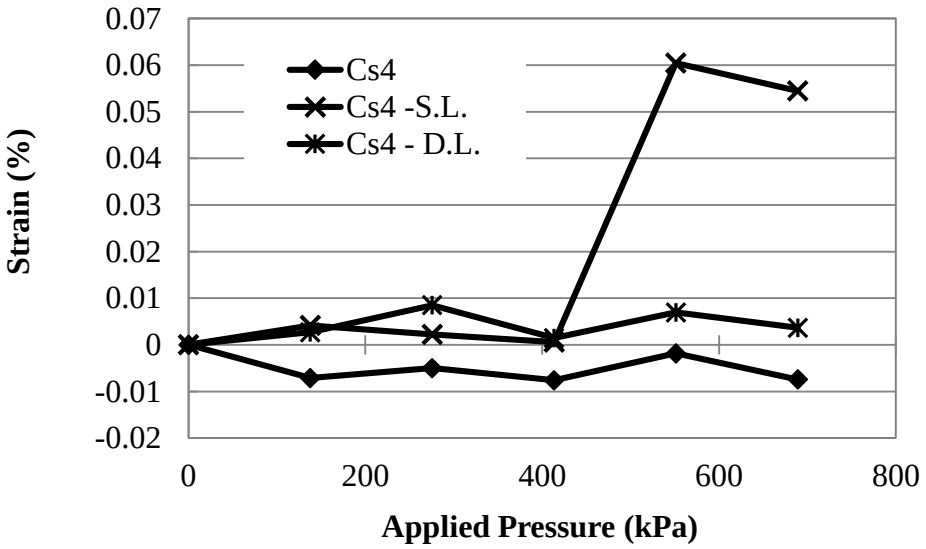

Figure C.4 Maximum Circumferential Strains at Invert (C_{s4})

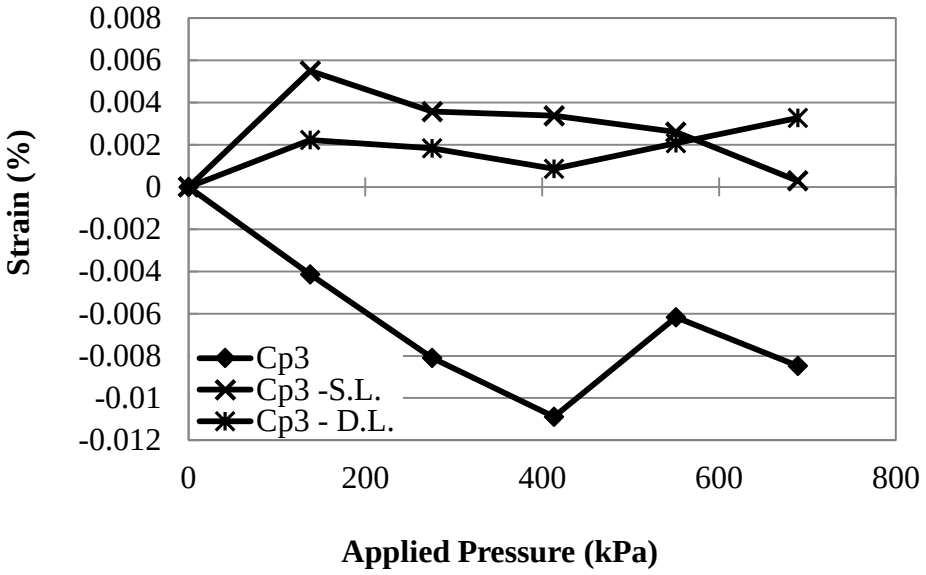

Figure C.5 Maximum Circumferential Strains at Invert (C_{p3})

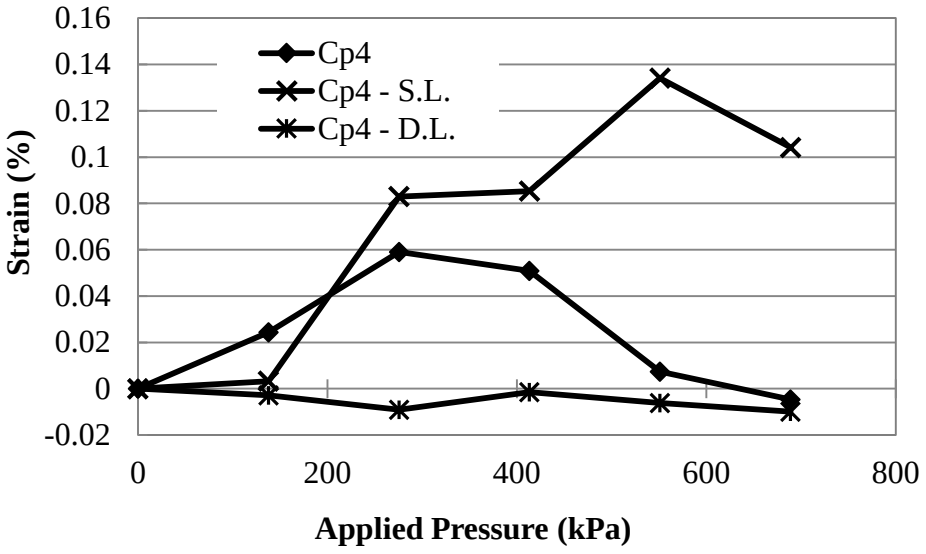

Figure C.6 Maximum Circumferential Strains at Invert (C_{p4})

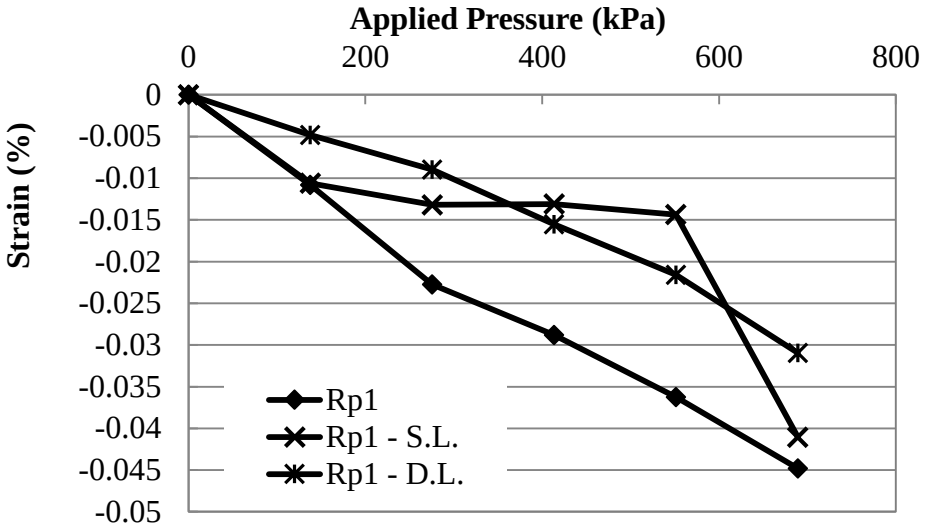

Figure C.7 Maximum Radial Strains at the Spring Line (R_{p1})

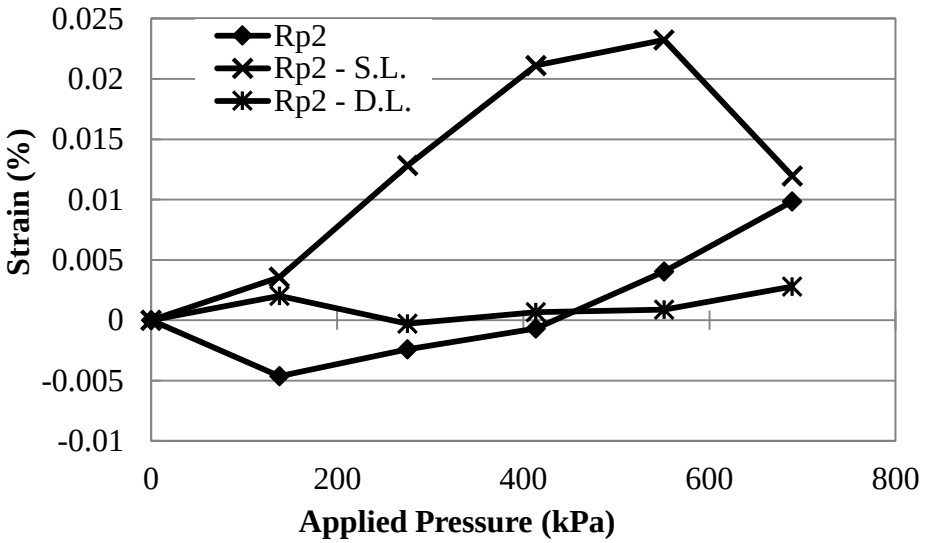

Figure C.8 Maximum Radial Strains at the Spring Line (R_{p2})

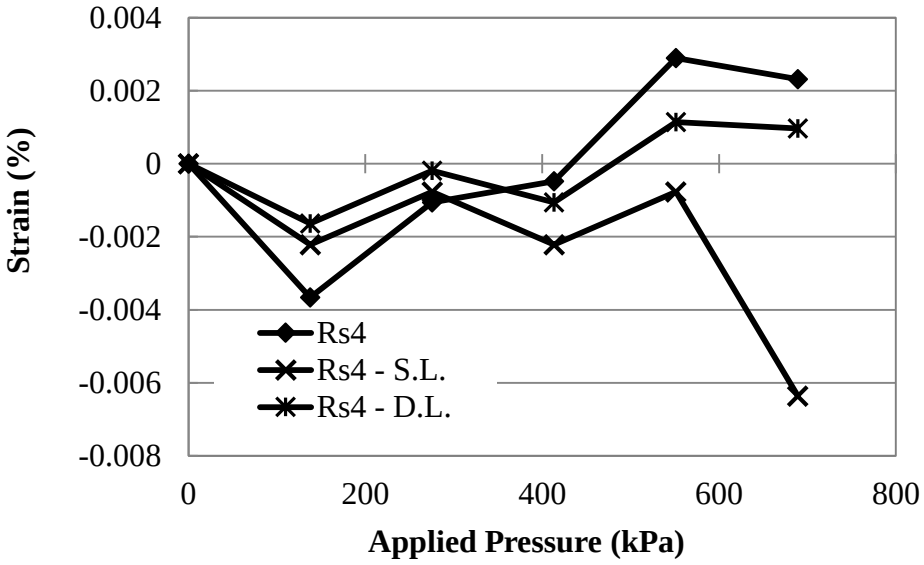

Figure C.9 Maximum Radial Strains at the Invert (R_{s4})

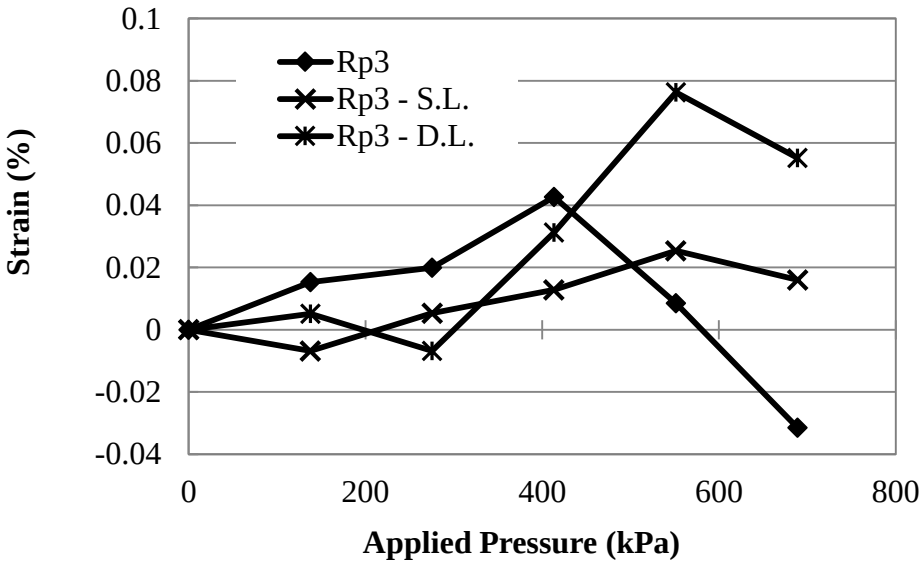

Figure C.10 Maximum Radial Strains at the Invert (R_{p3})

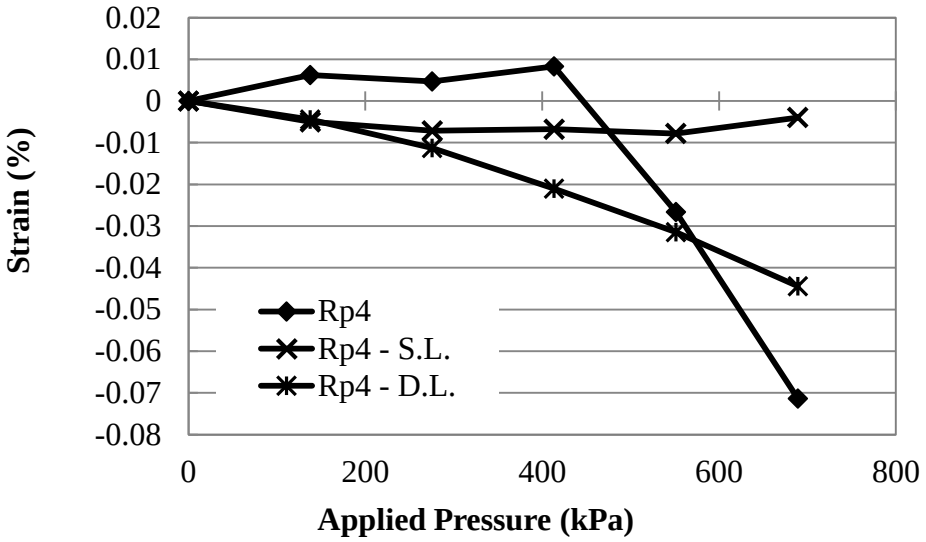

Figure C.11 Maximum Radial Strains at the Invert (R_{p4})

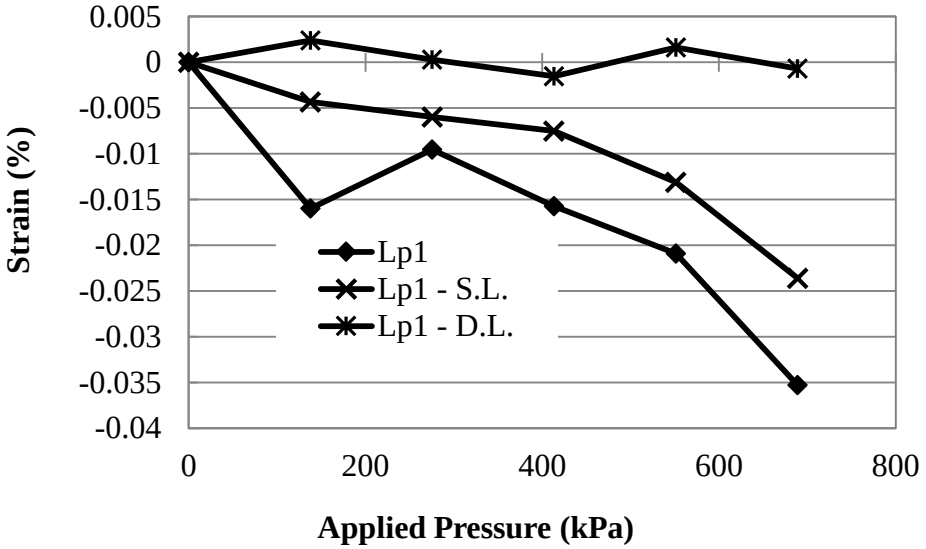

Figure C.12 Maximum Longitudinal Strains at the Spring Line (L_1)

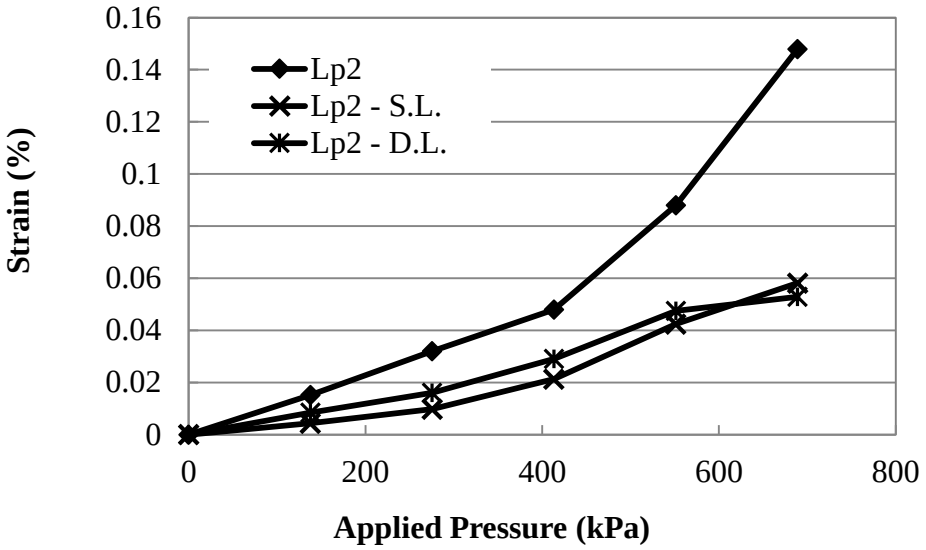

Figure C.13 Maximum Longitudinal Strains at the Spring Line (L_2)

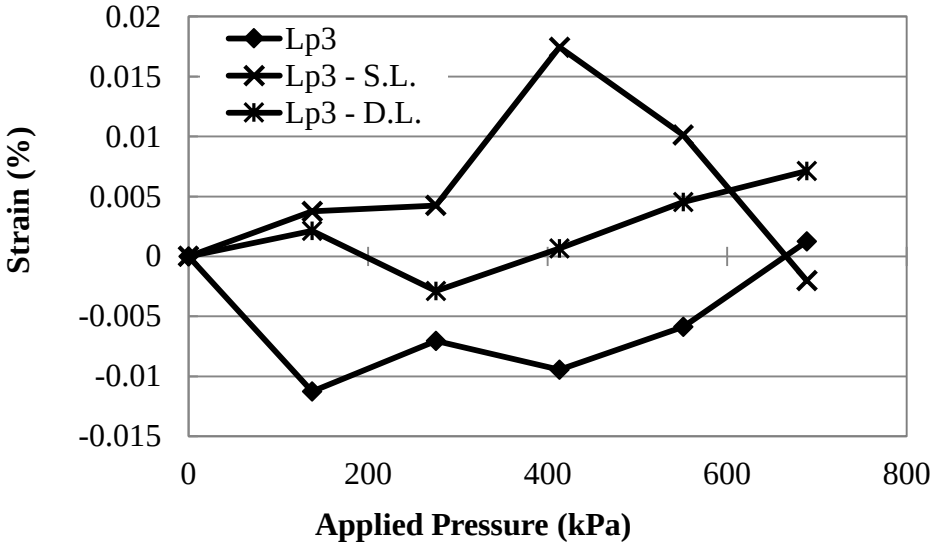

Figure C.14 Maximum Longitudinal Strains at the Invert (L_3)

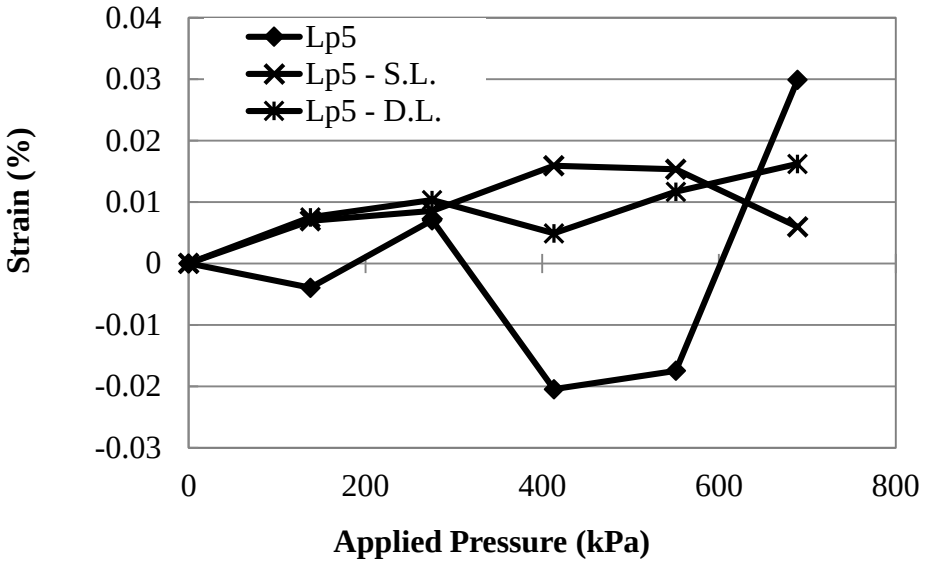

Figure C.15 Maximum Longitudinal Strains at the Spring Line (L_5)

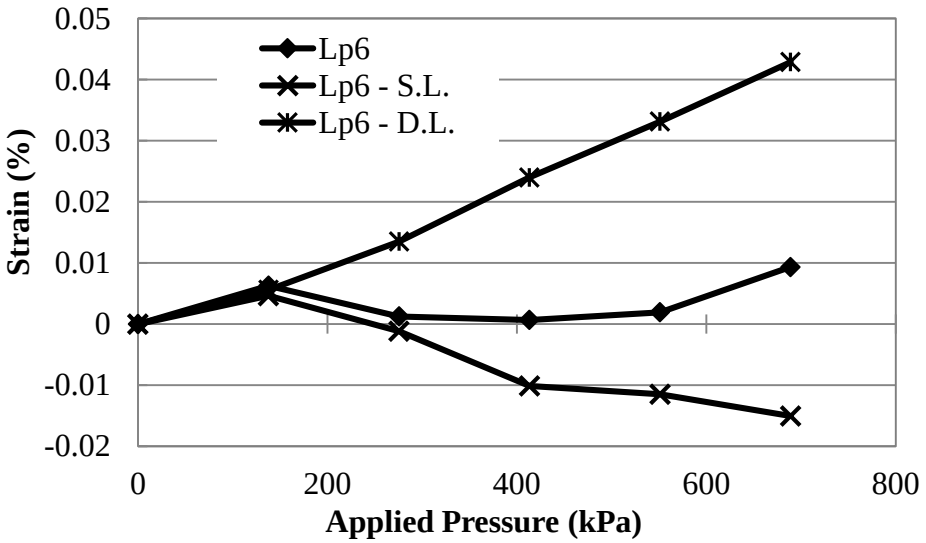

Figure C.16 Maximum Longitudinal Strains at the Spring Line (L_6)

Appendix D – Measured Pipe Strains in Penetration Load Tests

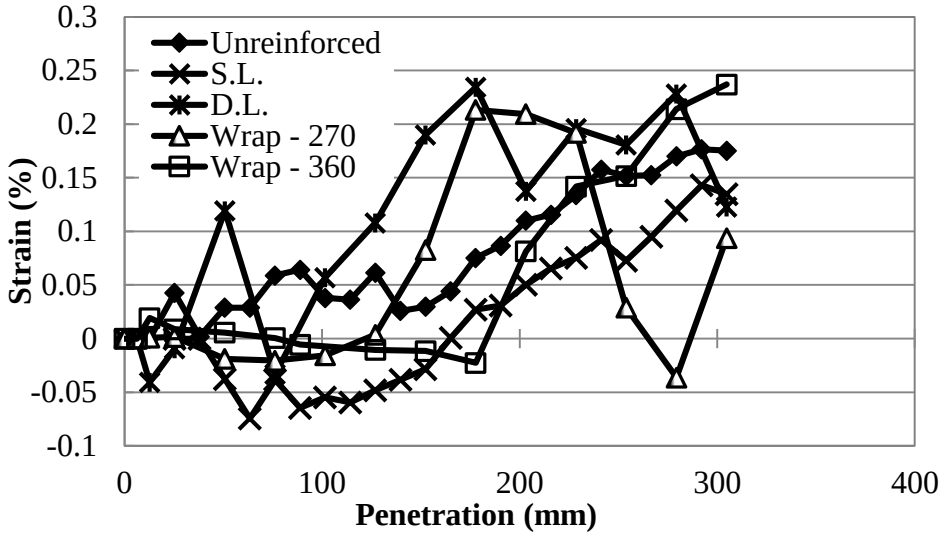

Figure D.1 Circumferential Strains at Spring Line – Steel C_{s2}

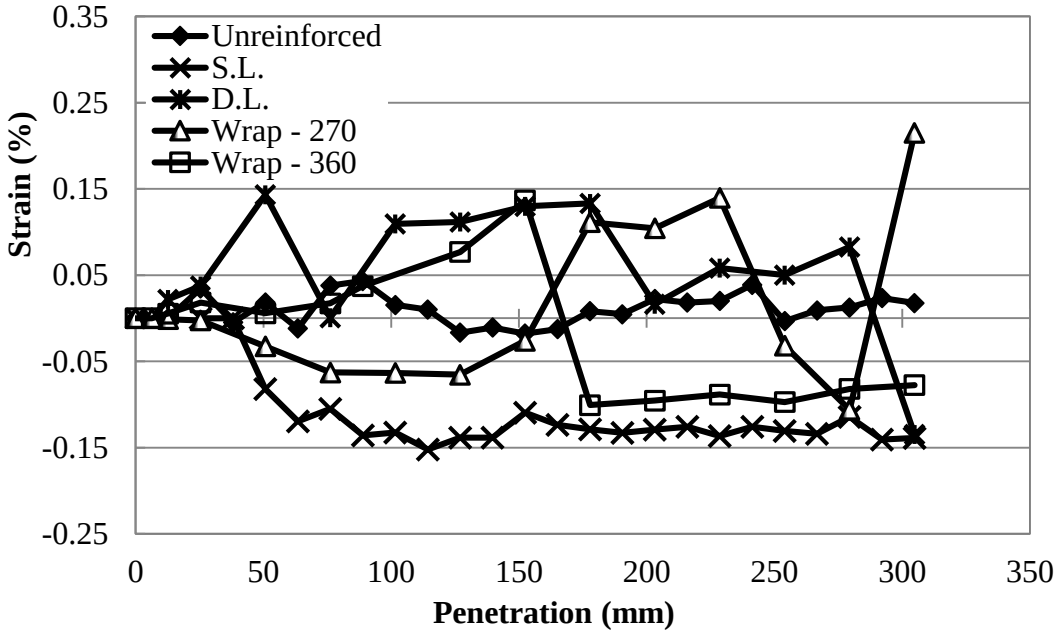

Figure D.2 Circumferential Strains at Spring Line – Plastic C_{p2}

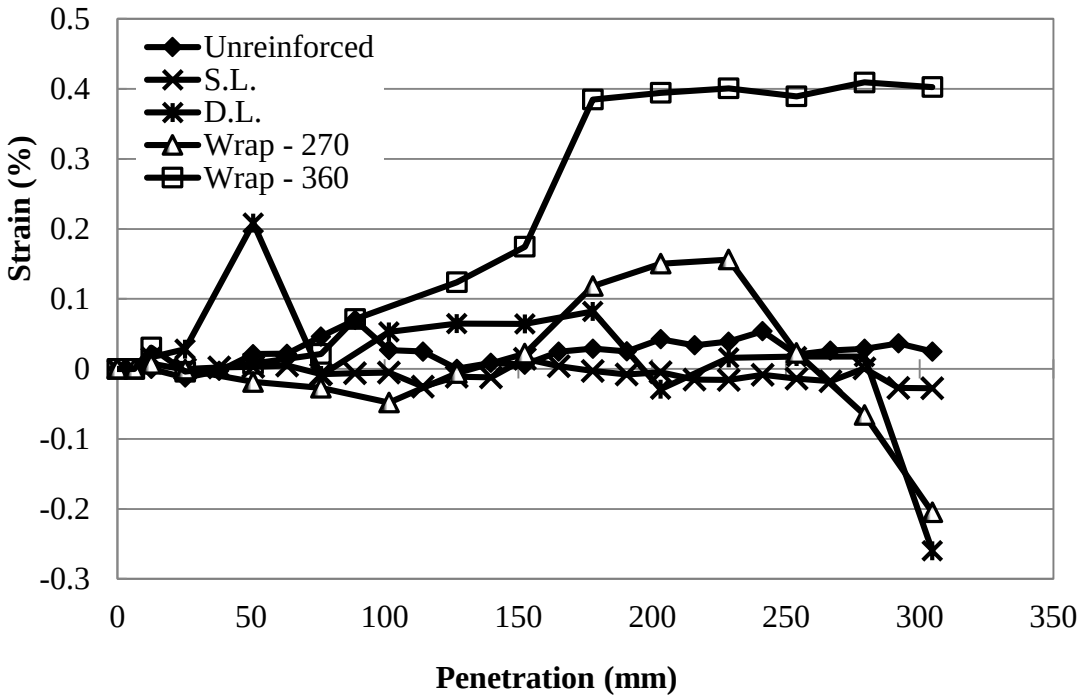

Figure D.3 Circumferential Strains at Invert – Steel C_{s4}

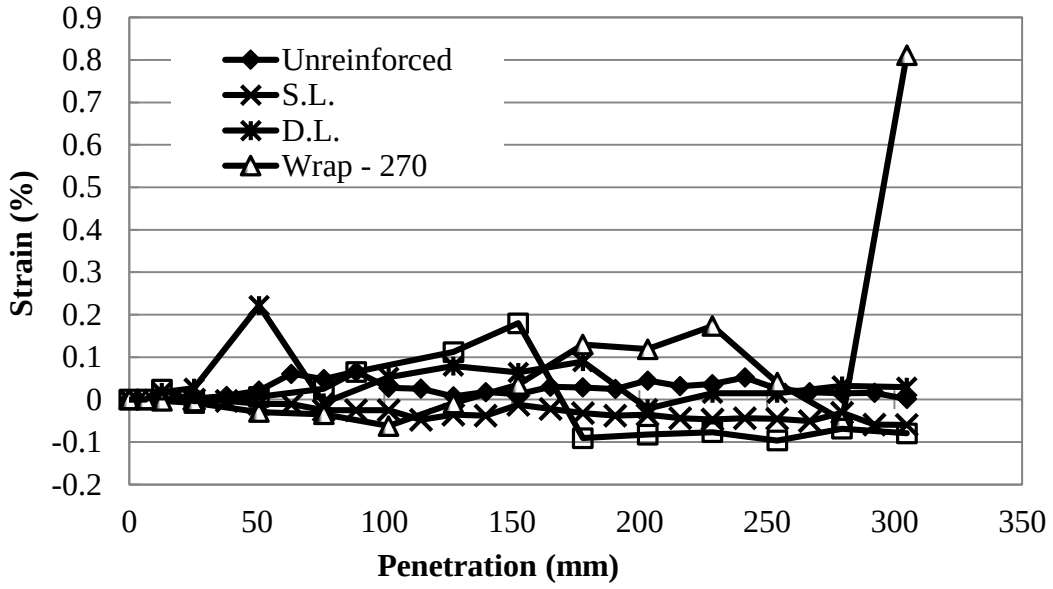

Figure D.4 Circumferential Strains at Invert – Plastic C_{p4}

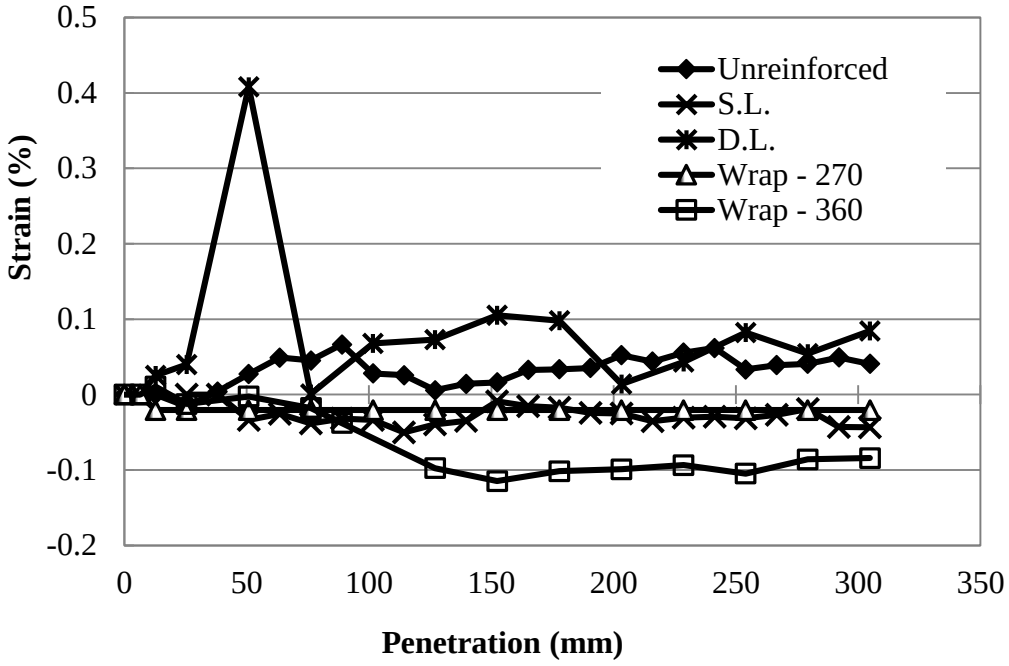

Figure D.5 Radial Strains at Spring Line – Steel R_{s1}

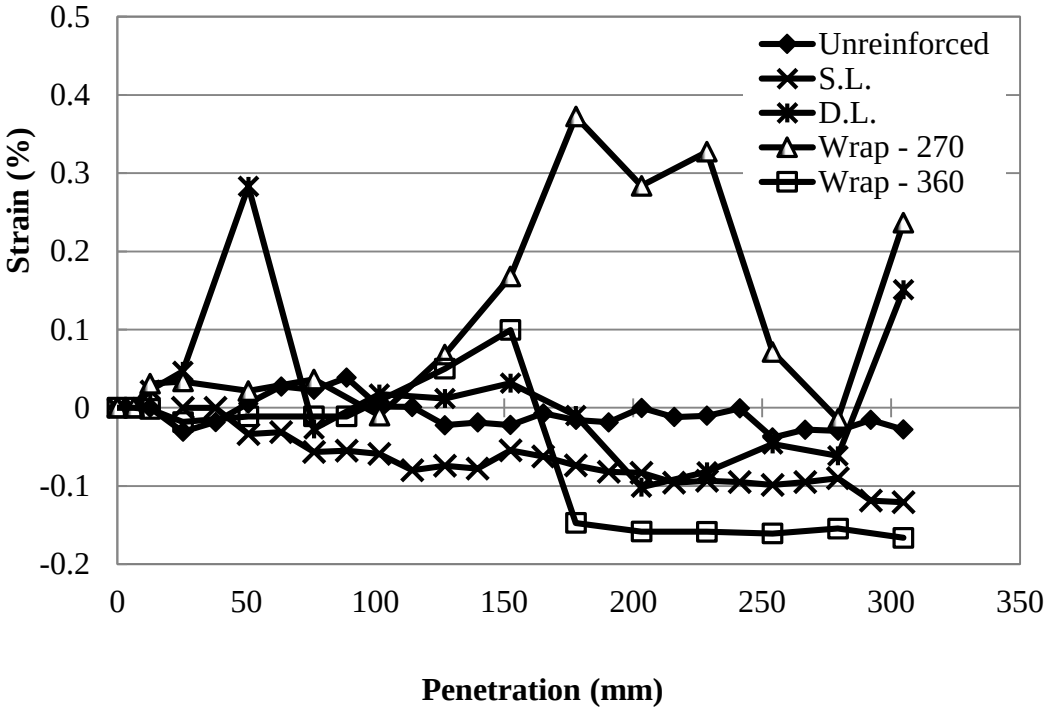

Figure D.6 Radial Strains at Spring Line - Plastic R_{p1}

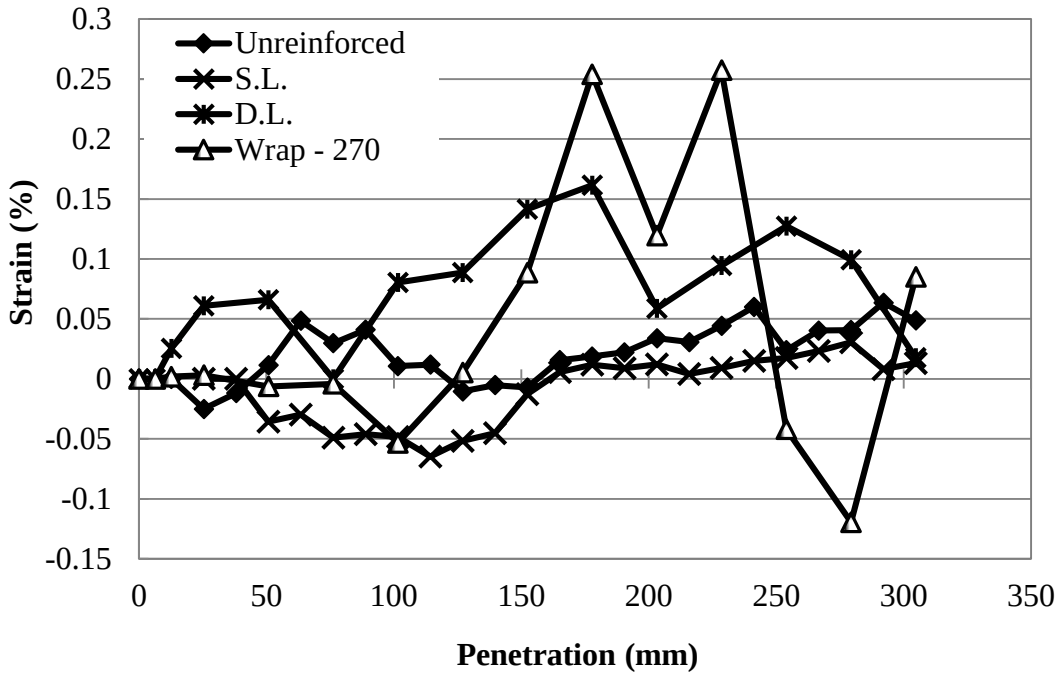

Figure D.7 Radial Strains at Spring Line - Plastic R_{p2}

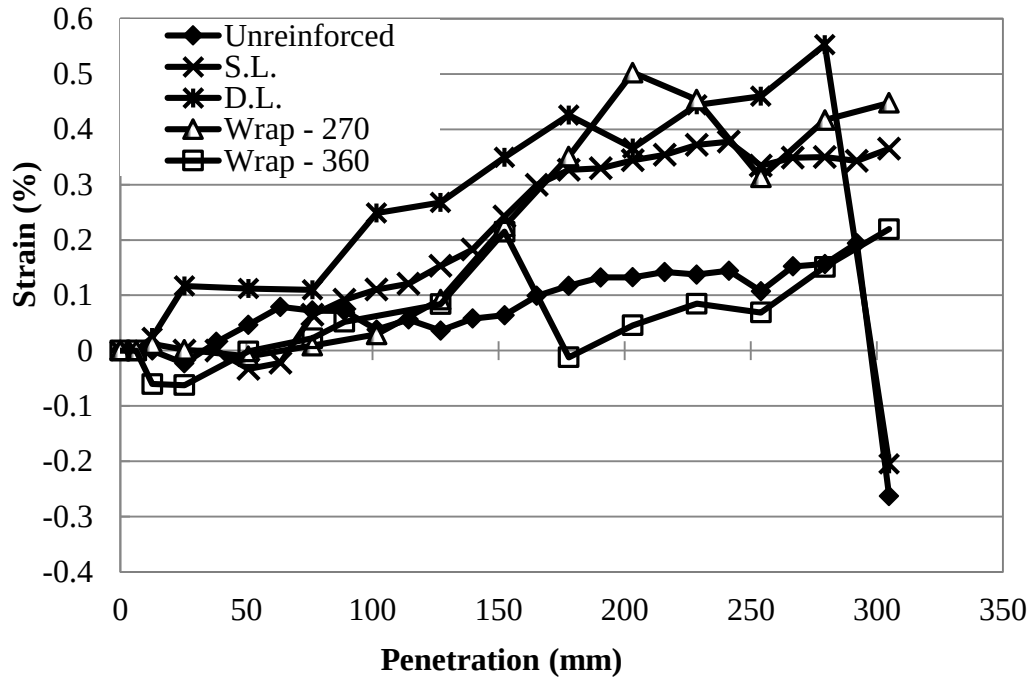

Figure D.8 Radial Strains at Crown - Plastic R_{p3}

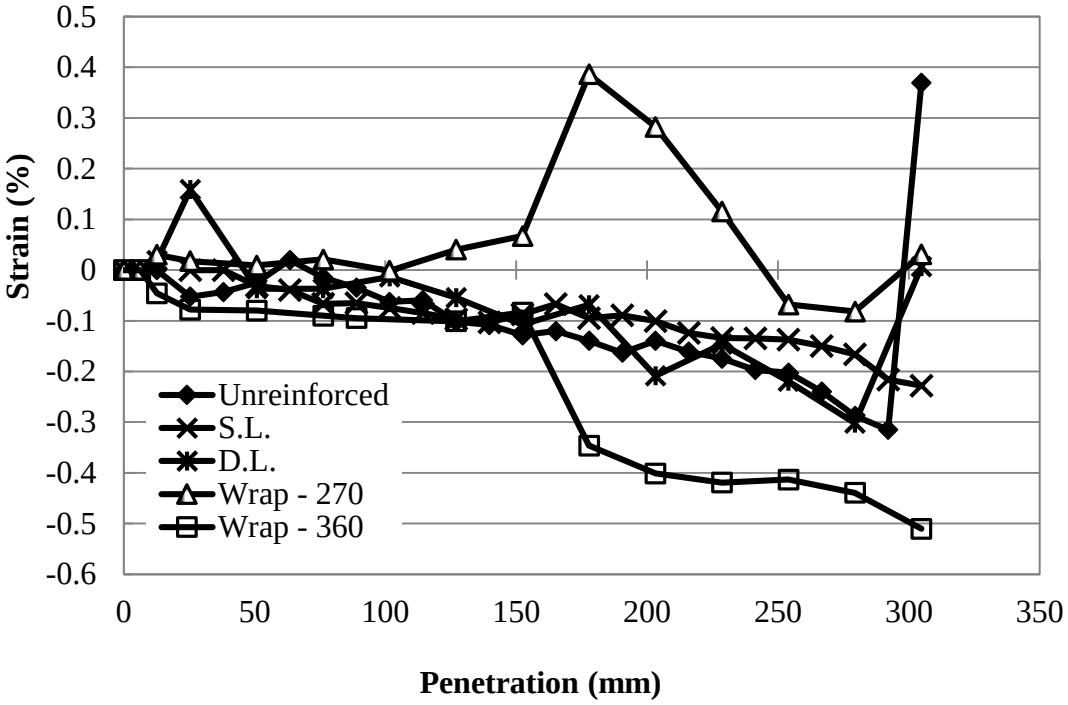

Figure D.9 Radial Strains at Crown - Plastic R_{p4}

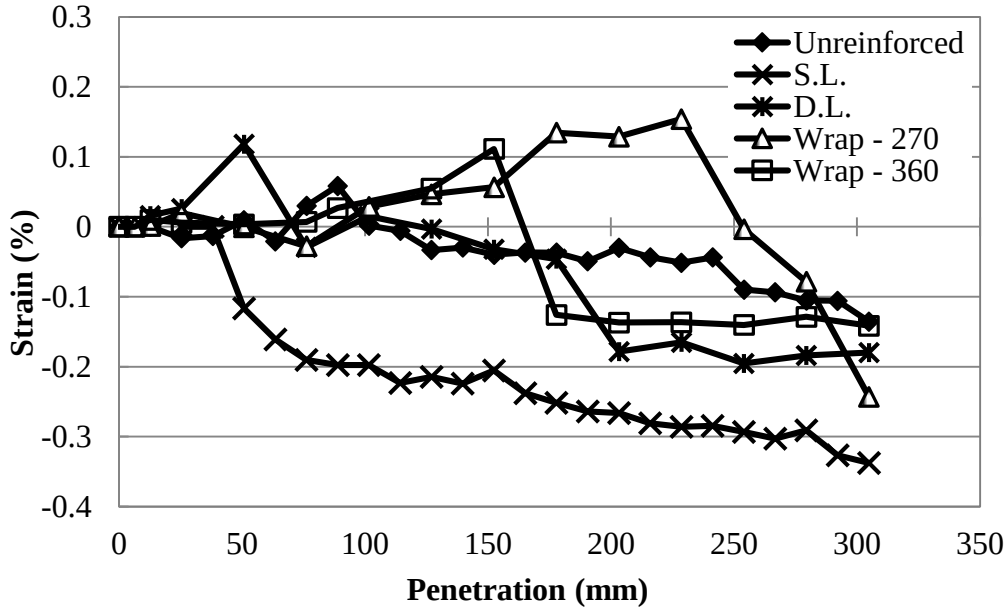

Figure D.10 Longitudinal Strains at Spring Line - L_1 (Outside)

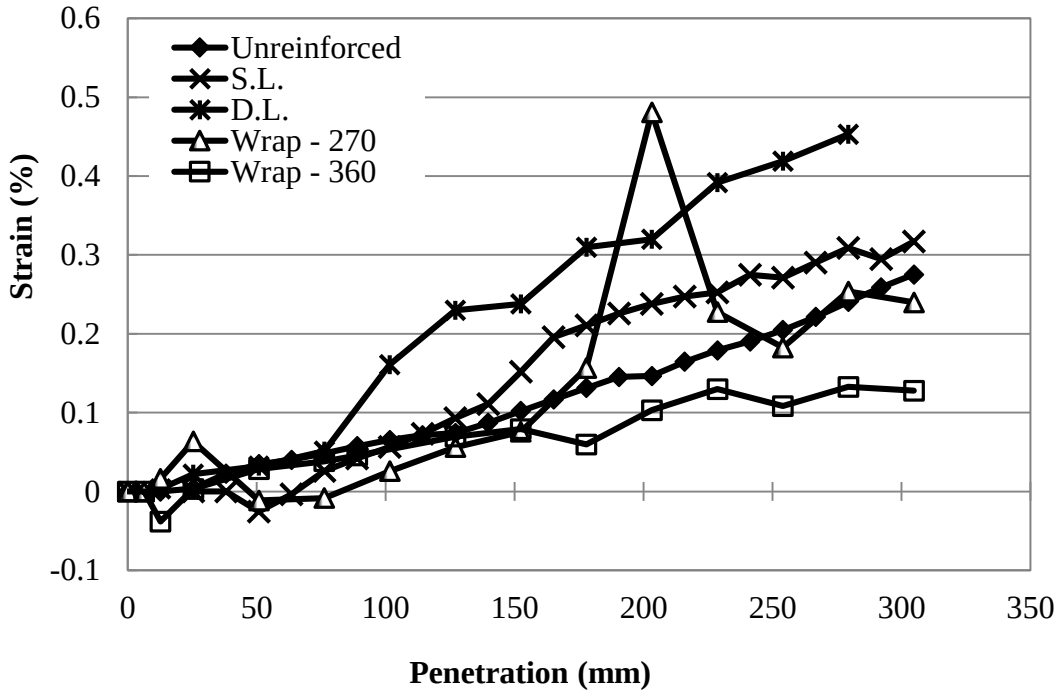

Figure D.11 Longitudinal Strains at Spring Line - L_2 (Inside)

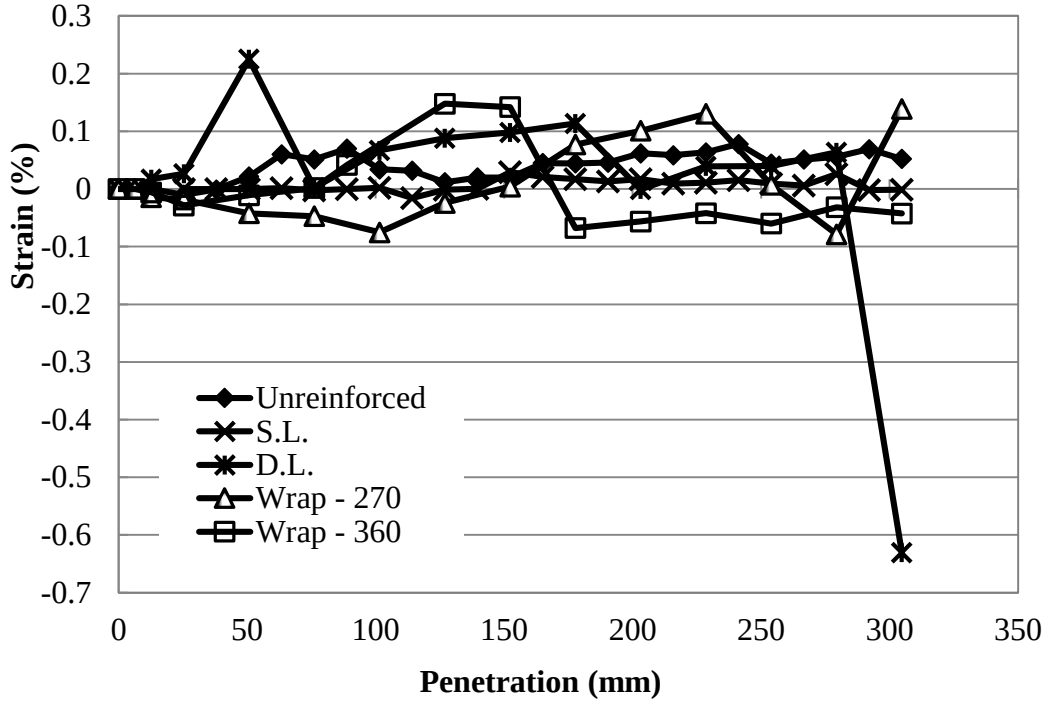

Figure D.12 Longitudinal Strains at Invert - L_3 (Outside)

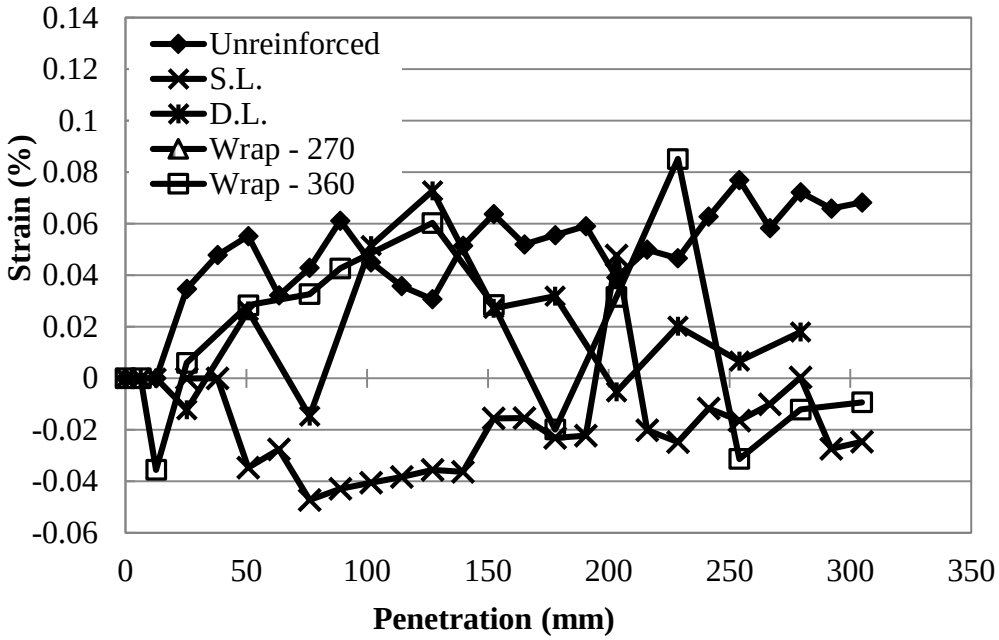

Figure D.13 Longitudinal Strains at Invert – L_4 (Inside)

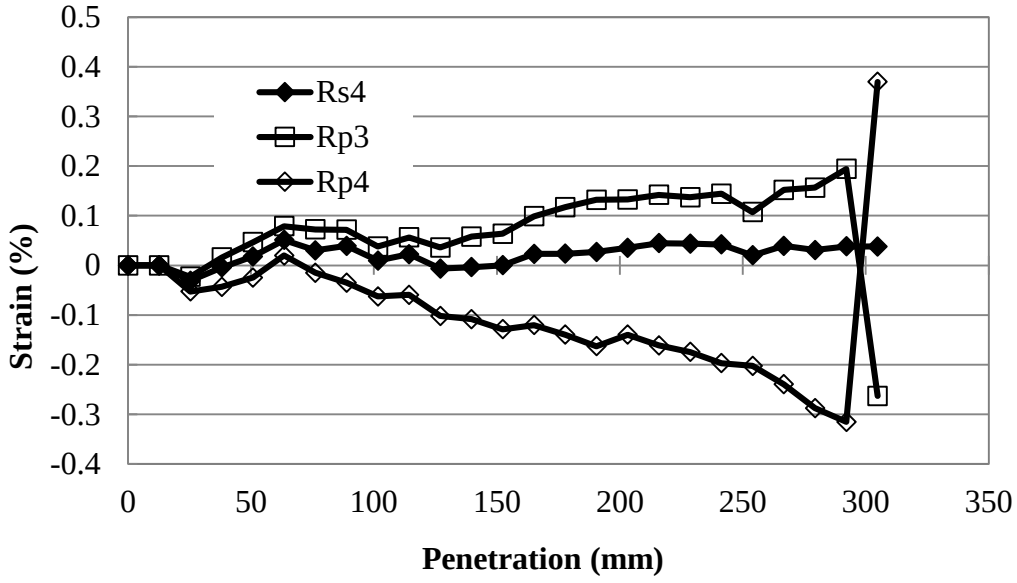

Figure D.14 Radial Pipe Strains in the Unreinforced Section (Test 11)

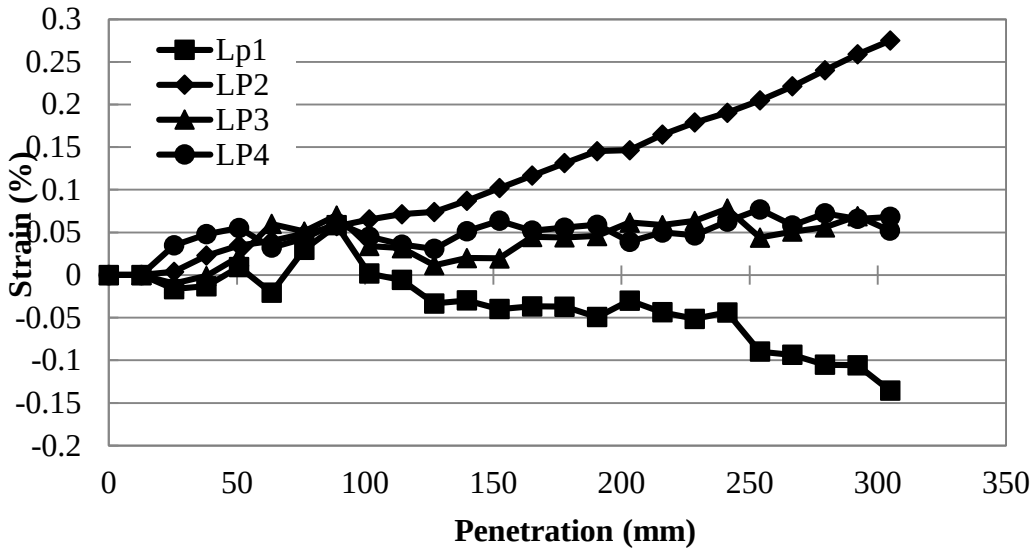

Figure D.15 Longitudinal Pipe Strains in the Unreinforced Section (Test 11)

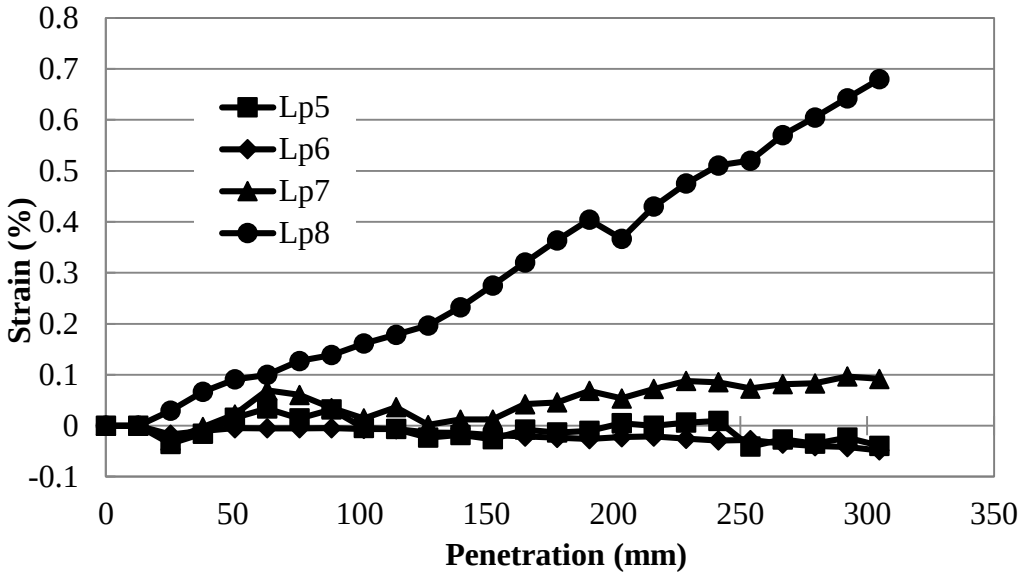

Figure D.16 Longitudinal Pipe Strains in the Unreinforced Section (Test 11)

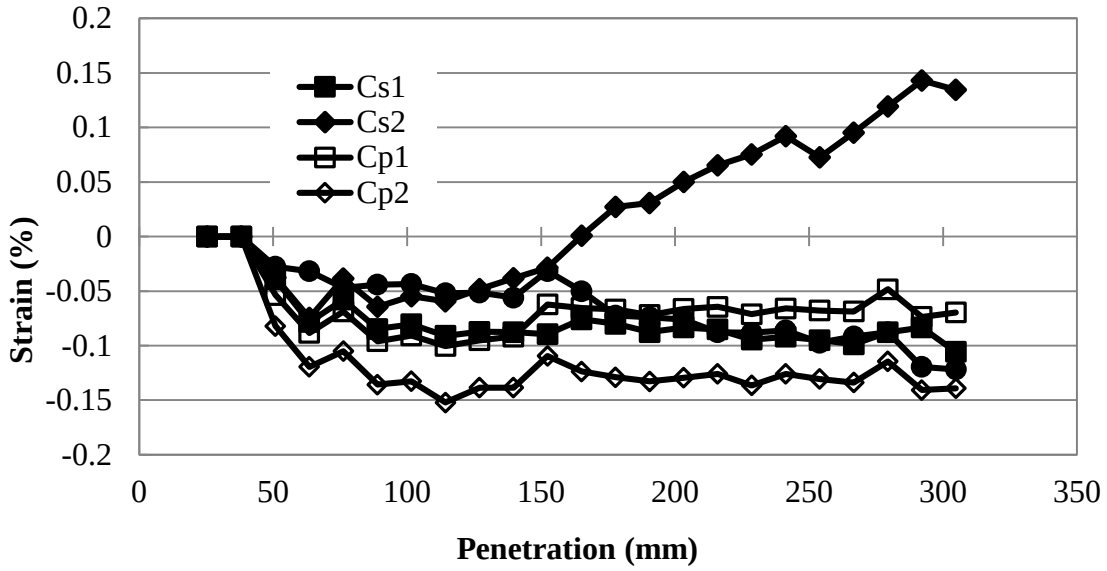

Figure D.17 Circumferential Pipe Strains in the Single Geogrid-Reinforced Section (Test 12)

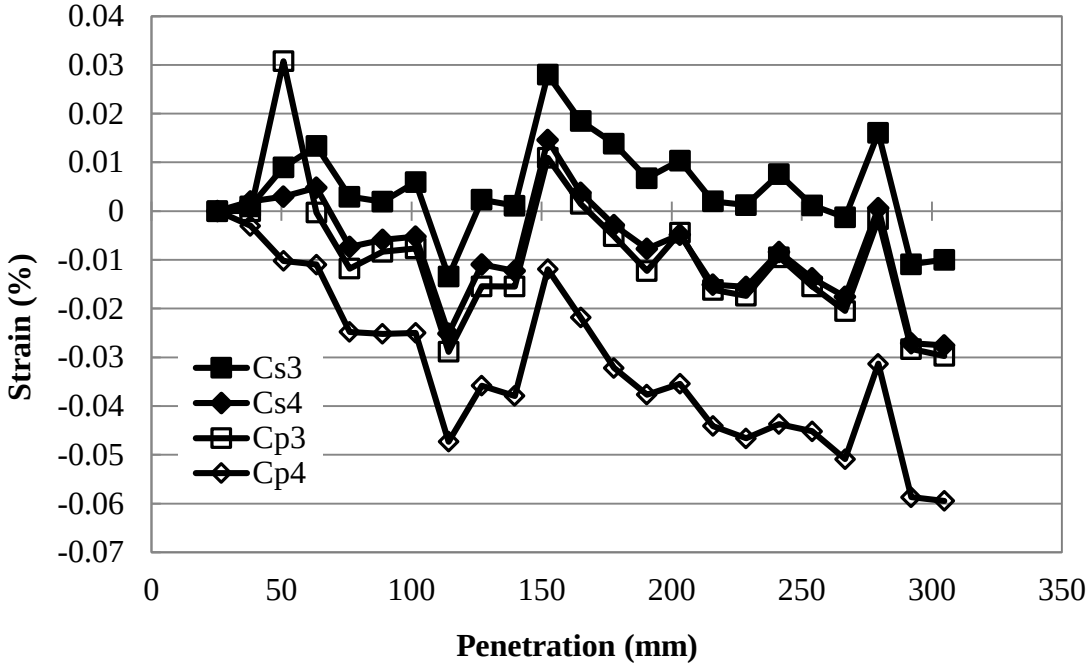

Figure D.18 Circumferential Pipe Strains in the Single Geogrid-Reinforced Section (Test 12)

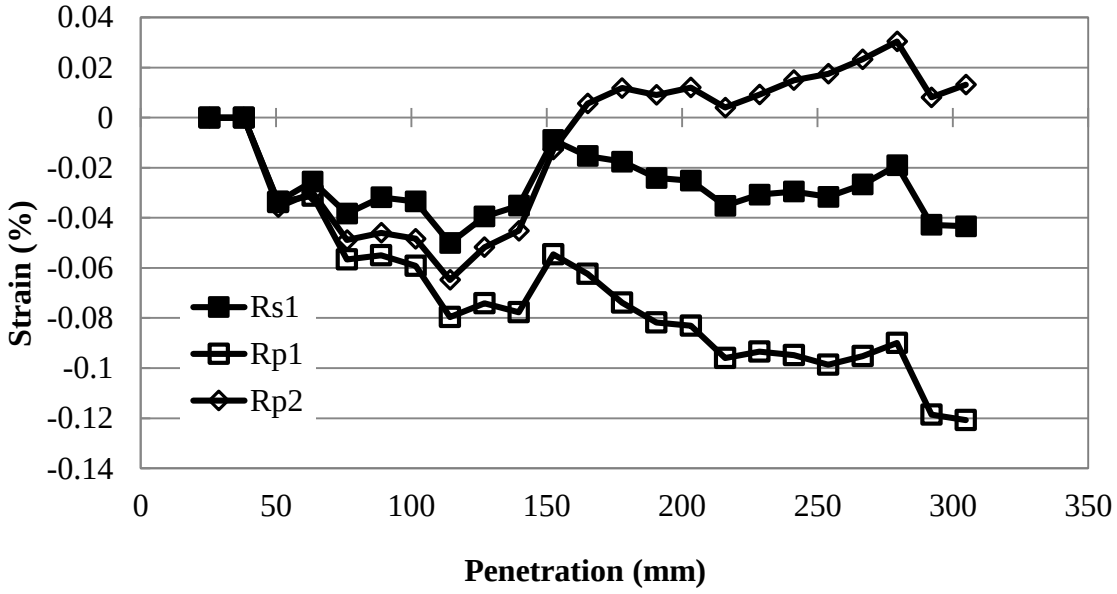

Figure D.19 Radial Pipe Strains in the Single Geogrid-Reinforced Section (Test 12)

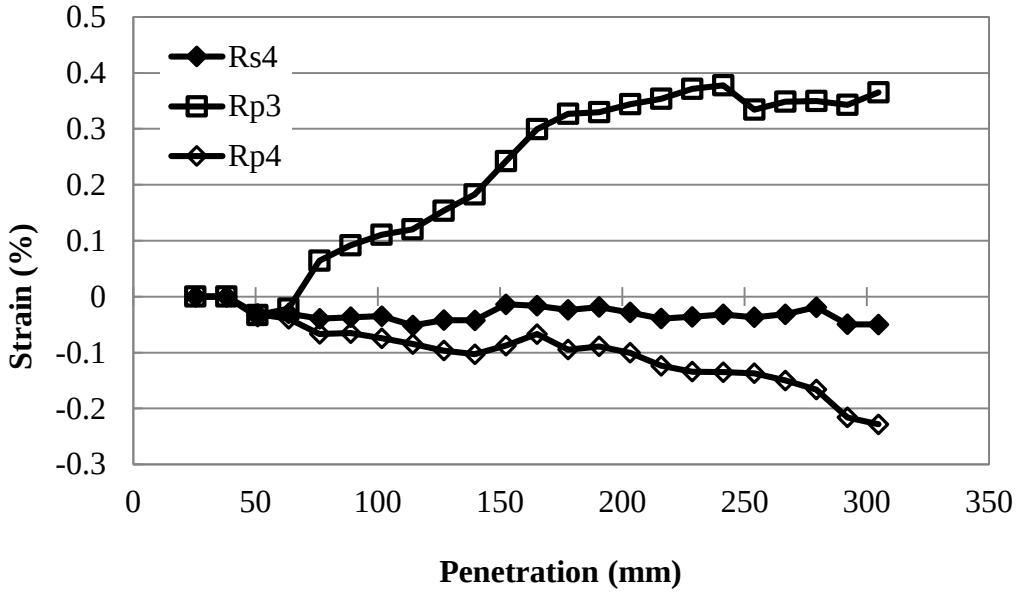

Figure D.20 Radial Pipe Strains in the Single Geogrid-Reinforced Section (Test 12)

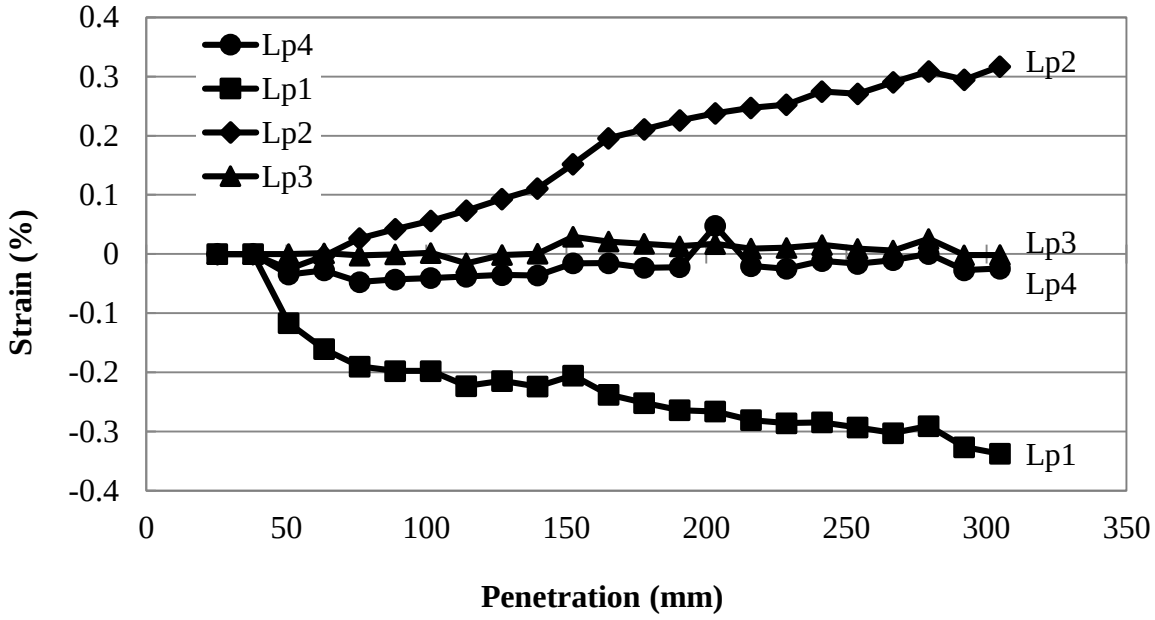

Figure D.21 Radial Pipe Strains in the Single Geogrid-Reinforced Section (Test 12)

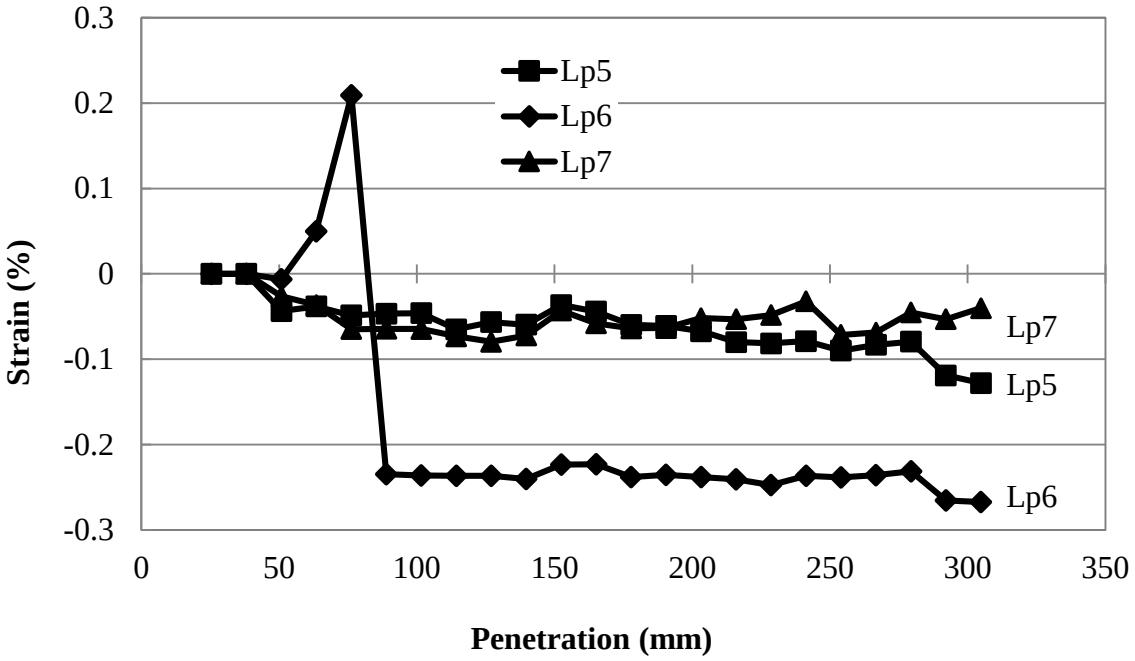

Figure D.22 Radial Pipe Strains in the Single Geogrid-Reinforced Section (Test 12)

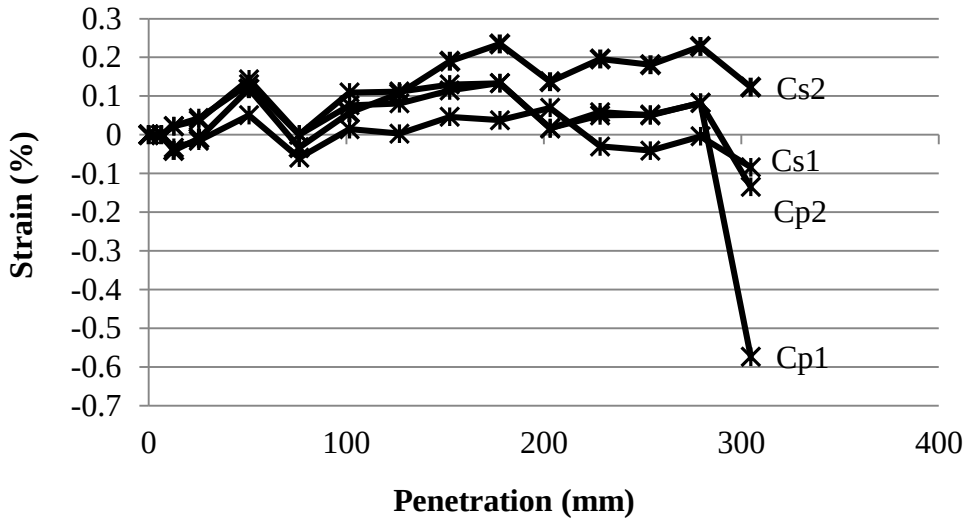

Figure D.23 Circumferential Pipe Strains in the Double Geogrid-Reinforced Section (Test 13)

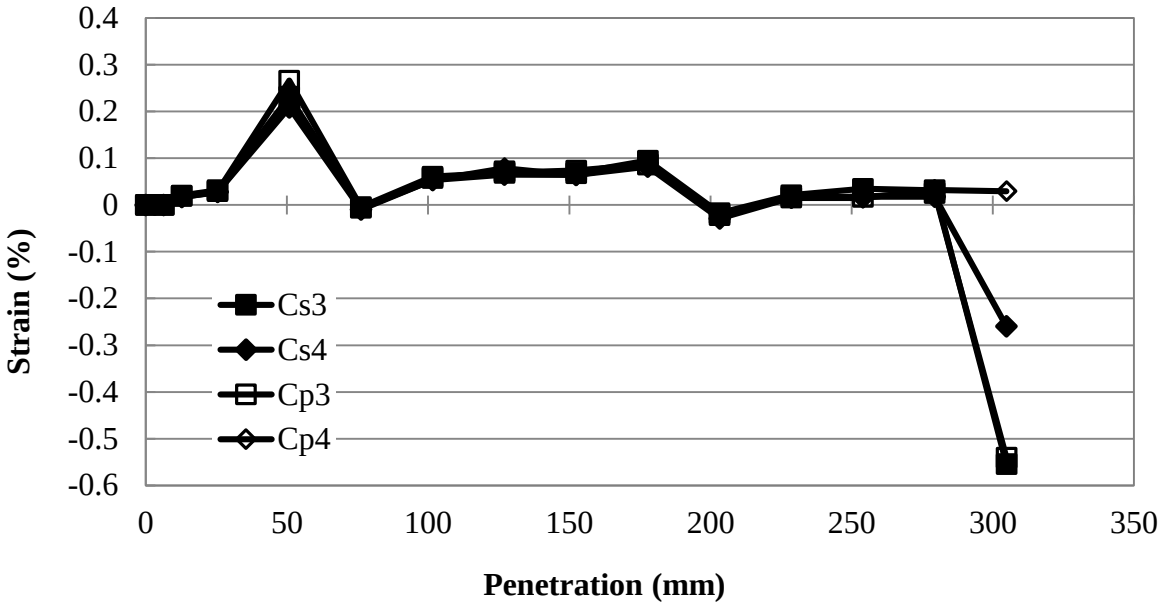

Figure D.24 Circumferential Pipe Strains in the Double Geogrid-Reinforced Section (Test 13)

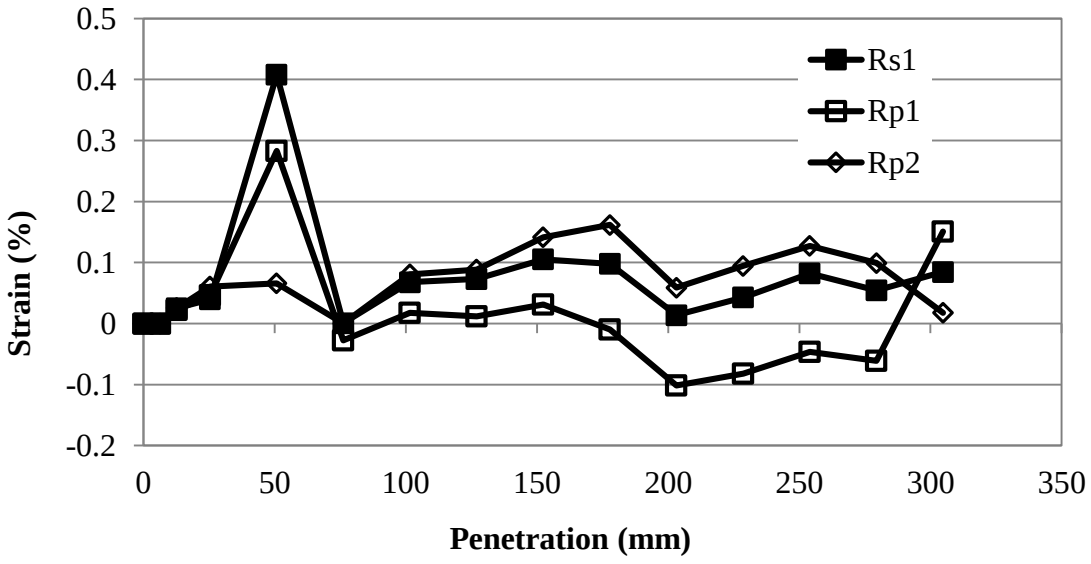

Figure D.25 Radial Pipe Strains in the Double Geogrid-Reinforced Section (Test 13)

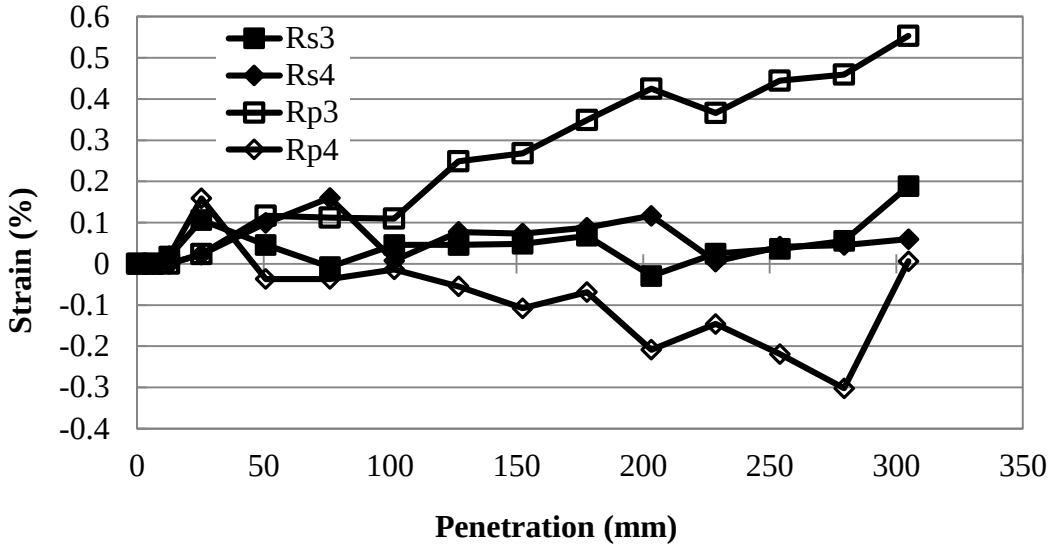

Figure D.26 Radial Pipe Strains in the Double Geogrid-Reinforced Section (Test 13)

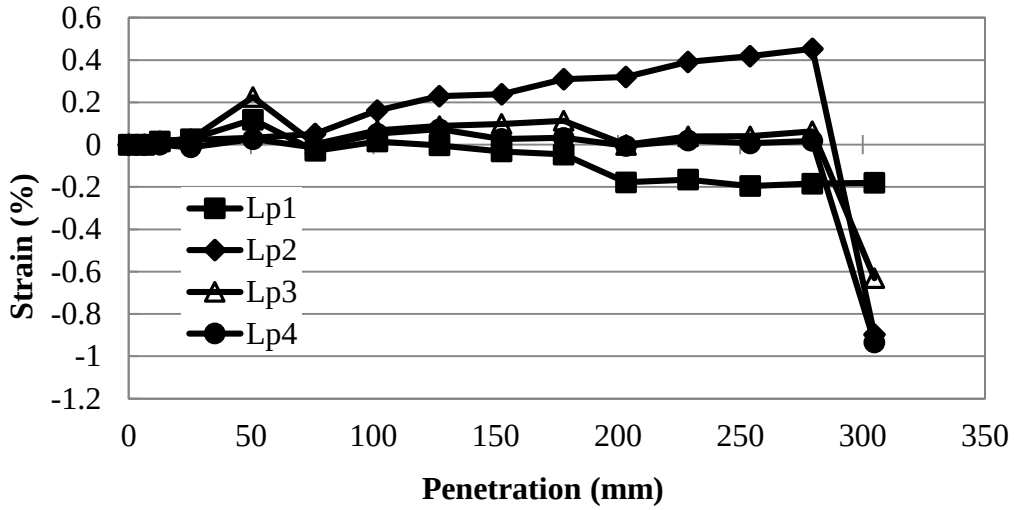

Figure D.27 Longitudinal Pipe Strains in the Double Geogrid-Reinforced Section (Test 13)

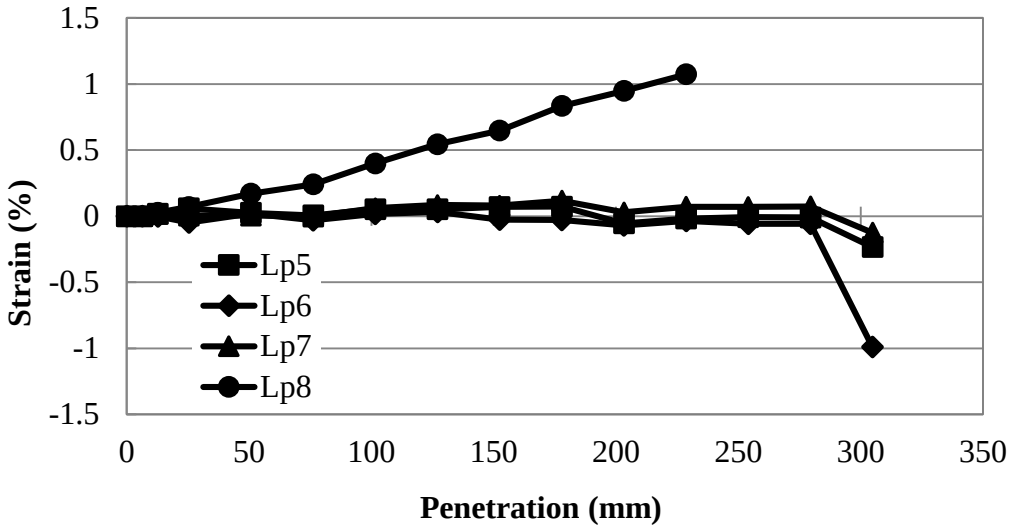

Figure D.28 Longitudinal Pipe Strains in the Double Geogrid-Reinforced Section (Test 13)

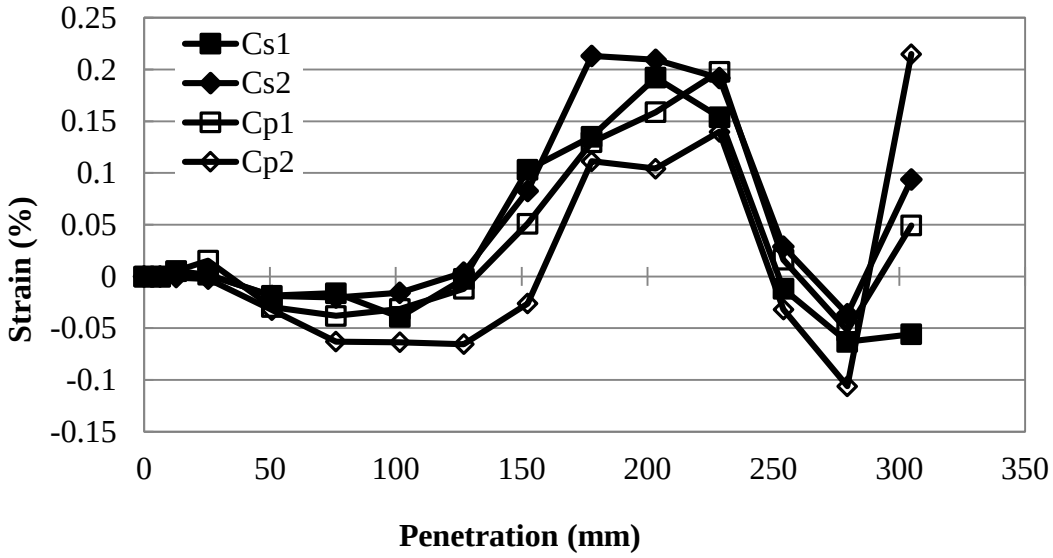

Figure D.29 Circumferential Pipe Strains in the Inverted U-Shape Geogrid-Reinforced Section (Test 14)

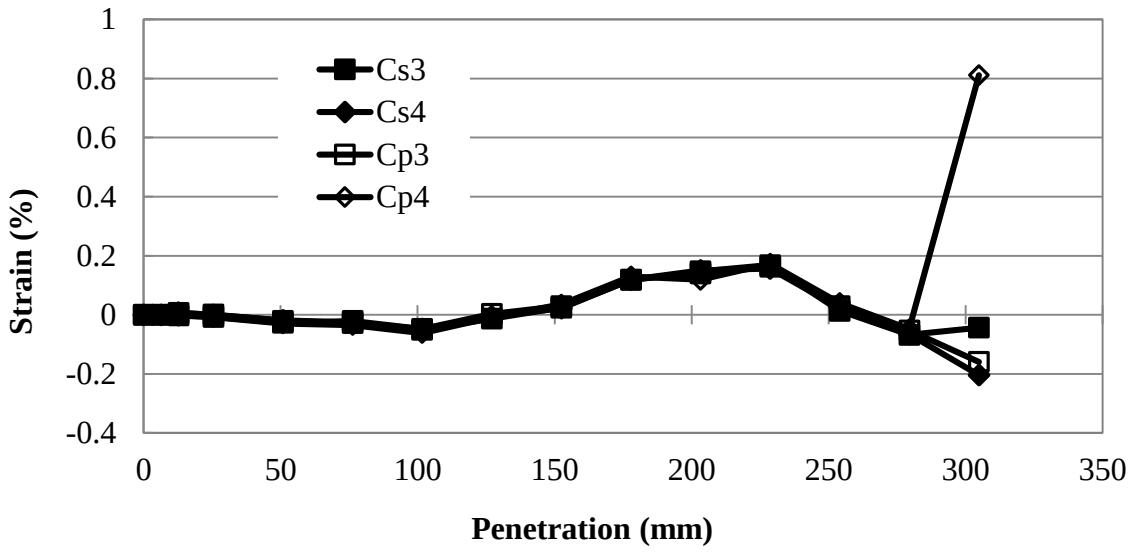

Figure D.30 Circumferential Pipe in the Inverted U-Shape Geogrid-Reinforced Section (Test 14)

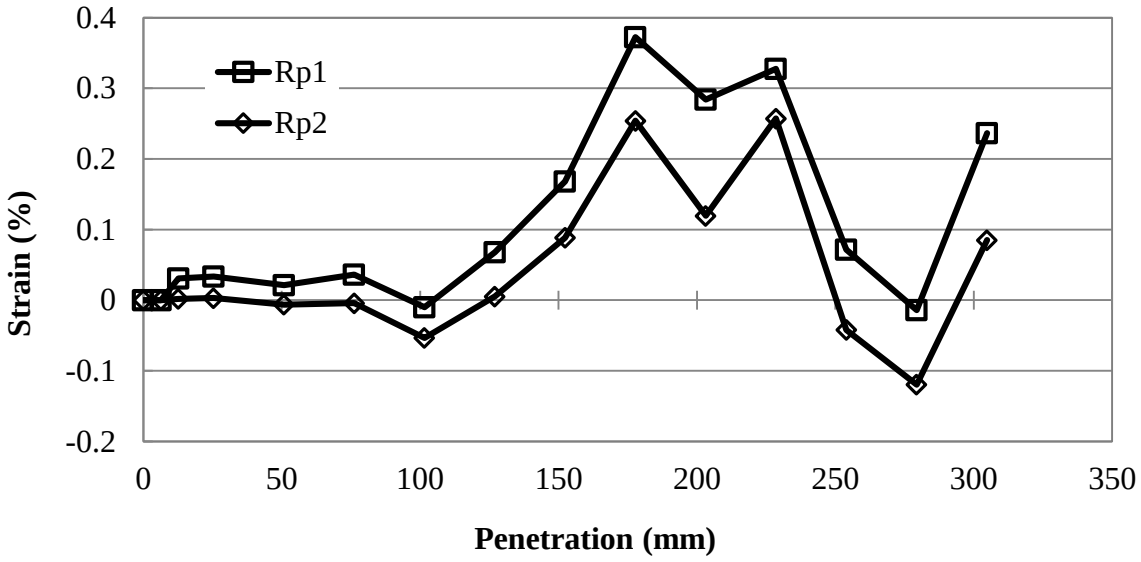

Figure D.31 Radial Pipe Strain in the Inverted U-Shape Geogrid-Reinforced Section (Test 14)

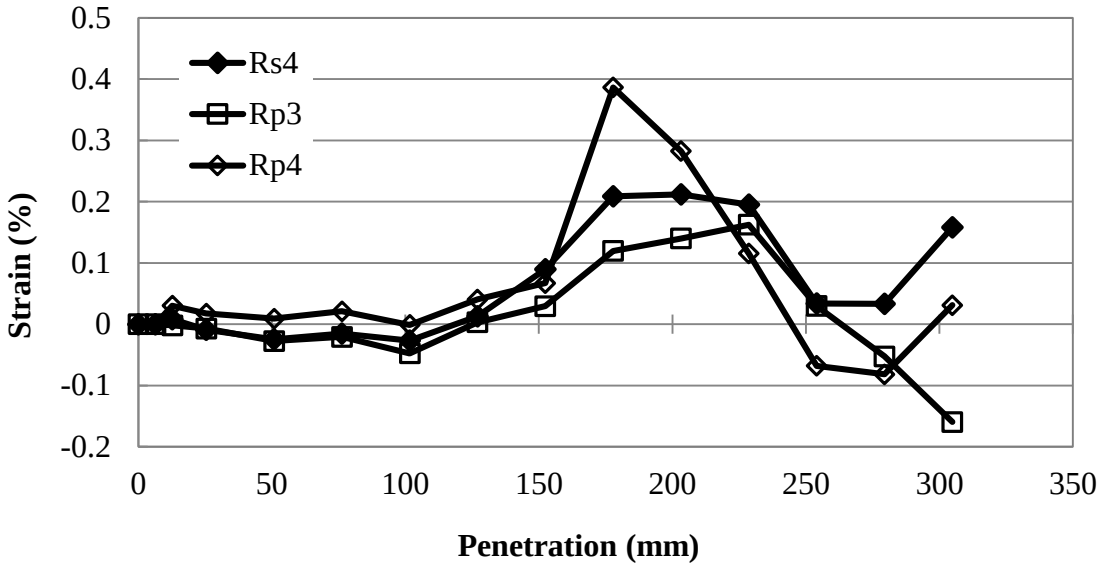

Figure D.32 Radial Pipe Strains in the Inverted U-Shape Geogrid-Reinforced Section (Test 14)

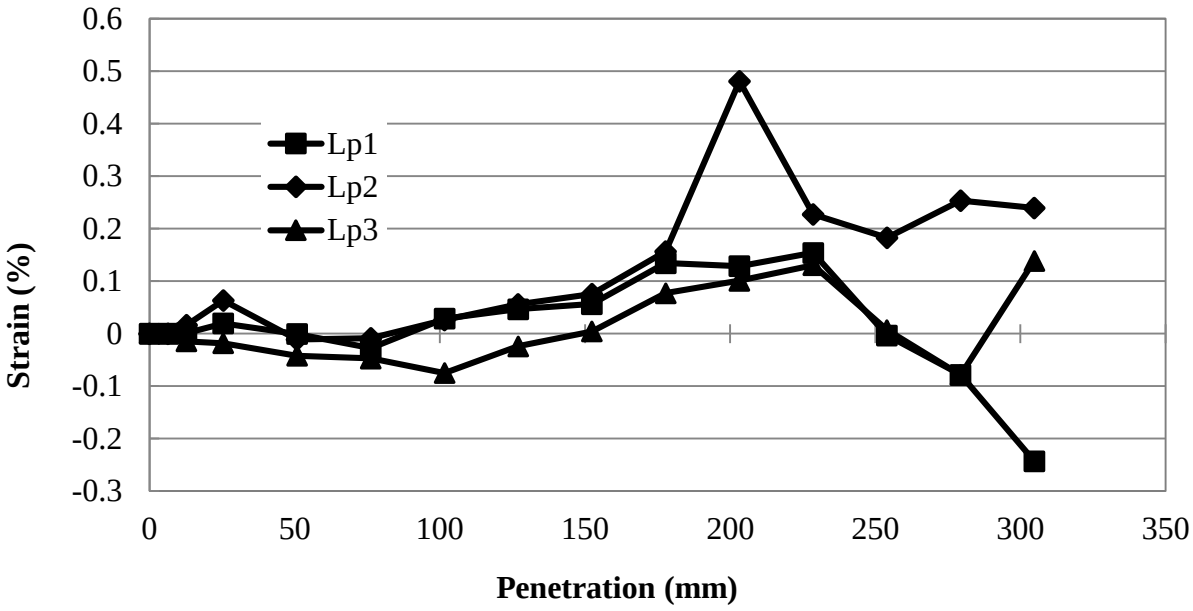

Figure D.33 Longitudinal Pipe Strains in the Inverted U-Shape Geogrid-Reinforced Section (Test 14)

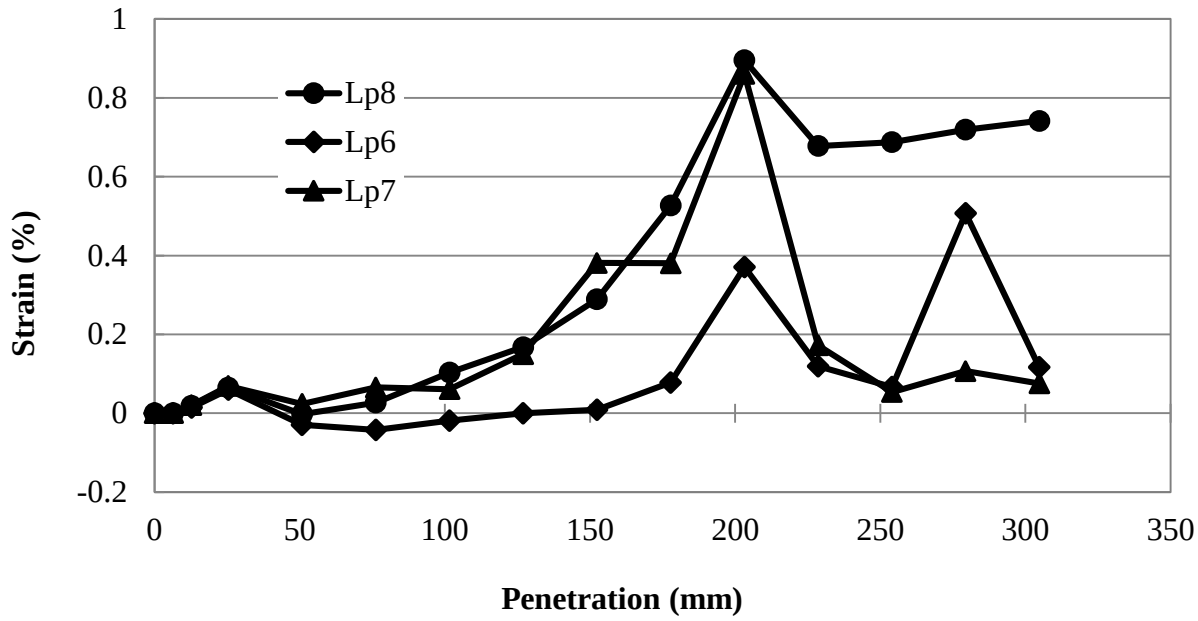

Figure D.34 Longitudinal Pipe Strains in the Inverted U-Shape Geogrid-Reinforced Section (Test 14)

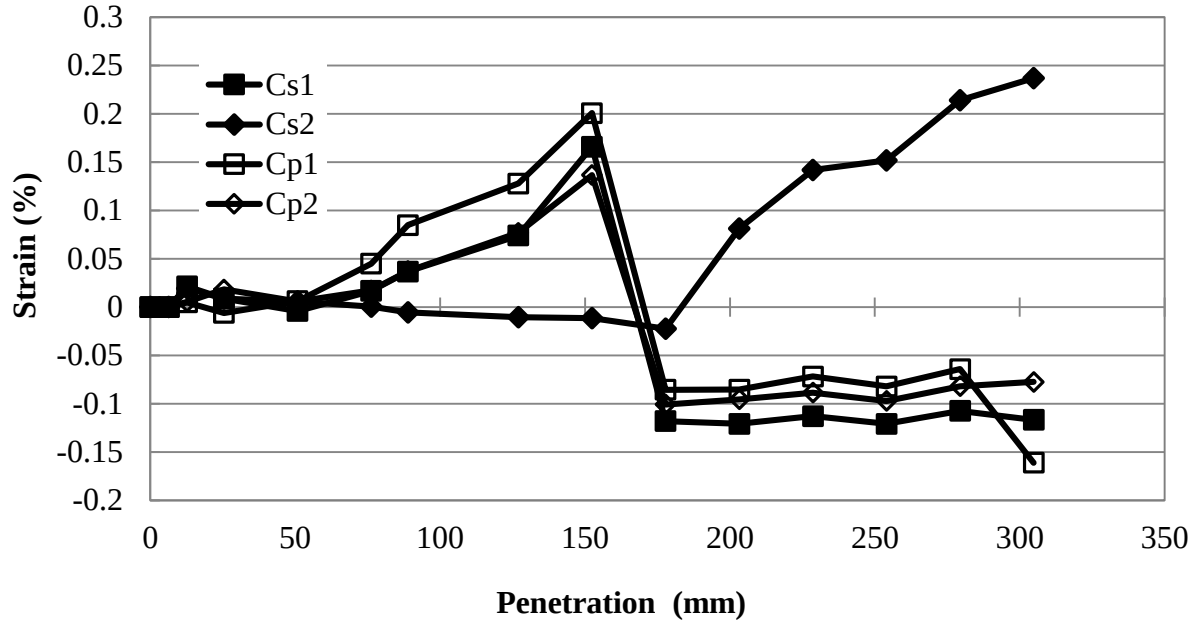

Figure D.35 Circumferential Pipe Strains in the Wrapped-around Geogrid-Reinforced Section (Test 15)

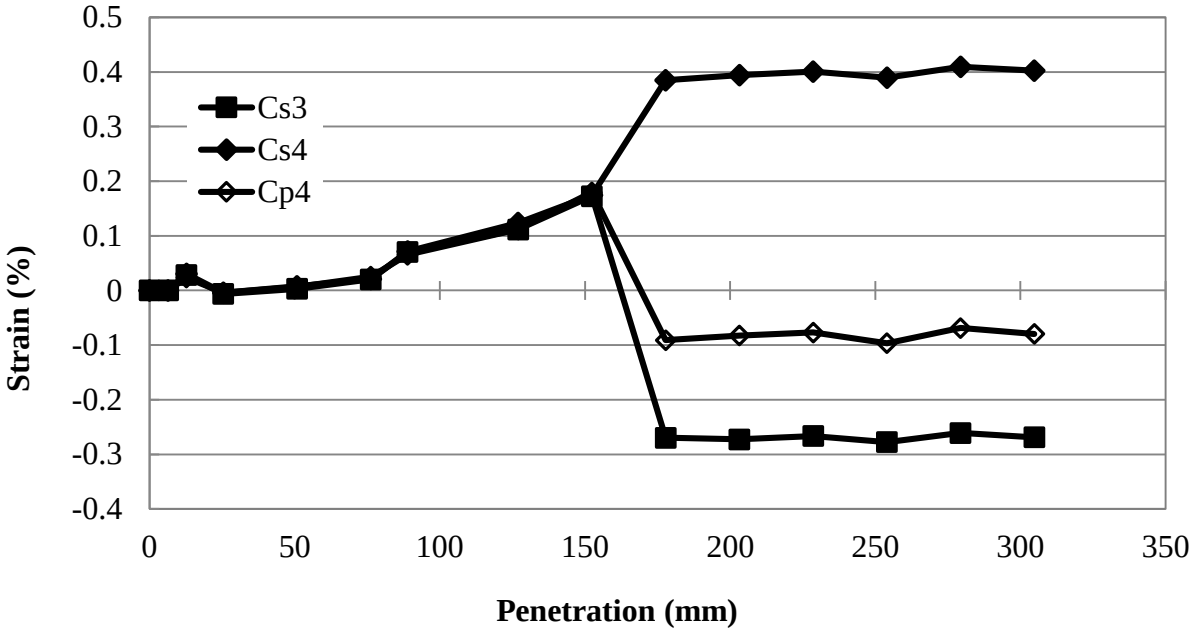

Figure D.36 Circumferential Pipe Strains in the Wrapped-around Geogrid-Reinforced Section (Test 15)

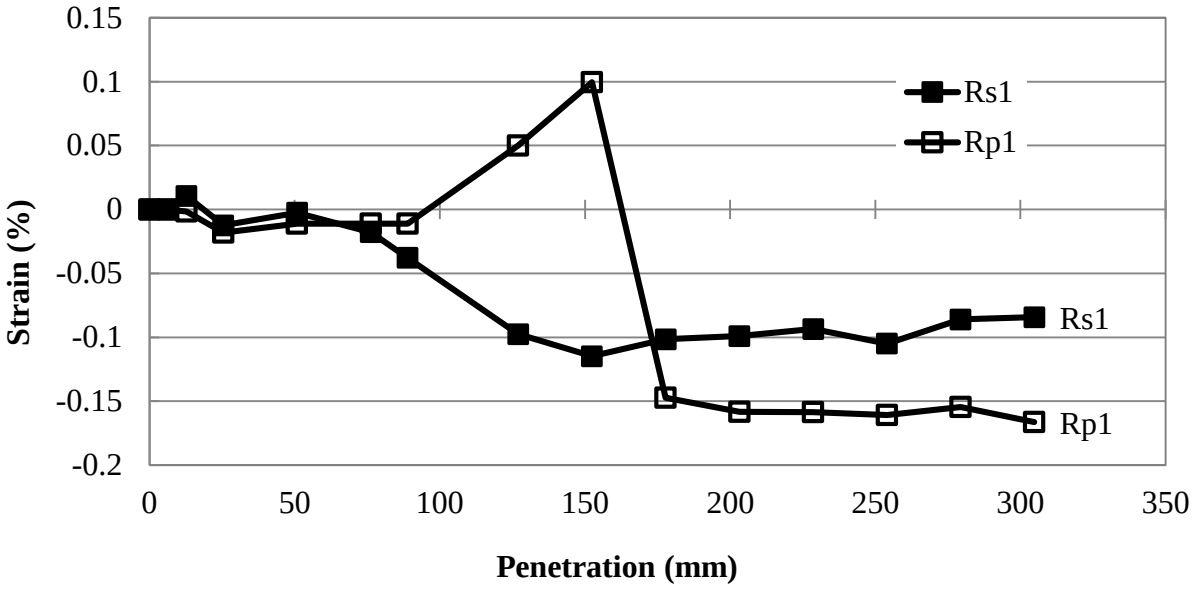

Figure D.37 Radial Pipe Strains in the Wrapped-around Geogrid-Reinforced Section (Test 15)

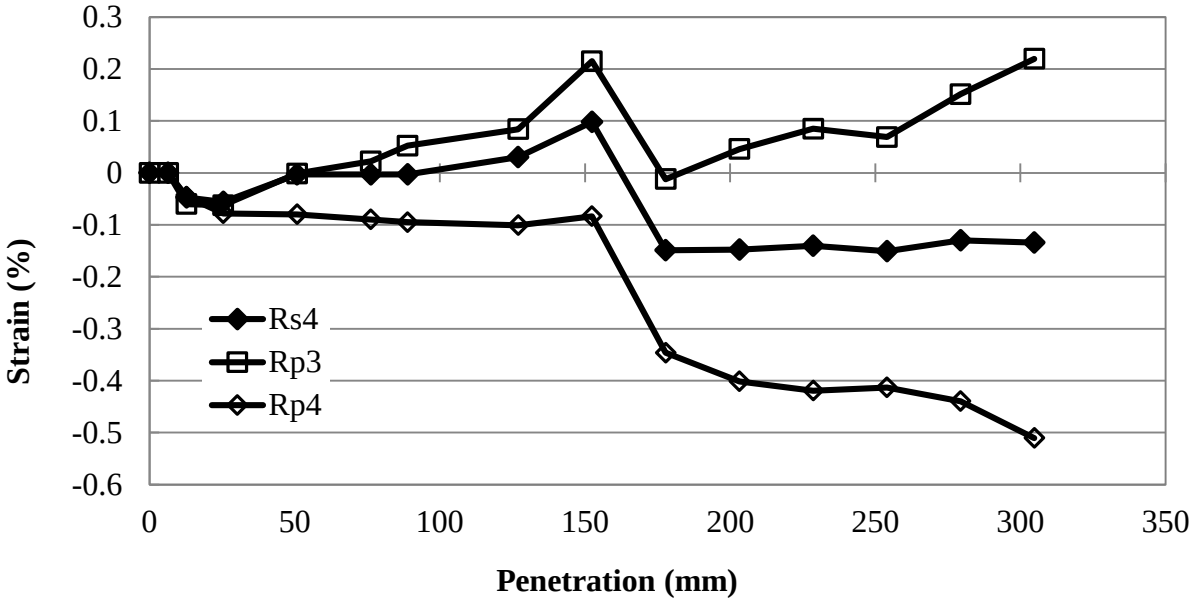

Figure D.38 Radial Pipe Strains in the Wrapped-around Geogrid-Reinforced Section (Test 15)

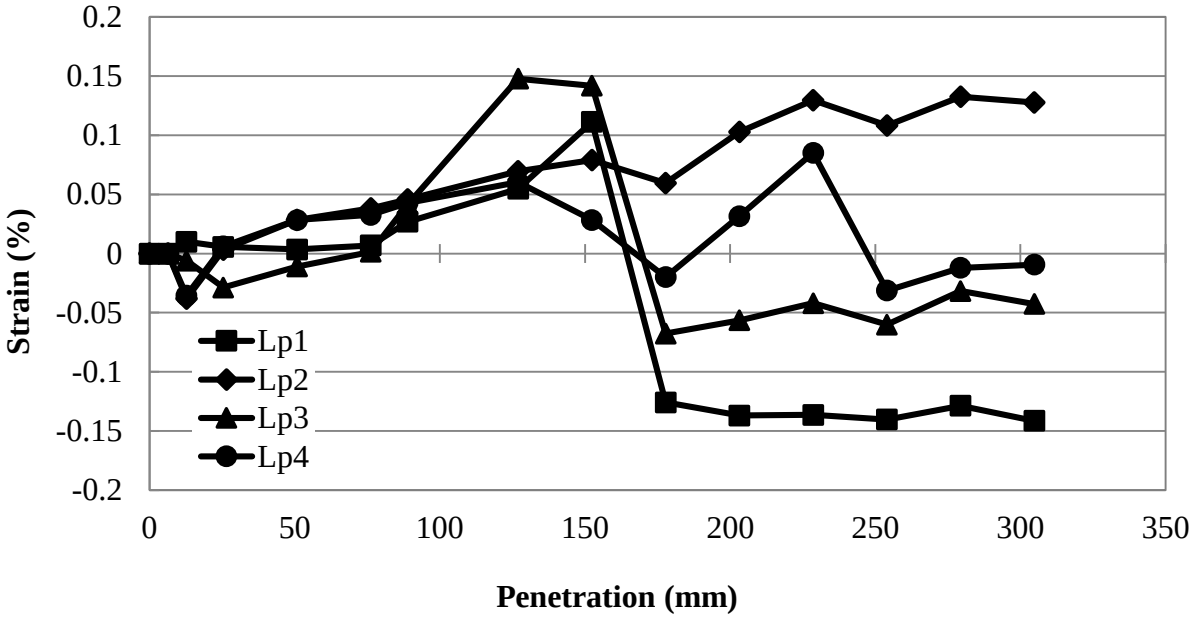

Figure D.39 Radial Pipe Strains in the Wrapped-around Geogrid-Reinforced Section (Test 15)

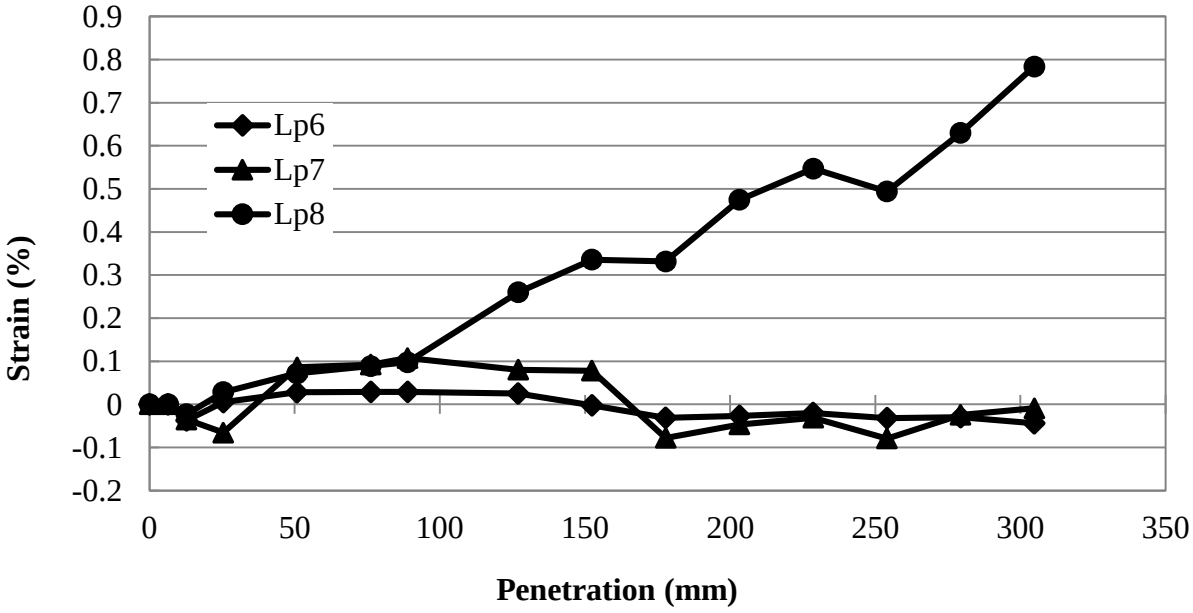

Figure D.40 Longitudinal Pipe Strains in the Wrapped-around Geogrid-Reinforced Section (Test 15)